

Fatigue Crack Growth Mechanisms in Al-Si-Mg Alloys

by

Diana Aida Lados

A Dissertation

Submitted to the Faculty

of the

WORCESTER POLYTECHNIC INSTITUTE

in partial fulfillment of the requirements for the

Degree of Doctor of Philosophy

in

Materials Science and Engineering

by

Diana Lados

January 2004

APPROVED:

Diran Apelian

Professor Diran Apelian, Materials Science and Engineering, Advisor

RD Sisson

Professor Richard D. Sisson, Materials Science and Engineering, Department Head

M. M.

Professor Makhlof M. Makhlof, Materials Science and Engineering

Satya Shivkumar

Professor Satya Shivkumar, Materials Science and Engineering

Peggy E. Jones

Dr. Peggy E. Jones, General Motors Powertrain

J. F. Major

Dr. Fred J. Major, Alcan International Ltd.

To
My Parents,
Julietta and Dumitru Lados

SUMMARY

In recent years, alloy microstructure, in relation to both crack initiation and propagation, has gained much attention considering that advanced casting techniques such as squeeze casting, thixocasting, rheocasting, etc. give rise to significantly fewer defects than conventional cast structures. Moreover, new developments in conventional casting technologies have significantly lowered the defect levels (especially in critically loaded areas). Under these circumstances predictive models based on the amount, size, and morphology of casting defects are neither as accurate nor as relevant to the alloys' behavior characterization. Thus, the understanding of the alloys' response based on crack-microstructure interactions becomes imperative for the development of predictive models. This research work was initiated to establish the active mechanisms at the microstructural level during dynamic loading and failure of conventional and SSM Al-Si-Mg alloys; the approach taken was based on a microstructural deconstruction/reconstruction model.

Al-Si-Mg alloys with Si level between 1 to 13% were specifically designed to separate out the major constituent phases, namely, α -Al dendrites and Al/Si eutectic phase. Five conventional alloys were designed to target first the α -Al dendritic structure (1%Si alloy), then the Al/Si eutectic phase (13%Si alloys), and finally a mixture of these two phases as found in A356 (7%Si alloys). The role of these constituent phases, as well as the effect of the Mg-Si strengthening precipitates were mechanistically investigated to relate microstructure to cracks' near threshold propagation (ΔK_{th} regime or Region I), Paris propagation regime (Region II), and fast growth mode (Region III). This was done for alloys having different Si composition/morphology, grain size level, dendrite arm spacing, and heat treatment. To reveal the importance of microstructure, porosity/inclusions levels were tightly controlled through appropriate molten metal practices.

In addition, a complex analysis of the Linear Elastic Fracture Mechanics (LEFM) and Elastic-Plastic Fracture Mechanics (EPFM/J-integral) approaches was performed to evaluate their applicability to ductile alloys and to delineate the validity boundaries for LEFM. A procedure to evaluate the "actual" as opposed to "pseudo" fracture toughness of the material from fatigue crack growth testing data was successfully developed.

Furthermore, the importance of residual stress-microstructure interactions, previously overlooked by researchers in the field, was clearly defined and accounted for both experimentally (by adjusting the quenching or testing procedures), and mathematically by corrective models. These findings were submitted to ASTM E647 committee, and are expected to be incorporated in a future specification revision.

Fatigue crack growth tests under various loading conditions were performed on compact tension CT specimens with both high and low residual stress. The study included tests at $R=0.1$, $R=0.8$, and constant K_{max} . All samples were tested at room temperature (75°F) in air with a relative humidity of 40-50%. The tests were conducted under K-control, first under a decreasing crack driving force range (Region I) to evaluate the thresholds, and then under increasing crack driving force range (Regions II and III). Above 10^{-5} inches/cycle, the tests were continued using a shallower K-gradient to obtain the steeper Region III data. Because valid crack growth specimens per ASTM E647 do not always meet the requirements for a plane strain fracture toughness test, the upper limit of the crack driving force corresponding to propagation rates faster than 0.025 in/cycle was considered the "pseudo" fracture toughness. The "pseudo" fracture toughness results were corrected for plasticity and tearing effects to estimate the true upper bound fracture toughness based on J_{max} criteria. The compliance technique was used to monitor the crack advance and the frequency was set to 25 Hz (except in Region III when it was decreased as low as 0.1 Hz to capture sufficient data points). After the fatigue crack growth tests were terminated, the fracture surfaces as well as the side views of the fracture path at mid-thickness were viewed and analyzed using optical microscopy and SEM.

Based on the aforementioned examinations and the established fatigue crack growth mechanisms at the microstructural level, the following main conclusions are drawn:

- The near threshold regime is controlled by closure phenomena mainly induced by residual stress and microstructure induced roughness. When residual stresses are high, they mask microstructural effects. When residual stress is reduced (below certain levels), the effect of microstructure becomes evident and a threshold ranking dependent on the Si level was observed: the higher the Si content, the lower the roughness induced closure level, and the lower the crack growth threshold respectively.
- In the Paris region (Region II), the effects of crack closure become less significant, and the fatigue crack growth mechanisms become strongly dependent on the matrix strength and the interface strength between primary α -Al structure and eutectic Si particles. With increasing ΔK from lower Region II to upper Region II and Region III, the fracture surface roughness increases. This increase is associated with a change in fatigue crack growth mechanisms. The change in mechanisms was explained using correlations of the plastic zone size at various ΔK levels with the microstructural features enclosed in it. Small plastic zones, in lower Region II, restrict the availability of damaged Si particles (or interfaces

with the Al matrix), and therefore restrain the possibility of crack meandering. This corresponds to a flat appearance of the crack propagating through the α -Al dendritic structure with sporadic Si encounters. In higher Region II, however, the larger plastic zone size permits crack meandering through severely damaged Si particles away from the crack front, and this results in a preferential growth through the Al-Si eutectic regions.

- In Region III, crack advances exclusively through the large Al-Si eutectic regions and ductile tearing becomes the dominant mechanism at high ΔK . A direct correlation between the Si particles' morphology and fracture toughness was observed (coarser and more irregular Si particles yield lower toughness). At high ΔK levels, fatigue crack growth behavior of cast Al-Si-Mg alloys is less accurately described by Elastic Fracture Mechanics definitions, and instead Elastic-Plastic Fracture Mechanics (J-integral) concepts need to be applied. As a result of plasticity and tearing corrections, the "actual" fracture toughness of the materials inferred from J_{\max} can be directly determined from fatigue crack growth tests.

ACKNOWLEDGEMENTS

My first and most grateful thoughts are directed to my teacher and advisor, Prof. Diran Apelian, for his sustained support and encouragement throughout my studies at WPI. His mentorship and friendship have always been a major source of professional and personal inspiration, making this journey a wholly satisfying experience. This has imparted to me a drive to excel, to explore my potential at so many levels, and in so many ways. It has been an honor and a pleasure knowing him, working with him, and learning from him.

A most heartfelt note goes to Dr. Peggy Jones of General Motors and Dr. Fred Major of Alcan for their significant contributions, continuous guidance, and valuable technical assistance during the entire duration of the study. Thank you for offering me your support and enduring, unremitting friendship!

Very special thanks are addressed to Mr. Keith Donald of Fracture Technology Associates for his active participation in this work, and his important contribution to the residual stress and Elastic Plastic Fracture Mechanics issues.

Dr. Libo Wang's assistance to the castings preparation is greatly appreciated.

My thanks go to Prof. Richard D. Sisson Jr. and Prof. Satya Shivkumar for their valuable input, and for serving on my dissertation committee.

I would like to thank General Motors Corp. for partly supporting the fatigue crack growth testing and Alcan for providing high purity aluminum needed in this work.

I would also like to thank Palmer Foundry, especially Mr. Doug Bator, Mr. Bob Logan, and Mr. Bill Towlson, for their expertise to the mold design and preparation of the molds.

Lastly, and most importantly, I want to thank the consortium members of the Advanced Casting Research Center and the director of the center, Prof. Makhlof, for their support of this research study, and for their mentorship. The saying that "it takes a whole village to raise a child" is certainly an appropriate metaphor for my educational experience at the Metal Processing Institute and the mentoring I received. Thank you!

TABLE OF CONTENTS

SUMMARY	i
ACKNOWLEDGEMENTS	iv
TABLE OF CONTENTS	v
INTRODUCTION	1
Chapter 1: Fatigue Performance of High Integrity Cast Aluminum Components	5
Chapter 2: Fatigue Crack Growth Characteristics in Cast Al-Si-Mg Alloys – Part I: <i>Effect of Processing Conditions and Microstructure</i>	26
Chapter 3: The Effect of Residual Stress on the Fatigue Crack Growth Behavior of Cast Al-Si-Mg Alloys – <i>Mechanisms and Corrective Mathematical Models</i>	48
Chapter 4: Validity Limits for Elastic Definitions in Cast Al-Si-Mg Alloys with Enhanced Plasticity – Linear Elastic Fracture Mechanics versus Elastic/Plastic Fracture Mechanics	77
Chapter 5: Operating Fatigue Crack Growth Mechanisms at the Microstructure Level in Al-Si-Mg Cast Components	109
Chapter 6: Fatigue Crack Growth Characteristics in Cast Al-Si-Mg Alloys – Part II: <i>Life Predictions Using Fatigue Crack Growth Data</i>	153
CONCLUSIONS	175
FUTURE WORK	178

INTRODUCTION

Due to the increasing use of cast aluminum components in automotive and aerospace applications that involve cyclic loading, fatigue and fatigue crack growth characteristics of aluminum castings are of great interest. In this context, in 1996, a project on fatigue performance interactions in aluminum casting alloys was initiated at the Advanced Casting Research Center (ACRC) at Worcester Polytechnic Institute with Dr. Qigui Wang (former research scientist at ACRC and current member of GM Powertrain's research team). During this initial study, entitled "Fatigue Performance Interactions in Aluminum Casting Alloys", the effects of casting defects and alloy chemistry on the fatigue behavior of A356/357 cast alloys were studied in great detail and significant causal relationships were developed. However, and despite the extensive research efforts dedicated to this topic, a fundamental mechanistic understanding of the behavior of these alloys when subjected to dynamic loading was still lacking. As a result, in May 2000, the work on fatigue was taken to the next level, to establish the operating fatigue crack growth mechanisms during dynamic loading and failure of Al-Si-Mg cast components.

The motivation for this research was to design Al-Si-Mg alloys with enhanced fatigue crack growth response based on an understanding of the mechanism of failure, considering the effects of an alloy's major constituents and applied temps. The ultimate goal was to establish a set of critical tools (parameters) allowing the designer to optimize alloys for a specific application. In order to attain these targets, the following objectives were established:

- *Develop a fundamental understanding of the effects of microstructural constituents (α -Al dendrites, Al/Si eutectic phase, and Mg_2Si strengthening precipitates) on fatigue crack growth resistance of cast Al-Si-Mg alloys.*
- *Predict fatigue crack growth in Al-Si-Mg alloys, and establish the critical design parameters at the microstructure level.*
- *Optimize the alloys microstructural architecture for fatigue resistance in various applications.*
- *Perform a parallel analysis Linear Elastic Fracture Mechanics (LEFM) vs. Elastic Plastic Fracture Mechanics (EPFM) to delineate the applicability boundaries of LEFM for alloys with enhanced ductility.*
- *Understand the effect of residual stress on fatigue crack growth behavior and decouple this effect from the total fatigue crack growth response.*

To meet these objectives, the microstructural architecture of an A356/357 alloy was deconstructed into its major constituent phases (each constituent phase being represented by a separate alloy) to shed light on each individual effect.

Specifically, five model alloys were designed, targeting the Al dendritic structure (1%Si), the Al/Si eutectic phase (13%Si), and a mixture of both phases as found in A356/357 (7%Si). For this study, the primary and eutectic Al in all alloys have a similar strength (based on a consistent microhardness) such that, when growing through the Al phase, the incoming crack faces the same matrix resistance. Based on an extensive aging treatment study, an artificial aging time of 12 hrs. was selected for all the alloys. The eutectic containing alloys (7 and 13%Si) were investigated in both unmodified and Sr-modified conditions. A separate investigation was conducted to select the adequate solution treatment time that preserves the characteristic Si morphology of the unmodified alloys, especially in 7%Si alloys. As a result of this investigation, the optimum solution treatment time was found to be 1.5 hrs.

Agitated room temperature water initially used for quenching left a significant level of residual stress in the samples; the lower the Si content the higher the residual stress. The presence of residual stress considerably affected the fatigue crack growth behavior of all alloys, and interfered with the mechanistic understanding of the microstructural constituents' effects. Therefore, a different quenching procedure, "uphill quench", was designed to produce residual stress free samples.

This "uphill quench" method uses a liquid nitrogen-boiling water reverse quench to eliminate residual stresses from the samples. The concept of an up-hill quench is based on the rationale that by developing thermal gradients (residual stresses) of an opposite nature one can counteract and cancel the original quenching stresses. The residual stress level in the CT specimens after the uphill quench was found to be near zero.

The results of this study are presented in six chapters, and each chapter consists of a paper (Journal manuscript) covering key findings in a specific area of the study, as well as a thorough literature review on the theme of that chapter. Each of these six chapters is briefly presented below.

Chapter 1 presents a general literature review on fatigue emphasizing the hierarchic effects of casting defects (when porosity and pore size are reduced below certain values, oxide films become the major factor controlling fatigue life), the impact of microstructural constituents and alloy chemistry on the fatigue life, the role of heat treatment, etc. In addition, the effects of residual stress and increased ductility are briefly reviewed.

Chapter 2 is an integrated study of the effects of microstructure on fatigue crack growth in cast Al-Si-Mg alloys. The role of the amount of Al-Si eutectic, α -Al primary phase, Si size/shape (dictated by the unmodified vs. Sr-modified

conditions), SDAS, grain size, matrix microhardness/ability to yield (as a result of two heat treatments T61 and T4), loading conditions, were investigated. Because the presence of residual stresses can overshadow the microstructural effects on the fatigue crack growth behavior of cast Al-Si-Mg alloys, residual stress-microstructure interactions were investigated. In addition, the effects of casting technology and the resulting changes in microstructure were studied through a comparison of the fatigue crack growth behavior of conventionally cast and semi-solid processed materials (SSM) of similar compositions.

Chapter 3 is concentrated exclusively on the effects of residual stress (resulting from quenching, as part of a T61 heat-treatment procedure) on the fatigue crack growth response of the studied alloys. The chapter is divided in three sections corresponding to three different ways of obtaining residual stress free data from fatigue crack growth experiments. In the first part, the behavior of compact tension specimens, with low and high residual stresses are analyzed, and fatigue crack thresholds are determined from the experimental data. In the second part, two methods to mathematically compensate for the presence of residual stress are developed. In the last part, two methods to produce residual stress free samples are introduced and the corrective methods are verified. Moreover, a method to predict residual stress distribution without physical measurements by simply using K_{res} data and weight functions is assessed through numerical integration techniques.

Chapter 4 provides a comparative analysis between the linear elastic stress intensity factors range, ΔK_{el} , a crack tip plasticity adjusted linear elastic stress intensity factors range, $\Delta K_{eff(pl)}$, and an elastic/plastic, J-integral based, stress intensity factor range, ΔK_J . ΔK_J was computed from load-displacement records captured during fatigue crack growth testing and accounts for "cumulative" cyclic damage. The "pseudo" fracture toughnesses evaluated through these three methods are finally compared to the limiting, upper bound fracture toughness of the materials determined from static fracture toughness tests, $\Delta K_{FT(J_{max})}$. A method to evaluate the limiting, upper bound fracture toughness of the material from fatigue crack growth experiments was developed and validated. A new relationship used to determine plastic zone size considering combined effects of plane strain and plane stress conditions was introduced and employed to compute plasticity corrected stress intensity factor ranges, ΔK_{eff} . A procedure to decouple and partition plasticity and tearing effects on crack growth is discussed. The static, tearing contributions are separated out by comparing the results of the two non-linear approaches in conjunction with the J_{IC} values.

Chapter 5 is directed towards establishing the operating mechanisms in the near threshold regime when crack closure (residual stress and roughness-microstructure induced) has a significant contribution, as well as in the Paris propagation regime (Region II), and fast propagation stage (Region III) where

significant changes in the local crack growth mechanisms were observed. These changes are explained at the microstructure level by the increase in the damaged zone (plastic zone) ahead of the crack tip with the increase in crack driving force and crack length. The type and amount of damaged microstructural features within the plastic zone are analyzed and used to explain crack's path selection at different stages during the fatigue crack growth process. Cast Al-Si-Mg alloys of various grain size levels, Si morphology, SDAS, matrix strength (resulting from different heat treatment, T4, T61, and T5), as well as different solidification structures (conventional casting and SSM) were used to understand and establish the mechanisms which are active at the microstructure level at different stages - during fatigue crack growth and fracture. Particular attention is given to the understanding of the effects of heat treatment, which is regarded as a convenient tool to improve fatigue crack growth resistance of the material without changes in the solidification process.

In Chapter 6 the practical aspects of the outcome of this study, as well as methods to integrate the two design concepts (safe life - *stress/strain life data*, and damage tolerant - *fatigue crack growth data*) are revealed through relevant AFGROW simulated case studies. Life predictions based on fatigue crack growth experimental data were performed to understand the benefits of each of the alloys and to determine the critical factors that have to be taken into account when designing for certain applications. AFGROW simulations can also be used to design new alloys (optimize the alloy) with certain behavior in certain stages of the fatigue crack growth process.

The six chapters are followed by conclusions, and recommendations for future work.

Chapter 1

Fatigue Performance of High Integrity Cast Aluminum Components

D. A. Lados, D. Apelian, and A. M. de Figueredo
Advanced Casting Research Center (ACRC)
Metal Processing Institute
WPI, Worcester, MA 01609 USA

ABSTRACT

The dynamic properties of aluminum alloys are critical in the design of high integrity cast components. Many of the relationships and formulations used have their foundations in ferrous systems, where the plastic and elastic zones are significantly different compared to aluminum alloys. At the ACRC, we embarked on a fundamental, in-depth study of the effect of processing parameters, including the influence of microstructural architecture on crack initiation and crack propagation. In this paper, fatigue behavior of cast aluminum alloys and the key metallurgical factors influencing it are reviewed. Effect of defects such as porosity, inclusions, and oxide films on fatigue are discussed, followed by a summary of the effect of microstructural constituents and alloy chemistry.

I. INTRODUCTION

Generally, failure of cast aluminum alloys through fatigue or other fracture modes is caused by cracks initiated from prominent defects. If these defects are eliminated, performance is improved. The strength and durability of parts are then limited by the next prominent family of defects, and so on. When the prominent defects are removed or tightly controlled, large intermetallic compounds or other brittle phases, mostly consisting of Fe and Mg, may cause failure. If these large compounds and phases exist at low levels (or small sizes), component failure is dictated by the microstructural characteristics of the material, such as slip resistance; once slip is initiated, slip distance will depend on dendrite arm spacing, etc.

Major defects in cast aluminum alloys that influence fatigue resistance are porosity and inclusions, especially oxide films. Porosity has been shown to be the most detrimental defect. In this case, besides the total porosity content, other important factors have to be considered, such as the size and morphology of pores and the pore distribution. For a given application, in addition to the fatigue life of castings with various defect levels, it is important to consider the maximum porosity, as well as the largest pore size that can be tolerated. When either porosity or pore size is reduced to below certain levels, other mechanisms may become operational and control the fatigue behavior.

A given alloy microstructure dictates the level of ductility which, in turn, determines the level of crack tip plasticity, and influences fatigue response. Another important and frequently neglected factor that significantly affects fatigue life and crack tip behavior is the residual stress introduced during processing, e.g. during heat-treating.

It can be seen that, in addition to their large number, there is also a hierarchy among the factors that control the fatigue behavior.

A. EFFECT OF CASTING DEFECTS

Many studies have shown that fatigue life of cast aluminum alloys is significantly influenced by fatigue cracks initiated from pores near the surface [1-7]. It has been reported that inclusions, intermetallic phases, and eutectic Si particles act as fatigue initiation sites. In many experiments, it was observed that in castings with either low or essentially zero levels of porosity [1,3-7] or with small DAS [2] cracks initiated from persistent slip bands on the surface. Generally, when the porosity of a casting is above a certain level and, in particular, when the pore size exceeds some value, the fatigue life of a component is strongly affected by porosity. In this case, other crack-initiating microstructural features become less important. Studies in the Advanced Casting Research Center (ACRC) showed the specific effects of porosity and other microstructural features on fatigue behavior of A356-T6 alloys [6]. The Weibull plot of Figure 1 shows fatigue data for Sr modified A356 alloys where failure was initiated from one of the following microstructural features: porosity, oxide films or slip bands. Figure 2 shows the fatigue lives of Sr-modified A356-T6 alloys vs. pore size. The data of Figure 1 clearly show that distinct, linear relationships were found for each one of the previous features. The figure clearly shows that porosity has the most detrimental effect on fatigue life, and overrides the influence of oxide films and slip bands.

Because porosity has a dominant effect when it exceeds a certain value, the effects of inclusions and other factors can only be revealed when porosity is eliminated or significantly reduced. This is probably why most studies of the effect of defects on fatigue properties of cast aluminum alloys conducted so far focused exclusively on porosity.

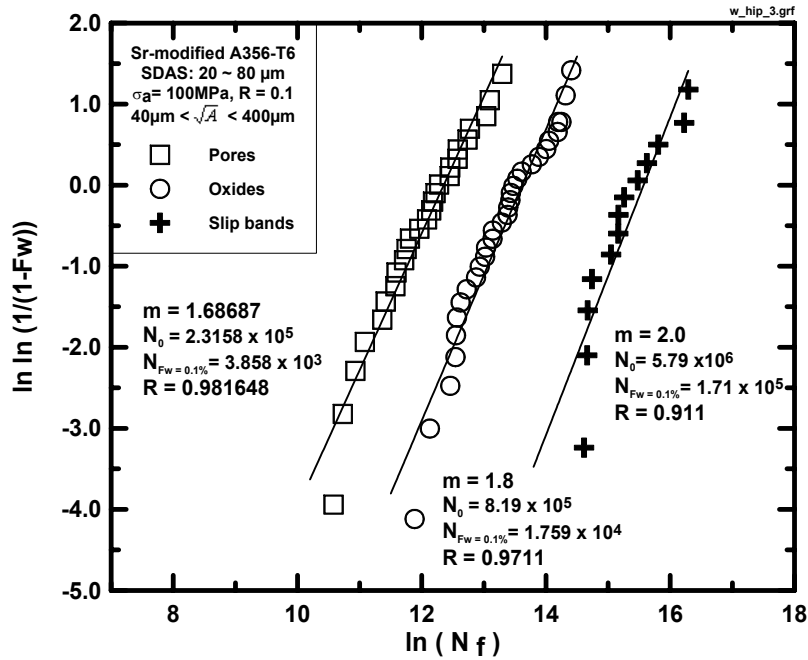


Figure 1. Two-parameter Weibull plot for fatigue life data of the Sr-modified A356 casting alloy containing a variety of defects [6].

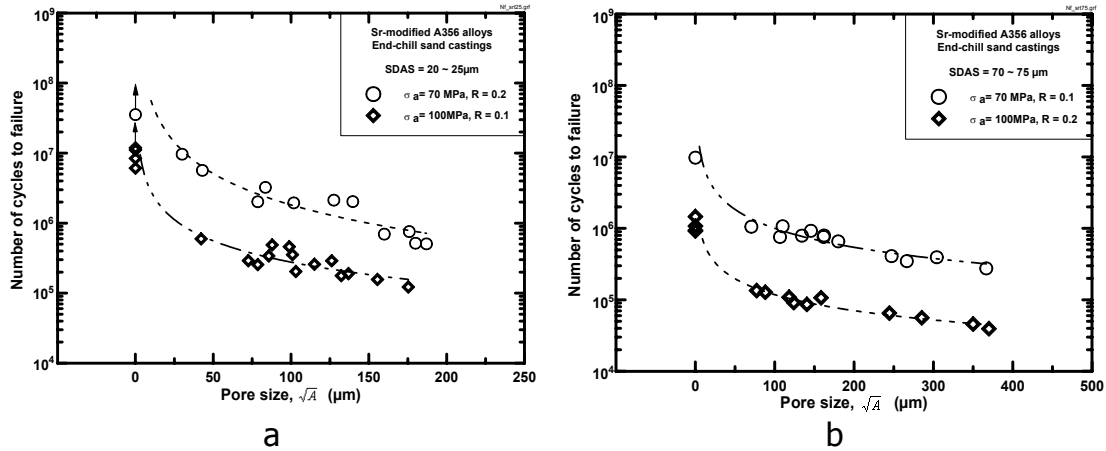


Figure 2. Fatigue life of Sr-modified A356-T6 alloys vs. pore size in specimens tested at ACRC [6]. The tests were conducted with stresses of 70 and 100 MPa and stress ratios of 0.1, 0.2 and -1. It can be clearly seen that the fatigue life decreased with increasing pore size in the specimens.

A1. Effect of Porosity

Sonsino et al. [8] investigated effects of varying levels of porosity on the fatigue strength of cast aluminum alloys. Constant- and variable-amplitude fatigue tests were performed on unnotched and notched samples of two types of alloys, age-hardened Al-7Si-0.6Mg and non age-hardened Al-11Si-Mg-Sr. In the study, porosity levels were classified as gas porosity degrees, P=0, 4, and 8 according to ASTM E155 [9]. The former levels corresponded to actual porosity values of 0, 3 to 3.7 and 8.6% by volume, respectively. A few pores were present in samples with a degree 0. Maximum pore sizes were 0.3, 0.6 and 1.0 mm for the degrees 0, 4 and 8, respectively. The results showed that the degree of porosity influenced fatigue strength in different ways. When porosity was increased from degree 0 to 8, fatigue strength in the unnotched condition was reduced by ~17% for both alloys. However, in the notched condition the age-hardened alloy displayed a reduction of 7%, while the non-age-hardened one showed a drop of 20% due to its lower yield strength. The author concluded that porosity could be tolerated even in safety parts but not in highly fatigue-stressed areas.

For the Al-7Si-0.6Mg alloy in the unnotched condition, the endurance limit decreased 11% and 17% when the porosity degree was increased from 0 to 4, and 0 to 8, respectively. This decrease was distinctly lower in the notched condition. An increase from degree 0 to 4 hardly brought any decrease in fatigue strength, and a 0 to 8 increase resulted in a drop of 7%. This suggested that in the presence of external notches, the existence of pores had hardly any influence on the fatigue strength of axially stressed components.

For the Al-11Si-Mg-Sr alloy in the unnotched condition, the endurance limit dropped 16% following an increase from degree 0 to 8, similarly to Al-7Si-0.6Mg alloy. However, in the notched condition, this limit dropped by 20% – a decrease much greater than that observed for the Al-7Si-0.6Mg alloy. The difference can be attributed to both the stress concentration and the yield strength of samples in the non-porous condition. In the unnotched specimens, the stress distribution in the non-porous condition is homogeneous. In the porous condition, the stress distribution increases uniformly through the pores. As the loaded porous material volume was the same for both alloys, the reduction in fatigue strength was comparable. However the external notch created an inhomogeneous stress distribution in the specimens. Whereas notch root stress was far below 0.2% yield strength for the non-porous age-hardened alloy, the outer notch of the non-age-hardened alloy already started yielding, but only in the vicinity of the surface of the outer notch. In the porous condition, there is a further increase in local notch root stress for the age-hardened alloy. However, due to the high 0.2% yield strength there was little plastic deformation near the surface. In the case of the non-age-hardened and porous alloy, the

plastically deformed volume was much greater because of the low 0.2% yield strength.

Zhang et al. studied the effect of porosity on fatigue life of A356.2 alloys [1]. Specimens were cast in permanent mold with dendrite arm spacing (DAS) in the 20 to 30 μm range, and given a T6 heat treatment. Tests were conducted with axial loading of strain/stress ratios of 0.1 (low/high cycle fatigue). Both Sr-modified and unmodified alloys with varying hydrogen content were tested. The porosity levels for the tested specimens ranged from 0.04% to 1.67%; with maximum pore size (expressed as the square root of the pore area) from 39 to 236 μm . The results showed that the deleterious effect of porosity obviously overshadowed the possible beneficial effect of Sr modification on the fatigue life. In all tests, the Sr modified alloy with highest porosity content showed the lowest fatigue strength. At maximum stresses below 175 MPa, the maximum fatigue lives of unmodified alloys were almost two orders of magnitude greater than those of the Sr modified alloys having the highest level of porosity. Fractography showed that cracks initiated exclusively from pores in the Sr modified alloy. The smallest pore, which initiated a fatigue crack, was about 75 μm in size. In tests at maximum stresses of 200, 175, and 150 MPa, the fatigue life decreased as the size of the initiation site increased. In unmodified alloys, the size of crack-initiating pores was consistently less than 100 μm and smaller than for Sr modified alloy. In the Sr-modified alloy, this size was between 150 to 800 μm , or even greater. In this study, no evidence for crack initiation at eutectic constituents (or at oxides) was found.

Odegard et al. performed similar experiments for an A356 type alloy (AlSi7Mg) [7]. The specimens were all T6 heat-treated but processed differently to obtain different levels of porosity and different microstructures. The first group of specimens was taken from conventional low-pressure die-cast wheels (WM-T6), the second group was taken from as-cast, direct-chill billets (DC-T6), and the third group was taken from extruded, direct-chill cast billets (DC-ET6). WM-T6 samples had a higher level of porosity (1% by volume; the average equivalent pore diameter was 100 μm and the average maximum diameter was 140 μm). Both DC-T6 and DC-ET6 were porosity-free but had different microstructures. The fully reversed ($R=-1$) fatigue tests showed significant differences in fatigue life for differently produced specimens. The fatigue strength at 10^7 cycles was 80 MPa for WM-T6, 100 MPa for DC-T6, and 120 MPa for DC-ET6, respectively. In the linear region of the S-N curve the WM-T6 showed an approximately 50% reduction in fatigue life compared with DC-T6.

Reducing pore size should always be beneficial to fatigue life. However, the above study showed that when the pore size was reduced to about 25 μm , the fatigue strength of the samples was similar to the specimens that were hot-isostatically pressed and pore-free. This suggested that $\sim 25 \mu\text{m}$ was the critical

pore size for the Sr-modified A356 alloys in the test conditions, R=0.1, 0.2 and – 1; $\sigma_a=70$ and 100 MPa.

A1.1. Crack Propagation Life Modeling

In castings containing defects such as pores, fatigue cracks initiate from sharp corners of the defects, where there is high stress concentration. The fatigue life in such cases consists mainly of crack propagation, because crack initiation under such circumstances is negligible. Therefore, it is possible to predict, with a reasonable degree of accuracy, the fatigue life of cast aluminum alloys with defects by using Linear-Elastic Fracture Mechanic (LEFM) analysis. For example, in the aforementioned experiments of Odegard et al. [7], it was found that the number of cycles required to produce a 200-300 μm long surface crack in DC-T6 was 20-50% of the total cycle life. By comparison, in WM-T6 specimens, the number of cycles required to initiate a surface crack from surface pores was less than 1% of the total fatigue life. Many attempts have been made to describe and model the fatigue process and crack propagation, and then predict fatigue life for cast aluminum alloys using LEFM [4, 6, 7, 10-13]. In all these models defects are generally simplified and treated as cracks. The following are a few examples.

For the Australian alloy CP601, Couper et al. proposed a simplified fatigue crack growth equation using linear elastic fracture mechanics for very short cracks, and at stresses near or above the yield stress [4]:

$$a_i \cdot N_p = [C \{Y(a_i)\sqrt{\pi}\}^4 \cdot \{U_R(a_i)\}^4 \cdot (\Delta\sigma)^4]^{-1}$$

where a_i : initial crack length
 N_p : number of cycles to grow a crack to failure [$N_p = N_f$ (final)- N_i (initiation)]
 $Y(a_i)$: compliance factor
 $U_R(a_i)$: closure factor
 $\Delta\sigma$: alternating stress range
 C : constant

The equation shows that fatigue life depends on three variables, namely, the stress amplitude, $\Delta\sigma/2$, the flaw size, a_i , and the closure factor U_R . It suggests that in practical applications the pore size plays a more important role in the fatigue of a component than the porosity volume fraction. In this work, the mathematical predictions were in good agreement with the experimental observations. As pointed out by the authors, due to the several assumptions involved in the derivation of the above equation, it needs to be checked for other applications. As mentioned earlier, although the fatal fatigue crack invariably started from a casting defect, there were also cracks initiated by other

mechanisms. This means that the fatigue limit would not be as high as inferred by the equation. Reducing the size of defects will increase the fatigue life, but only up to the point where the mechanism of crack initiation from persistent slip bands at the surface becomes operative.

Under other assumptions another simplified equation was derived based on fracture mechanics [6]:

$$a_i \cdot N_p = B \cdot (\Delta\sigma)^{-m}$$

where $B = \{ [(m-2)/2] \cdot CY(a_i)^m \cdot U_R(a_i)^m \cdot \pi^{m/2} \}^{-1}$ and m is a constant

This equation described well the test results for A356-T6 alloys. It also indicated that crack propagation comprised most of the total fatigue life of cast aluminum samples that failed from defects such as porosity and oxide films. The number of cycles required to initiate a fatigue cracks from defects could then be neglected.

Because real defects have various shapes and cannot always be considered as cracks, various modified models were derived, to more faithfully reflect the real conditions. For example, a simple method was proposed to estimate the fatigue limit of specimens containing a small surface defect [10]. It used only two easily obtainable parameters, the material hardness H_v and a geometrical parameter \sqrt{A} . "A" is the area of a defect projected in the direction of the maximum principal stress. The fatigue limit of a specimen containing defects, σ_w (MPa) was given by the equation:

$$\sigma_w = 1.43 \cdot (H_v + 120) / (\sqrt{A})^{1/6}$$

In another proposed method [11] the following issues were considered:

- 1) Calculating K-value with a 3-dimensional model.
- 2) Correcting the stress range according to the mean stress level.
- 3) Using the effective defect size.
- 4) Correcting the K_{th} (threshold of stress intensity factor) according to the defect's end curvature.

In this case, the stress intensity threshold, ΔK_{th} , was given by:

$$\Delta K_{th} = \Delta\sigma \cdot \sqrt{(\pi a)} \cdot F$$

where $\Delta\sigma$ is the fatigue limit of the material, a is the crack length, and F is a correction factor

The development of this method was based on experiments in which three cast alloys, including two cast aluminum alloys 326 and 308, were tested for fatigue limits. The authors reported that the test results did not agree with values estimated using earlier methods but were in agreement with their proposed method.

Because of its complexities, the fatigue behavior is influenced by numerous factors that are not related to the alloy itself. These include loading and surface conditions, geometry of the casting, etc. Even if many studies were devoted to the effects of porosity, there would still be no universally accepted operational guides and models to estimate the maximum pore size, above which fatigue life is porosity controlled. Different studies showed different results. For example, the ACRC work [6] gave $\sim 25 \mu\text{m}$ as a pore size threshold for A356 alloys and Zhang et al. [1] reported 75, 100, 150, 800 μm , and even higher values for their alloys in different conditions. It is well accepted that pore size is the critical parameter, and that it strongly affects the fatigue life. As a general rule, as the porosity level increases, so do the average and the maximum pore sizes. However, no model has been developed that allows for the determination of threshold porosity.

A2. Effect of Oxide Films

As mentioned above, most of the studies showed the dominant effect of porosity on fatigue life of cast aluminum alloys when the pore size was greater than a certain value. Some experimental results implied that the effect of oxide films was of the same order of magnitude as large phase constituents in the alloy [6]. However, according to Nyahumwa, Campbell, et al. the fatigue properties of cast aluminum alloys was controlled by double oxide films [14, 15]. They tested A356 alloys using filtered and unfiltered specimens cast in sand molds. Real-time x-radiography was used to observe the mold filling and find surface turbulence in the mold cavities without filters. The pull-pull fatigue tests (maximum stress: 150 MPa, $R=0.1$) showed that, on average, there was about a factor of 3 benefit in fatigue life of castings with filters, which helped to eliminate turbulence during filling. SEM fractography revealed that crack initiation sites were mostly oxide films and, occasionally, slip planes. In castings filled in a turbulent fashion, the failure was attributed to the combined effects of pores, old oxides, and new oxides. In filtered castings, failure was only due to old oxides. The new oxide films were generated during pouring and looked finely folded. In addition the new oxide films were associated with pores. Contrarily, old films were formed earlier, carried away by the melt, and appeared as thick chunks of refractory oxides, high in Mg due to the development of a spinel structure with time. These authors further predicted that grain boundaries could be locations for double films since the growing dendrites would not be able to cross a double oxide with an entrained layer of air. A second likely location could also be on or

in many intermetallics that might precipitate on oxide films. Therefore, failures from grain boundaries and intermetallics could also be associated with oxide films. The authors concluded that a combined attention to metal quality and casting technique could probably increase the fatigue life of the majority of cast aluminum alloys by a factor of 100 to 10,000 times.

There is no information available on the number or volume of pores that form because of film folding or nucleation on oxides. Regarding fatigue crack initiation, there is also no information on the relative effects of pores formed from oxides and pores that are unrelated to oxide films. Further studies are required to clarify what feature, oxide film or porosity, has the dominant impact on the fatigue properties of cast aluminum alloys. In the study of Nyahumwa et al. [14, 15], the failure in filtered castings was exclusively due to old oxides. However, many other studies found that cracks also form from eutectic Si or intermetallics, as well as slip bands. However, more studies are needed to verify if crack initiation from eutectic Si or intermetallics is in any way related to oxide films. The general belief is still that the effect of oxide films becomes pronounced only in the absence of porosity or when porosity is below certain levels. Investigations conducted at ACRC showed that compared to samples that failed due to porosity, the fatigue life of specimens with crack initiating from oxide films was about 4-5 times longer, and the fatigue life of specimens without defects (porosity or inclusions) was predicted to be about 25 times longer [6].

B. EFFECTS OF MICROSTRUCTURAL CONSTITUENTS AND ALLOY CHEMISTRY

It has been found that in the absence of porosity and inclusions, other microstructural features, such as DAS, grain size, alloying and impurity elements, phase compositions, morphology, and size become critical in determining the fatigue life of cast aluminum alloys.

B1. Effect of DAS

Allison et al. studied the effects of solidification rate on the fatigue life of A356 and W319 alloys [16]. It was found that solidification rate had a profound influence on high cycle fatigue (S-N) properties. Slow solidification reduced fatigue resistance, while fast solidification substantially improved it. Although these authors did not specifically mention it, the influence of DAS was obvious. They attributed this behavior to the influence of the solidification rate on the size and volume fraction of micropores, and the reduced fatigue crack propagation rates to the smaller cracks at initiation. Work conducted by Wickberg showed similar results [17]. The test alloy was A356, with DAS of 19, 25, 40, and 55 μm , and the test conditions were alternative bending ($R=-1$). The results showed that the fatigue life was proportional to $\text{DAS}^{-0.5}$.

The effect of DAS was also studied by Chen et al. [5, 18] for an alloy A356.2 in the T6 condition. Low- and high-cycle, both axial and reciprocating bending tests at stress ratios of -1 , 0.1 and 0.2 were conducted. The results showed that DAS was closely related to the total fatigue life, which decreased three times in low-cycle fatigue and six times in high cycle fatigue as DAS increased from 15 to $50\ \mu\text{m}$. In low-cycle fatigue conditions, fatigue life in the bending fatigue test was approximately 9000 cycles at DAS of $\sim 15\ \mu\text{m}$ and dropped to about 3000 cycles as DAS increased to about $55\ \mu\text{m}$. In high-cycle fatigue, the total life decreased from 1.5 million to $250,000$ cycles over the same DAS range. In the axial test similar results were obtained.

The crack initiation life as a percentage of the total fatigue life also depended on the DAS. In high-cycle bending for the specimen with small DAS (15 - $30\ \mu\text{m}$) fatigue cracks initiated at $\sim 75\%$ of the total life, whereas for specimens with large DAS ($>50\ \mu\text{m}$) fatigue cracks initiated at merely 15% of the corresponding total life.

It was also found that in both low- and high-cycle fatigue conditions, pores acted as crack initiation sites only when the DAS of the alloy was greater than $\sim 30\ \mu\text{m}$. In the alloys with smaller DAS the cracks initiated primarily from near-surface eutectic regions. Unfortunately, the porosity levels and pore sizes were not reported.

The ACRC data, obtained from porosity-free specimens produced by HIP and DensalTM, showed a slightly different pattern for DAS effect. For Sr-modified A356-T6, when DAS was less than $60\ \mu\text{m}$, fatigue life decreased with increasing DAS, whereas when DAS was greater than $60\ \mu\text{m}$, fatigue life increased with increasing DAS (see Figure 3). However, for unmodified A356-T6 alloys fatigue life decreased with increasing DAS, in both the fine and the coarse structures. At intermediate DAS, between 40 and $60\ \mu\text{m}$, fatigue life remained almost constant with DAS. The influence of DAS can be attributed to dispersion hardening.

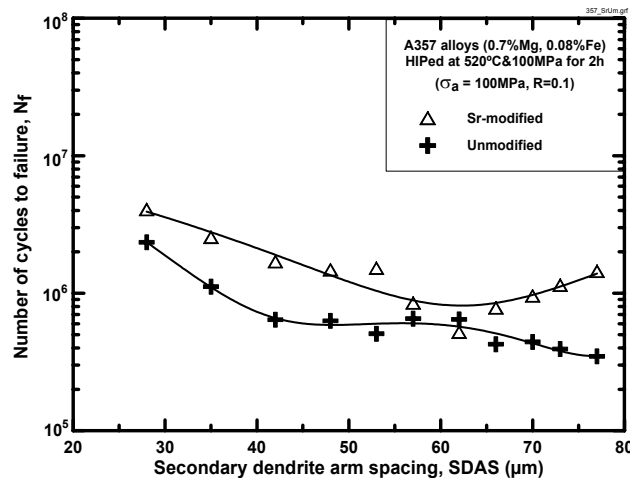


Figure 3. Fatigue life data for unmodified and Sr-modified A357-T6 alloys as a function of SDAS [19].

B2. Effect of Si and Eutectic Modification

Lee et al. systematically studied the effect of Si particle size on the fatigue crack growth (FCG) characteristics of unmodified and Sr-modified Al-12Si-0.35Mg alloys [20, 21]. Three different Si particle sizes were tested. Growth rate tests were conducted on compact tension specimens, with sinusoidal waveform loading and different stress ratios. A356 alloys with three different sizes of Si particles were tested for comparison. It was found that fatigue behavior of the AlSiMg casting alloys depended on the size, orientation, and local distribution of the Si particles, in addition to the resistance to cracking and/or decohesion of both the Si particles and the Si particle/matrix interface, plastic flow in the matrix, stress intensity factor range, ΔK , plastic zone size and stress ratio. For example, in the modified alloys (Si particle size ~ 1.5 - $2.5 \mu\text{m}$), decohesion of the Si particles from the Al matrix is predominant. The fracture crack advances mainly through the Al matrix between the fine Si particles. In the unmodified alloy (coarse Si particles, ~ 3 - $9 \mu\text{m}$) particle cleavage was the dominant feature. For an intermediate Si particle size (~ 2.5 - $5.5 \mu\text{m}$) and at low ΔK , a mixed mode of particle cracking and decohesion was observed. The tendency to particle cracking increases with increasing Si particle size and ΔK , as evidenced by the increase in fatigue crack rate with the increase in Si particle size. Figure 4 shows the relationship between fatigue crack growth rate, da/dN and the closure-corrected effective stress intensity factor range, ΔK_{eff} , for fine, intermediate, and coarse Si particle-containing structures. Three regions (or stages), can be distinguished: (1) the near threshold region below 10^{-9} m/cycle, where crack closure is the predominant shielding mechanism; (2) the log-log linear or intermediate growth rate region (Paris region), between $\sim 10^{-8}$ and 10^{-6} m/cycle, and the high growth rate region of $>10^{-5}$ m/cycle, approaching instability. From the figure, a noticeable threshold and crack growth rate dependency on the

average Si particle size is observed. The overall fatigue crack growth properties in the modified alloys and A356 alloys resulted from the increased levels of crack closure and branched crack paths. It was found that when Si particles fracture developed into one of the dominant fatigue crack growth mechanisms, the advantage of improving fatigue properties by the addition of Si to unmodified Al-Si alloy was lost.

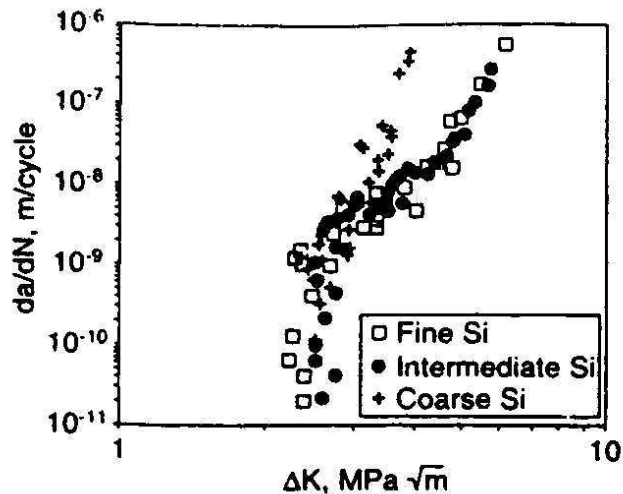


Figure 4. Variation in fatigue crack propagation rates, da/dN , with effective stress intensity factor range ΔK_{eff} ($R=0.8$) for fine, intermediate, and coarse Si particle-containing alloys [21].

ACRC studies also pointed to beneficial effects of modification of both porosity-free A356 and 357 [19]. The overall fatigue life of modified alloys was longer compared to unmodified alloys. As predicted by Weibull statistics, the characteristic fatigue life of modified alloys should be two to four times longer. According to the calculated internal stress on the eutectic particles in the plastically deformed regions, and the probability of fracture for particles with different sizes and aspect ratios, it can be seen that large and elongated particles tend to crack early during plastic deformation, resulting in microcracks in the microstructure. As deformation proceeds, microcracks continue to accumulate and grow. When the microcrack size exceeds a critical size, a fatigue crack forms. In addition, the presence of microcracks in the microstructure increases the fatigue propagation rate, and thus reduces the fatigue life.

B3. Effect of Mg

The effect of Mg can be observed in Figures 5 and 6 from the ACRC study [19]. This work showed that the fatigue life of alloys with both high and low levels of Mg was influenced by DAS in almost the same pattern presented in section B1. For both Sr-modified (Figure 5) and unmodified alloys (Figure 6), the higher Mg

content alloy (A357) showed lower fatigue life than the lower Mg content alloy (A356). For Sr-modified alloys the predicted characteristic fatigue life of A356 alloy was about 4 times longer than that of A357. For unmodified alloys, alloy A357 had shorter fatigue life at intermediate and large DAS than alloy A356, but at small DAS the differences between the two alloys became negligible.

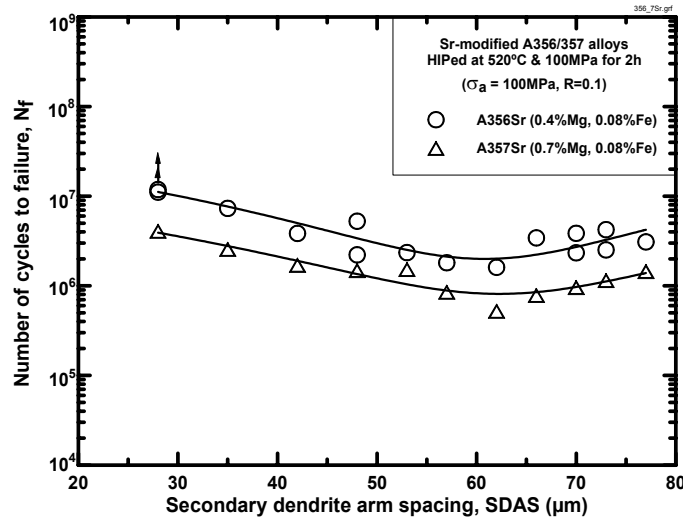


Figure 5. Fatigue life data for the HIP-ed and Densal™ treated Sr-modified A356/357-T6 alloys as a function of SDAS [19].

The reason for the decrease in fatigue life with increasing Mg content can be the occurrence of microcracking. Increasing Mg content increases the eutectic particle size, particularly in the Sr-modified alloy due to the formation of large Mg-containing Fe-rich phase. The increased particle size results in increased particle fracture and thus shorter fatigue life.

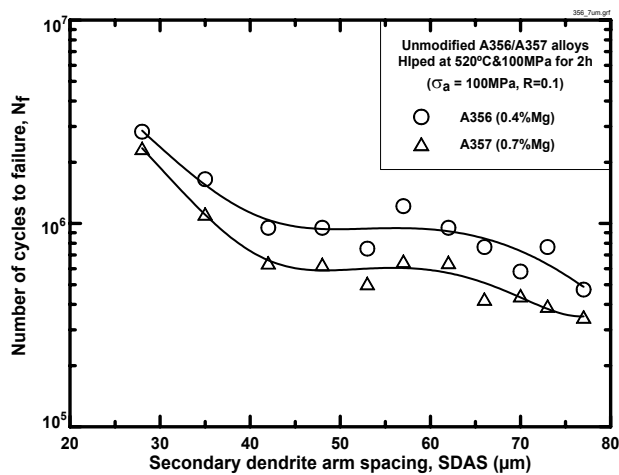


Figure 6. Fatigue life data for the HIP-ed and Densal™ treated unmodified A356/357-T6 alloys as a function of SDAS [19].

B4. Effect of Fe

As discussed above for Si and Mg, there is a higher tendency for particle cracking with increasing particle size. Similarly, the influence of Fe depends mainly on the size and morphology of its compounds. In the ACRC study [19], the effect of Fe content was investigated for the unmodified A357 alloys. Increasing Fe content from 0.08% to 0.14% decreased the fatigue life, particularly for very coarse microstructures (large DAS). However, no significant influence was found at small and intermediate DAS.

B5. Effect of Yield Strength

The influence of yield strength on fatigue behavior is complex. Based on fracture mechanics theories, increasing the yield strength results in lower values of the threshold stress intensity factor, ΔK_{th} and expedites the growth of microstructurally small cracks during the initiation period.

On the other hand, increasing the yield strength reduces the number and size of local plastic deformation zones in the material. This decreases the possibility of forming microcracks in front of the main fatigue crack. In addition, increasing the yield strength increases the matrix resistance to dislocation movement within dendrite cells, leading to fewer dislocations moving towards the cell/grain boundaries to interact with the eutectic particles. This decreases the long crack growth rate during the propagation period due to the reduced microcracks (damage) in the material [19].

Couper et al.'s experiments [3, 4] showed that, in contrast to wrought aluminum alloys, the S-N properties of an aluminum-casting alloy equivalent to A356 were remarkably insensitive to the heat treatment condition. This suggests that the fatigue life of these alloys was insensitive to the yield or tensile strengths, because heat treatment of these alloys increased their yield and tensile strengths significantly. The reason for the observed behavior was that the studied specimens contained porosity. Porosity led to fast crack initiation; after that the fatigue life was determined by the fatigue crack growth rate, which was insensitive to the heat treatment condition.

B6. Effect of Heat Treatment

Heat treatment changes both the size and the morphology of phases like the eutectic Si, improves both the tensile and the yield strength, reduces segregation, and relocates residual stresses. Consequently, fatigue life is also affected by heat treatment. The effect of heat treatment on the previous factors depends not only on the heat treatment parameters, but also on the alloy

chemistry, casting conditions, and even casting sizes and geometries. The literature lacks specific information about the influence of heat treatment on fatigue life of casting aluminum alloys. In the work performed at ACRC [19], the heat treatment effects on the fatigue properties of liquid HIP-ed Sr-modified A356 alloys were assessed. It was shown that the soft matrix produced by under aging resulted in lower fatigue life relative to that of a T6, near peak-aged heat treatment. The predicted characteristic fatigue life of peak-aged samples was about two times longer than that of under-aged samples. Under aged samples solution-treated for shorter time (1 hr) showed slightly lower fatigue life than compared to samples that were solution treated for longer times. Longer solution treatment times also reduced scatter in fatigue test results. As mentioned above, the experiments of Couper et al. on the effects of defects [3, 4] showed that the fatigue life (S-N data) of cast aluminum alloys was insensitive to the heat treatment parameters, because of the presence of porosity in the specimens.

B7. Effect of Alloy Chemistry on Fatigue Life of Aluminum Die Casting Alloys

Most of the aforementioned studies were conducted on AlSiMg (356 type) alloys. These alloys generally have narrow limits for alloying and impurity elements, and they are used in the heat-treated condition. For other types of alloys, such as aluminum die casting alloys, some of the effects on fatigue life of alloy chemistry might differ, and this requires a more careful consideration. This is so because these alloys contain a wider range of more alloying elements, are cooled fast and generally used in the as-cast condition. ACRC conducted a systematic study on the effects of alloying elements on the fatigue life of aluminum die casting alloys [22]. The ten most commonly used alloying and impurity elements and several of their interactions were studied using the R. R. Moore Rotating-Bending Fatigue Test - the standard fatigue test for aluminum die casting alloys. At the addition levels investigated, statistic analyses showed that fatigue life was mostly affected by Si. Cu followed in terms of influence. Mn, Zn, and Ti also affected fatigue life, but their effects were not significant. At higher levels, the above elements tend to increase the fatigue strength or do not affect it at all. At higher Si contents, the tendency of the alloy to form scattered shrinkage porosity is reduced, and the addition of Si significantly increases both the yield strength and the modulus of elasticity of the alloy. Cu, Mn, Zn, and Ti also increase yield strength. In addition, the interaction of Fe with Mn and Cr significantly affected the fatigue properties. The interaction among Fe, Mn and Cr promotes the formation of large Fe-rich needle phases that are detrimental to fatigue life.

B8. Effect of Closure

Crack closure occurs when the applied stress is less than the crack opening stress. During crack closure, the stress intensity range at the crack tip is less than ΔK and the crack growth is correlated to a ΔK_{eff} , or $K_{\text{max}} - K_{\text{opening}}$ instead of $\Delta K = K_{\text{max}} - K_{\text{min}}$. Crack closure has a significant effect on fatigue crack growth behavior particularly in near-threshold regime because crack tip displacements in this regime are very small, and the crack opening stress is close to the maximum applied stress.

C. EFFECT OF DUCTILITY/PLASTICITY

When the ductility of the material plays an important role, EPFM (Elastic-Plastic Fracture Mechanics) is a more accurate alternative to LEFM (Linear Elastic Fracture Mechanics) to evaluate the dynamic properties of cast aluminum alloys. LEFM correlates crack growth rates resulting from an applied cyclic load (da/dN) to the stress intensity factor ΔK ; this is given by:

$$\frac{da}{dN} = C (\Delta K)^m,$$

where da/dN is the crack growth increment per loading cycle, ΔK is the stress intensity factor range ($K_{\text{max}} - K_{\text{min}}$), and C and m are functions of the material variables, environment, frequency, temperature, stress ratio, etc.

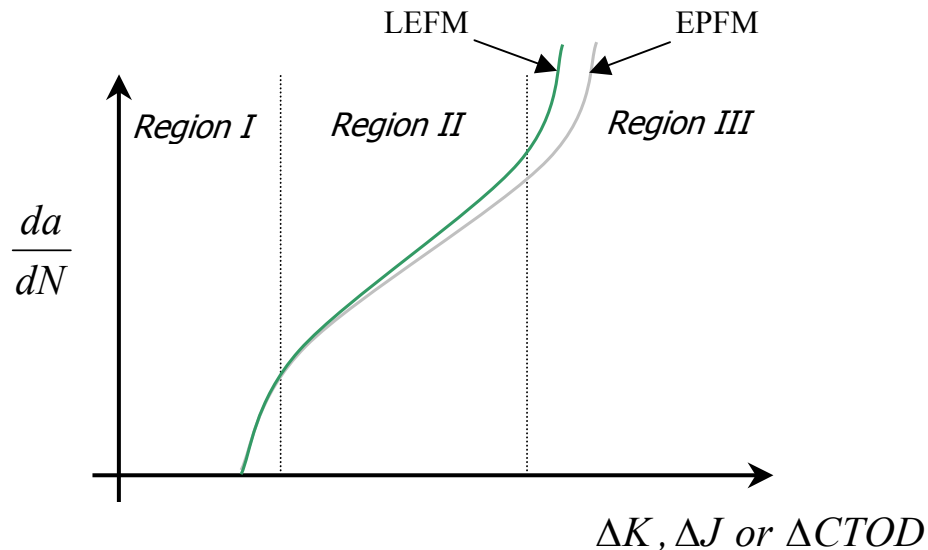


Figure 7. LEFM vs EPFM in high plasticity conditions [23].

In graphical form this relationship is seen in Figure 7. Regions I, II, and III correspond to the initiation, propagation, and final failure in crack evolution. It is

important to point out that for longer crack lengths, the plasticity region present in front of the crack becomes more and more significant. Therefore, because of yielding, LEFM becomes less and less accurate at higher ΔK values, and elements of EPFM, such as the J-integral or CTOD (Crack Tip Opening Displacement) need to be considered to obtain realistic representations of the upper Region II, Region III and fracture toughness of the material. K_{IC} values from LEFM evaluations underestimate the behavior of the material. A more accurate approach to both FCGR curves and fracture toughness should consider a cyclic J-analysis using the load-displacement data from the FCGR experiments [23].

D. EFFECT OF RESIDUAL STRESS

Most cast aluminum alloys are heat treated where a solution treatment stage is followed by quenching from a temperature of around 1000°F. As a result the residual stress level introduced in the samples (or components) is significant. These residual stresses are compressive on the surface, which cools first, and tensile in the center, which cools later. After quenching the tensile and compressive stresses present in the sample are balanced and the total net stress equals zero for the whole sample. Subsequent ageing treatment enhances the strength of the part without having any effect on the residual stresses in the part.

There are several ways to eliminate residual stresses, such as thermal (annealing), mechanical (mechanical deformation), and thermo-mechanical (so-called "up-hill" quench [24]). For aluminum alloys the last procedure is the most successful one, in terms of both eliminating the residual stresses and also preserving the shape and the mechanical properties of the part. Since the elimination of residual stresses is not always practical, ways to lucidly deal with it are required. As seen in Figure 8, schematically reproduced from [25], the presence of residual stresses has a very significant contribution to the fatigue crack growth behavior of several types of alloys. This is true for aluminum, superalloys, titanium, steels, and not only in castings, but also in forgings, extrusions, etc. This situation represents tests conducted on compact tension specimens. It can be noticed that the thresholds are shifted towards higher values of ΔK , due to the significant closure effects that result from the presence of residual stresses, in addition to the effects of the alloy microstructure. For high residual stresses, the thresholds can be increased by as much as a factor of two. It is important to note that residual stresses also affect the fracture toughness K_{IC} to a lower degree, i.e., up to 20-25%. On the other hand, for center-cracked tension specimens, thresholds are predicted to be lower than those obtained in the absence of residual stresses (in these specimens the notch is located in a region of tension as opposed to a region of compression in compact tension specimens). In conclusion, residual stress is a major issue that cannot be ignored, and mathematical and experimental ways to account for it

need to be created. In this sense, ASTM guidance should also be developed and added to the existent standard procedures for measuring crack growth rates.

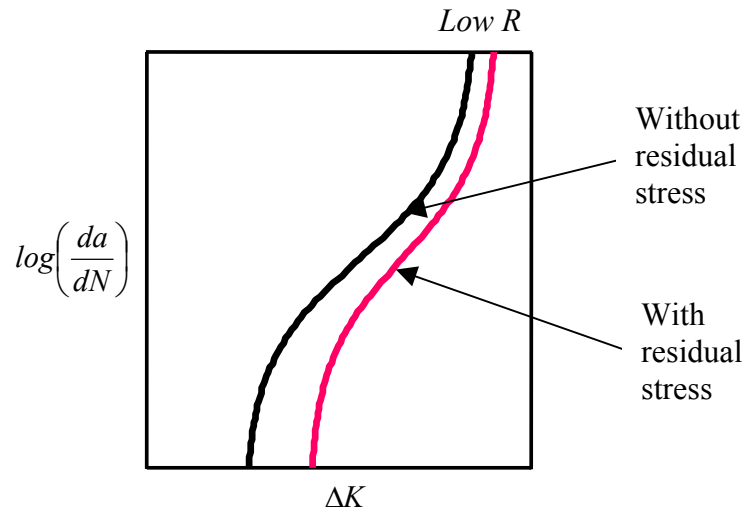


Figure 8. Influence of the residual stress on the FCG behavior of cast aluminum alloys [25].

SUMMARY

Because of the importance of fatigue in aerospace, automotive, and other industries, and the expanding use of cast aluminum alloys in these fields, significant research efforts have been undertaken in this area. Unfortunately, experimental results are often conflicting and some of the proposed mechanisms do not appear to be fully supported by experimentation.

Cast aluminum alloys contain defects and when these defects reach certain levels, they determine the alloy fatigue properties. Regarding the effect on fatigue properties, the major defects in cast aluminum alloys are porosity and inclusions, mainly oxide films. Porosity has been shown to be the dominant factor when the pore size is greater than a given value, and it overshadows the effect of other factors. Therefore, reducing porosity and, more so, the pore size, should be considered as the first step in improving fatigue life of cast aluminum alloys. When both the porosity and the pore size are reduced to below certain values, oxide films become the major controlling factor. To reduce the entrainment of oxides, good melting and casting practices are essential.

Experiments and Linear-Elastic Fracture Mechanic analyses all show that the detrimental effect of pores mainly depends on their size and morphology, such as aspect ratio and tip curvature, as well as location. Generally, the larger and sharper the pore, the more detrimental its effect on fatigue life. Similarly, the effects of Fe and Mg intermetallic compounds, and of other large phases like

eutectic Si particles, on fatigue life depend on their sizes and morphology. Generally, as these particles become smaller and rounder, the less detrimental to fatigue they become. Reducing the size of particles is an effective way to alleviate their detrimental effects and to improve the fatigue life of a casting. Several methods can be used to reduce particle size. Increasing cooling rate decreases DAS, refining the whole microstructure and, consequently, reducing the sizes of almost all other microstructural constituents, such as pores, eutectic Si, and intermetallic compounds. Therefore, the fatigue life is generally improved by decreasing DAS. Eutectic Si modification reduces the size of the Si particles and this also improves the fatigue life. Proper heat treatment reduces the size and aspect ratio of eutectic particles and also enhances tensile properties, thus improving fatigue life.

The ways the elements in cast aluminum alloys affect fatigue properties depend on their ability to effectively lead to the formation of a "desirable" microstructure, at the same time they affect both the ductility and the strength of the matrix. Generally, if an element forms small and round phases, or increases strength and does not significantly reduce matrix ductility, it should be beneficial or at least less harmful to fatigue properties.

There are numerous models that describe the fatigue process in cast aluminum alloys. These models are mostly based on crack propagation and can give either an estimation of fatigue life for given processing conditions, or the maximum allowable pore or crack size for a predetermined life. Because all the models are built under some assumptions and based on particular experiments, each model fits certain conditions, but so far none of the proposed models is general enough to be widely accepted and used in the prediction of fatigue properties. Recently, considerable attention has been devoted to the effect of oxides on fatigue properties, but work on this subject is still limited.

For correct estimations of the fatigue behavior of cast aluminum alloys, plasticity effects at the crack tip should be considered, especially at longer crack lengths (upper Region II and Region III of the FCGR curves). This can be achieved by using Elastic/Plastic formulations, where the material properties start playing a key role. In this way, a better modeling of the real behavior of the material is achieved by using its actual properties.

Another factor that should be given careful consideration is the presence of residual stress. Since not all components have the same residual stress level, even when produced in similar conditions, design calculations based on data that incorporate residual stresses will not be relevant. Therefore, a knowledge of residual stress free conditions should be developed, and this should be further related to various levels of extrinsic contributions from residual stresses.

REFERENCES

- [1]. B. Zhang, D.R. Poirier, and W. Chen, "Effect of Strontium Modification and Hydrogen Content on the fatigue Behavior of A356.2 Aluminum Alloy", Unpublished.
- [2]. B. Zhang, P.K. Sung, D.R. Poirier, and W. Chen, "Microstructural Effects on High Cycle Fatigue-Crack Initiation in A356.2 Casting Alloy", *Metallurgical and Material Trans. A*, Vol. 30A, p2659-2666, 1999.
- [3]. M.J. Couper, *Fatigue of an Al-Mg-Si Casting Alloy*, Ph.D. thesis, Monash University, Clayton Australia, 1982.
- [4]. M.J. Couper, A.E. Neeson, and J.R. Griffiths, "Casting Defects and the Fatigue Behavior of an Aluminum Casting Alloy", *Fatigue Fract. Eng. Mater. Struct.*, Vol. 13, No. 3, p213-227.
- [5]. W. Chen, B. Zhang, T. Wu, D. Poirier, P. Sung, and Q.T. Fang, "Microstructure Dependence of Fatigue Life for A356.2", in *Automotive Alloys II*, TMS, Warrendale, PA, p99-113.
- [6]. Q.G. Wang, D. Apelian, and D.A. Lados, "Fatigue Behavior of A356-T6 Aluminum Cast Alloys. Part I. Effect of Casting Defects", *J. of Light Metals*, Vol. 1, No. 1, 2001, p73-84.
- [7]. J.A. Odegard and K. Pedersen, "Fatigue Properties of an A356 (AlSi7Mg) Aluminum Alloy for Automotive Application – Fatigue Life Prediction", SAE Technical Pub. 940811, 1994.
- [8]. C.M. Sonsino and J. Ziese, "Fatigue Strength and Applications of Cast Aluminum Alloys with Different Degree of Porosity", *Int. J. Fatigue* 15 No 2, (1993), p75-84.
- [9]. ASTM E155-79 "Standard Reference Radiographs for Inspection of Aluminum and Magnesium Castings".
- [10]. Y. Murakami, 3rd Symposium of Fracture Mechanics of SMS, Japan (1985) p16-20.
- [11]. H. Nagata, T. Yoshimura, and M. Yamauchi, "Fatigue Strength Evaluation of Casting with Defects", SAE Technical Publication 860555, 1986.
- [12]. B. Skallerud, T. Iveland, and G. Harkegard, "Fatigue Life Assessment of Aluminum Alloy with Casting Defects", *Eng. Fracture Mechanics*, Vol. 44, No.6, 1993, p857-874.
- [13]. S. Gunggor and L. Edwards, "Effect of Surface Texture on Fatigue Life in a Squeeze Cast 6082 Aluminum Alloy", *Fatigue Fract. Eng. Mater. Struct.*, Vol. 16, No. 4, p391-403.
- [14]. C. Nyahumwa, N.R. Green, and J. Campbell, "The Concept of the Fatigue Potential of Cast Alloys", 1st Aluminum Symposium.
- [15]. C. Nyahumwa, N.R. Green, and J. Campbell, "Effect of Mold Filling Turbulence on Fatigue Properties of Cast Aluminum Alloys", *AFS Trans.* 1998, p215-223.
- [16]. J.E. Allison, J.W. Jones, M.J. Caton, and J.M. Boileau, "Microstructural Influences on the Fatigue of Cast Aluminum", *Proceedings of 7th*

- International Fatigue Congress, Fatigue '99, X.R. Wu and Z.G. Wang, Eds., 1999, EMAS/HEP Publishers, UK, Vol. 3, p2021-2028.
- [17]. A. Wickberg, G. Gustafsson, and L. E. Larsson, "Microstructural Effects on the Fatigue Properties of a Cast Al7SiMg Alloy", SAE Technical Publication 840121, 1984.
- [18]. W. Chen, B. Zhang, T. Wu, D. Poirier, P. Sung, and Q.T. Fang, "The Role of Dendrite Arm Spacing in Fatigue of Aluminum Castings. The 1st International Al Casting Tech. Symposium, Rosemont, Ill., 13-14 October 1998.
- [19]. Q.G. Wang, D. Apelian, and D.A. Lados, "Fatigue Behavior of A356-T6 Aluminum Cast Alloys. Part II. Effect of Microstructural Constituents", J. of Light Metals, Vol. 1, No. 1, 2001, p85-97.
- [20]. F.T. Lee, J.F. Major, and F.H. Samuel, "Effect of Silicon Particles on the Fracture Crack Growth of Al-12 Wt Pct Si-0.35 Wt Pct Mg-(0-0.02) Wt Pct Sr Casting Alloys", Mat. Trans. A, Vol. 26A, June 1995, p1553-1570.
- [21]. F.T. Lee, J.F. Major, and F.H. Samuel, "Fracture Behavior of Al-12wt.%Si-0.35wt.%Mg-(0-0.02)wt.%Sr Casting Alloys under Fatigue Testing", Fatigue Fract. Eng. Mater. Struct., Vol. 18, No. 3, 1995, p385-396.
- [22]. L. Wang, D. Apelian, and M.M. Makhlof, "Fatigue Properties of Aluminum Die-Casting Alloys", AFS Transactions, Vol. 106, 1998, p155-162.
- [23]. D.A. Lados "Ph.D. Thesis" (in progress)
- [24]. H.N. Hill, R.S. Barker, and L.A. Willey, "The Thermo-mechanical Method for Relieving Residual Quenching Stresses in Al Alloys", Trans. of the ASM, Vol. 52, 1959.
- [25]. D.A. Lados, D. Apelian, and J.K. Donald, "Effect of Residual Stress on the Fatigue Crack Growth Behavior of Cast Al-Si-Mg Alloys", AeroMat, session 2-Affordable Structures/Residual Stress, June 2002.

Chapter 2

Fatigue Crack Growth Characteristics in Cast Al-Si-Mg Alloys – Part I: *Effect of Processing Conditions and Microstructure*

D. A. Lados and D. Apelian
Worcester Polytechnic Institute, Worcester, MA, USA

ABSTRACT

Fatigue strength and crack propagation behavior are critical attributes when designing structural components for high integrity applications. Significant efforts have been directed in the past decade towards determining the effects of casting defects on fatigue response and many causal relationships are available in the literature. What has been missing, however, is a fundamental knowledge of the contribution of various constituent phases and features, specific to the alloy being considered, in governing fatigue crack initiation and propagation. In this work, model systems of Al based cast alloys were investigated for fatigue crack growth under constant stress ratios using compact tension specimens. Grain size, SDAS, modification, amount of Al-Si eutectic phase, α -Al phase, and other phases were controlled (kept constant/varied as needed to decouple effects) to determine their impact on fatigue crack growth. In addition, heat treatment effects and the influence of quenching residual stresses (macro-stresses) on fatigue crack growth have also been studied. Specifically, we will critically review and discuss the effects of critical casting parameters on the fatigue properties of cast Al components used for low cycle fatigue as well as high cycle fatigue applications.

Keywords: Al-Si-Mg alloys (conventionally cast and SSM); Fatigue crack growth; Threshold stress intensity factor; Microstructure; Heat treatment; Plasticity; Residual stress.

I. INTRODUCTION AND BACKGROUND

Fatigue performance of cast aluminum alloys is of great interest, because of the growing use of aluminum cast components in automotive and aerospace industries. Significant work has been carried out to determine the effect of casting defects on fatigue response. It is now well understood that, when present, defects such as porosity, oxides, and inclusions dominate fatigue response; moreover, the more and larger these defects are, the lower the fatigue life expectancy. There is a hierarchy among the factors that control fatigue behavior, and when one dominating factor is reduced, the next mechanism becomes active. Each of these factors is critically discussed by Lados et al. [1], and salient points are presented here.

Many researchers [2-7] have determined that porosity significantly influences fatigue life. Porosity has the most detrimental effect on fatigue properties, especially when pore size and amount exceed certain values [2,4]. Factors controlling porosity formation are systematically presented by other researchers [5], and include hydrogen content, local freezing rate, and alloy treatments such as Sr-modification, grain refinement, and metal cleanliness. When either pore size or amount of porosity is reduced below a certain critical level, the next mechanism in the hierarchy (i.e., inclusions, mainly oxides) becomes operational and dominates fatigue behavior. Several studies [8,9] emphasize the importance of both old and new oxides as well as the potential involvement of grain boundaries and intermetallics due to their association with oxide films; they also emphasize the association of pores with new oxide films. It is important to note that much of this work is not mechanistic in nature, but rather the work can be described as relating cause and effects, and establishing empirical relationships. What is lacking is a mechanistic understanding of the dynamic behavior of Al cast alloys.

As a result of many casting technology innovations, such as molten metal processing methods, and the ability to measure the level of defects, a dramatic improvement in the control of defects in metal cast components has been witnessed. When defect levels are decreased, the intrinsic microstructural features of the alloy have a critical role as they begin to dictate the dynamic loading behavior of the component. Unfortunately, a fundamental understanding of the effect of alloy's microstructural constituents on fatigue properties is not well established; particularly when related to fatigue crack growth mechanisms. The role of critical microstructural features such as amount of Al-Si eutectic, α -Al primary phase, Si size/shape (dictated by the unmodified vs. Sr-modified conditions), grain size, matrix microhardness/ability to yield (as a result of two heat treatments T61 and T4) were investigated.

The effects of secondary dendrite arm spacing (SDAS) have been investigated [10-14]; these findings mostly showed a decrease in fatigue life with increasing SDAS for both low cycle and high cycle conditions (in [14] however, an increase in the fatigue life of modified A356 alloys was observed at $SDAS > 60 \mu m$). The work to date indicates that pores act as crack initiators below a certain SDAS value, while above it other microstructural features such as eutectic Si are responsible for crack initiation [12]. The effects of microstructure can also be overshadowed by the presence of residual stresses [15]. This is a critical point, and it is important that the material evaluation is carried out on residual stress free samples, in order to allow the observation of the microstructure effects on fatigue crack growth behavior. In addition, a comparison of fatigue crack behavior of conventionally cast versus semi solid processed materials (SSM), was also investigated for T61 and T5 treat heating conditions.

II. EXPERIMENTAL PROCEDURE

II.A. Alloys, casting procedure, and heat treating conditions

Five Al-Si-Mg alloys of fixed Mg content (0.45%) at three Si levels 1, 7, and 13%, in both unmodified and Sr-modified conditions, were investigated. High purity alloys were used; all other elements were kept at low levels < 0.002%, and Fe concentration was <0.02%. The eutectic Si was modified using Al-10%Sr master alloy, and additions were made according to the Si content of the alloy (0.018-0.021%Sr for the 7%Si alloys, and 0.024-0.027%Sr for the 13%Si alloys) to achieve a constant level of modification. Three grain size levels were analyzed, and the Al-5%Ti-1%B grain refiner additions for each alloy and condition are given in Table 1. The amount of grain refiner added depends on the Si level of the alloy, as well as the extent of modification of the eutectic Si. SDAS was controlled for all the alloys by controlling freezing rate, and the SDAS of all samples were in the range of 20-30 μm .

Table 1. Titanium additions (in wt%) corresponding to three grain size levels for each alloy in unmodified and modified conditions

Grain size (μm)	Alloy Systems Examined				
	1%Si	7%Si-UM ^a (A356-UM)	13%Si-UM (Eutectic-UM)	7%Si-M ^b (A356-M)	13%Si-M (Eutectic-M)
180-220	0.0080-0.0090	0.080-0.090	--- ^c	0.070-0.080	0.27-0.33
280-320	0.0065-0.0075	0.035-0.045	0.25-0.30	0.025-0.035	0.20-0.25
~520	---	0.0007-0.0009	---	0.0004-0.0006	---

^a UM = unmodified eutectic Si. ^b M = Sr-modified eutectic Si.

^c = case not included in the study

For the fatigue crack growth studies, compact tension (CT) specimens were prepared using a specifically designed sand mold containing central top and bottom gray cast iron chills to insure that the desired SDAS was attained throughout the region of interest. The castings from which the CT samples were machined had the following dimensions: 4.4in x 4.4in x 0.8in (112mm x 112mm x 20.5mm).

In addition to the above five alloy systems, a sixth alloy was produced using semi-solid processing (SSM) methods. The alloy was brought to the semi-solid temperature range and cast into a die under high pressure. The process used the so-called "slurry on demand route" rather than the "billet reheating method". The composition of the SSM samples was similar to the conventionally cast modified A356 alloy.

Subsequently, the cast parts were solution treated at 1000°F (538°C) and water quenched. During quenching, residual stresses can be introduced in the samples

especially when room temperature water is used as a quenching medium. The surfaces of the samples cool faster than their interior and temperature gradients are created, causing different regions of the sample to contract at different rates. During the final stages of cooling these thermal gradients disappear, but their presence causes an uneven distribution of residual stresses in the part. These residual stresses are compressive on the surface of the sample and tensile in the center. Subsequent to quenching, the tensile and compressive stresses are balanced and the total net stress for the whole sample equals zero. For a correct interpretation of the test results, residual stresses need to be removed from the samples prior to conducting the fatigue crack growth experiments. Several heat treat procedures were applied, two different T61 treatments (uphill quench and room temperature), T4, and T5. These are detailed below.

Two T61 heat treat procedures were used. Both heat treatments resulted in samples with similar microhardness of the α -Al matrix in all the alloys (either primary or eutectic α) while maintaining distinctly different eutectic Si morphologies between unmodified and modified alloys. Residual stresses induced in the samples by these two heat treatments were also significantly different.

The first T61 heat treatment applied, also called "uphill quench", consists of the following steps:

- Solution-treatment for 1.5 hrs at 1000°F (538°C);
- Boiling water quench for 15 min;
- Liquid N₂ immersion for 30 min;
- Boiling water reverse quench for 15 min;
- Natural age for 12 hrs;
- Artificial age for 12 hrs at 311°F (155°C).

The role of liquid nitrogen-boiling water reverse quench is to eliminate residual stresses from the samples [16], so that the superimposed effects of residual stress on crack growth do not interfere with the analysis. The concept of an uphill heat treatment is based on the rationale that by developing thermal gradients (residual stresses) of an opposite nature one can counteract and cancel the quenching stresses. Uphill quenching eliminated residual stresses in the CT samples.

The second procedure applied is the room temperature T61 heat treatment which consisted of the following steps:

- Solution-treatment for 1.5 hrs at 1000°F (538°C);
- Room temperature water quench;
- Natural age for 12 hrs;
- Artificial age for 12 hrs at 311°F (155°C).

Room temperature water quenched specimens had significant residual stresses.

Effects of matrix strength and ductility on crack growth were studied by using a T4 heat treatment consisting of solutionizing followed by a natural age. The absence of artificial (high temperature) aging prevented the development of Mg_2Si strengthening precipitates and samples with lower yield strengths were obtained.

The T4 heat treatment procedure consisted of the following steps:

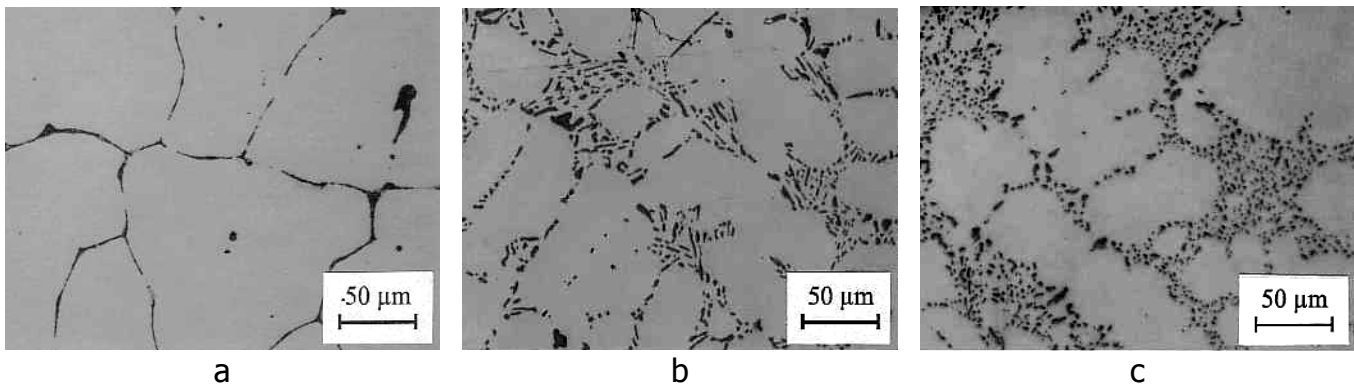
- Solution-treatment for 1.5 hrs at 1000°F (538°C);
- Boiling water quench for 15 min;
- Liquid N_2 immersion for 30 min;
- Boiling water reverse quench for 15 min;
- Natural age at room temperature.
-

Sample transfer time from one medium to another was less than two seconds for both the regular quench and the reverse (uphill) quench.

The SSM samples were additionally subjected to a T5 heat treatment consisting of:

- Artificial age for 8 hrs at 437°F (225°C).

The resultant microstructures of the alloys subsequent to heat treatment are shown in Figure 1.



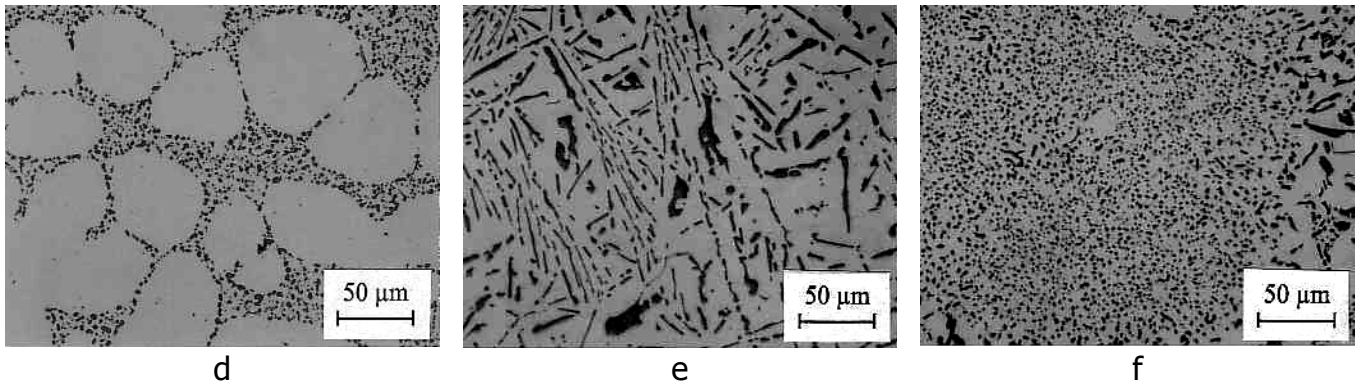


Figure 1. Alloy microstructures after heat treatment (etched with 1%HF for 10-15 seconds): 1%Si (a); 7%Si-UM (b); 7%Si-M (c); 7%Si-SSM-M (d); 13%Si-UM (e); 13%Si-M (f).

II.B. CT sample preparation and testing

II.B.1. CT specimens

CT samples conforming to ASTM E647 [17] with nominal dimensions of 3.75 in x 3.6 in x 0.4 in (95 mm x 91 mm x 10 mm) were machined from the heat treated castings. An end mill was used for the edges and a fly cutter was used for the reduction in thickness. Cracks were started from an electrodischarge machined notch made by a 0.006 in (0.15 mm) diameter wire. The notch length was 1.5 in (38 mm) measured from the front face of the sample, and 0.75 in (19 mm) measured from the pinholes.

II.B.2. Fatigue crack growth (FCG) testing

The compact tension specimens were tested per ASTM E647 [17]. Tests were conducted in laboratory air at room temperature (75°F) and relative humidity 40-50%. The specimens were tested under K-control, first under a decreasing crack driving force range (Region I) to evaluate the thresholds, and then under increasing crack driving force range (Regions II and III). Above 10^{-4} inches/cycle, the test was continued using a shallower K-gradient to obtain the steeper Region III data. The upper limit of the crack driving force was assumed to be the "pseudo" fracture toughness of the materials (because the CT samples in this study did not meet the plain strain fracture toughness requirements of ASTM E399, the measured fracture toughness values are referred to as "pseudo" fracture toughness). The compliance technique was used to monitor the crack advance and the frequency was set to 25 Hz (except in Region III where it was decreased as low as 0.1 Hz to capture sufficient data points). All the samples were tested under two constant stress ratios $R=0.1$ and $R=0.8$.

III. RESULTS AND DISCUSSION

To understand the role of the alloy's microstructure on the fatigue behavior two conditions need to be fulfilled. First, the alloy needs to contain a low defect level so that the crack interacts mostly with the intrinsic features characteristic to the alloy rather than random imperfections in the material. Second, the sample should have low residual stress. The latter aspect is commonly overlooked even though it has a significant influence on the fatigue behavior of the material. Residual stress can lead to serious design errors when it is not recognized and/or not appropriately accounted for. The effects of residual stress on fatigue crack growth are presented first, and subsequently microstructural effects are discussed for low residual stress samples.

III.A. Effect of residual stress

In Figure 2, fatigue crack growth characteristics of two sets of conventionally cast Al-Si-Mg alloys with high (T61-room temperature) and low (T61-uphill) residual stress are presented. When high, residual stress masks the effects of microstructure, all alloys having similar and high thresholds as seen in Figure 2a. However, when residual stress is reduced, the microstructure/roughness of the alloys becomes operative and a threshold ranking of the alloys is observed, Figure 2b.

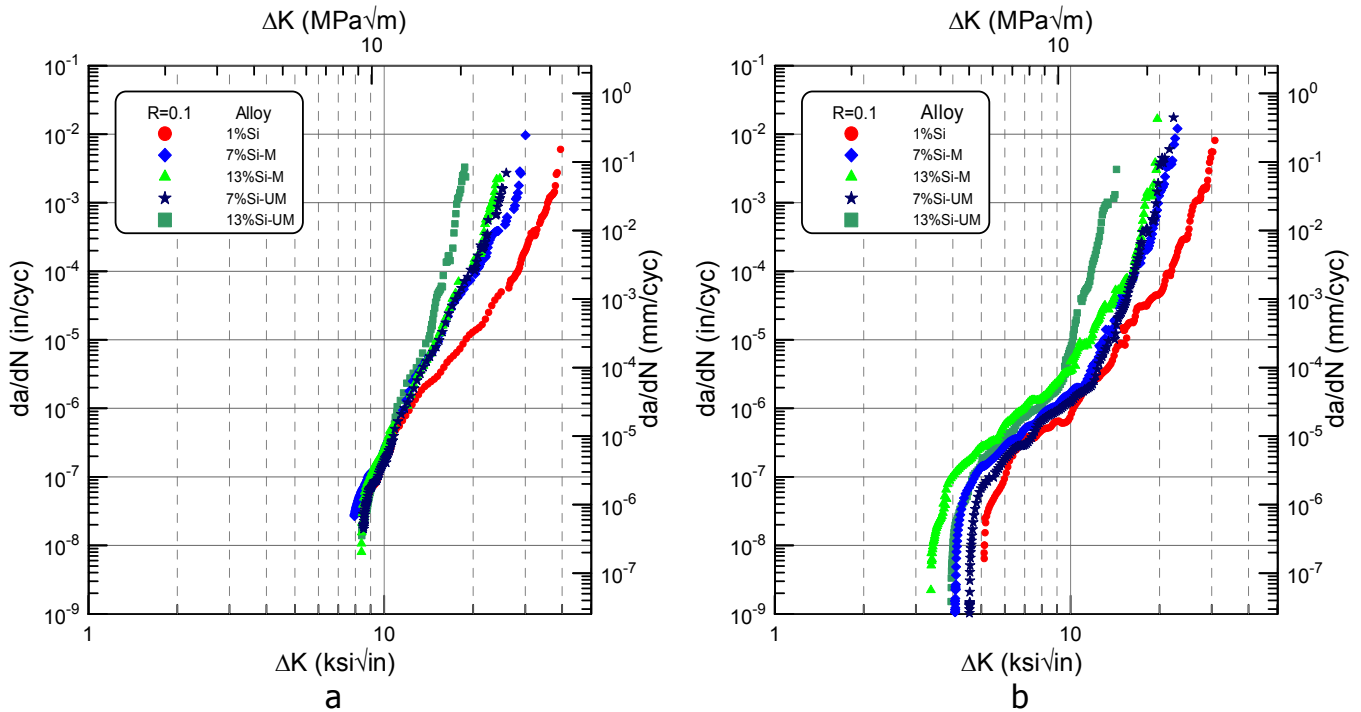


Figure 2. Fatigue crack growth behavior of alloys with residual stress (a) and without residual stress (b) under $R=0.1$.

Tests conducted on high residual stress samples were terminated prematurely due to high closure levels while the other set of samples with low residual stress did not have any residual stress induced closure, the only source of closure being related to the characteristic microstructural features of the alloys. It should be noticed that the 8-9 ksi $\sqrt{\text{in}}$ (9-10 MPa $\sqrt{\text{m}}$) crack growth thresholds of the high residual stress samples, Figure 2a, are unreasonably high for these types of cast aluminum alloys, while the samples without residual stress, Figure 2b, have thresholds in 3-5 ksi $\sqrt{\text{in}}$ (3.5-5.5 MPa $\sqrt{\text{m}}$) range. The residual stresses doubled the measured ΔK_{th} (all the other parameters being kept constant). The increase in thresholds can be explained by considering that the tip of the notch is subjected to compressive residual stresses that create higher closure. Higher closure implies less effective driving force, lower growth rates, which for a given stress, gives higher ΔK . Because of higher closure, less of the applied force actually acts on the crack tip (i.e. sheltering of the crack tip) and therefore a greater cyclic force is required to exceed the threshold and propagate the crack. On the other hand, if the notch is found in a tensile stress field (i.e. center crack tension specimen instead of compact tension specimen) the opposite effect is observed. In this case the thresholds are lower than the residual stress free thresholds because the crack is open at all times and the crack tip is exposed to the whole applied load range.

The effect of residual stress is more pronounced at low ΔK levels (ΔK_{th}) where the applied stresses are low and therefore the ratios of residual stresses to applied stresses are significantly higher. Fracture toughness, is affected by a similar residual stress level, but due to high applied stresses, the effect is considerably diminished.

Methods to **eliminate** residual stress include thermo-mechanical stress relieving techniques (for example uphill quench) or machining significantly smaller samples compared to the original size of the casting ($\sim 1/3$ of the original size). There are also methods to **account for** residual stress. They can be experimental compensation methods such as performing high stress ratio or constant K_{max} (closure free) tests or applying post testing ΔK corrective methods. The inconvenience of the latter methods however comes from the fact that they correct for both microstructure/roughness induced and residual stress induced closures; they are global closure corrections. Computational compensation methods can also be used to mathematically correct the additional contributions of the residual stress. These techniques were developed and experimentally verified [15], and more details can be found there.

III.B. Effect of microstructure on fatigue crack growth

III.B.1. Effect of Si content

Si level of the alloy plays an important role in the fatigue crack growth behavior of both unmodified and modified Al-Si-Mg alloys. The lower the Si content the better the fatigue crack growth resistance as shown in Figure 3. The dendritic alloy (1%Si, all in solid solution, no eutectic Si) has the highest threshold and pseudo-fracture toughness, and the lowest crack growth rate, followed by the A356 (7%Si) alloys and the eutectic (13%Si) alloys.

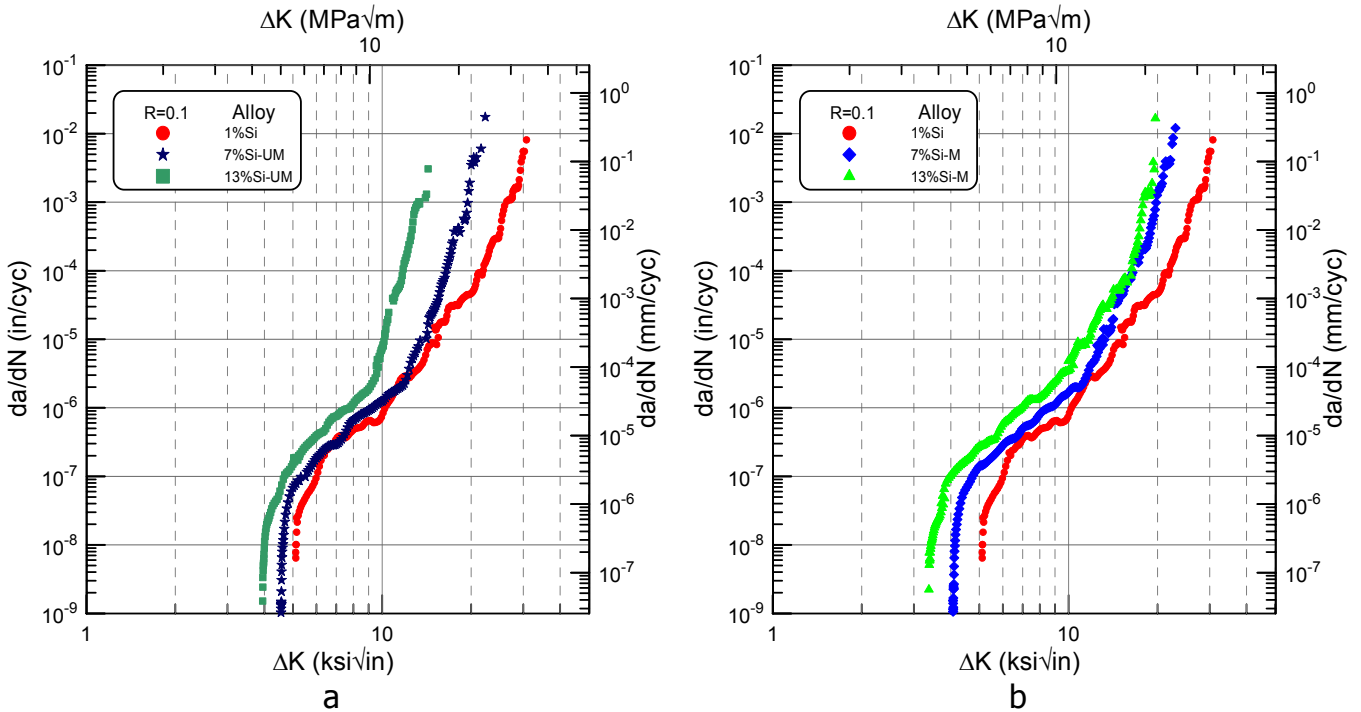


Figure 3. Effect of Si content on fatigue crack growth behavior of unmodified (a) and modified (b) alloys under $R=0.1$.

The higher thresholds of the low Si content alloys, characterized by large primary α -Al regions and small or no eutectic Si areas, are due to higher roughness-induced closure. A higher closure implies that less of the applied force is effectively acting on the crack tip (a certain amount of the applied force is spent to re-open the mating faces in contact near the crack tip) and thus a greater cyclic force is needed for the crack to progress. Roughness level is influenced by Si content as well as Si morphology. Si particles encountered along the crack path change the local slip orientation and crack path selection. In alloys with no eutectic Si (1%Si alloy), the crack advances by material separation on certain slip systems until an obstacle such as an imperfection in the crystal structure [e.g. a grain boundary, etc.], causes an orientation change. However, in higher Si

alloys, more frequent encounters with Si particles result in less variation in the crack path, lower overall roughness, and require lower cyclic force to propagate the crack. The low Si alloys, exhibit extended planar slip behavior that increases crack surface interferences resulting in higher thresholds, ΔK_{th} .

At low ΔK levels, the crack has a rather flat appearance and it advances through the constituents that lie ahead of it, Figure 4a. As the crack advances, the number of Si particles along the crack path increases, and at high crack driving force ranges, the crack appearance becomes torturous and the crack preferentially propagates both along/around and across Si particles found in the eutectic regions, Figure 4b. These correlations were observed in other investigations [18,19]. Therefore, the higher the Si content (more Si particles available) the faster the crack advance at high ΔK levels and lower the pseudo-fracture toughness of the material as seen in Figure 3. More details can be found elsewhere [19].

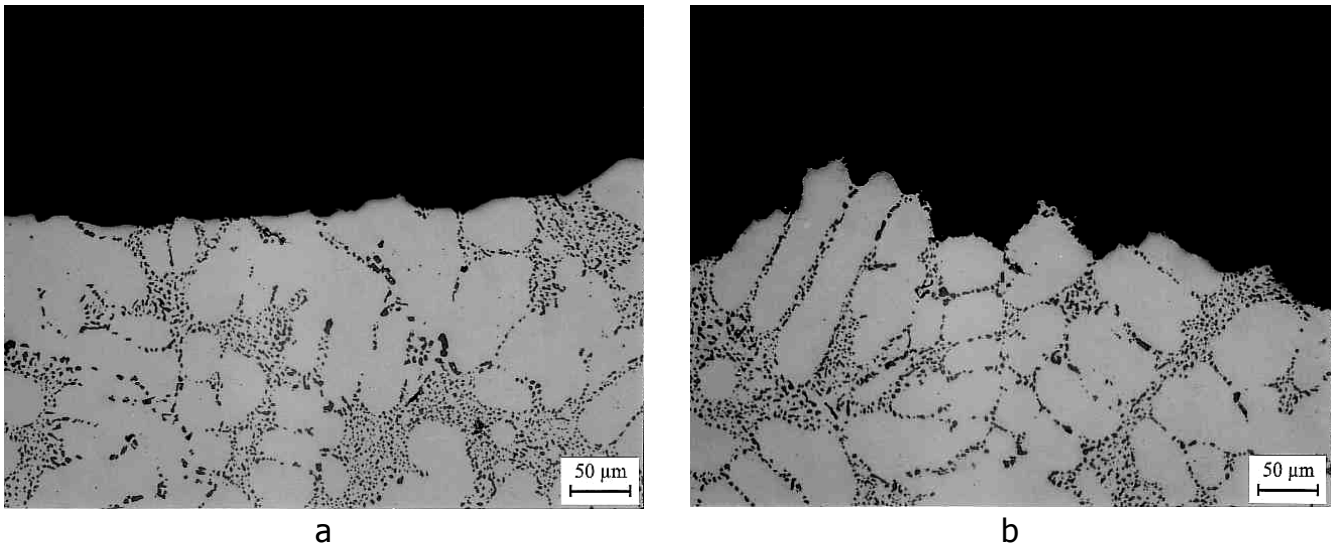


Figure 4. Fracture mode transition with increasing ΔK for a modified A356 (7%Si-M) for a stress ratio $R=0.1$: (a) lower region II ($\Delta K \sim 5 \text{ ksi}\sqrt{\text{in}}$ or $\sim 5.5 \text{ MPa}\sqrt{\text{m}}$), and (b) lower region III ($\Delta K \sim 11 \text{ ksi}\sqrt{\text{in}}$ or $\sim 12 \text{ MPa}\sqrt{\text{m}}$).

III.B.2. Effect of Si modification

Several differences between fatigue crack growth rates of unmodified and Sr-modified alloys at both 7%Si and 13%Si compositions have been observed. Unmodified alloys have higher threshold (high thresholds being associated with enhanced high cycle fatigue properties), while modified alloys present higher pseudo-fracture toughness (high toughness resulting in enhanced low cycle fatigue behavior). The behavior at low ΔK can be explained by considering the impact of Si morphology on the crack propagation path. The accommodation of

the advancing crack in unmodified alloys implies more path deflection, and local adjustment to the weakened regions, resulting in higher thresholds, ΔK_{th} . At high ΔK , once debonding and fracture of Si particles (the preferred fracture modes) occur, the coarse morphology provides convenient paths for the crack to slide along or cut through. However, the modified Si morphology is more resistant to brittle fracture, and offers more resistance by crack deflecting around Si particles. This can be clearly seen by analyzing Figure 5. Modified A356 alloys show slightly improved behavior in upper Region II and Region III compared to the unmodified A356 alloys, but the difference is less evident than in the case of 13%Si alloys. This proves the explained behavior, and also points out the fact that heat treatment minimizes the Si morphology differences between unmodified and modified alloys due to the thermal modification of the plate-like eutectic Si structure. The larger plates in 13%Si alloys require longer time to break and spheroidize during heat treatment, and the preservation of the plate-like structure specific to unmodified alloys drives larger differences between the fatigue crack growth behavior of unmodified and modified 13%Si alloys in upper Region II and Region III. Larger differences in pseudo-fracture toughness are caused by enhanced contrasts in Si morphology that are function of Si content and heat treat time. The size and aspect ratio of Si particles for all the alloys are given in Table 2.

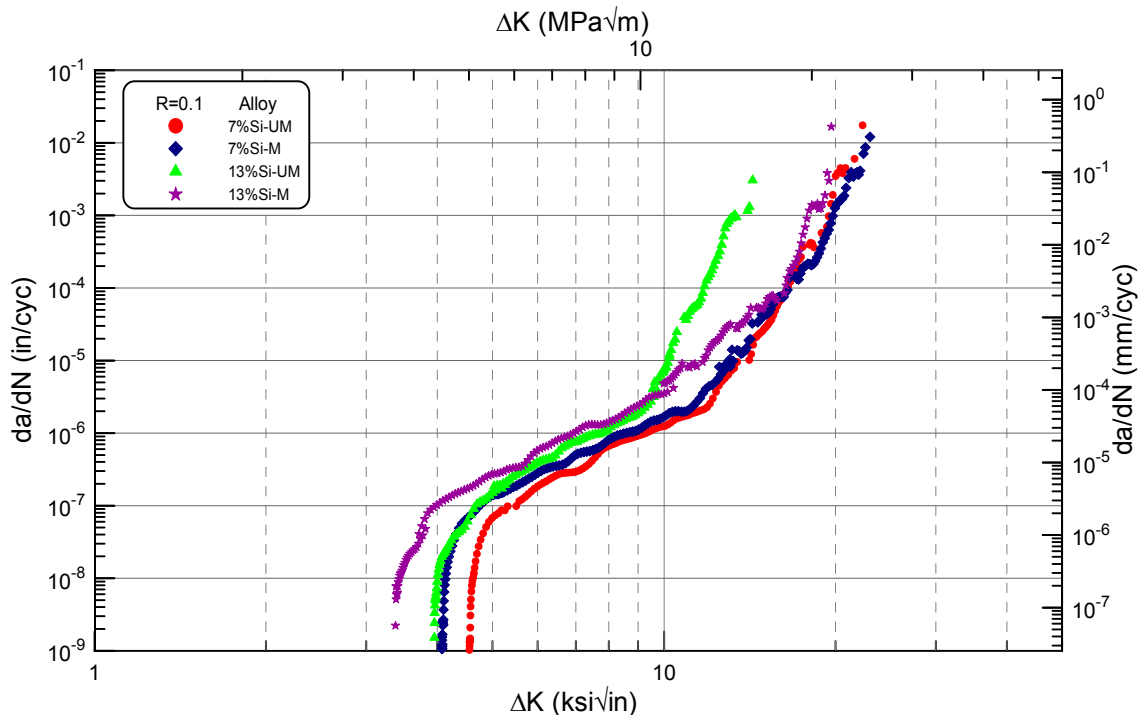


Figure 5. Effect of Si modification on fatigue crack growth behavior of 7%Si and 13%Si alloys.

Table 2. Si size and shape for the modified and unmodified alloys

	Alloy systems examined					
	7%Si-UM (A356-UM)	7%Si-M (A356-M)	7%Si-M (SSM-M)		13%Si-UM (Eutectic-UM)	13%Si-M (Eutectic-M)
			T61	T5		
Si avg. particle size (μm)	2.77	2.19	2.01	1.31	2.94	2.05
Si particle shape factor ^d	1.41	1.21	1.17	2.01	1.86	1.19

^d Shape factor was calculated as: shape factor = $\text{perimeter}^2 / (4 \cdot \pi \cdot \text{area})$.

Other researchers [20] also observed higher ΔK_{th} and lower fracture toughness for higher aspect ratio Si particles in SSM Al-Si-Mg alloys of similar grain size and α -Al particle size. Similar results were found for a JIS AC4CH (A356) alloy [21] and an Al-12%Si-0.35%Mg alloy [22] for tests conducted under constant stress ratio $R=0.1$. In other studies, modified alloys showed better fatigue crack growth characteristics at high ΔK levels, but no differences between unmodified and modified alloys were found in the near threshold regime for $R=0.1$ tests [23].

III.B.3. Effect of grain refinement (grain size)

It was shown in the literature that grain size influences the fatigue crack growth behavior of wrought superalloys [24], wrought aluminum alloys [25], aluminum-magnesium alloys [26], etc. Odegard, reported a grain size effect on the fatigue crack growth of wrought 7075 aluminum alloys. The large grained material showed a higher threshold compared to the small grained material for both underaged and overaged heat treated samples; the author related this behavior to the closure mechanisms. However, the effects of grain size on the fatigue crack growth of cast aluminum alloys (where other parameters besides grain boundaries have impact on crack advance) are not reported in the literature, and often times grain size level is not reported. Therefore, in this study three grain size levels were investigated, to understand the effects of grain size on the fatigue crack growth characteristics of cast Al-Si alloys, and the results are presented in Figure 6 for unmodified and modified A356 alloys.

Grain size has no significant effect on the fatigue crack growth behavior of any of the alloys. This result can be easily explained considering the propagation mechanisms explained in the previous two sections. Fatigue crack growth mechanisms, are governed by microstructural features smaller than grain size, and the spacing of grain boundaries becomes of secondary importance for cast alloys with typical grain size in the 100-1000 μm range.

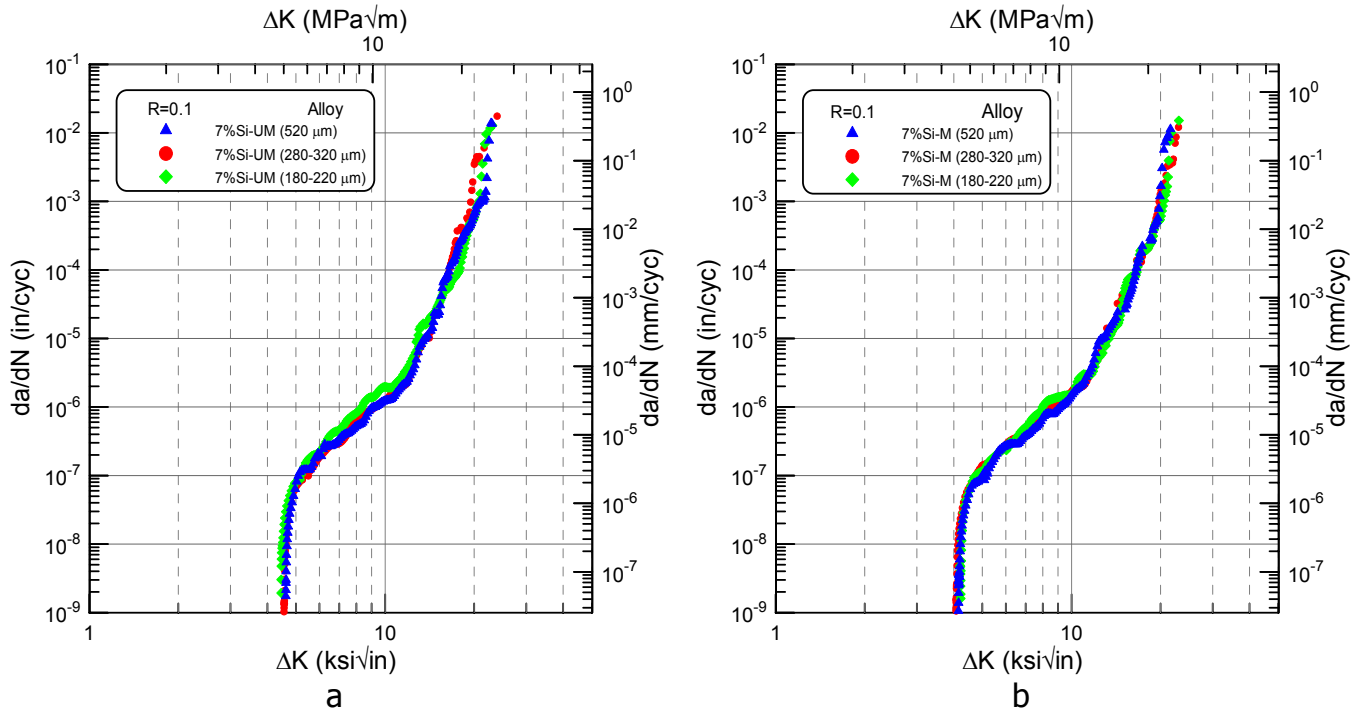


Figure 6. Effect of (primary a) grain size level on fatigue crack growth behavior of unmodified (a) and modified (b) A356 alloys.

It is important to remember that grain refinement is primarily used to improve feeding (delayed coherency), to create more finely dispersed porosity, and to better disperse secondary phases. Improved fatigue crack growth behavior is not the main reason for grain refining, and as long as it does not have a detrimental effect, it can be used to prevent some of the negative aspects encountered in castings.

III.B.4. Effect of SDAS

In this study SDAS was controlled to 20-30 μm . However, the understanding of the fatigue crack growth mechanisms developed for this class of Al-Si alloys was further extrapolated to coarser microstructures with larger SDAS, such as those presented in Figures 7b and c.

Alloys with large SDAS are characterized by large crack growth resistant α -Al dendritic regions, and large spacings between consecutively sampled Si regions. As a result, the roughness associated to these structures is higher than the roughness of small SDAS materials due to coarsely spaced crack-Si particle interactions, which results in higher closure, higher threshold, and better fatigue crack resistance in the near threshold regime. However, at high ΔK levels, the size of eutectic regions and the Si particle morphology dictate the crack growth resistance. For coarser structures the eutectic regions as well as Si particle size

are larger too, providing lower resistance to the crack advance. This behavior results in higher growth rates at high ΔK and lower pseudo-fracture toughness for the large SDAS materials.

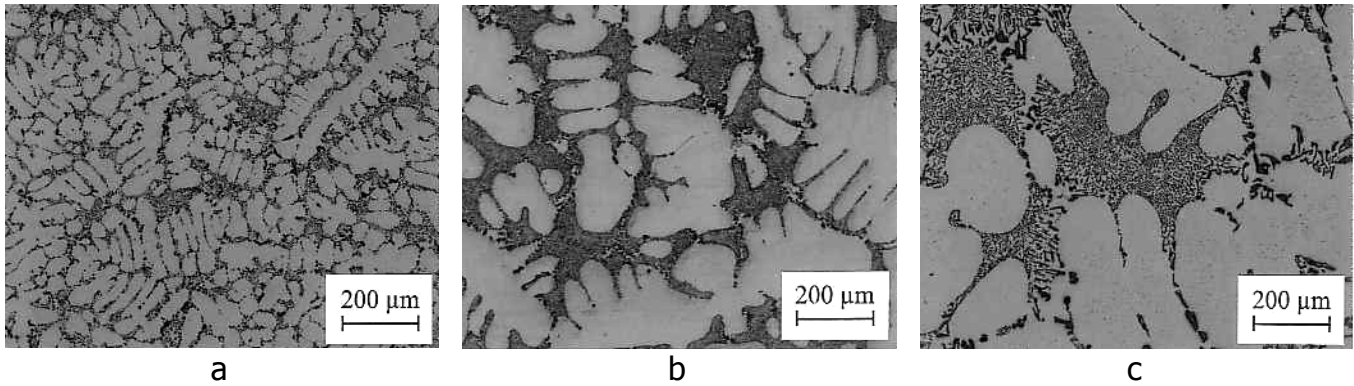


Figure 7. Microstructures of modified A356 alloys with different SDAS: small, 20-30 μm (a), large, 70-80 μm (b), very large, 150-170 μm (c).

Predictions for two additional samples with similar composition (modified A356), but larger SDAS values were created and are qualitatively presented in Figure 8. Similar behavior was experimentally observed for A356 squeeze and sand mold castings [27], A356 permanent mold and sand mold castings [21], and W319-type castings provided by a wedge mold with a copper chill at the nose of the wedge [28].

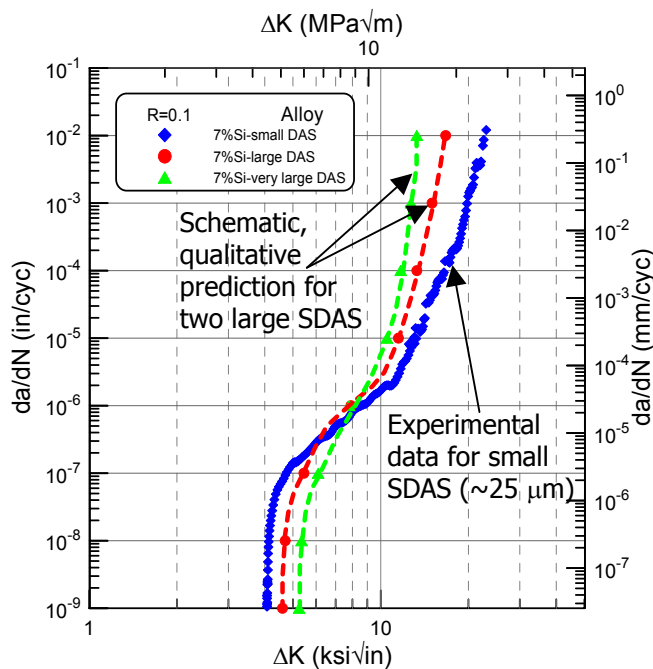


Figure 8. Predicted fatigue crack growth behavior of modified A356 alloys with large SDAS.

III.C. Effect of matrix strength (heat treatment)

The effect of matrix strength on fatigue crack growth resistance was determined by comparing the behavior of naturally aged (T4) and artificially aged (T61) A356 samples of both unmodified and Sr-modified Si morphologies. The artificial aging increased the matrix hardness from 80-85 HV to 100-105 HV. No significant differences were observed between the two conditions in the threshold and lower Paris regions where the crack advance is slow and closure mechanisms play a significant role, Figure 9.

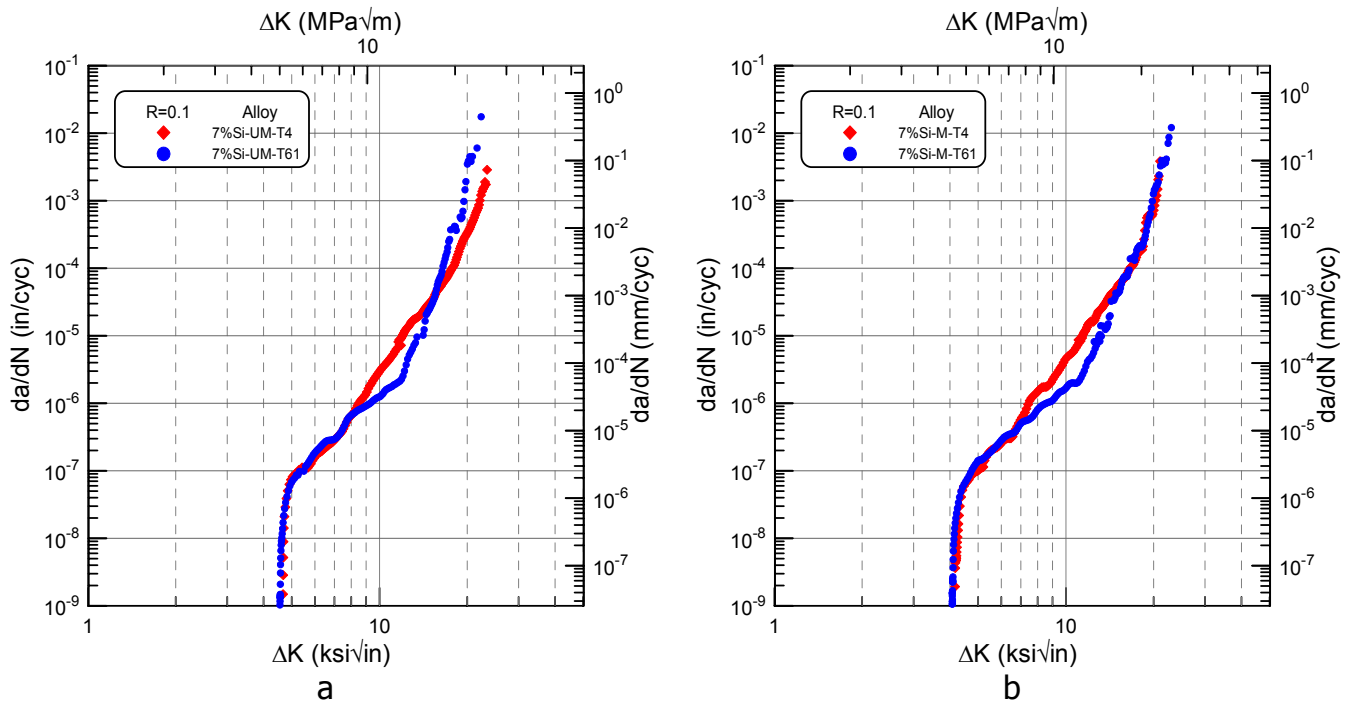


Figure 9. Fatigue crack growth behavior of unmodified and modified A356 alloys in T61 and T4 heat treat conditions.

In upper Region II and lower Region III, crack growth rates of both unmodified and modified alloys in T4 conditions are higher than in T61 conditions. The matrix of the T4 samples has a low yield strength (in contrast to T61), which provides a path of low resistance in front of the incoming crack in addition to the Si-particles/matrix interface. The reason for the observed higher propagation rate in T4 samples is because there are alternative least resistance local paths for the crack to follow. In upper Region III, T4 samples show a better fatigue crack growth resistance and higher pseudo-fracture toughness. The differences in upper Region III can be seen more evidently when the linear elastic fracture mechanics definitions are corrected for plasticity contributions [29]. Similar observations in the threshold and upper Region III regions were given in the literature for under-aged and peak aged samples of A356 alloys [27,30].

III.D. Effect of casting technology (conventional vs. SSM)

The differences between conventional casting and SSM processing produce two key differences in the microstructure: (1) mean spacing between eutectic pools and (2) size of the eutectic pools, Figure 10. The Si morphology of the two processes is similar for T61 heat treat condition (Table 2), and the matrix hardness is also comparable. In the T5 samples the as-cast Si morphology is preserved, Table 2.

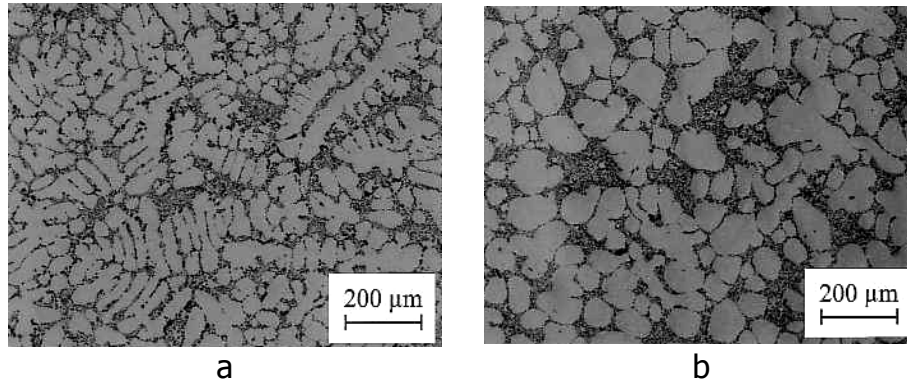


Figure 10. Microstructure characteristics of a modified A356 in conventional casting (a) and SSM casting (b).

By comparing the dendritic structure distribution in conventionally cast alloys and the globular structure of the semi-solid castings, Figure 10, fatigue crack growth characteristics specific to these two types of alloys can be rationalized. In the T61 heat treated condition the SSM samples have lower crack growth resistance compared to the conventional castings due to more frequent interactions of the crack (as it advances through the primary α globular structure) with larger Si regions. This results in less closure and faster growth rates. However, at high ΔK values when crack begins to follow exclusively the eutectic regions, the crack growth rates become similar, Figure 11, considering the similar Si morphology of the conventionally and SSM cast modified A356 alloys (see Table 2).

The differences between the fatigue crack growth behavior of T61 and T5 heat treated SSM samples are minimal in the near threshold regime due to similar roughness-induced crack wake effects (see T61 vs. T4 for conventional castings in the previous section). With increasing ΔK , the crack resistance of the T5 sample becomes visibly lower and pseudo-fracture toughness decreases by almost 50%. This poor response is caused by the T5 treatment that is thought of as a stabilization treatment providing lower yield strength and matrix hardness (70-75 HV). Moreover, the absence of solution treatment involves less spherical Si morphology, more favorable to faster propagation rates once the transition to

Si propagation mode occurred. Fatigue crack growth data for conventional and SSM cast samples are presented in Figure 11.

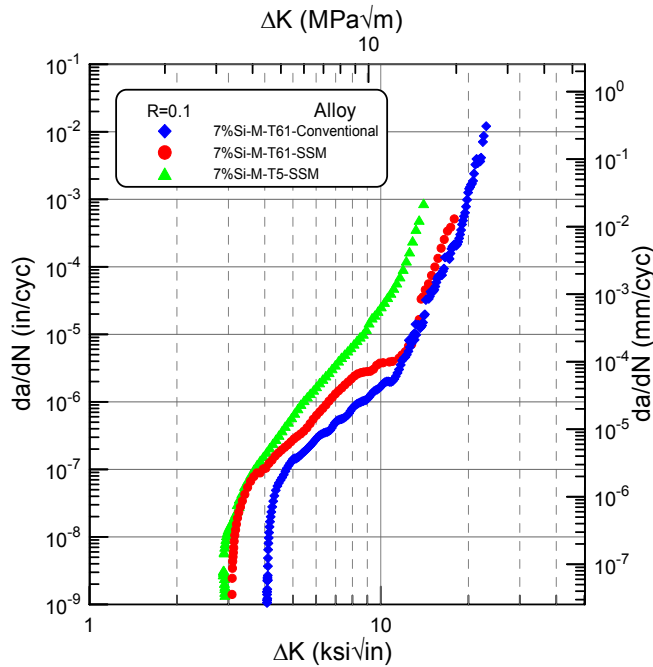


Figure 11. Fatigue crack growth characteristics of a modified A356 in conventional (a) and SSM (b) casting.

Even though the studied SSM material has lower performance than conventional castings, there are several aspects that need to be kept in mind. It is well known that SSM structures can be significantly different depending on the method by which they are produced. It is important to mention, that the near threshold regime of these materials is considerably affected by the size of the α globular structure, as well as the particle agglomeration level. The latter also dictates the size of the eutectic Si regions and consequently the growth rates in upper Region II and Region III. Further characterization of fatigue crack growth properties of a wider range of SSM structures is recommended.

III.E. Effect of plasticity

Linear elastic fracture mechanics (LEFM) assumptions hold true for Region I, and lower Region II; however, at high driving force levels, plasticity becomes increasingly significant, and elastic-plastic based fracture mechanics theories (EPFM) are needed to describe the material behavior, Figure 12. It is also known that, as plasticity increases, tearing becomes a significant failure mode. A cumulative cyclic J-analysis that accounts for both plasticity and tearing effects has been developed by Lados and Apelian [29]. This method appropriately characterizes the behavior of high ductility materials at high ΔK levels, and also

provides the actual fracture toughness of the material without the need for static fracture toughness testing. For all the alloys tested the fracture toughness computed using cyclic J-analysis is remarkably similar to the static fracture toughness despite the original differences in ductility or residual stress. An example of the cyclic J-analysis for the modified A356 alloy in T61 and T4 conditions is presented in Figure 12. This method can be used to determine the actual fatigue crack growth behavior as well as fracture toughness of the material.

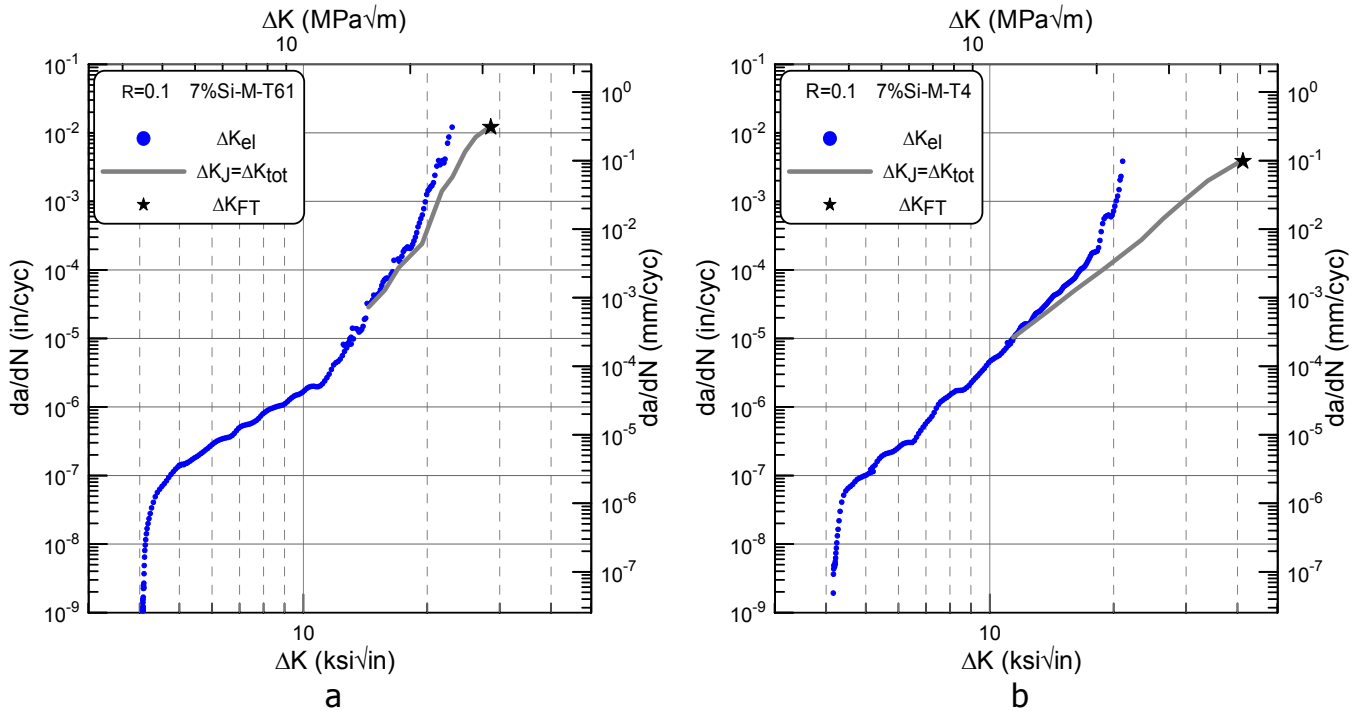


Figure 12. Elastic (ΔK_{el}) and elastic/plastic (ΔK_J) fatigue crack growth behavior of a modified A356 alloy in T61 (a) and T4 (b) heat treating conditions. ΔK_{FT} is the limiting, outer bound fracture toughness of the material.

III.F. Effect of stress ratio

The importance of closure is determined by comparing fatigue crack growth curves from tests conducted at high stress ratios ($R=0.8$) and low stress ratios ($R=0.1$). For high stress ratios, high minimum stresses are involved, and both threshold and overall life are decreased. High stress ratios prevent crack closure, which lowers the threshold. The tests done at $R=0.8$ are almost free of closure and the thresholds, Figure 13a, are similar to those provided by the closure corrected ΔK_{eff} results, Figure 13b. It can also be observed that increasing the stress ratio, the reduced influence of closure makes all alloys similar in threshold, and microstructure effects of each individual alloy become less obvious. Fatigue crack growth rates in Regions II and III are increased for all alloys; steeper curves for $R=0.8$, Figure 13a compared to $R=0.1$, Figure 2b are observed.

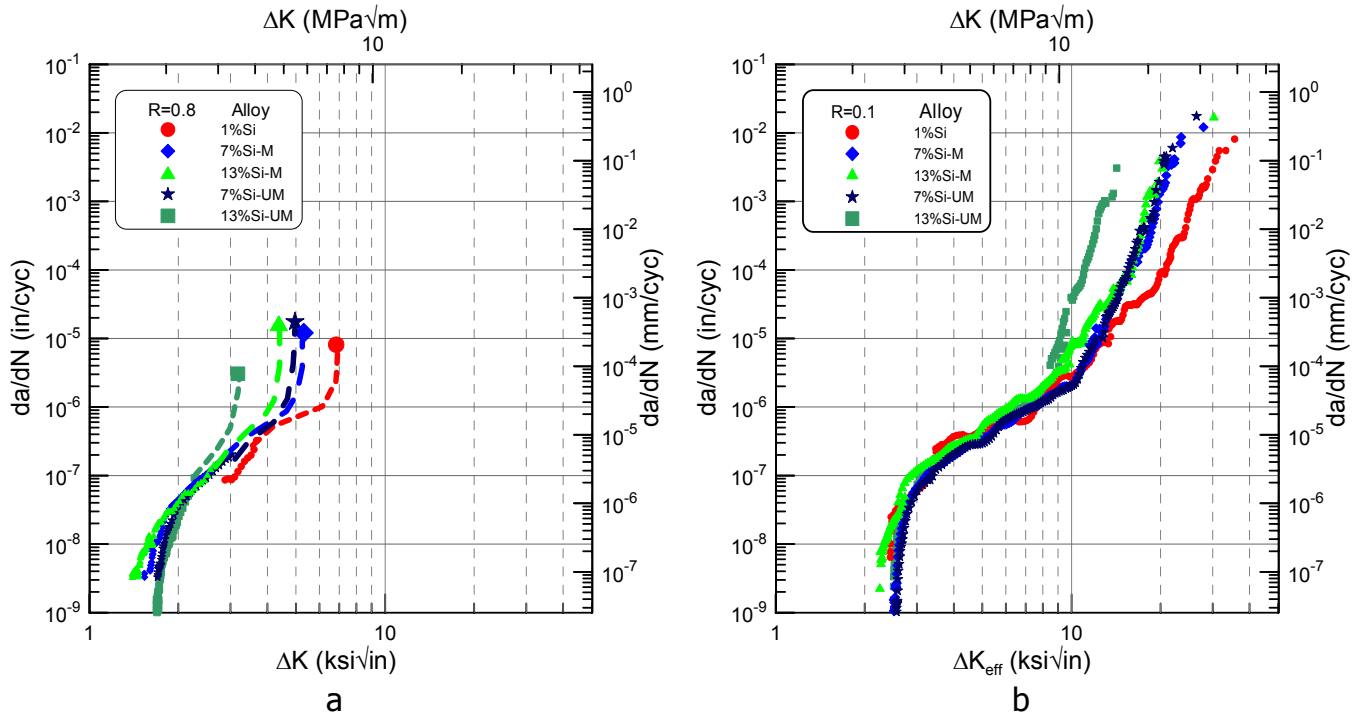


Figure 13. Fatigue crack growth behavior of the alloys under two stress ratios, $R=0.8$ (a), and $R=0.1$ after closure correction (b).

For the $R=0.8$ tests, the near threshold regions (Region I and lower Region II) were determined experimentally and the rest of the fatigue crack growth curves were estimated using the K_{max} values corresponding to the pseudo-fracture toughness obtained from the $R=0.1$ tests. The estimates were made by eq. [1]:

$$\Delta K_R = (1 - R) \cdot K_{max} \quad [1]$$

where $R=0.8$.

The impact of stress ratio on crack growth rates in this study is consistent with the cast aluminum literature. Similar effects of increased stress ratios, $R=0.5$ and $R=0.8$ on fatigue crack growth behavior of Al-12%Si-0.35%Mg were reported by others [22,23]. The same fatigue crack growth response was observed for an Al-7%Si-0.4%Mg alloy, when stress ratio was varied from 0.074 to 0.95 [31].

SUMMARY

Fatigue crack growth response of Al-Si-Mg alloys is influenced by residual stress and alloy microstructure (especially when the defect level in the alloy is low). The effects of residual stress on the fatigue crack growth behavior are more

prominent at low ΔK . When residual stress is higher than certain critical levels it masks microstructural effects, and residual stress induced closure overshadows microstructure (roughness)-induced closure.

The dendritic alloy (1%Si) shows the highest fatigue crack growth resistance at both low (threshold) and high ΔK (pseudo-fracture toughness) levels. It is followed by the A356 (7%Si) alloys and the eutectic (13%Si) alloys. Unmodified alloys have superior thresholds compared to the modified alloys for both hypo-eutectic (7%Si) and eutectic (13%Si) alloys. Modified alloys present better fatigue crack growth characteristics than unmodified alloys in Region III (more fracture resistant and thus higher toughness). The higher the Si level the larger the differences between the modified and the unmodified alloys due to the effect of Si morphology.

Grain size has no significant influence on the fatigue crack growth response of the studied alloys, the crack advance being controlled by microstructural features smaller than grain size. On the other hand, small microstructural features, such as SDAS, affect the crack propagation behavior. Higher thresholds and lower fracture toughness are predicted for large SDAS materials compared to small SDAS materials.

Enhanced levels of plasticity lead to increased inaccuracies at high ΔK levels, and plasticity corrections are required in upper Region II and Region III. An elastic-plastic model to compute the actual fracture toughness of the material from fatigue crack growth data has been developed and validated.

Stress ratio is an important parameter. As expected, higher stress ratios not only decrease the thresholds (less closure), but also increase the fatigue crack growth rates.

Conventional castings show better fatigue crack initiation and propagation characteristics compared to the selected SSM cast material. However, the size of the globular α particles, the degree of particle agglomeration, and the resulting size of the eutectic regions are critical and they can be appropriately controlled during the SSM casting process when improved fatigue crack growth resistance is needed.

In terms of life estimations, alloys with high toughness and low crack growth threshold (such as modified, A356, modified eutectic, large SDAS alloys, etc.) are recommended for low cycle fatigue, highly stressed applications (when large flaw sizes are expected in the structure). Alloys with high threshold (such as unmodified, A356, small SDAS alloys, etc.) are appropriate for high cycle fatigue when large numbers of cycles are expected (low stress applications, small initial flaw sizes, etc.). These choices are appropriate even if there is a trade off in

fracture toughness, considering that the propagation mode contributes with only a small percentage to the total life of the component.

The unmodified eutectic alloy with 13%Si is not recommended for fatigue or fracture toughness critical applications due to its low toughness. However, for less critical applications it can be an inexpensive and functional alternative.

ACKNOWLEDGMENTS

The authors express their thanks to General Motors Corp. for partly supporting the fatigue crack growth testing and Alcan for providing high purity aluminum needed in this work and evaluating the fracture surface roughness of the tested samples. Special thanks are directed to Palmer Foundry for the significant contribution in the sand mold design and the preparation of the molds. The authors address their gratitude to Dr. Peggy Jones of General Motors and Dr. Fred Major of Alcan for their contributions, guidance, and technical assistance during the entire duration of the study. Dr. Libo Wang's assistance during the casting runs is greatly appreciated. The fatigue crack growth testing was done at Fracture Technology Associates. Special thanks go to Mr. Keith Donald for his important contribution to the critical issues related to residual stress impact on the fatigue crack growth response.

REFERENCES

- [1]. D.A. Lados, D. Apelian, A.M. de Figueredo, in: M. Tiryakioglu, J. Campbell (Eds.), *Advances in Aluminum Casting Technology II, Proceedings from Materials Solutions 2002*, ASM, Metals Park, OH, 2002, pp. 185-196.
- [2]. M.J. Couper, A.E. Neeson, J.R. Griffiths, *Fatigue Fract. Engng Mater. Struct.* 13 (3) (1990) 213-227.
- [3]. B. Zhang, D.R. Poirier, W. Chen, "Effect of Strontium Modification and Hydrogen Content on the Fatigue Behavior of A356.2 Aluminum Alloy", Unpublished.
- [4]. Q.G. Wang, D. Apelian, D.A. Lados, *J. Light Metals* 1 (1) (2001) 73-84.
- [5]. J.F. Major, *AFS Trans.* 105 (1997) 901-906.
- [6]. J.A. Odegard, K. Pedersen, *SAE Technical Publication* 940811 (1994) 25-32.
- [7]. C.M. Sonsino, J. Ziese, *Int. J. Fatigue* 15 (2) (1993) 75-84.
- [8]. N.R. Green, J. Campbell, *AFS Trans.* 102 (1994) 341-347.
- [9]. C. Nyahumwa, N.R. Green, J. Campbell, *AFS Trans.* 106 (1998) 215-223.
- [10]. J.E. Allison, J.W. Jones, M.J. Caton, J.M. Boileau, in: X.R. Wu, Z.G. Wang (Eds.), *Proceedings of 7th International Fatigue Congress, Fatigue '99*, EMAS/HEP Publishers, UK, 3, 1999, pp. 2021-2028.
- [11]. A. Wickberg, G. Gustafsson, L.E. Larsson, *SAE Technical Publication* 840121 (1984).

- [12]. W. Chen, B. Zhang, T. Wu, D. Poirier, P. Sung, Q.T. Fang, in: S.K. Das (Ed.), *Automotive Alloys II*, TMS, Warrendale, PA, 1998, pp. 99-113.
- [13]. W. Chen, B. Zhang, T. Wu, D. Poirier, P. Sung, Q.T. Fang, *The 1st International Aluminum Casting Tech. Symposium*, Rosemont, IL, 13-14 October 1998.
- [14]. Q.G. Wang, D. Apelian, D.A. Lados, *J. Light Metals* 1 (1) (2001) 85-97.
- [15]. D.A. Lados, D. Apelian, "The Effect of Residual Stress on the Fatigue Crack Growth Behavior of Cast Al-Si-Mg Alloys – Mechanisms and Corrective Mathematical Models", to be submitted to *Metall. Mater. Trans. A*.
- [16]. D.A. Lados, D. Apelian, "Quenching Modes and Residual Stress Levels in Cast Al-Si-Mg Alloys - Mechanisms and Effects on Static and Dynamic Properties", to be submitted to *Metall. Mater. Trans. A*.
- [17]. ASTM Standard E647, *Standard Test Method for Measurement of Fatigue Crack Growth Rates*, Annual Book of ASTM Standards, Vol. 03.01, 2000.
- [18]. K. Gall, N. Yang, M. Horstemeyer, D.L. McDowell, J. Fan, *Metall. Mater. Trans. A* 30A (1999) 3079-3088.
- [19]. D.A. Lados, D. Apelian, "Operating Fatigue Crack Growth Mechanisms at the Microstructure Level in Al-Si-Mg Cast Components", to be submitted to *Acta Met.*
- [20]. S.-W. Kim, S.-W. Han, U.-J., Lee, K.-D. Woo, *Materials Letters* 58 (2003) 257-261.
- [21]. S. Kumai, S. Aoki, S.-W. Han, A. Sato, *Mater. Trans., JIM*, 40 (7) (1999) 685-691.
- [22]. F.T. Lee, J.F. Major, F.H. Samuel, *AFS Trans.* 104 (1996) 785-795.
- [23]. M. Schaefer, R.A. Fournelle, *Metall. Mater. Trans. A* 27A (1996) 1293-1302.
- [24]. G.A. Osinkolu, G. Onofrio, M. Marchionni, *Mater. Sci. Eng. A356* (2003) 425-433.
- [25]. J.A. Odegard, "Fatigue Behavior in a DC-Cast A356 (AlSi7Mg) Aluminum Casting Alloy", Ph.D. thesis (1992).
- [26]. A. Turnbull, E.R. de los Rios, *Fatigue Fract. Engng Mater. Struct.* 18 (11) (1995) 1355-1366.
- [27]. S. Kumai, J. Hu, Y. Higo, S. Nunomura, *J. Jap. Inst. Light Metals* 45 (4) (1995) 198-203. (in Japanese)
- [28]. M.J. Caton, J.W. Jones, J.M. Boileau, J.E. Allison, *Metall. Mater. Trans. A* 30A (1999) 3055-3068.
- [29]. D.A. Lados, D. Apelian, "Validity Limits for Elastic Definitions in Cast Al-Si-Mg Alloys with Enhanced Plasticity-Linear Elastic Fracture Mechanics versus Elastic/Plastic Fracture Mechanics", to be submitted to *Engng Fract. Mechanics*.
- [30]. B. Skallerud, T. Iveland, G. Harkegard, *Engng Fract. Mechanics* 44 (6) (1993) 857-874.
- [31]. M.J. Couper, J.R. Griffiths, *Fatigue Fract. Engng Mater. Struct.* 13 (6) (1990) 615-624.

Chapter 3

The Effect of Residual Stress on the Fatigue Crack Growth Behavior of Cast Al-Si-Mg Alloys – Mechanisms and Corrective Mathematical Models

D. A. Lados and D. Apelian
Worcester Polytechnic Institute, Worcester, MA, USA

ABSTRACT

Fatigue crack growth behavior of various types of alloys is significantly affected by the presence of residual stress induced by manufacturing and post-manufacturing processes. There is a qualitative understanding of the effects of residual stress on fatigue behavior, but the effects are not comprehensively quantified and/or accounted for. The difficulty in quantifying these effects is mostly generated by the complexity of residual stress measurements (especially, considering that parts produced in similar conditions have different residual stress levels) and the lack of mathematical models able to convert experimental data with residual stress into residual stress free data. This paper provides experimental, testing, and mathematical techniques to account for residual stress effects on crack growth rate data together with two methods to eliminate residual stresses in crack growth test specimens. Fracture mechanics concepts are used to calculate, in simple and convenient ways, stress intensity factors caused by residual stresses. The main advantage consists in the possibility of determining stress intensity factors before the tests are conducted. Further, residual stress intensity factors are used to predict residual stress distribution in compact tension specimens before testing. Five cast Al-Si-Mg alloys with three Si levels (both unmodified and Sr-modified) are analyzed both with and without residual stress. Fatigue cracks are grown under both constant stress ratio, $R=0.1$, and constant maximum stress intensity factor, K_{max} , conditions. The mechanisms involved in crack growth through residual stress fields are presented.

Keywords: residual stress, quenching, Al-Si-Mg alloys, compact tension specimens, fatigue crack growth in residual stress fields, fatigue thresholds, fracture toughness, fracture mechanics, fatigue crack propagation mechanisms.

I. INTRODUCTION AND BACKGROUND

Residual stresses are self-equilibrating internal or locked-in stresses remaining in a material that is free of applied (external) forces, external constraints, or temperature gradients [1,2]. In most cases, residual stresses are an undesired result of material processing and they persist in the material unless eliminated through subsequent stress relieving techniques. They are commonly found in weldments, complex forged and extruded parts, castings, especially when heat

treated. In some cases, compressive near surface residual stresses are purposely introduced (e.g. shot peening) to improve fatigue life. The major difference, however, consists in the type of residual stress (*compressive*-retards fatigue crack growth or *tensile*-accelerates fatigue crack growth) and the knowledge of residual stress level. In the first case, the residual stress level is difficult to predict, while in the second case, it is known and quantified. In general, residual stresses may develop in the material as a response to the following: plastic deformation processes such as machining, grinding, forming, a phase transformation that is induced upon cooling wherein parent and product phases have different densities and/or crystal structures, or nonuniform cooling of a piece that was fabricated or processed at elevated temperatures [3]. The most common severe residual macro-stresses, however, are introduced by the non-uniform cooling. Residual stresses are found in all alloy systems: aluminum alloys, superalloys, titanium alloys, and steels.

Knowledge of the residual stress level in the component is very important, particularly when techniques to account for it are developed. There are several methods (non-destructive, partly-destructive, and destructive) to measure initial residual stress fields in the materials. All stress measurements are based on the evaluation of actual strain or changes in strain, and they can be either qualitative or quantitative. Most commonly used stress measuring techniques have been summarized elsewhere [4-6] and they will be briefly mentioned here: photo-stress coatings, ultrasonic (acoustics), electromagnetic (including Barkhausen noise analysis), photoelasticity, X-ray diffraction, neutron diffraction, hole drilling, positron annihilation, nuclear hyperfine (including Mossbauer), spectroscopy, chemical etching, sectioning strain gauged samples, and indentation and microhardness mapping. X-ray diffraction is recognized to be the only truly non-destructive technique that is reliable. However, its severe limitations are that it can be applied non-destructively only on the surface, and it is a long and expensive procedure. The difficulties and limitations associated with all these techniques reduce the possibility of accurate residual stress measurements and open the door for more research in the quest to find practical and accurate ways to determine residual stresses.

Despite these difficulties, determining the presence, magnitude, and distribution of residual stresses is vital for the correct interpretation of fatigue crack growth experimental data and implicitly the real service life predictions. It has been known for a long time that residual stress has a strong impact on fatigue crack growth behavior, da/dN vs. ΔK [7-18]. Even if residual stresses affect only mean stresses, or stress ratios, they do influence crack initiation, propagation, and closure significantly [15,18-23]. The most frequently used approach to account for the effect of residual stress on crack growth involves the superposition of the stress intensity factors from the initial residual stress and the applied loads, $K_{eff}=K_{res}+K_{app}$, [7,10,11,15,16,18]. However, when at minimum load cracks are

only partially opened (bulge effect – crack surfaces close far behind the crack tip), the superposition model could become invalid due to non-linear contact unless the appropriate stress intensity factor range is used. From this perspective, corrective methods for residual stress compensation, based on linear elastic fracture mechanics concepts (such as stress intensity factor, K), are most desirable so that existing $da/dN-\Delta K$ data with residual stress may be directly adjusted and further utilized for residual stress free applications. As a result, residual stress intensity factors, K_{res} , are of greater interest than residual stresses because they can be used directly in the fatigue crack growth and fracture relationships. K_{res} have been calculated for several crack types and crack face stress distributions mostly using weight function models (WFM) [7,10,11,15,16,18], a method that requires the prior knowledge of the residual stress profile. More recently, a simple and promising technique was developed based on successive extensions of the compact tension (CT) specimen notch while the strain changes on the back face of the specimen are captured. This “cut compliance” technique evolved from a relatively inaccurate method first presented by Reid [24], further developed by Schindler [25], and successfully applied by Prime [26] and others. This new technique provides residual stress intensity factors directly from the measured strains without first solving for the residual stresses. Subsequently, residual stress profiles can be back-calculated using weight functions. The major assumption here is that residual stresses do not change or redistribute with the crack growth. Depending on crack closure mechanisms (residual stress, roughness, plasticity, oxides) this assumption could potentially overestimate the effect of residual stresses on fatigue crack growth. However, even if changes in magnitude and redistributions of residual stresses can theoretically occur during crack growth, residual stress induced closure and roughness induced closure interact in a complex, non-linear fashion in low stress ratios. This interaction may in fact overcome the magnitude change and residual stress redistribution.

This paper contains three sections corresponding to three ways of deriving residual stress free data from fatigue crack growth experiments. Residual stresses are a result of quenching, as part of a T61 heat-treatment procedure applied to Al-Si-Mg alloys. In the first part, the behavior of compact tension specimens, with high and low residual stresses are analyzed, and residual stress free fatigue crack thresholds are determined from the experimental data. In the second part, two methods to mathematically compensate for the presence of residual stress are developed. In the third part, two methods to produce residual stress free samples are introduced and the corrective methods are verified. Finally, a method to predict residual stress distribution without physical measurements by simply using K_{res} data and weight functions is addressed using numerical integration.

II. EXPERIMENTAL PROCEDURE

II.A. Alloys, casting procedure, and heat treating conditions

Cast Al-Si-0.45%Mg specimens with Si in both unmodified (UM) and Sr-modified (M) conditions were tested. The levels of Si used in this work are 1%, 7%, and 13%. Grain size in all the alloys was kept constant ($\sim 280 \mu\text{m}$) by appropriate additions of 5:1 TiBor™ master alloy and Sr-modification was done using Al-10%Sr master alloy. High purity alloys were used so that all the other elements were kept at very low levels $<0.002\%$; Fe concentration was $<0.02\%$. DAS was controlled for all alloys in the range 20-30 μm . For the fatigue growth studies compact tension (CT) specimens were prepared using a specifically designed sand mold containing central top and bottom gray cast iron chills to insure the desired DAS throughout the region of interest. The original castings used to prepare the CT samples had the following dimensions: 4.4in x 4.4in x 0.8in (112mm x 112 mm x 20.5mm).

Most commercial aluminum alloys reach a desired level of strength through heat treatment, one of the most significant sources of residual stress. A solution treatment stage is followed by a quenching procedure from a solution treatment temperature of around 1000°F (538°C). The residual stress level introduced in the samples when room temperature water quench is used is very high. The explanation for this phenomenon is that during quenching, the surfaces of the samples cool faster than their interior and so temperature gradients are created, causing different regions of the sample to contract at different rates. During the later stages of cooling these gradients disappear, but their presence sets up an uneven distribution of residual stress. These residual stresses are compressive on the surface of the sample, which cools first and tensile in the center, which cools later. After quenching the tensile and compressive stresses present in the sample are balanced and the total net stress equals zero for the whole sample. The aging treatment applied after quenching enhances the strength of the part through the development of strengthening precipitates, but it has no significant effect on the residual stresses.

For our work, two T61 heat treating procedures were used. Both treatments maintained distinction in Si morphology between unmodified and modified alloys [27], and produced a consistent matrix microhardness in all alloys [28] ("matrix" refers to either primary or eutectic α). However, the level of residual stress induced in the samples during these two heat treatments was significantly different.

The ***first*** heat treatment procedure ("RT water quench") consisted of the following steps:

- Solution-treatment for 1.5 hrs at 1000°F (538°C);
- Water quench in agitated water at room temperature;
- Natural age for 12 hrs;
- Artificial age for 12 hrs at 311°F (155°C).

The residual stress level introduced in the samples by the RT water quench was found to be very high. Therefore, an alternative heat treatment was designed to alleviate the residual stress contribution, and provide residual stress free CT specimens.

The ***second*** heat treatment procedure ("uphill quench") consisted of the following steps (details about this procedure and the operating mechanisms are given by Lados and Apelian [29]):

- Solution-treatment for 1.5 hrs at 1000°F (538°C);
- Boiling water quench for 15 min;
- Liquid N₂ immersion for 30 min;
- Boiling water reverse quench for 15 min;
- Natural age for 12 hrs;
- Artificial age for 12 hrs at 311°F (155°C).

The sample transferring time from one medium to another was two seconds.

Briefly, the idea of an "uphill quench" first came about based on a logical rationale that since the residual stresses on quench results from thermal gradients induced when the part is being cooled, it should be equally possible to develop thermal gradients and consequently residual stresses of an opposite nature by subjecting a cold sample to rapid heating, i.e. by an uphill quench. Residual stresses developed in this way counteract and tend to cancel the quenching stresses. This is why the residual stress level measured on the CT samples after this heat treatment was near zero.

II.B. Sample preparation and testing

II.B.1. Specimens

Compact tension specimens were machined after heat treatment to 3.75 in x 3.6 in x 0.4 in (95 mm x 91 mm x 10 mm). One sample was machined to smaller dimensions, 1.56 in x 1.5 in x 0.4 in (40 mm x 38 mm x 10 mm), from a large sample with high residual stress (this specimen size is used only in section III.D.2). Both sample configurations comply with ASTM E647. For material

removal, an end mill was used for the edges and a fly cutter was used for the reduction in thickness. A 0.006 in (0.15 mm) diameter wire was used for the wire EDM notch. After the blanks were milled to final size, they were scribed with reference marks at a spacing of 0.4 in (10 mm) (0.2 in (5 mm) on each side of the central line - Figure 1) on the edge of the sample. After the pin holes and the notch were machined, these reference lines were measured again to an accuracy of 0.0001 in (2.5 μm).

The notch length is 1.5 in (38 mm) measured from the front face of the sample, and 0.75 in (19 mm) measured from the pin holes.

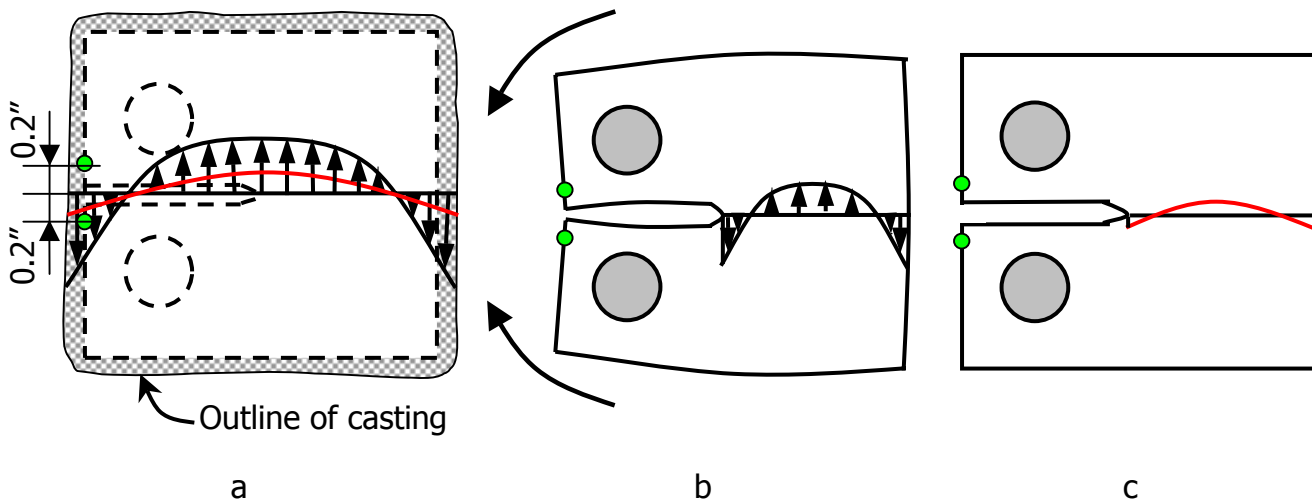


Figure 1. (a) Scribed samples after machining and before notching with high and low residual stress; (b) Sample with high residual stress (HRS) after notching – visible notch clamping effect; (c) Sample with low residual stress (LRS) after notching – no notch clamping.

II.B.2 Residual stress measurement through notch clamping

Residual stress levels were inferred from the displacement of the mating faces after the notch was cut into the CT specimens. These displacements were found to be compressive at the notch, in the range of 0.0036 to 0.0085 in (91 to 216 μm) on different samples (different alloy compositions) after "RT water" quench, and in the range 0.0000 to 0.0016 in (0 to 40 μm) after "uphill" quench. The sum of the scribe displacements for both halves of the CT specimens will be called from here forth notch clamping (NC). NC, was used as a measure of the residual stress level in the sample, the larger the clamping the higher the residual stress.

During fatigue crack growth, the additional contribution of residual stress to closure level is observed by examining the load-displacement records. The sample with low residual stress has less closure, which is due to other closure mechanisms (roughness, plasticity, oxides). These observations are presented in Figure 2.

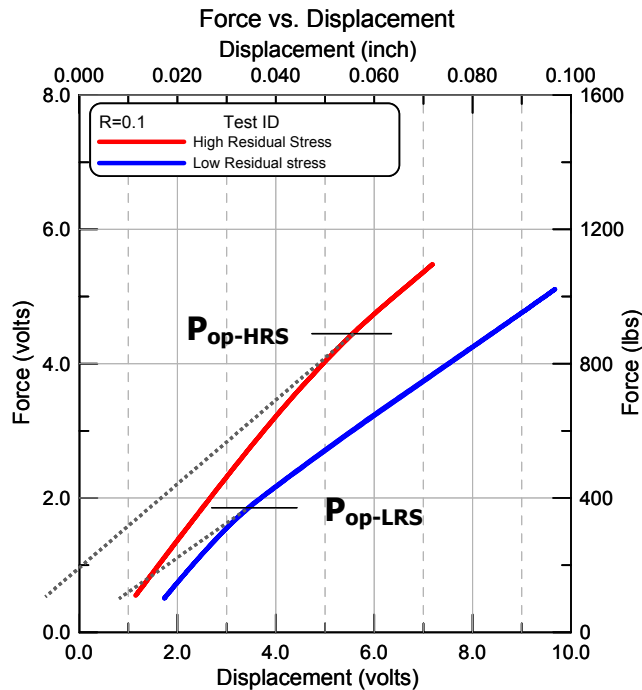


Figure 2. Load displacement records showing the additional effect of residual stress on crack closure level (left curve). P_{op} is the force required to fully open the crack under high (HRS) and low (LRS) residual stress conditions.

Crack closure measurements shown in Figure 2 cannot directly partition the individual contributions to total closure. Low values of residual stress are not sufficient to overcome the effects of roughness-induced closure active in the vicinity of the crack tip. However, if the residual stress is significant, then the crack tip can remain open while the surfaces near the notch are closed with no external force applied (bulge effect – Figure 3a). Therefore, the impact of roughness-induced closure is minimized due to the fact that interference is no longer near to the crack tip and the height of the interfering features near the notch have less contribution to the total crack closure level.

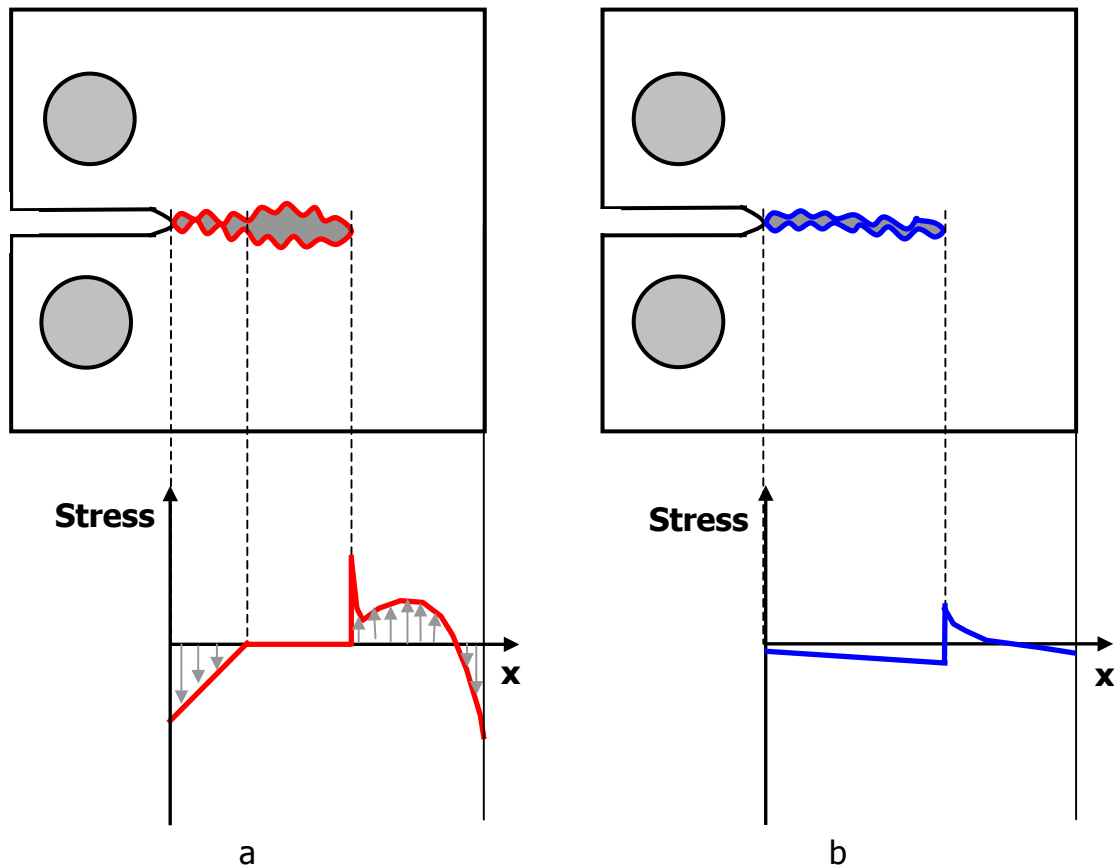


Figure 3. Typical interference of the crack mating faces at minimum load of the FCG curves:
 (a) high residual stress and (b) low residual stress conditions.

II.B.3. Fatigue crack growth testing (FCG)

The compact tension specimens were tested per ASTM E647 [30] in room temperature (75°F) air with relative humidity 40-50%. The specimens were tested under K-control, first under a decreasing crack driving force range (Region I) to evaluate the thresholds, and then under increasing crack driving force range (Regions II and III). Above 10^{-4} inches/cycle, the test was continued using a shallower K-gradient to obtain the steeper Region III data. The upper limit of the crack driving force was assumed to be the "pseudo" (linear elastic) fracture toughness of the materials (because the CT samples in this study did not meet the plain strain fracture toughness requirements of ASTM E399, the measured fracture toughness values are referred to as "pseudo" fracture toughness). The compliance technique was used to monitor the crack advance and the frequency was set to 25 Hz (except in Region III when it was decreased

as low as 0.1 Hz to capture sufficient data points). All alloys with both high and low residual stress levels were tested under both constant stress ratio, $R=0.1$, and constant K_{max} (closure free) conditions.

III. RESULTS AND DISCUSSION

III.A. Determination of residual stress free thresholds from FCG experiments on specimens with high and low residual stress

Paired samples from all alloys, one with high residual stress and the other with almost zero residual stress, were FCG tested ($R=0.1$) under identical conditions. Results are presented in Figure 4. It is important to notice that high residual stress curves have steeper slopes (higher m in Paris law: $da/dN=C(\Delta K)^m$) due to proportionally higher residual stress effects at lower ΔK , a feature well captured by the log-log representation.

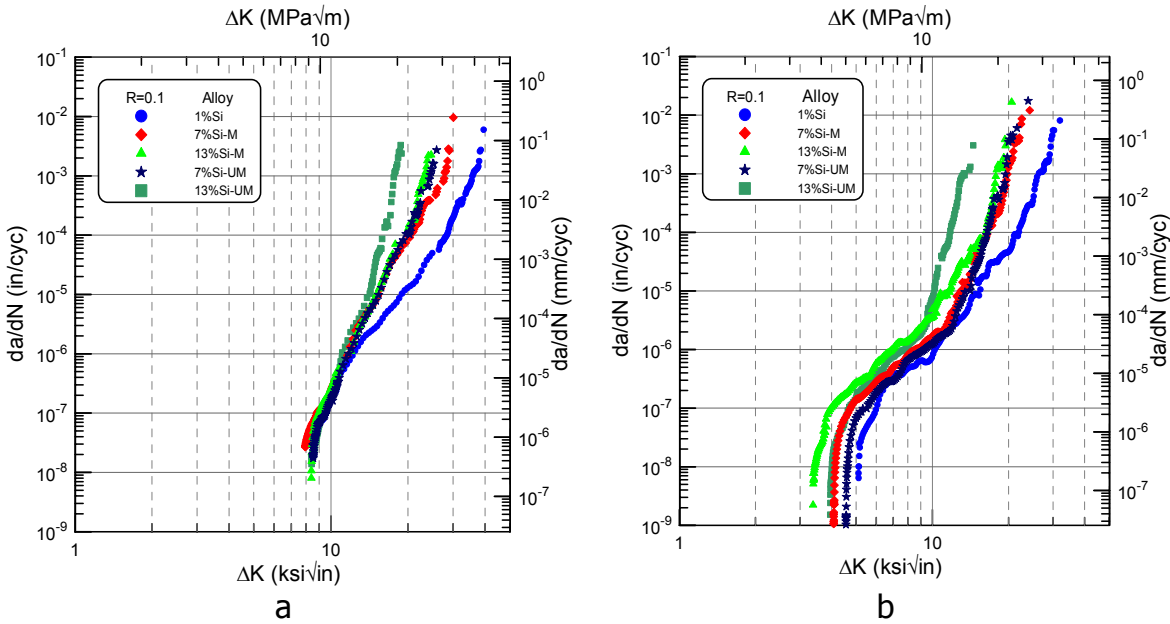


Figure 4. FCG curves for all alloys: (a) w/ residual stress and (b) w/o residual stress, under $R=0.1$.

Tests conducted on high residual stress samples were terminated prematurely due to high closure levels and the true thresholds were calculated by extrapolating the experimental data down to 10^{-7} mm/cycle. The other set of samples did not have residual stress induced closure, the only source of closure being the characteristic features of the alloys.

Thresholds of the high residual stress samples, 8-9 $\text{ksi}\sqrt{\text{in}}$ (9-10 $\text{MPa}\sqrt{\text{m}}$, Figure 4a) are unreasonably high for these types of cast aluminum alloys. Samples

without residual stress (Figure 4b) show thresholds in the 3-5 ksi $\sqrt{\text{in}}$ (3.5-5.5 MPa $\sqrt{\text{m}}$) range, a 100% difference due to the presence of residual stresses (all the other parameters being kept constant). The increase in thresholds is explained by considering that the tip of the notch is subjected to compressive residual stresses (Figures 1b and 3a) that create higher closure. Higher closure implies less effective driving force, lower growth rates, which for a given stress, gives higher ΔK . Because of higher closure, less of the applied force actually acts on the crack tip (i.e. sheltering of the crack tip), and therefore a greater cyclic force will be required to reach the threshold and propagate the crack. On the other hand, if the notch is found in a tensile stress field (center crack tension specimen, MT) the opposite effect is expected as schematically presented in Figure 5. This behavior was observed by Bucci [8], for 7XXX aluminum alloy extruded rods. In this case the thresholds are lower than the residual stress free thresholds considering that the crack is open at all times, and the crack tip is exposed to the whole applied load range.

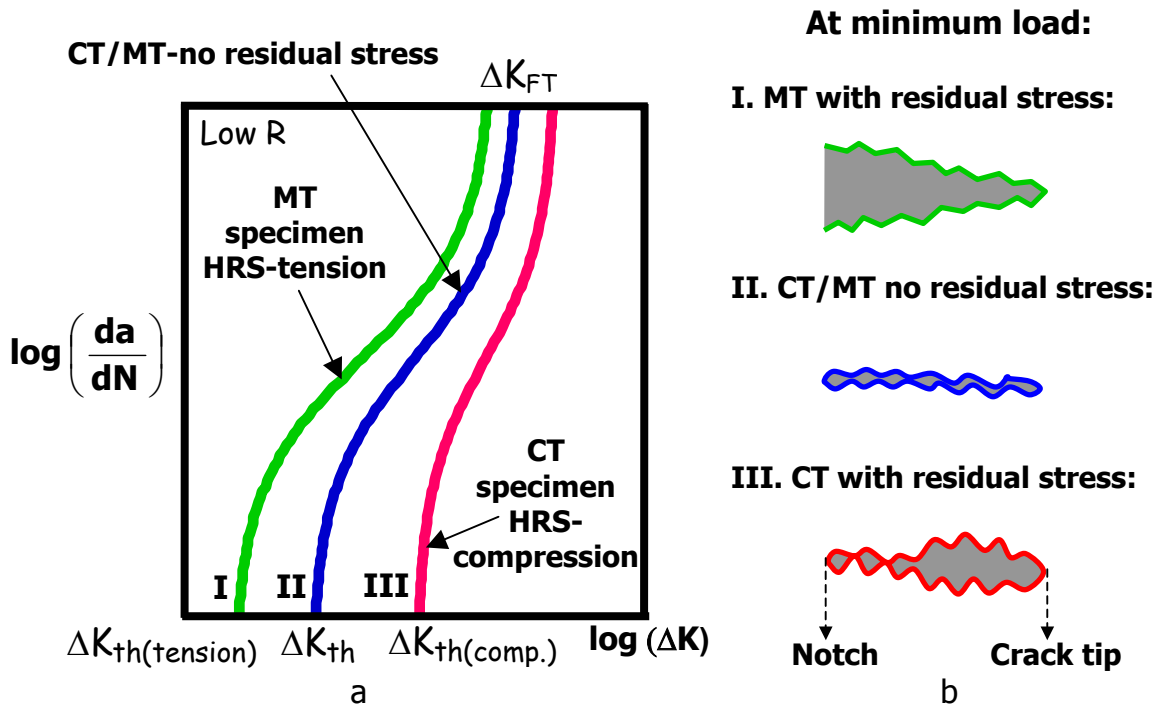


Figure 5. (a) Effects of compressive (CT specimen) and tensile (MT specimen) residual stresses on FCG behavior and (b) crack behavior at minimum load.

By plotting the thresholds versus notch clamping for each sample tested, a linear relationship was observed, Figure 6. This linearity holds true down to a critical value of notch clamping below which the threshold remains constant as demonstrated by the plateau below 0.0015 in (38 μm) notch clamping for 7%Si alloys. This implies that under a certain level of residual stress, the samples can be considered residual stress free; the contact due to closure changes from "near

the notch” to “near the crack tip”, and closure mechanisms are mostly controlled by the alloys intrinsic microstructural features. There is a critical notch clamping below which that happens, which is function of the roughness level of the material: the lower the roughness the lower the critical notch clamping. Therefore, microstructural features do not have a significant contribution to closure unless the sample is virtually residual stress free.

It is also observed in Figure 6 that ΔK_{eff} data (see also section III.C.2) converge at low values of residual stress. This suggests that the variation in the residual stress free ΔK_{th} is mostly the result of microstructure differences causing variations in roughness-induced closure.

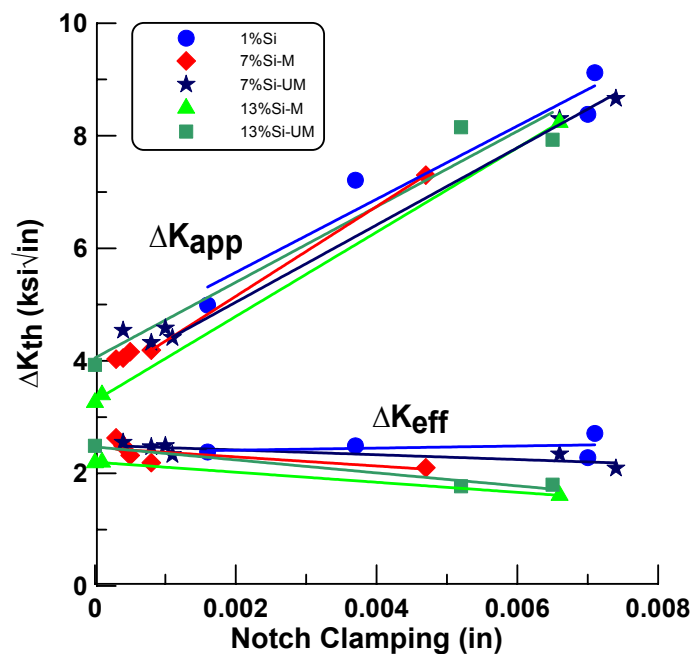


Figure 6. ΔK_{th} vs. notch clamping.

Empirical relationships between threshold and notch clamping (Figure 6) can be derived from such data. However, the development of such relationships requires for each material the knowledge of at least two residual stress conditions to obtain a linear fit. A better approach is to apply mathematical models to correct high residual stress data in a more general way. Thus, two mathematical models have been developed to account for the presence of residual stress directly from data with high residual stress. These two approaches are presented next and compared to residual stress free experimental data.

III.B. Mathematical models to account for residual stress

III.B.1 Restoring force model for clamping effect

This model is designed to calculate the force required to restore the original notch spacing of the CT sample (Figure 7b), then use that force to compute the stress intensity due to the residual stress, which caused that notch clamping (Figure 7a). Physically, by restoring the original notch spacing the surface of the sample is forced from a compression state into a tension state. However, the idea is to create a neutral state at the notch tip, and this equilibrium condition can be achieved by applying half of the force necessary to restore the original notch mouth (Figure 7c).

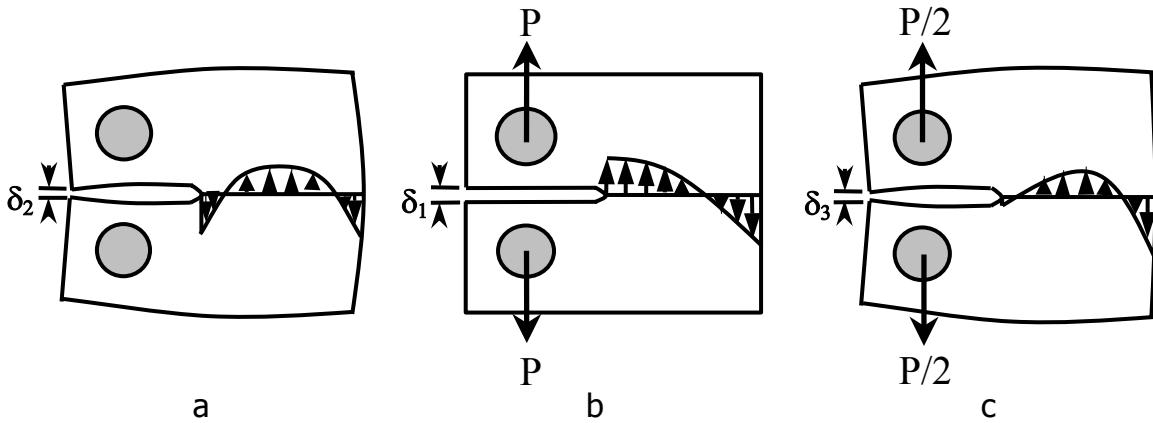


Figure 7. Restoring force model: (a) original residual stress distribution; (b) residual stress distribution after restoring the original notch; (c) residual stress free notch tip.

The two necessary relationships are:

$$P = \frac{E \cdot \Delta\delta \cdot B}{m_1(a/W)} \quad [1]$$

where

$$m_1(a/W) = 1.00098 - 4.66951 \cdot u + 18.4601 \cdot u^2 - 236.825 \cdot u^3 + 1214.88 \cdot u^4 - 2143.58 \cdot u^5$$

$$u = \left[\left(\frac{E\delta B}{P} \right)^{\frac{1}{2}} + 1 \right]^{-1}$$

and :

$$K = \frac{1}{2} \cdot \frac{P \cdot m_2(a/W)}{B\sqrt{W}} \quad [2]$$

where

$$m_2(a/w) = \frac{2 + \frac{a}{W}}{\left(1 - \frac{a}{W}\right)^{\frac{3}{2}}} \left[0.886 + 4.64 \cdot \frac{a}{W} - 13.32 \cdot \left(\frac{a}{W}\right)^2 + 14.72 \cdot \left(\frac{a}{W}\right)^3 - 5.6 \cdot \left(\frac{a}{W}\right)^4 \right]$$

For the CT geometry used in this study, $a/W=0.25$, at the beginning of the test, and K_{res} is calculated as:

$$K_{res} = \frac{1}{2} \cdot \frac{E \cdot \Delta\delta \cdot m_2(a/W)}{m_1(a/W) \cdot \sqrt{W}} \quad [3]$$

This approach is attractive through its simplicity and generality, but it has to be used with discernment. Commonly, samples with low yield strength retain higher residual stresses (or larger notch displacements) than samples with high yield strength [29]. This holds true at both high and low residual stress levels. In our case, the first alloy (1%Si) retains more residual stress than the 7%Si alloys, and these have higher residual stresses than the 13%Si alloys. If we correct all the alloys down to zero residual stress, the 1%Si alloy is overcorrected while the 13%Si alloys can be undercorrected. As a result, the microstructure influence especially on the threshold will be altered, and the material ranking is lost. Based on the results of this study a yield stress dependent residual stress correction is recommended. For low yield alloys (1%Si) a correction down to a notch clamping of 0.0015-0.0025 in (38-64 μm) is sufficient to consider the sample residual stress free. Alloys with 7%Si require a correction to 0.001-0.0015 in (25-38 μm) notch clamping, and the eutectic alloys (13%Si) down to 0.0000-0.0005 in (0-13 μm). For simplicity we corrected all our models to an average value of 0.0015 in (38 μm) notch clamping using 7%Si alloys as a baseline. Unless the Si level is very high, a correction down to 0.001-0.0015 in (25-38 μm) notch clamping is generally sufficient, and for lower initial residual stresses no correction is needed. This phenomenon can be explained, as already mentioned before, by considering the combined effects of residual stress and microstructure roughness. When residual stress is high, it dominates the closure mechanism, but for low residual stress the controlling closure mechanism is roughness. Therefore, corrections applied to already low residual stress levels lead to less accurate data. Low yield materials, having more roughness, are predisposed to higher inaccuracies when corrected down to zero residual stress because microstructure effects start interfering at higher residual stress levels than in other materials. In such cases, corrections below 0.0015-0.0025" notch clamping do not correct residual stress anymore, and in fact incorrectly start eliminating microstructure effects.

In the general sense, when there is insufficient data on the material, and the specimen size-residual stress relations are not known, a conservative correction down to essentially zero residual stress level is advisable.

The results of the restoring force correction can be seen in Figure 8. Good agreement with the experimental data from residual stress free samples (Figure 4b) are observed even if the correction was not considering the yield effect on critical notch clamping.

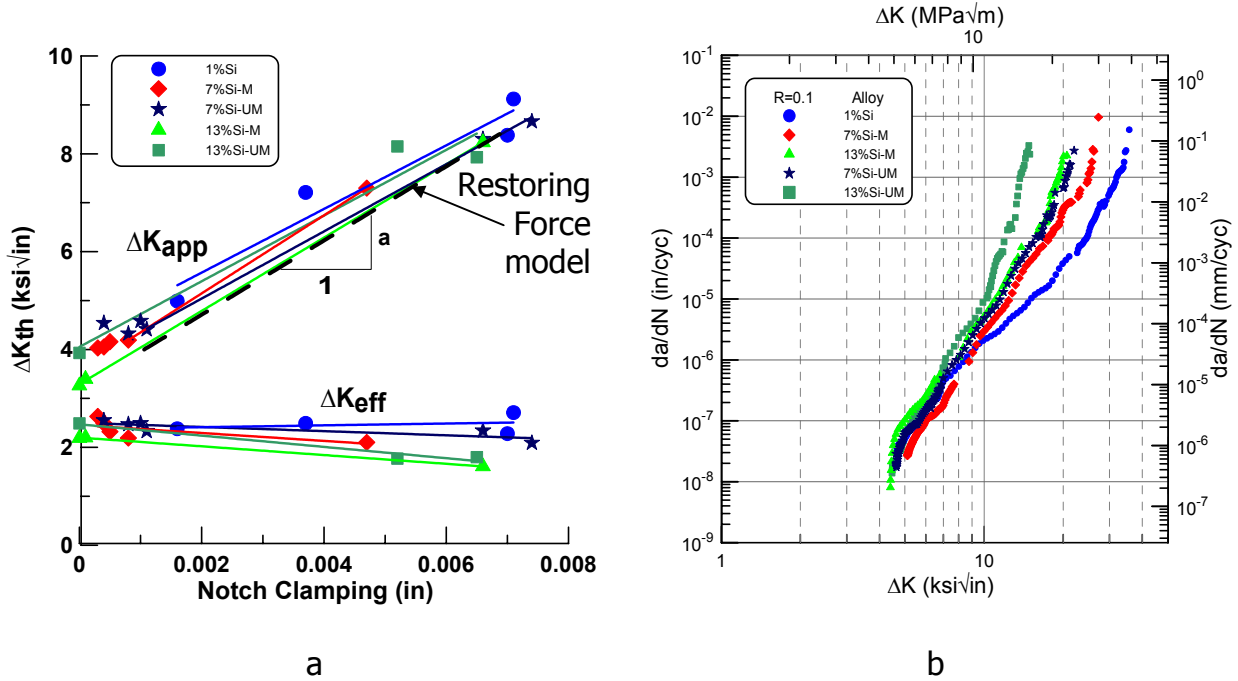


Figure 8. Residual stress correction using restoring force model (a $\Delta K_{th} \sim 4 \text{ ksi}\sqrt{\text{in}}$ is predicted for a 0.0015 in notch clamping).

III.B.2 Cut compliance model for clamping effect

This method targets the measurement of the residual stress and residual stress intensity factor through the remaining ligament of a compact tension specimen. A slot or notch is successively extended through the part and the resulting strain is measured at the appropriate location (displacements measured at the front face of the specimen in this study). It is based on a fracture mechanics approach developed by Schindler [25] that determines stress intensity factors caused by the residual stresses with a very simple calculation. The main benefit, just like in the previous model, comes from the fact that it can evaluate the stress intensity contribution from residual stress prior to a fatigue or fracture test by measuring strains during the specimen preparation (during notch cutting more precisely). This approach was successfully used and verified by Prime [26]

on a compact tension specimen with residual stresses introduced by preloading the samples beyond yielding. The method can be even further simplified if the residual stress intensity factor can be correlated directly with the final notch length and the corresponding front face induced displacement, so that the notch does not need to be machined in successive steps (this simplified approach is followed here).

The model treats the notch introduced to relieve residual stress as a mathematical crack. This approximation holds true for cracks with a depth-to-width ratio greater than five as shown by Cheng and Finnie [32]. Schindler's equation, based on Castigliano's theorem, provides a very simple equation to calculate the stress intensity factor K_{res} for a crack growing into a residual stress field:

$$K_{res}(a) = \frac{E}{Z(a)} \frac{d\delta}{da} \quad [4]$$

where $Z(a)$ is an influence function which depends on the geometry of the specimen (CT in this work) and the location of the strain measurement (front face of the CT specimen in this work). For a standard CT specimen with a crack depth of $a/W \geq 0.5$, and strain measurements taken at the back face directly opposite to the cut, $Z(a)$ was given by Schindler [33] as:

$$Z(a) = -\frac{2.532}{(W - a)^{3/2}} \quad (\text{CT specimen \& back face strain measurements}) \quad [5]$$

However, in this research strain measurements were taken at the front face where the cut was made (Figure 9) and so a new expression for $Z(a)$ was developed.

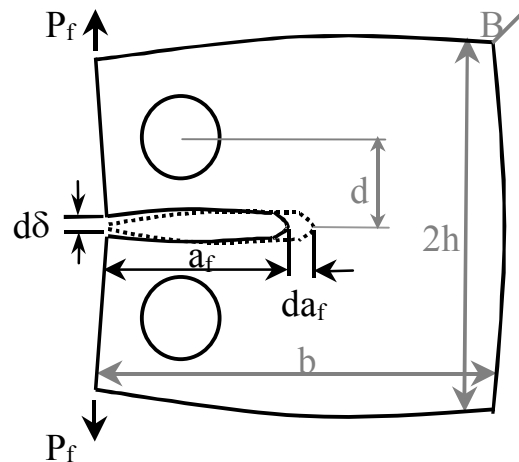


Figure 9. Compact tension specimen – front face strain measurements.

The stress intensity factor can be written in terms of the crack driving force G and Young's modulus as:

$$K^2 = EG = \frac{1}{2} \left(\frac{P_f}{BW} \right)^2 W \frac{d \left(\frac{E\delta B}{P_f} \right)}{d \left(\frac{a_f}{W} \right)} = \frac{1}{2} \frac{P_f}{B} E \frac{d\delta}{da_f} \quad [6]$$

Therefore,

$$E \frac{d\delta}{da_f} = \frac{2K^2 B}{P_f} \quad [7]$$

From eq. [4], the influence function can be written as:

$$Z(a_f) = \frac{1}{K} E \frac{d\delta}{da_f} \quad [8]$$

Combining equations [7] and [8] we get the expression of the influence function:

$$Z(a_f) = \frac{2KB}{P_f} \quad [9]$$

Now, K can be written as:

$$K = \sigma_N \sqrt{b - a_f} \cdot F_2 \left(\frac{a_f}{b}, \frac{h}{b}, \frac{d}{h} \right) = (\sigma_{N-Tension} + \sigma_{N-Bending}) \sqrt{b - a_f} \cdot F_2 \left(\frac{a_f}{b}, \frac{h}{b}, \frac{d}{h} \right) \quad [10]$$

where

$$\sigma_{N-Tension} = \frac{P_f}{B(b - a_f)} \quad \text{and} \quad \sigma_{N-Bending} = \frac{6P_f \left(a_f + \frac{b - a_f}{2} \right)}{B(b - a_f)^2} \quad [11]$$

Using eq. [11] in [10], K becomes:

$$K = \left[\frac{2P_f(2b + a_f)}{B(b - a_f)^2} \right] \sqrt{b - a_f} \cdot F_2 \left(\frac{a_f}{b}, \frac{h}{b}, \frac{d}{h} \right) \quad [12]$$

By introducing relation [12] in eq. [9], $Z(a_f)$ can be determined as:

$$Z(a_f) = \frac{4(2b + a_f)}{(b - a_f)^{3/2}} \cdot F_2 \left(\frac{a_f}{b}, \frac{h}{b}, \frac{d}{h} \right) \quad [13]$$

Finally, the expression of the residual stress intensity factor for a CT specimen and strain measurement at the front face of the sample becomes:

$$K_{res} = \frac{E}{Z(a_f)} \cdot \frac{d\delta}{da_f} = \frac{E}{4(2b + a_f)} \cdot \frac{d\delta}{(b - a_f)^{3/2}} \cdot F_2 \left(\frac{a_f}{b}, \frac{h}{b}, \frac{d}{h} \right) \cdot \frac{d\delta}{da_f} \quad [14]$$

F_2 can be determined using the chart presented in Figure 10 [34]. For specimen geometries with $a/b > 0.4$, the d/h contribution is not significant, and eq. [14] can be re-written as:

$$K_{res} = \frac{E}{4(2b + a_f)} \cdot \frac{d\delta}{(b - a_f)^{3/2}} \cdot F_2 \left(\frac{a_f}{b}, \frac{h}{b} \right) \quad (\text{CT sample \& front face measurements}) \quad [15]$$

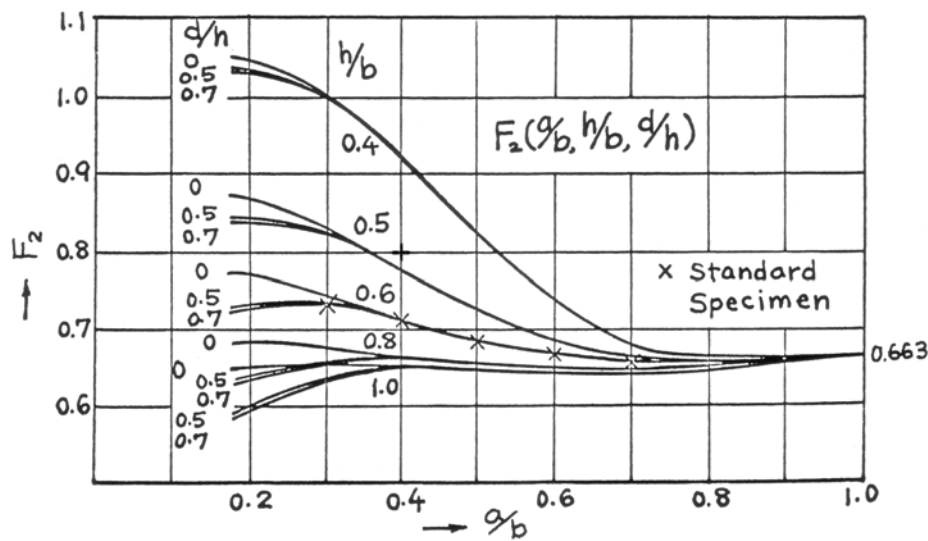


Figure 10. Variation of F_2 parameter as function of the specimen geometry [34].

Thus, given the notch clamping for a certain notch length, the stress intensity factor due to the presence of residual stresses can be determined using the very simple and user friendly relation given by eq. [15].

The results of the corrections using the cut compliance method are presented in Figure 11. A 15% difference was observed when comparing these results with the restoring force model results, which means stress intensity factors are lowered by 15%.

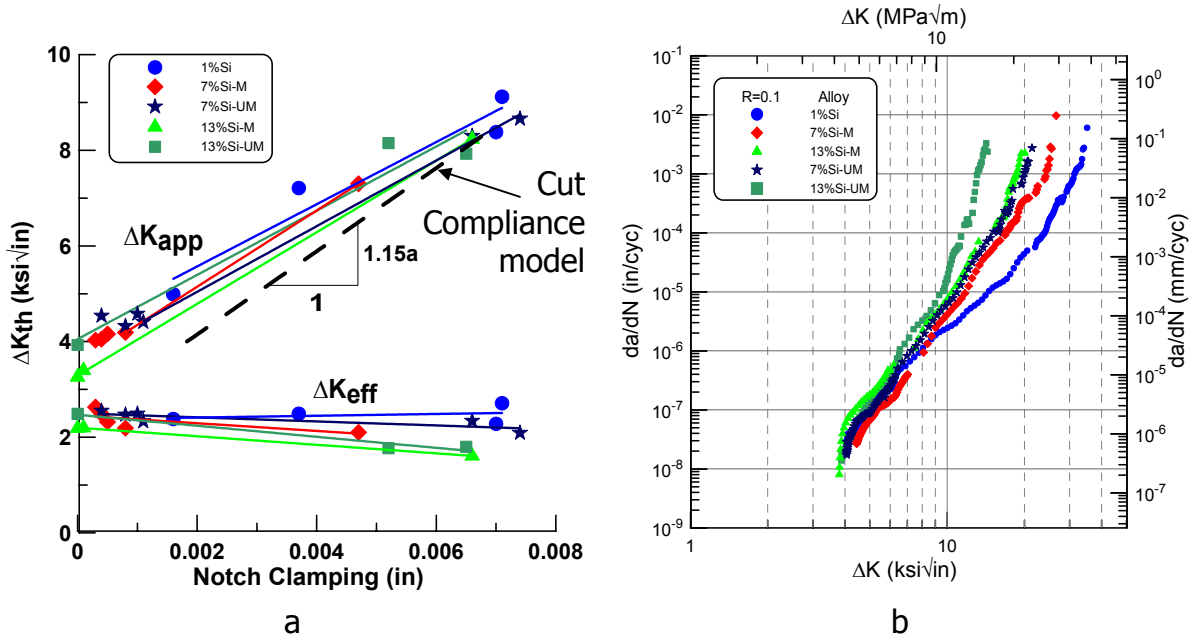


Figure 11. FCGR curves of high residual stress samples after cut compliance corrections.

Both corrections (Figures 8b and 11b) were done using ΔK_{corr} as (for low stress ratios, R):

$$\Delta K_{\text{corr}} = K_{\text{max}} + K_{\text{res}} - K_{\text{min}} = \Delta K_{\text{app}} + K_{\text{res}} \quad [16]$$

K_{res} correction was applied to the K_{max} component only because when the crack is fully open there is no contact and the principle of superposition is valid. However, applying the same correction to K_{min} is not appropriate because non-linear contact in the crack wake has already occurred due to other closure mechanisms (i.e. roughness, plasticity, oxides). Consequently, the effective stress intensity range ΔK is reduced by the amount of the K_{res} . Therefore, it is imperative that the reduction in ΔK (ΔK_{corr}) follows the same rationale.

In both correction models presented above, K_{res} were calculated based on the notch length alone, and the samples were FCG tested after notch clamping evaluations. Additional samples and castings were reserved for evaluating K_{res} through successive incremental saw cuts and notch clamping measurements beyond the notch. The results for two machined samples (one high and one low residual stress) as well as one casting are shown in Figure 12.

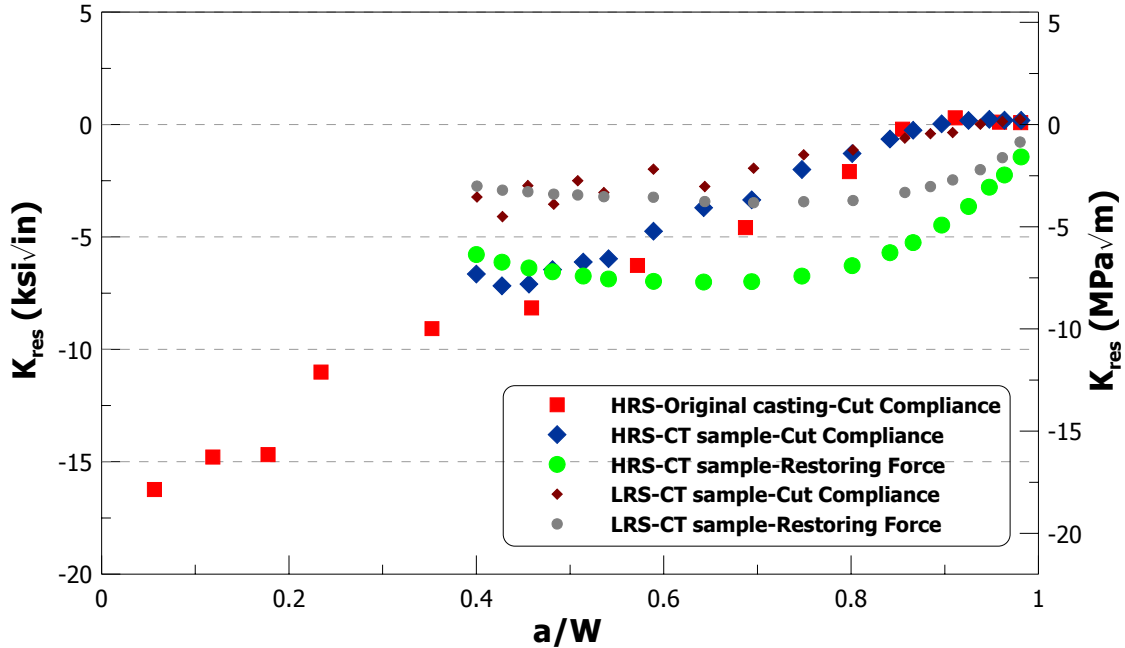


Figure 12. K_{res} variation with crack length.

The casting and the sample with HRS give nearly identical results indicating that little residual stress reduction occurred when the samples were machined from near net shape castings. The two corrective methods, restoring force model and cut compliance model, share similar behavior only at the initial notch length. The overall behavior of the two models is different however.

For the analysis, a constant K_{res} value was used for the full range of crack growth rates, calculated based on the initial notch length (eqs. [3] and [15]). The assumption of constant K_{res} is supported by three observations. First, it was observed that successive thresholds at different crack lengths have similar values indicating that the effect of the residual stress was not diminished with the advance of the crack up to $a/W=0.45$. Second, the restoring force model (see Figure 12) shows a nearly constant value of K_{res} over the range of crack length used for crack growth testing. Third, although the cut compliance method shows diminishing K_{res} with crack length, this approach is based on no contact of the mating faces. However, the additional clamping beyond the notch proves that contact (closure) would occur raising the value of K_{res} above the cut compliance calculated value. In these conditions it is evident that contact and closure compensate for the diminishing tendency of the residual stress with the crack growth, and therefore it is appropriate to assume a constant K_{res} along the whole range of stress intensity factor. The residual stress corrected data presented in Figures 8b and 11b are based on two constant K_{res} values calculated using the two mathematical models presented above.

III.C. Testing methods to account for residual stress

Besides mathematical models, there are certain testing conditions (high stress ratio or $K_{\max}=\text{constant}$ tests) or post-testing data processing that can provide closure free data.

III.C.1 $K_{\max}=\text{constant}$ tests

High stress ratio data were generated in an attempt to obtain a closure free response. Tests under stress ratios up to 0.8 were terminated prematurely due to high closure levels. In order to eliminate this problem, constant K_{\max} tests (closure free tests) were conducted. These test procedures resulted in stress ratio as high as $R\sim 0.9$ at threshold. Due to the fact that K_{\max} remains constant, steep K-gradients can be used without the risk of crack growth retardation. Since K_{\min} is increased as the crack advances, closure becomes less important and it quickly disappears at lower values of ΔK .

The closure free tests bring the thresholds down to 1-2 $\text{ksi}\sqrt{\text{in}}$ as expected for closure free tests, when the faces of the crack are prohibited from interacting with each other, Figure 13a. As a result, both residual stress and roughness-induced closures become insignificant. In Figure 13b residual stress closure was removed, but roughness-induced closure is still present.

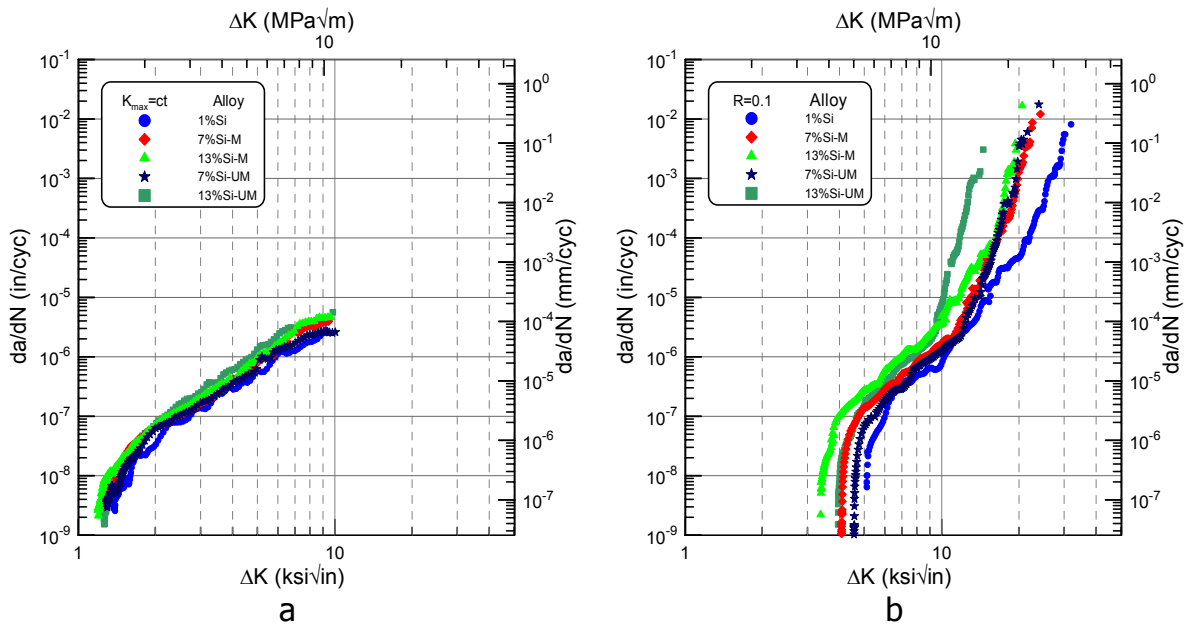


Figure 13. Results of (a) closure free and (b) residual stress free tests.

The shortcoming of this method, however, comes from the fact that it corrects not only for residual stress, but also for the roughness-induced closure and it can be affected by second order K_{max} effects.

III.C.2 $\Delta K_{effective}$ computation using test data closure corrective methods (ACR method)

In Figure 14, the closure corrected data determined using the adjusted compliance ratio (ACR) method [31] resemble the residual stress free data near the threshold better than the $K_{max}=constant$ test results. This can be explained considering that the clamping force in the crack wake is more pronounced near the notch rather than the tip of the crack. This situation is best accounted for by calculating ΔK_{eff} using the ACR method. However, this method as well as all the other available closure corrective methods account for closure in general and not particularly for residual stress induced closure.

In the presence of significant residual stress, the ACR method appears best even in region II since the clamping forces appear to be distributed along the entire length of the crack and may, in fact, be higher at the notch than at the crack tip. Therefore, the ACR method is recommended to correct for closure due to residual stress while partly preserving roughness-induced closure. In region III this method is not accurate and other methods would better reflect the fatigue crack growth behavior of the material (i.e. opening load method [35]).

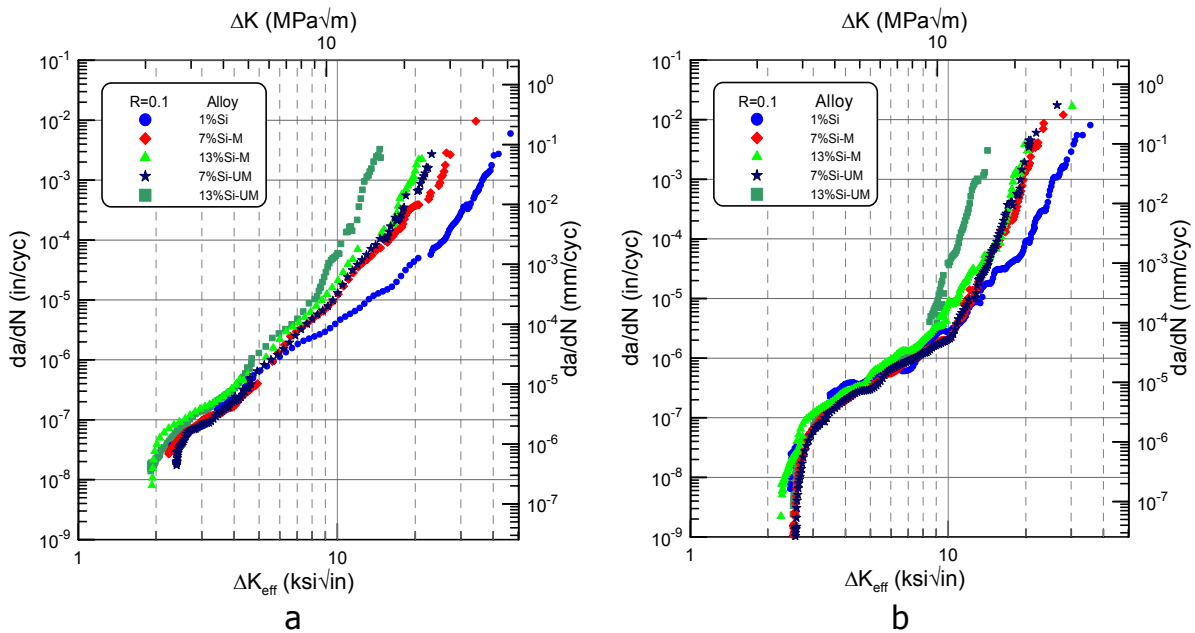


Figure 14. Closure corrected data using ACR method for (a) high residual stress and (b) low residual stress samples.

III.D. Procedures to eliminate residual stress from CT specimens

To understand the real behavior of the material and determine the effect of the residual stress, residual stress free samples of the same composition and mechanical properties need to be produced and compared with samples of known residual stress level. There are several ways available to produce residual stress free samples and two of them will be presented below.

III.D.1 Use a different quenching procedure (uphill quench recommended)

For almost complete elimination of residual stress the agitated room temperature water quench (main source of residual stress) needs to be replaced or adjusted. The usual, "downhill", quench can be either done in a less severe medium, such as warm or boiling water, or it can be combined with a subsequent uphill quench. The latter procedure is presented elsewhere [29] and it was briefly described in section II.A. Fatigue crack growth data from uphill quenched samples shown in Figure 4b, restores the thresholds (ΔK_{th}) to expected values for Al-Si-Mg alloys, 3-5 ksi $\sqrt{\text{in}}$. It should be also clarified that the difference, in thresholds and generally in the whole FCG curves, between samples with residual stress (room temperature water quenched) and samples without residual stress (uphill quenched), is entirely due to the presence of residual stress (Figure 4a,b). By comparing the results of these two sets of experiments the effect of compressive residual stresses can be determined and the corrective models introduced in section III.B can be validated. The accuracy of the mathematical models can be assessed comparing Figures 4b with 8b and 11b.

III.D.2 Use smaller samples cut from large samples with high residual stress

Another way to produce residual stress free samples is to machine specimens much smaller than the initial size of the casting. It was found that by removing $\sim 2/3$ from the initial size casting, a virtually residual stress free sample was obtained (Figure 15).

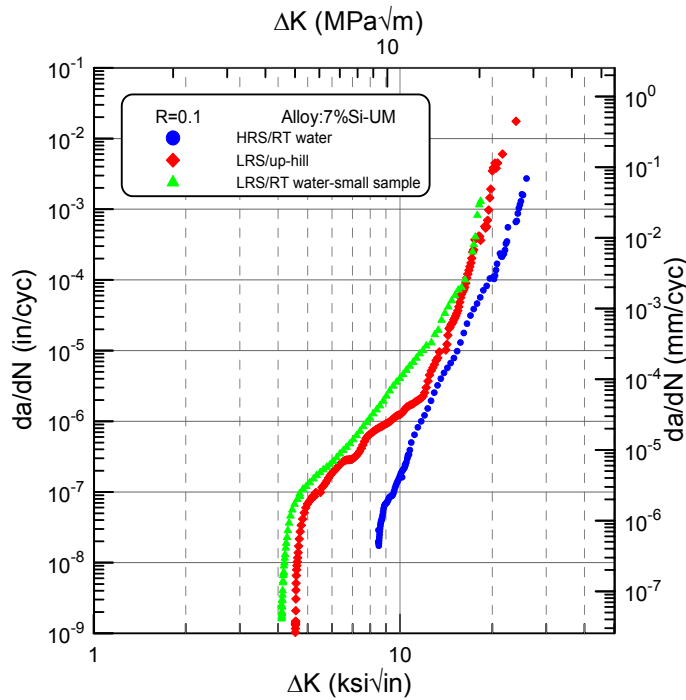


Figure 15. Comparison of FCG behavior of large samples with high and low residual stresses with a small sample with low residual stress after being cut from a large sample with high residual stress.

III.E. Numerical determination of residual stress profiles from K_{res}

Using the cut compliance method, performing a series of successive cuts across the CT specimen ligament, and recording the notch clamping for every cut, a set of stress intensity factors across the entire sample were calculated (Figure 12), using eq. [15]. Further, a relationship between stress intensity factors due to residual stresses (K_{res}) and the actual values of the residual stresses present in the CT sample (σ_{res}), can be determined. The relationship $K_{res}-\sigma_{res}$ is based on weight function solutions as shown in eq. [17].

$$K_{res}(a) = \int_{a_0}^a h(x, a) \sigma_y(x) dx \quad [17]$$

Eq. [17] can be solved for the residual stress (when K_{res} is known) by assuming that the stress, σ_j , is constant in each of the n intervals, between each a_{n-1} and a_n . Therefore, eq. [17] can be re-written in discrete form as:

$$K_{res}(a_i) = \sum_{j=1}^i \sigma_j \int_{a_{j-1}}^{a_j} h(x, a_i) dx \quad [18]$$

Slightly different formulations of the weight functions, h , have been used by several researchers [7,10,11,15,16,18]. In this work, the weight function formulation given by Fett and Munz [35] for a CT specimen was followed:

$$h(x, a_i) = \sqrt{\frac{2}{\pi a_i}} \frac{1}{\sqrt{1 - \frac{x}{a_i}}} \left[1 + \frac{1}{\left(1 - \frac{a_i}{W}\right)^{\frac{3}{2}}} \sum_{v,\mu} A_{v,\mu} \left(\frac{a_i}{W}\right)^\mu \left(1 - \frac{x}{a_i}\right)^{v+1} \right] \quad [19]$$

where coefficients $A_{v,\mu}$ are listed in the Table 1 below and a_i are the cuts measured from the load line (pin holes):

Table 1. $A_{v,\mu}$ coefficients in eq. [19]

v/μ	0	1	2	3	4
0	2.673	-8.604	20.621	-14.635	0.477
1	-3.557	24.9726	-53.398	50.707	-11.837
2	1.230	-8.411	16.957	-12.157	-0.940
3	-0.157	0.954	-1.284	-0.393	1.655

The mathematical approach is complex and it requires numerical integration, but once solved the residual stress distribution can be quantified and also a relationship notch clamping-residual stress level can be established. Prime [26], used this equation to determine the residual stress distribution in a CT sample overloaded prior to the cuts. In the present study, residual stress is a pre-existing condition (introduced during quenching), before the notch was cut, but the stress distribution was determined in the remaining ligament after the notch was machined.

This approach allows each σ_j to be uniquely determined, and the numerical results are given in Figure 16.

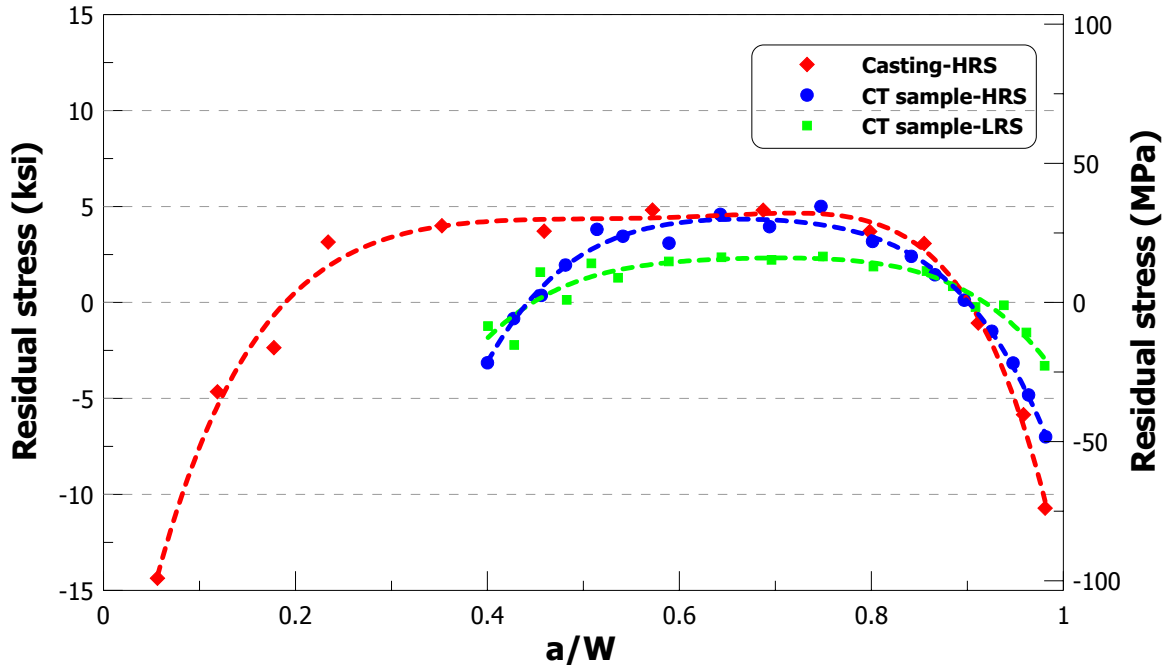


Figure 16. Residual stress profiles for two CT samples and a casting.

Residual stress profiles are consistent with the expectation that surface has compressive stresses, while the interior is in tension. For both the casting and the CT sample, the residual stress in the interior is fairly uniform and lower in absolute value than the surface compression. This is expected because the thermal gradients due to quenching are greater at the surface than in the interior. The stress distribution in the CT specimen represents in fact the residual stress profile after the notch has been cut, representing the state of stress in the sample just before testing.

There is a direct correlation between notch clamping and residual stress amplitude that can be observed by analyzing the residual stress profile of CT samples with HRS and LRS in Figure 16. A two times larger notch clamping (0.0076 in for HRS vs. 0.0036 in for LRS) leads to an approximately double maximum residual stress amplitude.

For the CT specimens sufficient material was removed from the thickness direction, so that the residual stress profile in z-direction was negligible. This was confirmed by the experimental observation that the crack fronts were straight through the thickness (no bowing effects were observed).

SUMMARY

Residual stress can be a result of different processing and post-processing techniques such as castings, forgings, extrusions, weldings, etc. (especially after heat treatment), and it can affect any alloy system (i.e. aluminum, titanium, steel, superalloys, etc).

Residual stress can have a positive or a negative impact on the fatigue behavior (depending whether the stresses are compressive or tensile). However, when present in crack growth samples, the residual stress can mask/bias the true response of the material.

The effect of residual stress on crack growth rates is most pronounced at low ΔK levels (ΔK_{th}) where the applied stresses are low and therefore the ratios of residual stresses to applied stresses are high. Fracture toughness, is also affected by residual stresses, but due to high applied stresses, the effect is considerably diminished relative to the impact on ΔK_{th} .

Clamping measurements before and after notch cutting are good indicators of the residual stress severity. There are also other good testing indicators, such as closure measurements through load-displacement records. However, these records cannot separate the effect of residual stress-induced closure from the microstructure-induced closure.

Through the evaluation of experimental results with both high and low residual stresses, two mathematical models were validated to adequately quantify the effect of residual stress on FCG data. The corrective methods apply to specimen geometries where notch clamping can be measured (i.e. edge crack type specimens such as CT) as well as cases where residual stress distribution is symmetrical, compression on the surface and tension in the interior.

Quantifying residual stress effects on FCG data is insufficient to accurately characterize the intrinsic microstructural characteristics of the material. For that purpose residual stress free samples were needed. Methods to reduce residual stress include thermal stress relieving techniques and proper selection of specimen geometry, size, and location from the original casting that maintains the symmetry of the residual stress profile.

When residual stress is under certain critical values, notch clamping is small, and it can be ignored; the bulge effect is not operative, and intrinsic microstructural closure effects are dominant. At high levels, residual stresses mask microstructure effects and judicious mathematical corrections need to be applied.

ACKNOWLEDGEMENTS

The FCG testing was done at Fracture Technology Associates. Special thanks go to Mr. Keith Donald for his important contribution to this work and his insight and guiding directions to the critical issues related to residual stress impact of fatigue crack growth response. The authors address their thanks to GM for partly supporting the FCG testing, Alcan for providing high purity aluminum, and Palmer Foundry for preparing the sand molds needed in this work. The authors address their gratitude to Dr. Peggy Jones of GM and Dr. Fred Major of Alcan for their sustained support and valuable technical assistance.

NOMENCLATURE

NC	= notch clamping
HRS	= high residual stress conditions
LRS	= low residual stress conditions
da/dN	= crack growth rate
K	= stress intensity factor
$K_{app}, K_{eff}, K_{res}$	= applied, effective, residual K values
K_{max}, K_{min}, K_{op}	= maximum, minimum, and crack opening K values
P_{op}	= crack opening load
ΔK_{app}	= $K_{max} - K_{min}$ = applied stress intensity factor range
ΔK_{eff}	= $K_{max} - K_{op}$ = effective stress intensity factor range
$\Delta K_{th}, \Delta K_{th(rst)}, \Delta K_{th(rsc)}$	= threshold stress intensity factor range, and thresholds affected by tensile and compressive residual stresses
ΔK_{corr}	= residual stress corrected stress intensity factor range
G	= crack extension force or elastic energy release rate
E	= Young's modulus
B	= CT specimen thickness
W	= CT specimen width (from pin holes)
b	= CT specimen width (from front face)
d	= distance notch-pin holes
h	= CT specimen half height
$\delta, d\delta, \Delta\delta$	= notch (mouth) opening and change in notch opening
a, da	= crack length and change in crack length (from pin holes)
a_f, da_f	= crack length and change in crack length (from front face)
P	= load applied at the pin holes
P_f	= load applied at the front face
Z(a)	= influence function
h(x,a)	= weight function
σ_{res}, σ_j	= residual stress and residual stress on a certain interval

REFERENCES

- [1]. T. Hanabusa and H. Fujiwara: Proc. 32nd Jpn. Congr. Res., 1989, pp. 27-36.
- [2]. G.E. Dieter: Engineering Design, McGraw-Hill, 1982.
- [3]. W.D. Callister, Jr.: Materials Science and Engineering-An Introduction, 4th ed., 1996
- [4]. C.O. Ruud: in Residual Stress Effects in Fatigue, ASTM STP 776, American Society for Testing and Materials, 1982, pp.3-5.
- [5]. D. Walker: Advanced Materials and Processes, August 2001, pp.30-33.
- [6]. L. Mordfin: in Residual Stress Effects in Fatigue, ASTM STP 776, American Society for Testing and Materials, 1982, pp. 6-12.
- [7]. G. Glinka: in Fracture Mechanics, ASTM STP 677, American Society for Testing and Materials, 1979, pp. 198-214.
- [8]. R.J. Bucci: in Fracture Mechanics-Thirteenth Conference, ASTM STP 743, American Society for Testing and Materials, 1981, pp. 28-47.
- [9]. G.E. Nordmark, L.N. Mueller, and R.A. Kelsey: in Residual Stress Effects in Fatigue, ASTM STP 776, American Society for Testing and Materials, 1982, pp. 44-62.
- [10]. A.P. Parker: in Residual Stress Effects in Fatigue, ASTM STP 776, American Society for Testing and Materials, 1982, pp. 13-31.
- [11]. D.V. Nelson: in Residual Stress Effects in Fatigue, ASTM STP 776, American Society for Testing and Materials, 1982, pp. 172-194.
- [12]. W. Geary and J.E. King: Int. J. Fatigue, 9, No. 1, 1987, pp. 11-16.
- [13]. G.A. Webster and A.N. Ezeilo: Int. J. Fatigue, 23, 2001, pp. S375-S383.
- [14]. S. Sirtori and L. Vergani: Metal Sci. Technol., 6, 1988, pp. 40-46.
- [15]. Y.C Lam and K.S. Lian: Theoretical and Applied Fracture Mechanics, 12, 1989, pp. 59-66.
- [16]. M. Beghini and L. Bertini: Engng Fracture Mech., 36, No. 3, 1990, pp. 379-387.
- [17]. R.W. Bush, R.J. Bucci, P.E. Magnusen, and G.W. Kuhlman: in Fracture Mechanics-Twenty-Third Symposium, ASTM STP 1189, American Society for Testing and Materials, 1993, pp. 568-589.
- [18]. S.R. Daniewicz, J.A. Collins, and D.R. Houser: Int. J. Fatigue, 16, 1994, pp. 123-133.
- [19]. S.J. Maddox: Int. J. Fracture, 11, 1975, pp. 389-408.
- [20]. R.D. Brown and J. Weertman: Engng Fracture Mech., 10, 1978, pp. 757-771.
- [21]. W.O. Soboyejo and J.F. Knott: Int. J. Fatigue, 12, 1990, pp. 403-407.
- [22]. K. Tokaji and T. Ogawa: Fatigue Fract. Engng Mater. Struct., 13, 1990, pp. 411-421.
- [23]. A.M. Korsunsky and P.J. Withers: Key Engng Mater., 127, 1997, pp. 1183-1190.
- [24]. C.N. Reid: Scripta Metall., 22, 1988, pp. 451-456.
- [25]. H.-J. Schindler: Int. J. Fracture, 74, 1995, pp.R23-R30.

- [26]. M.B. Prime: *Fatigue Fract. Engng Mater. Struct.*, 22, 1999, pp. 195-204.
- [27]. D.A. Lados and D. Apelian: "The Effects of Solution Treatment and Si Content on the Microstructure and Mechanical Properties of Cast Al-Si-Mg Alloys", to be submitted to *Metall. Mater. Trans. A*.
- [28]. D.A. Lados and D. Apelian: "The Effect of Si Content on the Aging Behavior of Cast Al-Si-Mg Alloys", to be submitted to *Metall. Mater. Trans. A*.
- [29]. D.A. Lados and D. Apelian: "Quenching Modes and Residual Stress Levels in Cast Al-Si-Mg Alloys – Mechanisms and Effects on Static and Dynamic Properties", to be submitted to *Metall. Mater. Trans. A*.
- [30]. ASTM Standard E647, Standard Test Method for Measurement of Fatigue Crack Growth Rates, Annual Book of ASTM Standards, Vol. 03.01, 2000.
- [31]. G.H. Bray and J.K. Donald: in *Advances in Fatigue Crack Closure Measurement and Analysis, Second Volume*, ASTM STP 1343, American Society for Testing and Materials, 1999, pp. 57-78.
- [32]. W. Cheng and I. Finnie: *J. Engng Mater. Technol.*, 115, 1993, pp. 220-226.
- [33]. H.-J. Schindler: in *Advances in Fatigue Crack Closure Measurement and Analysis-Second Volume*, ASTM STP 1343, American Society for Testing and Materials, 1999, pp. 175-187.
- [34]. H. Tada, P.C. Paris, and G.R. Irwin: *The Stress Analysis of Cracks Handbook*, 3rd ed., 2000.
- [35]. J.K. Donald: in *Mechanics of Fatigue Crack Closure*, ASTM STP 982, American Society for Testing and Materials, 1988, pp. 222-229.
- [36]. T. Fett and D. Munz: *Computational Mechanics Publications*, Southampton, UK, 1997.

Chapter 4

Validity Limits for Elastic Definitions in Cast Al-Si-Mg Alloys with Enhanced Plasticity – Linear Elastic Fracture Mechanics versus Elastic/Plastic Fracture Mechanics

D. A. Lados and D. Apelian
Worcester Polytechnic Institute, Worcester, MA, USA

ABSTRACT

Linear elastic fracture mechanics was developed for and appropriately describes the fracture behavior of materials and components that respond elastically under loading. This approach is valuable and accurate for the continuum analysis of crack growth in brittle and high strength materials, but it introduces increasing inaccuracies for low strength-high ductility alloys (particularly low-carbon steels and light metal alloys). In the case of ductile alloys, different degrees of plastic deformation precede and accompany crack initiation and subsequent propagation, and therefore, a nonlinear ductile fracture mechanics approach better characterizes the fatigue and fracture behavior under elastic/plastic conditions.

This paper provides a comparative analysis between the linear elastic stress intensity factor range, ΔK_{el} , a crack tip plasticity adjusted linear elastic stress intensity factor range, $\Delta K_{eff(pl)}$, and an elastic/plastic, J-integral based, stress intensity factor range, ΔK_J , computed from load-displacement records captured during fatigue crack growth testing. The highest stress intensity factor ranges or “pseudo” fracture toughnesses computed by these three methods are compared to the limiting, upper bound, fracture toughness of the material, $\Delta K_{FT(J_{max})}$, determined from the static fracture toughness test results. $\Delta K_{FT(J_{max})}$ is a geometry dependent value of toughness associated with final failure and computed from J_{max} values. A method to evaluate this limiting, upper bound fracture toughness of the material directly from fatigue crack growth experiments was developed and validated. A new relationship used to determine plastic zone size considering combined effects of plane strain and plane stress conditions was introduced and employed to compute plasticity corrected stress intensity factor ranges, ΔK_{eff} . A procedure to decouple and partition plasticity and tearing effects on crack growth rates is also discussed.

Five cast Al-Si-Mg alloys with different levels of ductility, provided by different Si concentrations and heat treatments (T61 and T4) are evaluated, and the effects of crack tip plasticity on fatigue crack growth are assessed. The combined effects of plasticity and residual stress are studied for one of the alloys produced with both low and high residual stress levels. The fatigue crack growth testing was done at constant stress ratio, $R=0.1$ on compact tension specimens. The

significance of specimen size as well as specimen size requirements for different alloys and heat treat conditions are addressed.

Keywords: linear elastic fracture mechanics (LEFM), elastic/plastic fracture mechanics (EPFM), fracture toughness, Al-Si-Mg alloys, compact tension specimens, fatigue crack growth, crack tip plastic zone, high stress intensity factor ranges, plasticity, tearing.

I. INTRODUCTION AND BACKGROUND

First, the beginnings and the fundamental concepts of linear elastic fracture mechanics are presented together with their limitations when elastic/plastic conditions are encountered. The origins of what is known today as linear elastic fracture mechanics go back more than 80 years, when Griffith [1] first proposed the energy based theory of brittle fracture. Griffith realized that the critical parameter needed to explain the discrepancies between the theoretical cohesive stress and the observed fracture stress of metals when defects or cracks are present is the stress required to grow microcracks to complete fracture. Griffith's theory for elastic materials was modified by Orowan [2] to accommodate plasticity effects that are encountered in the fracture of metals. At the same time, Irwin [3] was adapting Griffith's theory to metals by including the energy dissipated by local plastic flow. In 1956, Irwin [4] developed the energy release rate concept, making Griffith's theory a more useful tool for engineering applications. After studying Westergaard's [5] analysis of stresses and displacements ahead of a sharp crack, Irwin [6] showed that the stresses and displacements near the crack tip could be incorporated in a single parameter related to the energy release rate. This parameter, characterizing the stress field ahead of the crack tip, is the *stress intensity factor*. In 1960, Paris [7] first proposed the extension of these static fracture mechanics concepts to fatigue crack growth.

Linear elastic fracture mechanics is based on the idea that elastic stresses surrounding a crack tip are distributed independently of the applied load and geometry [6,8]. Therefore, stress intensity factors, which are unique functions of the applied load, specimen geometry, and crack length, could be employed to describe the material response to both static [9] and dynamic [10] loading. However, the equations used to determine stress intensity factors were derived for linear elastic behavior, and severe limitations occur when plastic deformation is associated with crack propagation and failure. Linear elastic fracture mechanics becomes invalid when the plastic zone at the crack tip is significant in size compared to both crack length and remaining ligament of uncracked material, and also for small cracks in a region of plasticity associated with a notch.

The first attempts to extend the validity of linear elastic definitions to cases with plasticity were done by simple corrections for yielding at the crack tip, such as Irwin's [11] crack length plastic zone correction ($a_{\text{eff}}=a+r_p$). Other researchers derived more complex models, one example being Dugdale's plane stress plastic zone model [12] based on narrow strips of yielding material at the crack tip. However, there are limits on the extent to which linear elastic relations can be adjusted for crack tip plasticity. Under pronounced plasticity, Wells [13] observed that crack faces moved apart and this observation led to the development of a new parameter named crack tip opening displacement (CTOD), a concept largely used in the UK.

Another parameter to describe the nonlinear behavior of the materials ahead of a crack was developed by Rice [14]. He generalized the energy release rate concept to nonlinear materials and calculated it as a path independent line integral, identified as the J-integral, computed along an arbitrary contour around the crack. The value of J, obtained under elastic-plastic conditions, was demonstrated to be numerically equal to the strain-energy release rate G (which is directly related to the stress intensity factor K), for the same material under fully elastic conditions (Begley and Landes [15]). Therefore, J_{IC} can be used as a fracture criterion, to characterize fracture toughness in the same way K_{IC} and G_{IC} were used. Several J-integral studies demonstrated success in determining J_{IC} in steels [16], titanium [17], and aluminum [18]. However, material toughness was not sufficient to apply fracture mechanics concepts to design problems, and therefore, Shih and Hutchinson [19] developed the necessary fracture mechanics relationships between toughness, stress, and flaw size based on the J-integral.

The next important step in the development of J-integral was its extension to cyclic loading. There were questions as to whether or not J-integral concepts were applicable in this situation because the deformation theory of plasticity could not account for plasticity effects upon unloading. The initial investigations of J on cyclic loading were done by Dowling and Begley [20] on A533B steels, using an approximation of the J-integral based on the area under load-displacement curves (a simplified model first proposed by Rice et al. [21]). Dowling and Begley assumed that ΔJ defines the stress and strain fields near the crack tip only during the loading half of the cycle, despite cyclic loading, and their success in modeling low cycle fatigue encouraged other researchers to use this same interpretation. The J integral approximation proposed by Rice et. al. was developed for a deeply-cracked bend-type specimen using a single load-displacement record and slight inaccuracies were observed by Merkle and Corten [22] when applied to compact tension specimens (that are in fact bend specimens with a small tension component superimposed and not always deeply cracked). As a result, they developed a new approximation of the J-integral, which was subsequently simplified by the same authors. A further simplification of Merkle and Corten formulation was suggested by Landes et al. [23]; this

definition was found to be the most accurate approximation of the J-integral, for geometries with crack length-to-width ratios greater than 0.5.

J integral treatments of fatigue crack growth are most often used for steels. Brose and Dowling [24] studied planar size effects on fatigue crack growth of annealed AISI 304 stainless steel using the cyclic J-integral. Mowbray [25] used cyclic J-integrals to study fatigue crack growth in Cr-Mo-V steel. Dowling [26] applied the J-integral concept to the behavior of small cracks in A533B steel subjected to cyclic strain fatigue with J being estimated from stress-strain hysteresis loops. Wang et al. [27] investigated 15CDV6 tempered steel using J determined from load-displacement hysteresis loops. El-Haddad and Mukherjee [28] used A516 Grade 70 steel compact tension specimens of different thickness to correlate fatigue crack growth with cyclic J data. Tanaka et al. [29] analyzed the effect of loading conditions and sample geometry on fatigue crack growth in low-carbon steel JIS SM41B using the cyclic J-integral. Cyclic J behavior of A533B steels was investigated for both increasing and decreasing load gradients by Jolles [30]. A good correlation between the J-integral concept and fatigue crack propagation was also found by Lambert et al. [31] for AISI 316 stainless steel. However, limited J related research has been done on other alloy systems, such as light metal alloys, that can often experience high levels of ductility. Very few studies on wrought aluminum alloys, such as Banks-Sills and Volpert's [32], show that ΔJ calculated from both a path independent integral and also load-displacement data may be employed as a crack growth parameter. Even fewer investigations have been carried out on cast aluminum alloys and therefore, this paper was directed towards this important class of materials.

It is important to notice that in all the studies mentioned above, ΔJ_{cyclic} was calculated for each individual cycle, by adding the plastic contributions, calculated using the area under the load-displacement curves, to the elastic terms. No cycle to cycle cumulative effects were considered. Therefore, in this work a different approach, based on the static fracture toughness test method described in ASTM E1820 [33], was used to account for cumulative cyclic damage. The accuracy of linear elastic fracture mechanics for cast aluminum alloys at high ΔK levels is investigated by comparing the linear elastic approach with two plasticity/tearing corrected approaches; one uses Irwin's plastic zone crack length correction, and another is based on a cumulative cyclic J analysis. The pseudo fracture toughness values calculated by these three methods are compared against the limiting values of the static fracture toughness. The static, tearing contributions are separated out by comparing the results of the two non-linear approaches in conjunction with the J_{IC} values.

II. EXPERIMENTAL PROCEDURE

II.A. Alloys, casting procedure, and heat treating conditions

Al-Si-Mg cast alloys of fixed Mg composition (0.45%) were investigated in the study. Different levels of ductility were induced in the alloys by varying the Si composition from 1% to 13%. Eutectic Si in both unmodified (UM) and Sr-modified (M) conditions were considered for both hypoeutectic (A356-type) alloys (7%Si), and eutectic alloys (13%Si). The same level of modification in the 7% and 13%Si alloys was achieved by using the right amounts of Al-10%Sr master alloy. Appropriate additions of Al-5%Ti-1%B master alloy were introduced to attain a constant grain size level in all the alloys (~280 μm). High purity alloys were used so that all the other elements were kept at low levels <0.002%; Fe concentration was <0.02%. DAS was 20-30 μm for all the alloys. For the fatigue growth studies compact tension (CT) specimens were produced using a specifically designed sand mold containing central top and bottom gray cast iron chills to insure the desired DAS throughout the regions of interest. The original castings used to prepare the CT samples were 4.4 in x 4.4 in x 0.8 in (112 mm x 112 mm x 20.5 mm).

A high ductility condition was created in the Al-7%Si alloys by using a T4 heat treatment consisting of solutionizing and natural aging. The absence of artificial (high temperature) aging prevented the development of Mg-Si strengthening precipitates and samples with low yield strength/high ductility were obtained (Table 1). However, the majority of the samples in this work were T61 heat treated, where the solutionizing step was followed by natural and artificial aging.

Table 1. Ultimate tensile strength (UTS), yield strength (YS), and elongation (e%) for unmodified and Sr-modified 7%Si alloys in T61 and T4 heat treating conditions tested at room temperature

Alloy	UTS		YS		Total Elongation (%)
	US (ksi)	SI (MPa)	US (ksi)	SI (MPa)	
1%Si-T61	40.6	280.2	29.6	204.2	13.93
7%Si-UM ^a -T61	45.1	311.3	33.9	233.7	7.34
7%Si-M ^b -T61	45.2	312.0	34.9	241.0	6.08
7%Si-UM-T4	38.5	265.8	20.1	138.7	11.95
7%Si-M-T4	38.3	264.5	20.2	139.4	14.69
13%Si-UM-T61	51.5	355.0	38.3	264.1	7.47
13%Si-M-T61	49.7	342.7	39.0	269.1	7.33

^a UM = Unmodified conditions

^b M = Sr-modified conditions

The two heat treating procedures are detailed below. The role of liquid nitrogen-boiling water reverse quench (uphill quench), was to eliminate residual stresses [34].

The uphill T61 heat treatment consisted of:

- Solution-treatment for 1.5 hrs at 1000°F (538°C);
- Boiling water quench for 15 min;
- Liquid N₂ immersion for 30 min;
- Boiling water reverse quench for 15 min;
- Natural age for 12 hrs;
- Artificial age for 12 hrs at 311°F (155°C).

The T4 heat treatment followed the same steps except the artificial aging was not performed.

A room temperature T61 heat treatment (room temperature water quench) was applied to one of the samples. This procedure induced high residual stresses in the sample and provided us with a means to understand the combined effects plasticity/residual stress and to assess the possibility of accounting for plasticity in the presence of residual stresses.

The room temperature T61 heat treatment consisted of:

- Solution-treatment for 1.5 hrs at 1000°F (538°C);
- Room temperature water quench;
- Natural age for 12 hrs;
- Artificial age for 12 hrs at 311°F (155°C).

The transferring time of the samples from one medium to another was two seconds for both the regular and the reverse (uphill) quench.

II.B. Sample preparation and testing

II.B.1. Specimens

The heat treated rectangular block castings were machined to ASTM E647 [35] compact tension specimens with nominal dimensions 3.75 in x 3.6 in x 0.4 in (95 mm x 91 mm x 10 mm). An end mill was used to machine the edges and a fly cutter was used for the reduction in thickness. A 0.006 in (0.15 mm) diameter wire was used for the wire EDM notch. The notch length is 1.5 in (38 mm) measured from the front face of the sample, and 0.75 in (19 mm) measured from the pin holes.

II.B.2. Fatigue crack growth (FCG) and fracture toughness (FT) testing

The CT specimens were tested as spelled out by ASTM E647 specifications [35]. Tests were conducted in air at room temperature and relative humidity 40-50%. The specimens were tested under K-control, first under a decreasing crack driving force range (Region I) to evaluate the thresholds, and then under increasing crack driving force range (Regions II and III). Above 10^{-5} inches/cycle ($\sim 2.5 \times 10^{-4}$ mm/cycle), the test was continued using a shallower K-gradient to obtain the steeper Region III data. The upper limit of the stress intensity factor range (highest ΔK value of the fatigue crack growth curve) was considered the "pseudo" fracture toughness of the material. This pseudo fracture toughness corresponded to a crack growth rate between 0.1 and 0.5 mm/cycle. Although the specimens were valid for crack growth testing per ASTM E647, they did not meet the plane strain fracture toughness criteria to obtain valid measurements of K_{IC} . The compliance technique was used to monitor the crack advance and the frequency was set to 25 Hz (except in Region III when it was decreased to as low as 0.1 Hz to sufficiently capture the cyclic and tearing instability behavior). All the samples were tested under a constant stress ratio $R=0.1$.

Load-displacement records were captured for all the fatigue crack growth tests for growth rates above 10^{-5} inches/cycle. These data were used for cyclic J computations in section III.B.

Fracture toughness testing was done for each alloy and heat treat condition in accordance with ASTM standard E1820 [33] on identically produced and sized samples. These tests determined the J_{IC} values characterizing the toughness of the material near the outset of crack extension. The determination of J_{IC} by this method involves the measurement of J values from multiple loadings of single samples. After the sample is loaded to a certain load and displacement level, the load is reduced by approximately 10%. By measuring the elastic compliance on this slight unloading step, the crack length corresponding to this compliance value can be determined. Further on, the load is increased again until another slight unloading event is introduced. Here, again, the new crack length is calculated using the same technique. From a number of such loading/unloading slopes, Δa values can be determined along with the associated values of J corresponding to the respective locations along the load-displacement plot. This information is used to obtain an R curve with a J- Δa plot, characterized by a best-fit power law relation. J_{IC} is defined at the intersection point with an offset line parallel to the computed blunting line (See Figure 1). The blunting line was found to be well defined by $J=2\sigma_{flow}\Delta a$ where $\sigma_{flow}=(\sigma_{YS}+\sigma_{UTS})/2$, which takes into account strain hardening in the material. Additional lines parallel to the

blunting line are then constructed with offsets of 0.15, 0.5, 1.00, and 1.5 mm (0.006, 0.02, 0.04, and 0.06 in), respectively.

ASTM E1820-02 Standard Test

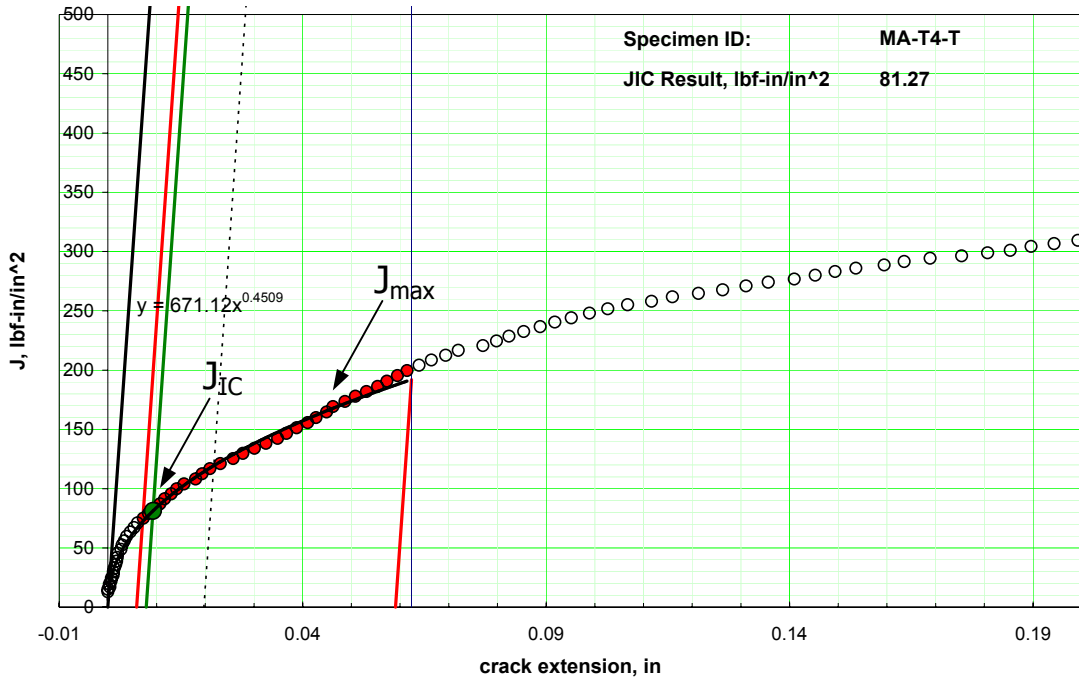


Figure 1. J vs. Δa plot used to determine J_{IC} and J_{max} .

When selecting the J- Δa data for the R curve, one data point must lie within the 0.15 and 0.5 mm offset lines, as well as within the 1.0 and 1.5 mm lines. Several additional points are then taken from the acceptable region of valid data (between 0.15 and 1.5 mm offset lines) for the regression analysis. The value J_Q is then obtained by noting the intersection of the best fit power law J- Δa curve with a 0.2 mm offset line (the latter corresponding to a fracture-toughness determination for 0.2 mm crack extension). Finally $J_Q = J_{IC}$ if $B, b \geq 25 * J_Q / \sigma_{ys}$. For each alloy, J_{max} was also determined using the crack extension Δa corresponding to the maximum load. The two parameters, J_{IC} and J_{max} , represent the lower and upper bound toughness values associated with the onset of unstable fracture and failure respectively. The use of J_{IC} is a conservative approach, which can give rise to fracture toughness values lower than the one provided by the elastic K analysis from the fatigue crack growth experiments (because the CT specimens were not sufficiently large to meet the plane strain conditions for K_{IC}). Therefore, the limiting, upper bound static fracture toughness of the materials was calculated based on J_{max} values. Even though, unlike J_{IC} , J_{max} is specimen size/geometry sensitive this choice is valid considering that fatigue crack growth and fracture toughness tests were performed on identical samples. Moreover, to assess the validity limits of the LEFM and EPFM models of crack growth at high

ΔK levels associated with final failure, a similar parameter from the static fracture toughness test was needed for appropriate comparison. The parameter associated with failure in a static fracture toughness test is J_{max} .

III. RESULTS AND DISCUSSION

Theoretically a material can behave elastically from fracture mechanics point of view if it is used to produce real components or experimental specimens of sufficiently large dimensions (width and thickness) to accommodate the increasing extent of the plastically deformed zone ahead of the crack tip. However, this is a very demanding requirement and it can involve specimens with width and thickness in the order of tens of inches (several hundreds of mm). These unrealistically large sizes are never used in practice when most of the experimental samples as well as real parts are restricted to much smaller dimensions. Under these conditions, plasticity effects ahead of the crack can become significant at certain levels of the fatigue crack growth process depending on the material properties and part size. In these cases corrective methods for plasticity effects are needed for accurate interpretations of the experimental data and appropriate design criteria. Two such methods are presented next. The first method uses elastic/plastic fracture mechanics (EPFM) definitions while second method represents a plasticity corrected linear elastic fracture mechanics (LEFM) model.

III.A *Mathematical modeling of **plasticity and tearing** effects using EPFM considerations (cyclic J analysis based on FCG load-displacement data)*

The values of the elastic-plastic energy release rate parameter, ΔJ , can be directly obtained from a path independent J-integral as first proposed by Rice [14], but the analysis is rather laborious. Therefore, a simplified ΔJ calculation model using load-displacement records was proposed by Rice et al. [21] and further improved by Merkle and Corten [22] and Landes et al. [23]. ΔJ calculated from load-displacement data were used by several researchers [20,24-32] to correlate fatigue crack growth data in steels. In these studies, ΔJ values at each cycle were calculated using the total area, A_{tot} , under the loading part of the load-displacement curve using the following type of relations:

$$\Delta J = \frac{2A_{tot}}{Bb} \cdot \frac{1 + \alpha}{1 + \alpha^2} \quad [1]$$

where α is a function of a/b

Even though this procedure was successfully used in steels, for the alloys and conditions of this work, plasticity effects were not satisfactorily modeled by this method mostly due to its inability to account for "cumulative plastic damage" during crack advance. Cumulative effects from cycle to cycle cannot be captured

by simply using the area under the load-displacement curve for each cycle. Therefore, a new procedure accounting for the incremental increase in the plastic area under the load-displacement curves for successive records as well as the increase in displacement from cycle to cycle was developed. This technique follows a procedure similar to ASTM E1820 [33] standard recommendations for fracture toughness determination.

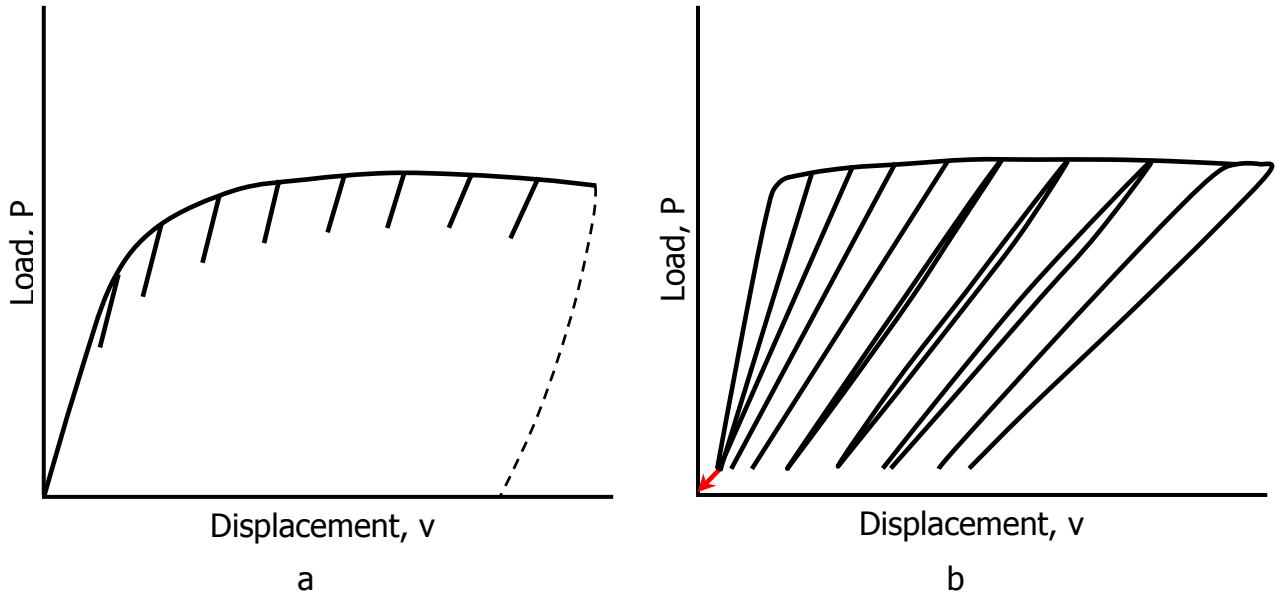


Figure 2. Loading-unloading cycles analogy between (a) fracture toughness test and (b) fatigue crack growth test.

In this study, instead of using the area under the load-displacement curve to compute ΔJ for each individual cycle, the incremental increases in the plastic area under the load-displacement records are used to compute current ΔJ_i by adding their contribution to prior calculated ΔJ_{i-1} values. This “cumulative effects procedure” is used in ASTM E1820 standard [33] to determine the fracture toughness J_{IC} . The main difference consists in the use of fatigue crack growth load-displacement records instead of the succession of loading-partial unloading-reloading cycles characteristic of a fracture toughness test, as schematically illustrated in Figure 2.

In this technique, load-displacement records are analyzed by considering the maximum load of each cycle, P , the corresponding displacement, v , and compliance, v/P . The values of the compliance were determined from the normalized compliance EvB/P , computed automatically for each cycle during the unloading part of the fatigue crack growth test. However, in order to follow the cyclic J computation procedure provided by standard ASTM E1820, an adjustment of the displacement was needed. For each test, minimum load displacement measurement of the first cycle used in the cyclic J analysis was back-extrapolated to zero load, and taken as reference (zero displacement).

Usually this first cycle corresponded to a growth rate around 10^{-5} in/cycles, the value below which no plasticity contributions were found. In the next step, the displacement corresponding to the maximum load of each cycle was recalculated according to the new reference.

The results of the cyclic J analysis provide combined effects of plasticity and tearing. Plasticity is the dominant contributor until the value of ΔK corresponding to J_{IC} is reached. Beyond this stage both plasticity and tearing effects are responsible for the increase in fracture toughness. A simple method to partition these two effects is presented in section III.D.

Using the aforementioned loading/unloading analogy with the appropriate corrections, a cyclic J analysis based on standard ASTM E1820 recommendations was performed:

$$\Delta K_{J(i)} = K_{J_{max}(i)} \cdot (1 - R) \quad [1]$$

where $K_{J_{max}}$ is determined as:

$$K_{J(i)} = K_{pl+tearing(i)} = \sqrt{\frac{J_{(i)} \cdot E}{1 - \nu^2}} \quad [2]$$

J values are calculated by adding the elastic contributions represented by K to the plastic terms:

$$J_{(i)} = \frac{K_{(i)}^2 (1 - \nu^2)}{E} + J_{pl(i)} \quad [3]$$

where

$$J_{pl(i)} = \left[J_{pl(i-1)} + \left(\frac{\eta_{(i-1)}}{b_{(i-1)}} \right) \frac{A_{pl(i)} - A_{pl(i-1)}}{B} \right] \left[1 - \gamma_{(i-1)} \frac{a_{(i)} - a_{(i-1)}}{b_{(i-1)}} \right] \quad [4]$$

and

$$\eta_{(i-1)} = 2 + 0.522 \cdot b_{(i-1)} / W ; \quad \gamma_{(i-1)} = 1 + 0.76 \cdot b_{(i-1)} / W$$

as given by standard ASTM E1820 [33].

In eq. [4], all the terms are known from the previous cycle calculations or evaluated at every instant during the FCG test excepting the plastic area that needs to be calculated separately. Load-displacement records for two samples with different degrees of ductility are presented in Figure 3. To understand the exact meaning of plastic area, a schematic graphical representation of a load-displacement record is also given, Figure 4.

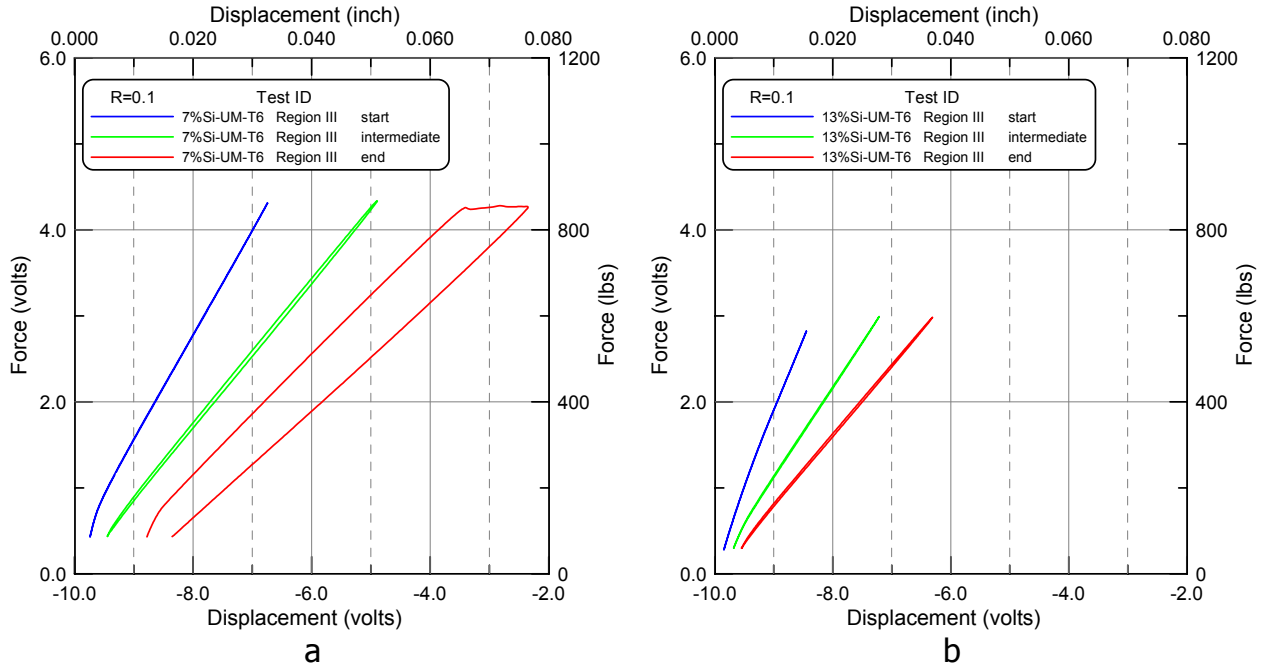


Figure 3. Load-displacement records at high ΔK levels (Region III) for (a) unmodified 7%Si alloy, and (b) unmodified eutectic alloy 13%Si.

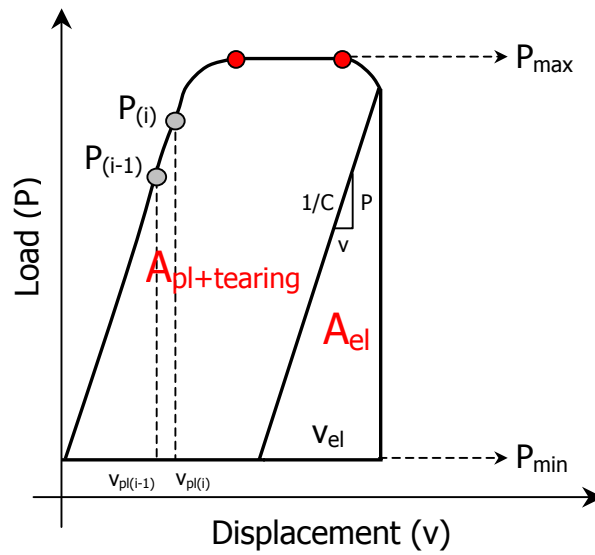


Figure 4. Typical load vs. clip gauge displacement curves.

$$A_{pl(i)} = A_{pl(i-1)} + \frac{[P_{max(i)} - P_{max(i-1)}] \cdot [v_{pl(i)} - v_{pl(i-1)}]}{2} \quad [5]$$

$$v_{pl(i)} = v_{(i)} - v_{el(i)} \quad [6]$$

where

$$v_{(i)} = v_{(i)\text{-corr}} = v_{(i)\text{-exp}} \cdot CF \quad [7]$$

$$v_{el(i)} = v_{el(i)\text{-corr}} = P_{\max(i)} \cdot C_{(i)} \quad [8]$$

In eqs. [5]-[8] a corrected displacement was used to account for the displacement measurement location. Due to the fact that clip gauge displacement measurements were taken at the front face of the samples (Figure 5) a displacement adjustment for the off load-line clip gauge measurement location was needed.

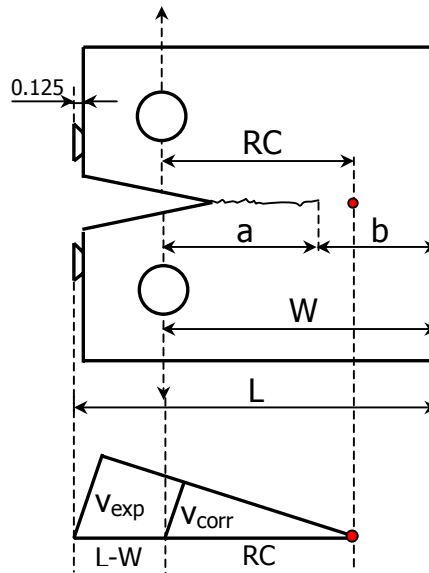


Figure 5. CT specimen – displacement adjustment for off load-line measurements.

$$v_{(i)\text{-corr}} = v_{(i)\text{-exp}} \cdot CF \quad [11]$$

where

$$CF = \frac{v_{(i)\text{-corr}}}{v_{(i)\text{-exp}}} = \frac{RC_{(i)}}{(L - W) + RC_{(i)}} = \frac{RC_{(i)}}{W \cdot (\mu - 1) \cdot RC_{(i)}} \quad [12]$$

and

$$\mu = \frac{L}{W} \quad [13]$$

$$RC_{(i)} = a_{(i)} + PR_{(i)} \cdot b_{(i)} = a_{(i)} + PR_{(i)} \cdot (W - a_{(i)}) \quad [14]$$

$$PR_{(i)} = 0.4 \cdot (1 + \alpha_{PR(i)}) \quad [15]$$

$$\alpha_{PR(i)} = \left[\left(\frac{2a_{(i)}}{b_{(i)}} \right)^2 + 2 \left(\frac{2a_{(i)}}{b_{(i)}} \right) + 2 \right]^{\frac{1}{2}} - \left(\frac{2a_{(i)}}{b_{(i)}} + 1 \right) \quad [16]$$

The results of the cyclic J analysis for different alloys, heat treatments, and residual stress levels are presented in section III.D, Figures 9-14.

III.B Mathematical modeling of plasticity effects using LEFM crack length adjustments

In the previous section a corrective model for combined plasticity and tearing effects on crack growth rates was presented. Even though a separation of these two effects is important and needed, there are no established procedures to provide it because of the complex interactions of the two components. To partition the two effects, a method that captures mostly plasticity effects had to be determined first. This method was found to be an extension of the ΔK based, linear elastic fracture mechanics approach, incorporating crack length plasticity corrections. Elastic definitions are still used, but with adjustments for plasticity ahead of the crack tip. Tearing effects are not part of the analysis due to the way in which the crack length is determined. Both purely elastic definitions and plasticity corrected models are based on the physically measured crack, which includes when appropriate, the increase in the crack length due to material separation by tearing. However, in this model, plasticity effects are mainly captured, by adding the contribution of plastic zone radius at the crack tip. A new equation to determine plastic zone radius taking into account combined effects of plane strain and plane stress conditions, was developed for this study and it is presented first.

III.B.1 Plastic zone size computation

When the local stresses ahead of the crack tip exceed the yield strength of the material, a region of plasticity is always developed. The existence of the plastic zone makes the material behave as though the crack were slightly longer than physically measured, and the "effective" crack length is assumed to be the physical crack length plus some fraction of the plastic zone diameter. Irwin [11], considered this fraction to be the plastic zone radius; this concept is also used in this work. For plane-strain conditions where the triaxial stress field suppresses the plastic zone size, the plane-strain plastic zone radius is given by McClintock and Irwin [36] as:

$$r_{p(6\pi)} \approx \frac{1}{6\pi} \frac{K_{\max}^2}{\sigma_{YS}^2} \quad [17]$$

However, it should be noted that the size of the plastic zone also varies with the circular coordinate, θ (Figure 6). In a more general sense, by using the distortion energy theory, where the stress components are described in terms of both radius, r , and angular orientation, θ , the equation above should be re-written as:

$$r_{p(6\pi)} \approx \frac{1}{6\pi} \frac{K_{\max}^2}{\sigma_{YS}^2} \cos^2 \frac{\theta}{2} \left(1 + 3 \sin^2 \frac{\theta}{2} \right) \quad [18]$$

The plastic zone shape given by this equation was confirmed by etch pit studies done by Hahn and Rosenfield [37] in an iron-silicon alloy (Figure 6). It can be observed that for $\theta=0$, the simplified equation, eq. [17], is reached, and a circular shape of the plastic zone is assumed.

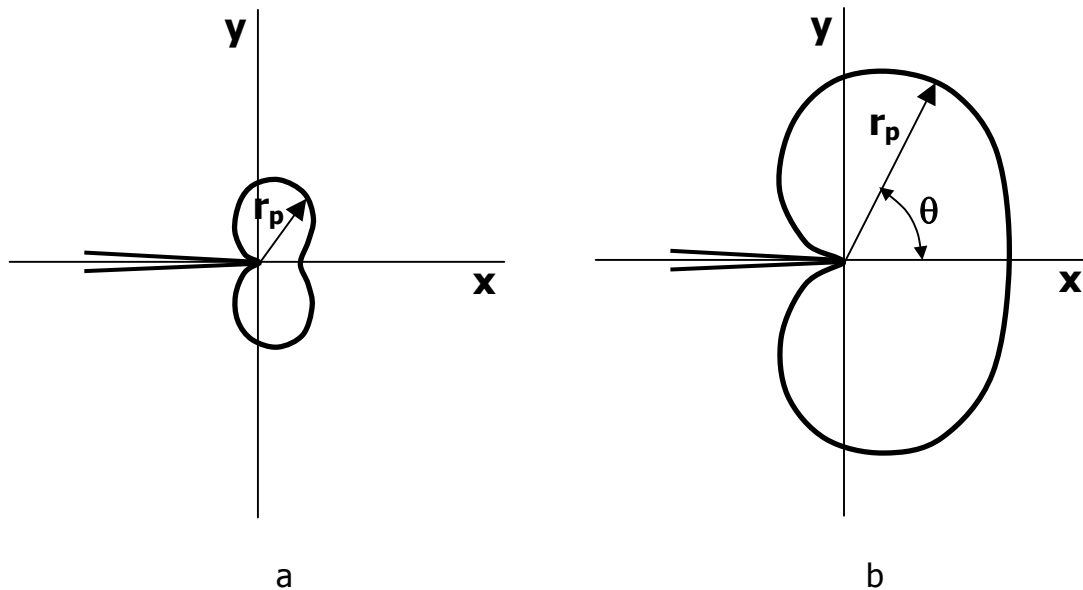


Figure 6. Plastic zone at the crack tip in (a) plane strain and (b) plane stress conditions.

It should be recognized that eqs. [17] and [18] are appropriate for cases when fully plane strain conditions apply; these conditions are fulfilled when the radius of plastic zone is very small compared to the specimen thickness. When the plastic zone becomes large compared to the sample thickness, plane stress conditions prevail and eqs. [17] and [18] should be re-written as:

$$r_{p(2\pi)} \approx \frac{1}{2\pi} \frac{K_{\max}^2}{\sigma_{YS}^2} \quad [19]$$

and

$$r_{p(2\pi)} \approx \frac{1}{2\pi} \frac{K_{\max}^2}{\sigma_{YS}^2} \cos^2 \frac{\theta}{2} \left(1 + 3 \sin^2 \frac{\theta}{2} \right) \quad [20]$$

In practice, very few cases meet fully plane-strain or plane-stress conditions, most materials being subjected to mixed modes, when the two conditions coexist. Therefore, a new mathematical expression to reflect mixed mode conditions with appropriate contributions from each constituent, needed to be developed. This tool characterizes more accurately the real behavior of the materials. The new equation for plastic zone calculations under combined effects of plane strain and plane stress is given in equation [21]:

$$r_{p(\text{combo})} \approx \left(\frac{1}{2\pi} \right)^n \left(\frac{1}{6\pi} \right)^{1-n} \frac{K_{\max}^2}{\sigma_{YS}^2} \cos^2 \frac{\theta}{2} \left(1 + 3 \sin^2 \frac{\theta}{2} \right) \quad [21]$$

where $n = \text{degree of plane stress} = \frac{m \cdot r_{p(2\pi)}}{B} \quad 0 < n \leq 1; \quad [22]$

Calculation of the degree of plane stress coefficient, m , was based on the following rationale. According to eqs. [18] and [20], the plastic zone radius in plane stress conditions is three times larger than the plastic zone radius in plain strain conditions:

$$r_{p(2\pi)} = 3 \cdot r_{p(6\pi)} \quad [23]$$

The planar representation of the plastic zones is shown in Figure 6. Even though there are slight differences in shape, the following calculation assumes both plane strain and plane stress plastic zones to have similar, cardioid-like, shapes (Figure 6b), the only difference being the size. When plane strain conditions are predominant the plastic zone is fairly uniform across the specimen thickness and only flares out at the two side surfaces (a cylindrical shape with a cardioid base across the thickness, and two cone trunks with cardioid bases on the surfaces, Figure 7a). The cylindrical zone in the center narrows as the crack advances (K increases) and eventually the two cone trunks representing plane stress conditions will touch, as shown in Figure 7b. From this point forward, fully plane stress conditions are assumed. Using these geometrical assumptions the degree of plane stress coefficient, m , was mathematically computed using a 45° apex angle of the cone trunks. The apex angle was chosen based on the fracture mode differences between plane strain conditions (flat crack) and plane stress conditions which leads to shear lips and slant fracture (45° deflection angle).

It can be observed (Figure 7b) that to satisfy eq. [23] under a 45° angle, the height of the cone trunk needs to be:

$$\frac{B}{2} = \frac{2 \cdot r_p(2\pi)}{3} \quad [24]$$

Eq. [24] can be now introduced in eq. [22] to solve for m , remembering that $n=1$ for fully plane stress conditions. From this calculation the degree of plane stress coefficient turns out to be:

$$m = 1.333 \quad [25]$$

In conclusion, using eq. [21], the whole range from fully plane-strain conditions to fully plane-stress conditions is covered. A simplified representation of these conditions is presented in Figure 7.

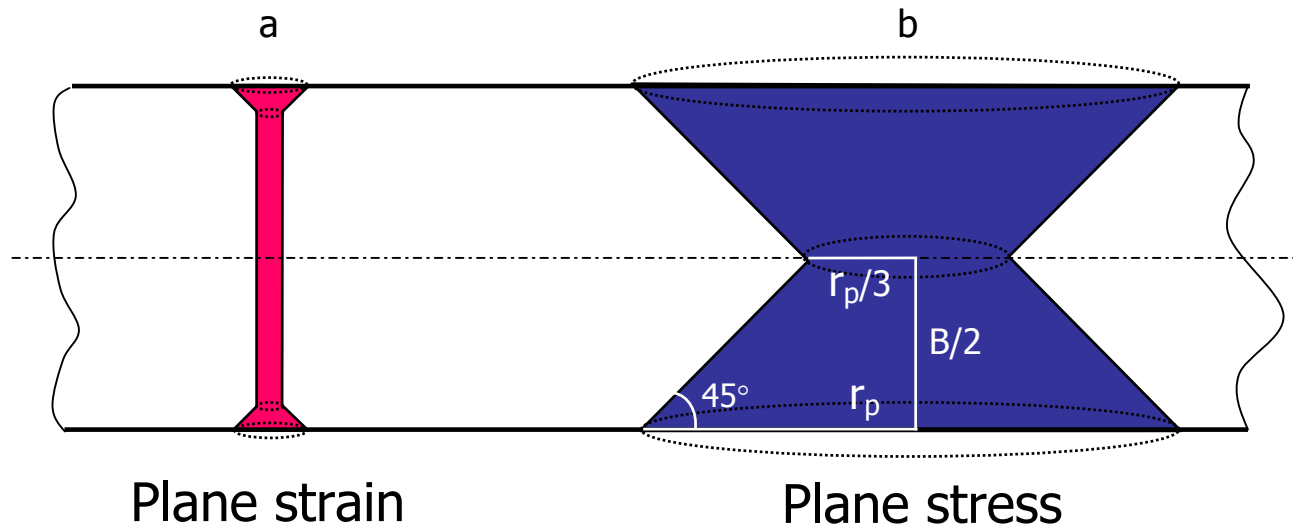


Figure 7. Plastic zone across thickness in (a) plane-strain and (b) plane-stress conditions when the applied stress is normal to the page.

For all the studied cases, fully plane stress conditions are never achieved. It was also observed that plane strain conditions and LEM definitions appropriately describe the behavior of the material below certain growth rates. For the class of cast aluminum alloys and specimen geometry investigated in this study, plastic zone contributions become critical at crack growth rates greater than 10^{-5} in/cycle, corresponding to the upper region II and region III of the FCG curves, where combined plane strain-plane stress conditions coexist and eq. [21] applies. As a result, in this work, the plastic zone size computations are based on eq. [21], accounting for plane strain conditions as well as increasing contributions from plane stress.

III.B.2. ΔK_{eff} calculation using plastic zone corrected crack length

As mentioned earlier, a region of plasticity is developed near the crack tip whenever the local stresses exceed the yield strength of the material. If the crack tip plasticity is accounted for and the crack length is adjusted accordingly, a re-evaluation of the stress intensity factor ranges becomes imperative.

Using the plastic zone radius given by eq. [21], an effective crack length was calculated based on Irwin's assumption [11] that, due to plasticity contributions, the physically measured crack is longer by the amount of the plastic zone radius:

$$a_{\text{eff}} = a_{\text{phy}} + r_p \quad [26]$$

It is important to re-emphasize that this approach is still using LEFM concepts and it only corrects for dynamic plasticity effects. This procedure is attractive through its simplicity and it gives acceptable corrections until severe plasticity are tearing are encountered.

To readjust the stress intensity factor ranges for the plastic corrected crack length the standard equation given in ASTM standard E647 [35] was used.

$$\Delta K = \frac{\Delta P}{B\sqrt{W}} \frac{\left(2 + \frac{a}{W}\right) \left(0.886 + 4.64 \frac{a}{W} - 13.32 \left(\frac{a}{W}\right)^2 + 14.72 \left(\frac{a}{W}\right)^3 - 5.6 \left(\frac{a}{W}\right)^4\right)}{\left(1 - \frac{a}{W}\right)^{\frac{3}{2}}} \quad [27]$$

Substituting a_{eff} for $a=a_{\text{phy}}$, equation [27] gives the effective stress intensity factor ranges.

The results of this method and the cyclic-J analysis data are compared to the static fracture toughness values in section III.D (Figures 9-14).

III.C Fracture toughness results, J_{IC} versus J_{max}

The most appropriate way to compare static fracture toughness results, J , with pseudo-fracture toughness values determined from FCG experiments (K-analysis), is to calculate a J_{max} value using the crack extension Δa corresponding to the maximum load. From J_{max} the values of $K_{J_{\text{max}}}$ are calculated as

$$K_{J_{\text{max}}} = \sqrt{\frac{J_{\text{max}} E}{1 - \nu^2}}. \text{ The } \Delta K \text{ values based on } K_{J_{\text{max}}} \text{ are further compared to the}$$

pseudo fracture toughness determined from the FCG experiments. The decision to use J_{max} instead of J_{IC} comes from the fact that these two parameters represent the upper and the lower bound toughness. The use of J_{IC} leads to

conservative estimations, ignoring tearing effects, which in practice may result in a fracture toughness lower than the one provided by the K-based analysis. On the other hand, J_{max} , accounts for tearing effects, and therefore, it provides a more realistic evaluation of material's fracture toughness for a given sample size/geometry. Even though J_{max} is geometry sensitive, this choice is acceptable keeping in mind that in this work fatigue crack growth and fracture toughness tests were performed on samples of identical geometry.

The different response of ductile materials (higher curves) and brittle materials (lower curves) can be observed by plotting the measured J values vs. Δa for each alloy (see Figure 8). The more ductile the material the higher the J_{IC} and J_{max} values.

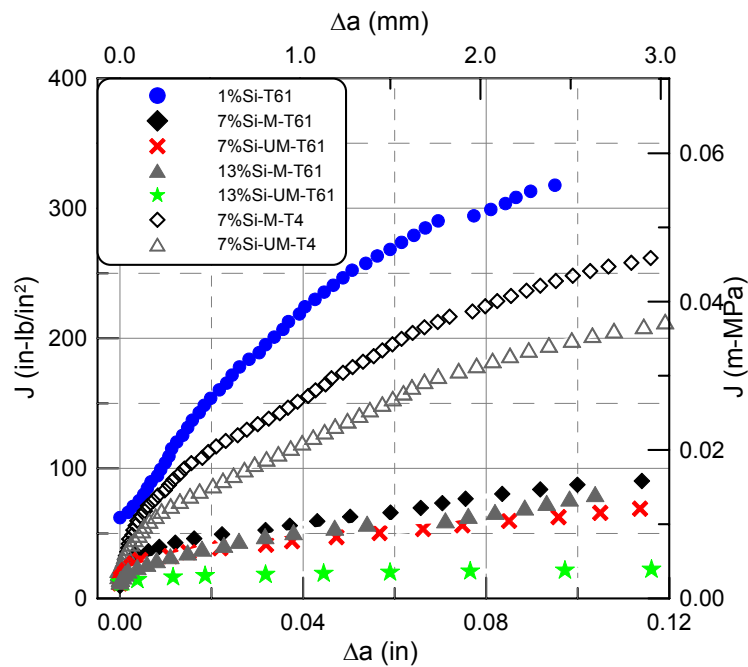


Figure 8. J vs. Δa curves for all alloys in the peak strength T61 condition and two A356-type alloys in low strength/high ductility T4 condition.

III.D Validity limits for K , plasticity and tearing effects at high ΔK

This proposes down validity limits for linear elastic definitions and provides elastic-plastic methods to compensate for plasticity and tearing at increasing ΔK levels. At the same time, it is meant to give the reader a tool to determine the limiting, upper bound fracture toughness of the material directly from the FCG tests without performing separate fracture toughness tests.

The results of the cyclic J -analysis, $\Delta K_J = \Delta K_{tot(pl+tearing)}$, and the the plastic zone crack length corrected data, $\Delta K_{eff} = \Delta K_{pl}$ are compared to the elastic

formulations of the FCG analysis, ΔK_{el} . The pseudo-fracture toughness calculated by these three analyses are then compared to the limiting, upper bound static fracture toughness, $\Delta K_{J_{max}} = \Delta K_{FT}$. J_{IC} is used to calculate $\Delta K_{J_{IC}}$ as a limit beyond which tearing contributions become increasingly significant and simple adjustments for plasticity are insufficient. A method to separate plasticity and tearing effects is presented.

In Table 2, the values of stress intensity factor ranges are provided for all the alloys, heat treatments, and residual stress levels.

Table 2. Stress intensity factor ranges for all alloys, heat treat conditions, and residual stress levels

Alloy	ΔK_{el}		ΔK_{pl}		$\Delta K_{J(tot)}$		ΔK_{JIC}		$\Delta K_{FT(Jmax)}$	
	US (ksi√in)	SI (MPa√m)	US (ksi√in)	SI (MPa√m)	US (ksi√in)	SI (MPa√m)	US (ksi√in)	SI (MPa√m)	US (ksi√in)	SI (MPa√m)
1%Si T61-LRS ^c	30.8	33.9	36.7	40.4	41.2	45.3	30.9	34.0	40.8	44.9
1%Si T61-HRS ^d	39.4	43.3	51.4	56.5	61.1	67.2	44.1	48.5	58.6	64.5
7%Si UM-T61	22.3	24.5	23.3	25.6	27.0	29.7	18.8	20.7	27.6	30.4
7%Si M-T61	23.0	25.3	24.4	26.8	28.3	31.1	19.8	21.8	28.6	31.5
7%Si UM-T4	23.4	25.7	32.2	35.4	39.7	43.7	25.2	27.7	40.5	44.6
7%Si M-T4	21.0	23.1	31.1	34.2	40.7	44.8	28.6	31.5	41.3	45.4
13%Si UM-T61	14.3	15.7	14.5	16.0	14.8	16.28	12.4	13.6	13.1	14.4
13%Si M-T61	19.7	21.7	20.7	22.8	23.4	25.7	17.1	18.8	23.9	26.3

^c LRS = low residual stress conditions

^d HRS = high residual stress conditions

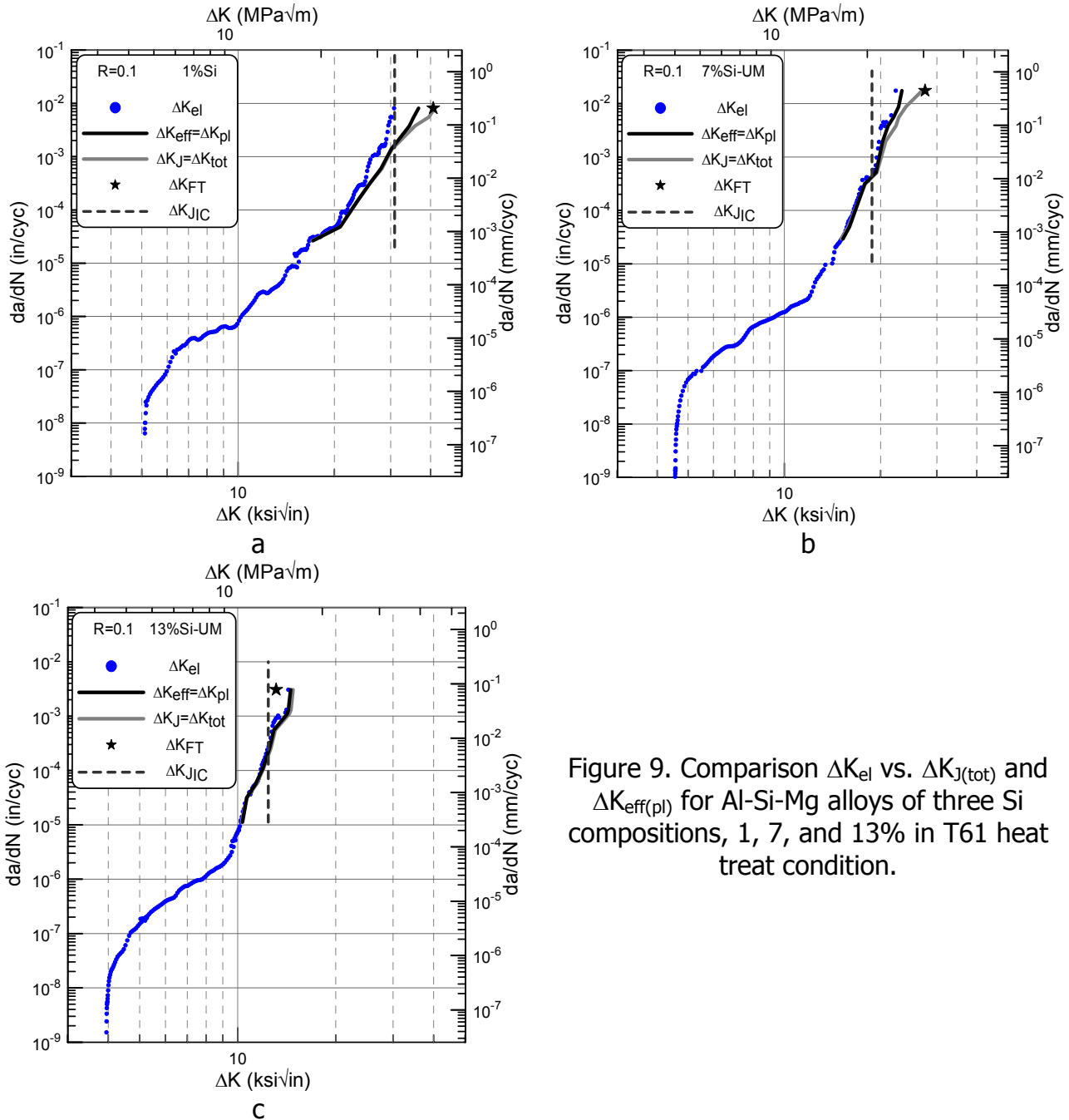


Figure 9. Comparison ΔK_{el} vs. $\Delta K_{J(tot)}$ and $\Delta K_{eff(pl)}$ for Al-Si-Mg alloys of three Si compositions, 1, 7, and 13% in T61 heat treat condition.

Figure 9 presents the differences in FCG behavior for three alloys with decreasing ductility resulting from increasing Si composition from 1 to 7 and 13%. Increased levels of plasticity are predominantly observed in Region III. The more ductile the material, the more extended the plastic zone ahead of the crack tip at the same ΔK level and the larger the differences between the elastically calculated values, ΔK_{el} , and the plasticity corrective models, $\Delta K_{J(tot)}$ and $\Delta K_{eff(pl)}$. It should be emphasized that the ΔK_J term, determined from the cyclic J analysis, incorporates elastic, plastic, and tearing contributions, based on a cumulative

damage analysis. Plasticity and tearing effects are combined at high ΔK levels, and the cyclic J model reflects a summation of these two effects when the “plasticity term” is computed. Plasticity damage is due to a dynamic additive process while tearing is a static process, and it essentially represents a crack extension (material tearing) at constant load. On the other hand, the crack length corrected linear elastic stress intensity factor ranges, $\Delta K_{eff(pl)}$, are not computed in a cumulative manner, the values at step i being dependent on the corresponding radius of the plastic zone, but independent of the events at step $i-1$.

It is understood that above J_{IC} , tearing of the material occurs, and for any ΔK higher than ΔK_{JIC} , the increase in the corrected driving force magnitude is due to both plasticity and tearing. However, the crack length corrected linear elastic model captures mostly plasticity effects, while the cyclic J-analysis incorporates both dynamic plasticity and static tearing contributions. Even though the two models are fundamentally different and a direct comparison is rather complex, an attempt to use the results of the two models to determine the tearing contributions was made, and a schematic of the procedure is presented in Figure 10.

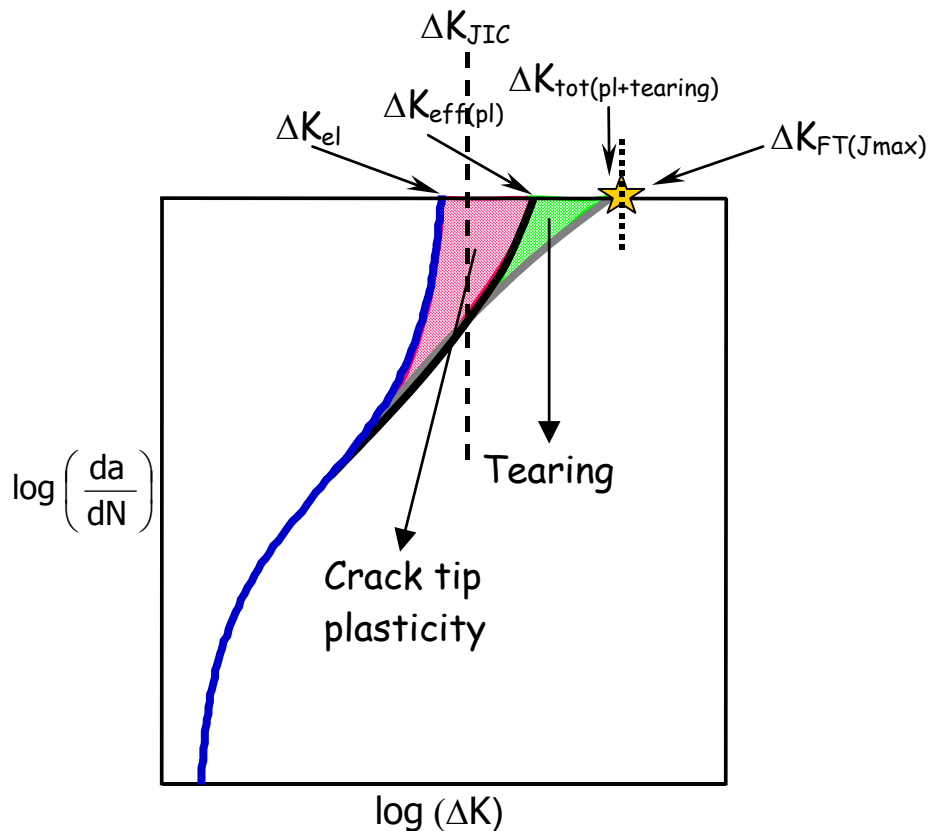


Figure 10. Enlargement of upper Region II and Region III showing the effects of plasticity and tearing and their interactions.

Tearing effects become increasingly significant at high crack growth rates as also observed by Skallerud and Zhang [38]. It is appropriate to assume that cyclic J analysis captures this tendency accurately due to consideration of incremental changes in the crack length, and cumulative changes in plastic area under load-displacement records. At the same time, it can be observed in Figures 9 and 10 that before tearing becomes significant, below ΔK_{JIC} , the two corrective methods (corrected LEFM and EPFM) account for plasticity in a similar manner. This behavior could be rationalized based on the maximum plastic zone size, which is not sufficiently large to make Irwin's LEFM corrective method invalid, and plane stress conditions are never achieved. As a result, the split observed at stress intensity factor ranges higher than ΔK_{JIC} is mostly attributed to the increase in tearing contributions captured by the cyclic J analysis (the square hatched area in Figure 10). An additional observation in favor of this explanation is based on the shape of the da/dN vs. ΔK_J curve. For materials that experience high ductility, the Region II linear slope extends to higher growth rates in Region III. This is a sign of irregular increases in crack length (larger and larger crack length increments for small changes in crack driving force) due to enhanced tearing. Even though the two analyses are different, and plasticity effects can potentially be higher in the cyclic J analysis, the differences are not significant for our class of alloys and heat treat conditions, and this procedure is applicable for these cases.

However for very large amounts of plasticity, significantly higher than the ones found in this study, plasticity contributions in cyclic J analysis can be notably higher than plasticity effects provided by the crack length corrected linear elastic model. In that case a direct comparison would not be exact. Therefore, a further validation of the approach for highly ductile materials is recommended.

It is observed that 1 and 7%Si alloys show plastic contributions in upper Region II and Region III, but the unmodified eutectic alloy (13%Si) shows neither plasticity nor tearing effects, and it is the only alloy that meets the size requirements for plane strain given by eq. [28] during the entire FCG test.

$$B, a, \text{ and } b \geq 2.5 \left(\frac{K_{max}}{\sigma_{YS}} \right)^2 \quad [28]$$

In Figure 11 parallel results for an unmodified and a Sr-modified A356-type alloy with the same Si content, are presented. It can be observed that similar results are obtained for both alloys with the only remark that the fracture toughness is slightly higher for the modified alloy. The differences observed in the fatigue crack growth behavior at high crack driving forces are driven by the Si morphology-crack interactions; details are given by Lados and Apelian [39].

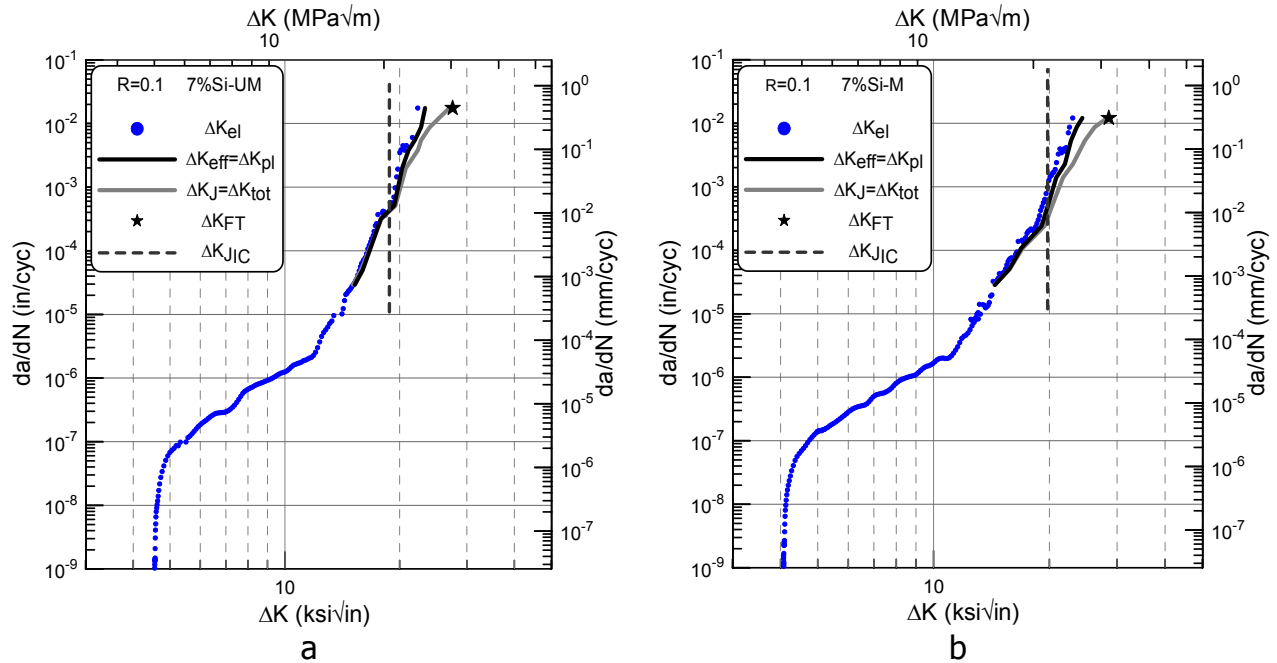


Figure 11. Comparison ΔK_{el} vs. $\Delta K_{J(tot)}$ and $\Delta K_{eff(pl)}$ for (a) unmodified and (b) modified A356-type alloy with 7%Si, in T61 heat treat condition.

A similar comparison between unmodified and modified eutectic alloys (13%Si) can be observed in Figure 12. Unlike the unmodified eutectic, the modified eutectic shows plasticity and tearing contributions, but its toughness is lower than both unmodified and modified A356-like alloys (7%Si). An important observation is that the differences in toughness between unmodified and modified alloys are more pronounced for the 13%Si alloys than 7%Si alloys (see Figures 11 and 12). This is due to larger differences in Si morphology after heat treatment, Table 3.

Table 3. Average Si particle size and shape factor for the modified and unmodified alloys

	Alloy systems examined			
	7%Si-UM (A356-UM)	7%Si-M (A356-M)	13%Si-UM (Eutectic-UM)	13%Si-M (Eutectic-M)
Si avg. particle size (μm)	2.77	2.19	2.94	2.05
Si particle shape factor ^e	1.41	1.21	1.86	1.19

^e Shape factor was calculated as: shape factor = $\text{perimeter}^2 / (4 \cdot \pi \cdot \text{area})$.

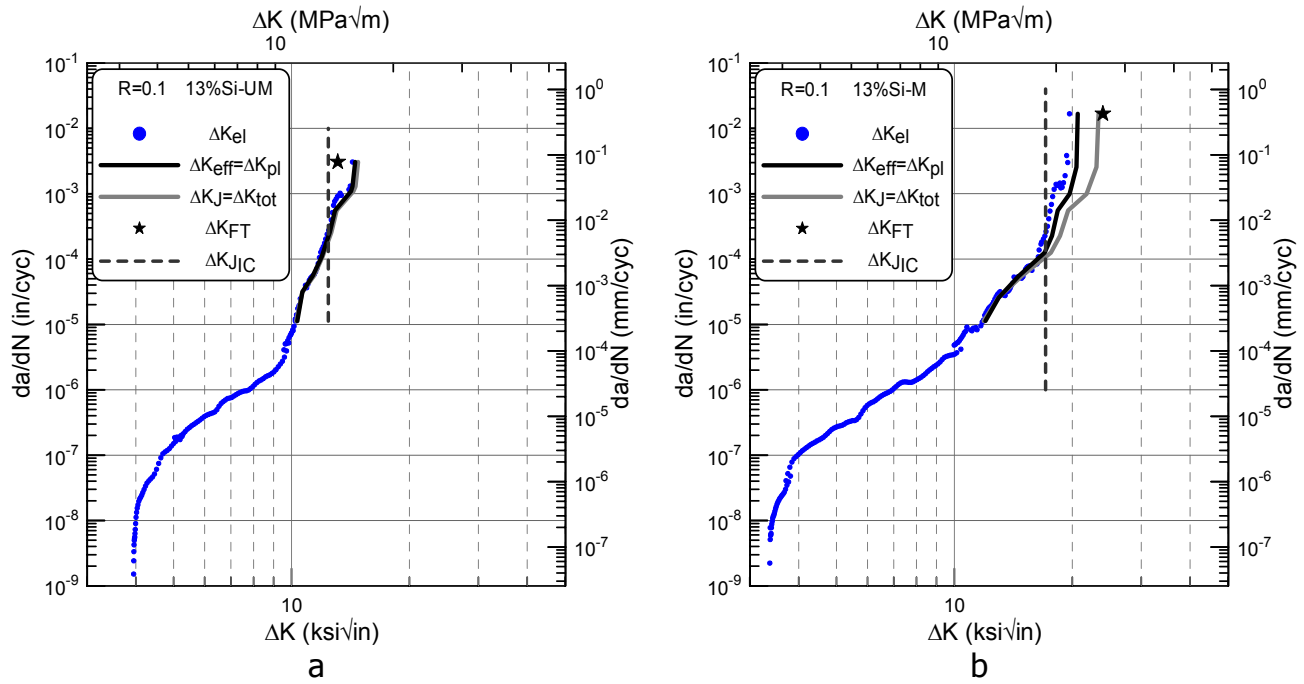


Figure 12. Comparison ΔK_{el} vs. $\Delta K_{J(tot)}$ and $\Delta K_{eff(pl)}$ for (a) unmodified and (b) modified eutectic alloys with 13%Si, in T61 heat treat condition.

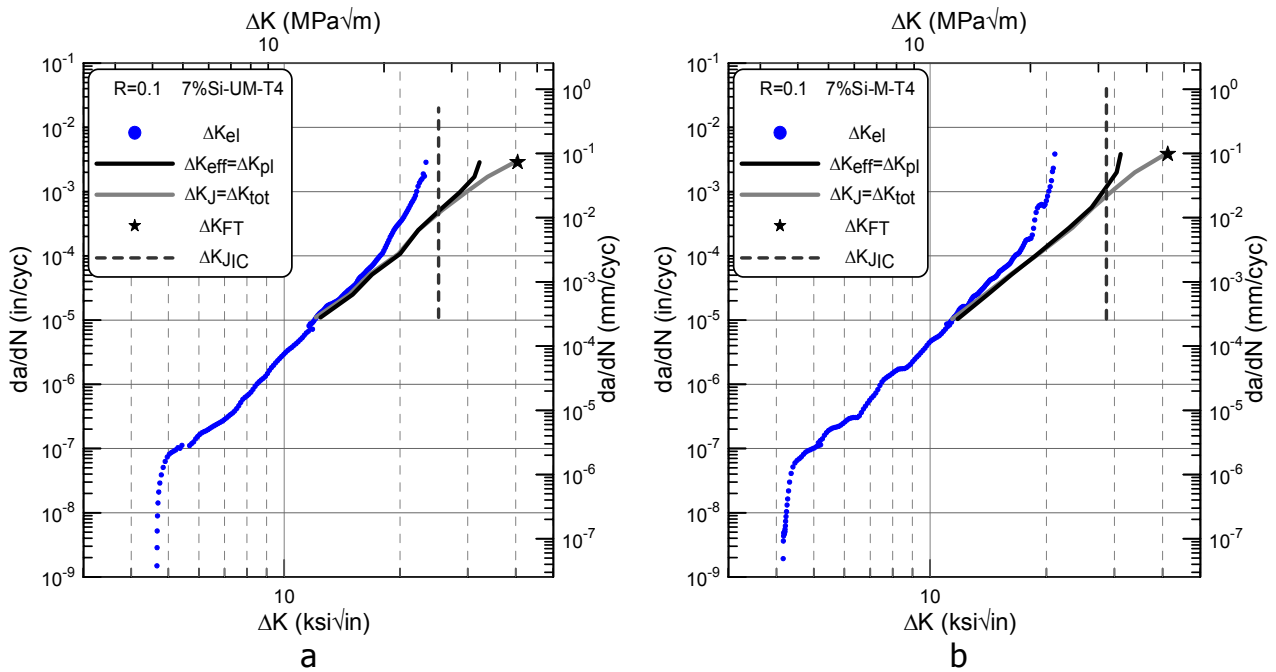


Figure 13. Comparison ΔK_{el} vs. $\Delta K_{J(tot)}$ and $\Delta K_{eff(pl)}$ for (a) unmodified and (b) modified A356-type alloys with 7%Si, in the T4 heat treat condition.

Additional levels of plasticity were introduced for the 7%Si, A356-type alloys by applying a T4, solutionizing only heat treatment, to samples of similar size. Comparing Figures 11 and 13, increased plasticity contributions, induced by the T4 heat treatment, are observed for both unmodified and Sr-modified alloys. After plasticity corrections, the maximum stress intensity factor ranges of T4 heat treated samples are 40-50% higher than the corresponding T61 heat treated samples even though the elastic formulations give almost identical results. It should be also noticed that for the T4 samples the elastic definitions become inaccurate at approximately 50% lower stress intensity factor ranges compared to the T61 treated samples.

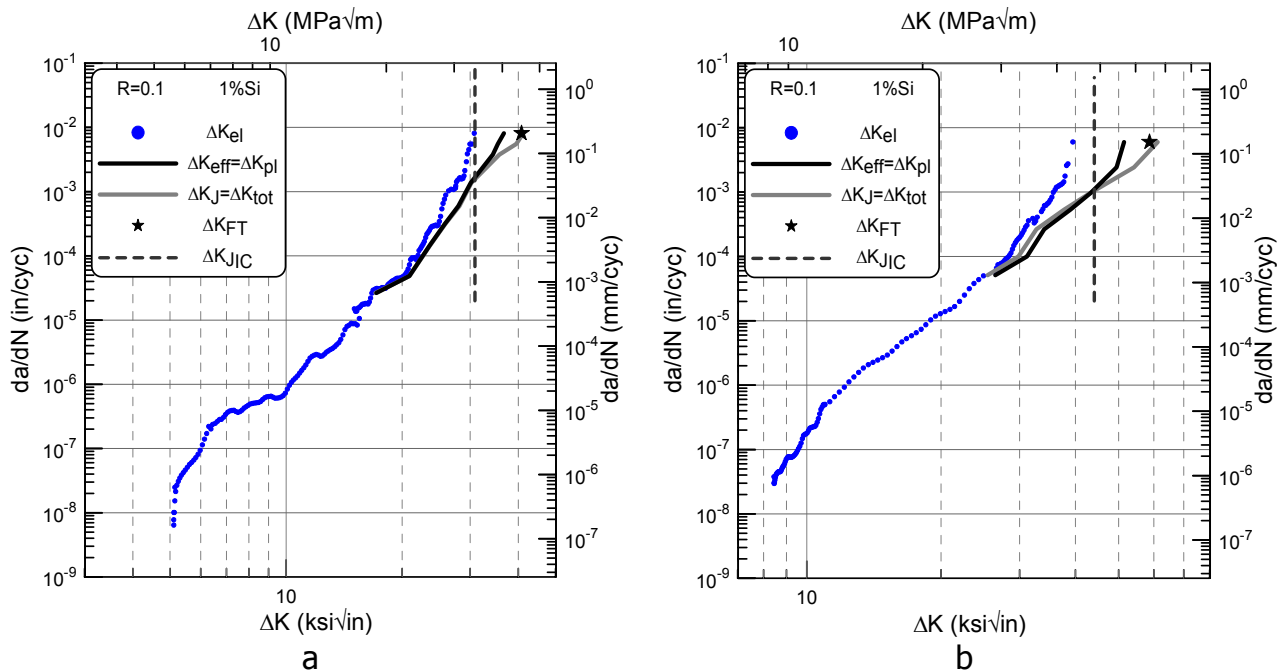


Figure 14. Comparison ΔK_{el} vs. $\Delta K_{J(tot)}$ and $\Delta K_{eff(pl)}$ for (a) low residual stress and (b) high residual stress 1%Si alloys, in T61 heat treat condition.

For one alloy system, 1%Si in the T61 heat treat condition, the influence of residual stress on plasticity and tearing effects was investigated. When correcting for plasticity and tearing effects, a $\sim 30-35\%$ fracture toughness increase for the sample with low residual stress, and an over 50% increase for the sample with high residual stress were observed, Figure 14. Residual stress has a direct impact on the way plasticity damage occurs. The high residual stress sample shows an additional 15-20% elevation in fracture toughness due to the combined residual stress and plasticity effects; the percentage increase is a variable function of the material properties. Compressive residual stresses do bring additional contributions over the pure plasticity/tearing effects, and combined effects of plasticity and residual stress, need to be taken into account for correct interpretations of the results.

LEFM holds true for Region I, and lower Region II; however, at high driving force levels, plasticity becomes increasingly significant, and elastic-plastic (EPFM) methods become necessary to accurately model the material behavior. The increased plasticity at higher stress intensity factor ranges can be also visualized by inspecting the fracture surfaces as seen in Figure 15. The presence of increased plasticity is associated with rougher surfaces and characteristic dimples.

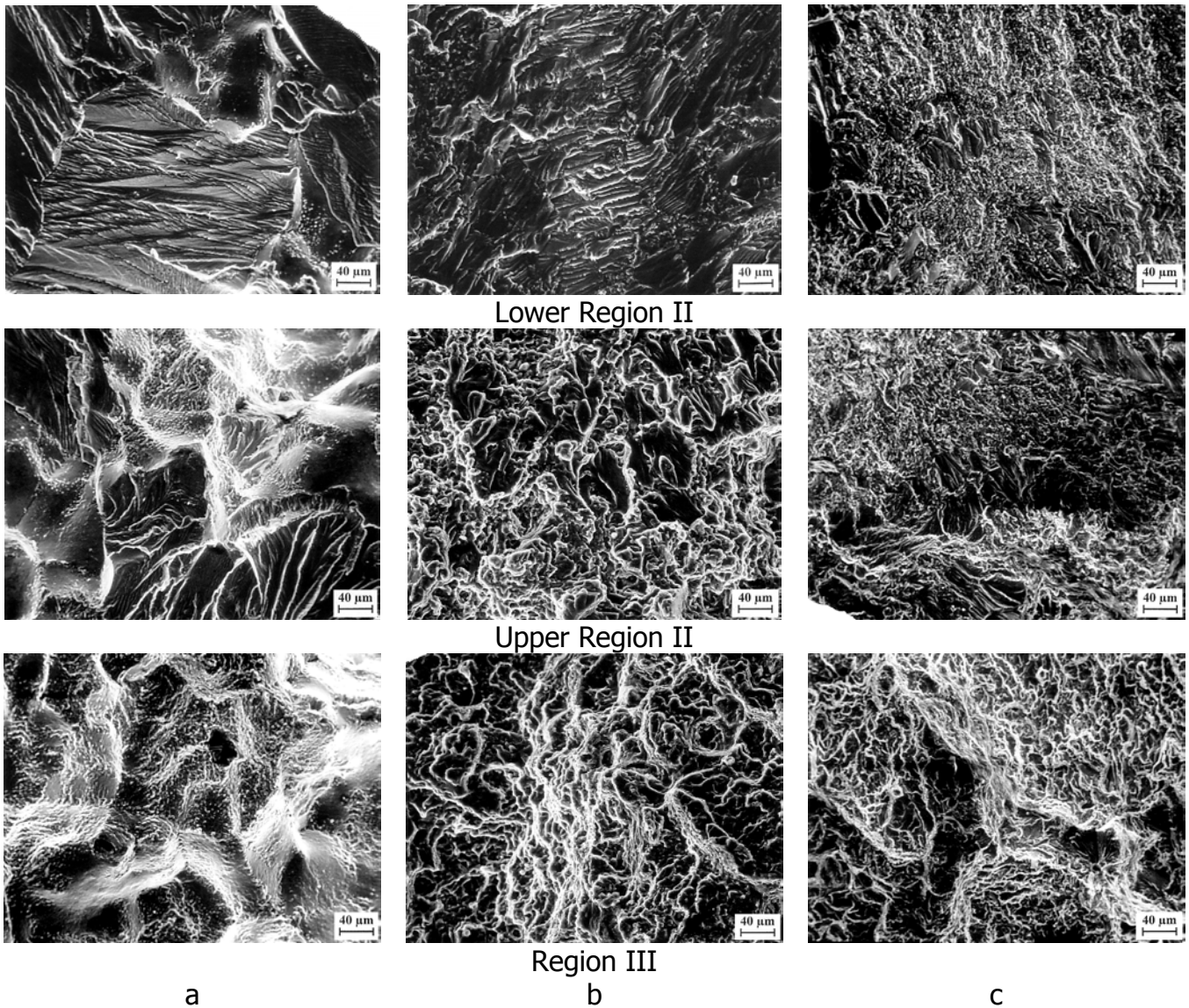


Figure 15. SEM micrographs showing fracture surfaces at different driving forces corresponding to lower and upper Region II and Region III of the FCG curves; (a) 1%Si alloys, (b) 7%Si alloys, and (c) 13%Si alloys.

SUMMARY

Fracture mechanics was developed for brittle materials and therefore, for ductile materials, it only applies accurately up to levels below which the presence of plasticity does not significantly alter the behavior of growing cracks. To correctly characterize fatigue crack growth behavior of such materials, especially when the presence of plastic zone ahead of the crack tip is responsible for gradual increases in stress intensity factor ranges, elastic/plastic fracture mechanics methods need to be adopted.

Two methods to account for plasticity/tearing effects in Al-Si-Mg alloys with different degrees of ductility and residual stress were used and validated against static fracture toughness results.

The first method is based on Irwin's approach, and it only corrects for plasticity effects by adding plastic zone radius to the experimentally measured crack length, and re-evaluating stress intensity factor ranges accordingly. A new method to calculate plastic zone size under combined plane strain and plane stress conditions was developed and used to compute effective crack lengths. Even though this method is convenient, the absence of cumulative plasticity considerations it makes it increasingly inaccurate when severe plasticity occurs. Regardless of the degree of damage created in prior loading cycles, the corrected stress intensity factor ranges at current loading cycles are always calculated only by adding current plastic zone radii. An additional inconvenience of this method comes from the lack of means to capture tearing effects leading to lower fracture toughness compared to the real static fracture toughness of the material.

It is known that, as plasticity increases, the super-imposed effects of tearing on the fatigue crack growth response are unavoidable. Therefore, another method was developed to include both plasticity and tearing damage. This method appropriately characterizes the behavior of high ductility materials at high ΔK levels, and also provides the real fracture toughness of the material without the need of additional static fracture toughness testing. For all materials in this study, the fracture toughness computed from this method is remarkably similar to the limiting, upper bound static fracture toughness despite the original differences in ductility or residual stress. This method can be used to determine the actual fatigue crack growth behavior as well as the upper bound fracture toughness of the material.

A partition of the two effects, plasticity and tearing, was also addressed. It was observed that a separation of the two curves, one representing plasticity (plastic zone crack length corrected method) and the second combined plasticity/tearing

effects (cyclic J-analysis) occurred at ΔK_{JIC} . The coincidence of the two curves below ΔK_{JIC} is an indication that both methods account similarly for plasticity effects, and implicitly that plasticity damage is not severe enough to invalidate Irwin's approach. Remembering that J_{IC} represents a lower bound fracture toughness beyond which tearing occurs, it also becomes evident that cyclic J-analysis captures the additional tearing effects at ΔK higher than ΔK_{JIC} . Therefore, the cumulative cyclic J-analysis is recommended for elastic/plastic assessments of fatigue crack growth behavior, as well as upper bound fracture toughness estimation from fatigue crack growth test data.

ACKNOWLEDGEMENTS

The authors express their gratitude to Mr. Keith Donald of Fracture Technology Associates for his valuable insight of elastic/plastic fracture mechanics concepts.

NOMENCLATURE

da/dN	= crack growth rate
E, ν	= Young's modulus, Poisson's ratio
$\sigma_{YS}, \sigma_{UTS}, \sigma_{flow}$	= yield strength, ultimate tensile stress, flow stress
R	= stress ratio
W, L, B	= width (measured from load line), total width, and thickness of the compact tension specimens
$a, a_{(i)}$	= crack length, current crack length
a_{phy}, a_{eff}	= physically measured and plastic zone corrected crack length
$r_p, r_{p(6\pi)}, r_{p(2\pi)}, r_{p(combo)}$	= plastic zone radius under, plane strain, plane stress, and combined plane strain-plane stress conditions
n, m	= degree of plane stress and plane stress coefficients
θ	= plastic zone variation angle
$b, b_{(i)}$	= unbroken ligament ($W-a$), unbroken ligament at $a_{(i)}$
$A_{el}, A_{pl}=A_{pl+tearing}$ and $A_{pl(i)}, A_{tot}$	= elastic, plastic/tearing and current plastic/tearing, total areas under load versus load-line displacement records
$V_{(i)}=V_{(i)-corr}, V_{(i)-exp}$	= clip gage opening displacement measured at the load-line and front-face respectively
$V_{el(i)}=V_{el(i)-corr}, V_{el(i)-exp}$	= elastic components of the clip gage opening displacement measured at the load-line and front-face respectively
$V_{pl(i)}=V_{pl(i)-corr}, V_{pl(i)-exp}$	= plastic components of the clip gage opening displacement measured at the load-line and front-face respectively
$P, \Delta P, P_{min}, P_{max}$	= load, load range, minimum, and maximum load (index (i) represents current loads)
$C, C_{(i)}$	= general compliance and current compliance

CF	= correction factor
RC	= rotation center
PR	= plastic rotation factor
γ	= ratio of the total specimen width, L , to load-line specimen width, W
$K, J, (\Delta K, \Delta J)$	= linear elastic and cyclic elastic/plastic stress intensity factors (stress intensity factor ranges)
$\Delta K = \Delta K_{el}$	= elastic stress intensity factor range
$\Delta K_{eff} = \Delta K_{pl}$	= plastic zone radius corrected stress intensity factor range
$\Delta K_J = \Delta K_{tot}$	= cyclic elastic/plastic stress intensity factor range
$= \Delta K_{pl+tearing}$	= limiting, upper bound elastic/plastic fracture toughness range calculated from J_{max}
ΔK_{FT}	= limiting, upper bound elastic/plastic fracture toughness range calculated from J_{IC}
ΔK_{JIC}	= lower bound elastic/plastic fracture toughness range calculated from J_{IC}
J_{max} and J_{IC}	= elastic/plastic upper and lower bound fracture toughness
K_{max}	= maximum elastic stress intensity factor
K_{Jmax}	= maximum elastic/plastic stress intensity factor calculated from J_{max}
J_{el}, J_{pl}	= elastic and plastic components of J ($J=J_{el}+J_{pl}$)
LRS	= low residual stress
HRS	= high residual stress

REFERENCES

- [1]. A.A. Griffith: Philos. Trans. R. Soc. London, Vol. 221A, 1920, pp. 163-198 (This paper has been republished with additional comments in Trans. ASM, Vol. 61, 1968, pp. 871-906).
- [2]. E. Orowan: Fatigue and Fracture of Metals, Reports on Progress in Physics, Vol. XII, 1948, pp. 185-232.
- [3]. G.R. Irwin: Fracturing of Metals, ASM, Cleveland, OH 1948, pp. 147-166.
- [4]. G.R. Irwin: Sagamore Research Conference Proceedings, Vol. 2, 1956, pp. 289-305.
- [5]. H.M. Westergaard: Journal of Applied Mechanics, Vol. 6, 1939, pp. 49-53.
- [6]. G.R. Irwin: Journal of Applied Mechanics, Vol. 24, 1957, pp. 361-364.
- [7]. P.C. Paris, M.P. Gomez, and W.P. Anderson: The Trend in Engineering, Vol. 13, 1961, pp. 9-14.
- [8]. P.C. Paris and G.C. Sih: in Fracture Toughness Testing and Its Applications, ASTM STP 381, American Society for Testing and Materials, 1965, pp. 30-83.
- [9]. W.F. Brown Jr. and J.E. Srawley: Plane Strain Crack Toughness Testing of High Strength Metallic Materials, ASTM STP 410, American Society for Testing and Materials, 1966.
- [10]. P.C. Paris: in Fatigue – An Interdisciplinary Approach, Syracuse University Press, Syracuse, NY, 1964, pp. 107-127.

- [11]. G.R. Irwin: Sagamore Research Conference Proceedings, Vol. 4, 1961.
- [12]. D.S. Dugdale: Journal of the Mechanics and Physics of Solids, Vol. 8, pp. 100-104.
- [13]. A.A. Wells: Proceedings of the Crack Propagation Symposium, Vol. 1, Paper 84, Cranfield, UK, 1961.
- [14]. J.R. Rice: Journal of Applied Mechanics, Vol. 35, 1968, pp. 379-386.
- [15]. J.A. Begley and J.D. Landes: in Fracture Toughness, Proceedings of the 1971 National Symposium on Fracture Mechanics, Part II, ASTM STP 514, American Society for Testing and Materials, 1972, pp. 1-20.
- [16]. J.D. Landes and J.A. Begley: in Fracture Analysis, Proceedings of the 1973 National Symposium on Fracture Mechanics, Part II, ASTM STP 560, American Society for Testing and Materials, 1974, pp. 170-186.
- [17]. G.R. Yoder and C.A. Griffis: " J integral and the Initiation of Crack Extension in a Titanium Alloy", NRL Report 7662, Naval Research Laboratory, 1974
- [18]. C.A. Griffis and G.R. Yoder: "Application of the J integral to Crack Initiation in a 2024-T351 Aluminum Alloy", NRL Report 7676, Naval Research Laboratory, 1974.
- [19]. C.F. Shih and J.W. Hutchinson: Journal of Engineering Materials and Technology, Vol. 98, 1976, pp. 289-295.
- [20]. N.E. Dowling and J.A. Begley: in Mechanics of Crack Growth, ASTM STP 590, American Society for Testing and Materials, 1976, pp. 82-103.
- [21]. J.R. Rice, P.C. Paris, and J.G. Merkle: in Progress in Flaw Growth and Fracture Toughness Testing, ASTM STP 536, American Society for Testing and Materials, 1973, pp. 231-245.
- [22]. J.G. Merkle and H.T. Corten: Journal of Pressure Vessel Technology, Transactions of the ASME, Vol. 96, 1974, pp.286-292.
- [23]. J.D. Landes, H. Walker, and G.A. Clarke: in Elastic-Plastic Fracture, ASTM STP 668, American Society for Testing and Materials, 1979, pp. 266-287.
- [24]. W.R. Brose and N.E. Dowling: in Elastic-Plastic Fracture, ASTM STP 668, American Society for Testing and Materials, 1979, pp. 720-735.
- [25]. D.F. Mowbray: in Elastic-Plastic Fracture, ASTM STP 668, American Society for Testing and Materials, 1979, pp. 736-752.
- [26]. N.E. Dowling: in Cyclic Stress-Strain and Plastic Deformation Aspects of Fatigue Crack Growth, ASTM STP 637, American Society for Testing and Materials, 1977, pp. 97-121.
- [27]. S.-Z. Wang, Z. Yang, and Mo-Kuang Kang: Engineering Fracture Mechanics, Vol. 18, No. 4, 1983, pp. 895-902.
- [28]. M.H. El-Haddad and B. Mukherjee: in Elastic-Plastic Fracture: Second Symposium, Volume II-Fracture Resistance Curves and Engineering Applications, ASTM STP 803, American Society for Testing and Materials, 1983, pp. II-689-II-707.
- [29]. K. Tanaka, T. Hoshide, and M. Nakata: in Elastic-Plastic Fracture: Second Symposium, Volume II-Fracture Resistance Curves and Engineering

- Applications, ASTM STP 803, American Society for Testing and Materials, 1983, pp. II-708-II-722.
- [30]. M. Jolles: in Fracture Mechanics, Sixteenth Symposium, ASTM STP 868, American Society for Testing and Materials, 1985, pp. 381-391.
- [31]. Y. Lambert, P. Saillard, and C. Bathias: in Fracture Mechanics, Nineteenth Symposium, ASTM STP 969, American Society for Testing and Materials, 1988, pp. 318-329.
- [32]. L. Banks-Sills and Y. Volpert: Engineering Fracture Mechanics, Vol. 40, No. 2, 1991, pp. 355-370.
- [33]. ASTM Standard E1820, Standard Test Method for Measurement of Fracture Toughness, Annual Book of ASTM Standards, Vol. 03.01, 2000.
- [34]. D.A. Lados and D. Apelian: "Quenching Modes and Residual Stress Levels in Cast Al-Si-Mg Alloys – Mechanisms and Effects on Static and Dynamic Properties", to be submitted to Metall. Mater. Trans. A.
- [35]. ASTM Standard E647, Standard Test Method for Measurement of Fatigue Crack Growth Rates, Annual Book of ASTM Standards, Vol. 03.01, 2000.
- [36]. F.A. McClintock and G.R. Irwin: in Symposium on Fracture Toughness Testing and its Applications, ASTM STP 381, American Society for Testing and Materials, 1964, pp. 84-113.
- [37]. G.T. Hahn and A.R. Rosenfield: Acta Met., Vol. 13, 1965, pp. 293.
- [38]. B. Skallerud and Z.L. Zhang: Fatigue Fract. Engng Mater. Struct., Vol. 23, 2001, pp. 81-86.
- [39]. D.A. Lados and D. Apelian: "Operating Fatigue Crack Growth Mechanisms at the Microstructure Level in Al-Si-Mg Cast Components", to be submitted to Acta Met.

Chapter 5

Operating Fatigue Crack Growth Mechanisms at the Microstructure Level in Al-Si-Mg Cast Components

D. A. Lados and D. Apelian
Worcester Polytechnic Institute, Worcester, MA, USA

ABSTRACT

Due to the increasing use of cyclically loaded cast aluminum components in automotive and aerospace applications, fatigue and fatigue crack growth characteristics of aluminum castings have become of great interest. However, despite the extensive research efforts dedicated to this topic, a fundamental and mechanistic understanding of the behavior of these alloys when subjected to dynamic loading is still lacking. This fundamental research study investigated the active mechanisms at the microstructure level during dynamic loading and failure of conventional and SSM hypoeutectic and eutectic Al-Si-Mg alloys by means of a microstructural deconstruction/reconstruction model. Five model alloys were used to isolate the contribution of each characteristic microstructural feature to fatigue resistance. The roles of the major constituent phases, α -Al dendrites, Al/Si eutectic phase, and Mg-Si strengthening precipitates, were mechanistically investigated to relate microstructure to near-threshold crack growth (ΔK_{th}) and crack propagation regimes (Paris Region II and Region III) for alloys of different Si composition/morphology, grain size level, dendrite arm spacing, and heat treatment. Moreover, the importance of residual stress-microstructure interactions, commonly overlooked by researchers in the field, was also clearly defined and explained from microstructure point of view.

The crack growth threshold ranking of the materials investigated is attributed to closure phenomena, mainly caused by residual stress and microstructure related roughness characteristics of the alloy. With increasing stress intensity, in Regions II and III, the crack path evolves from rather flat to highly torturous. This change in crack appearance was associated with a change in propagation mechanisms from the constituents that lie directly ahead of the crack (which appears as an advance predominantly through primary α -Al) to exclusively Al-Si eutectic islands. These observations were directly correlated to the amount of damaged material ahead of the crack. A relationship between the plastic zone size ahead of the crack tip and the type and amount of microstructural features enveloped in it was successfully used to explain the change in mechanisms as well as extrapolate the knowledge to other structures. The fatigue crack growth tests were conducted on compact tension specimens under constant load ratio at ambient conditions.

Keywords: Hypoeutectic and eutectic cast Al-Si-Mg alloys; Microstructure; Heat treatment; Fatigue crack propagation mechanisms; Residual stress and microstructure (roughness) induced closure; Plastic zone.

I. INTRODUCTION AND BACKGROUND

Fatigue properties of cast aluminum alloys have become some of the most challenging and researched topics in recent years, considering the increasing use of these alloys in critical automotive and aerospace applications. Significant efforts have been geared towards determining the effects of casting defects on the fatigue response of aluminum alloys, as well as finding technically and economically feasible methods to alleviate them. There is a hierarchy among the factors that control fatigue behavior [1], and when one dominating factor (defect) is reduced under certain levels, the next mechanism becomes active. It is now well understood that, when present, casting defects such as porosity (shrinkage and gas), oxides, and other types of inclusions dominate fatigue behavior, and the more and larger these defects are, the lower the fatigue performance. Under such circumstances, interdendritic shrinkage pores [2-6], gas pores of different amount, size, and distribution [5-12], old and new oxide films or inclusions [3,4,9] act as crack initiators especially when located at the surface or near the surface of the specimens. Subsequently, these defects also favor the crack advance resulting in an overall lower performance of the component.

Understanding the negative impact of these defects on the fatigue properties, all modern casting technologies are designed to reduce the amount and size of casting defects especially in the critically loaded areas by appropriate liquid metal practices, sufficient degassing and additional chilling where required, proper filtering, filling, and feeding. Hot isostatic pressing (HIP-ing) is also an available practice when the elimination of shrinkage and gas porosity is needed and no changes in the solidification process are intended. Squeeze casting and semi-solid processing are also suitable methods to decrease the defect levels when differences in microstructure, compared to conventional casting, are acceptable. As the defect levels are decreased, the intrinsic microstructural features of the alloy begin to dictate the dynamic loading behavior of the component. In these conditions, fatigue crack initiation from pre-existing casting defects is replaced by initiation from either persistent slip bands in the dendrite cells [3,6] or at the eutectic Si particles [10,11,12]. As a result, predictive models based on the amount, size, and morphology of casting defects are less accurate. Therefore, a good understanding of the mechanisms at the microstructure scale in terms of both initiation and propagation becomes imperative. The small scale microstructural features, such as SDAS (in relation to the strength of the α -Al matrix as a result of heat treatment) [13-18], and Si particles morphology and

distribution, as well as Si particle/matrix interface strength [17,19,20] play a critical role in the fatigue and fatigue crack growth behavior of cast Al-Si alloys.

In the initial stages of crack formation and slow propagation mode, roughness-induced crack closure dominates the material behavior [21-25]. The closure level is a direct function of the second phase microstructural constituents that dictate the level of crack deflection and resulting roughness respectively. The presence of residual stress has a considerable effect on both closure level and closure mechanisms [26]; high residual stresses mask the effect of microstructure, and roughness induced closure becomes of secondary importance under such circumstances.

This work investigated the operating crack growth mechanisms from near threshold regime to catastrophic failure. Changes in crack growth mechanisms are explained at the microstructure level by the increase in the damaged zone ahead of the crack tip with the increase in crack driving force and crack length. The type and amount of damaged microstructural features within the plastic zone are analyzed and used to explain crack's path selection at different stages during the fatigue crack growth process. Cast Al-Si-Mg alloys of various grain size levels, Si morphology, matrix strength, as well as different microstructures (conventional casting and SSM) were used to understand and establish the mechanisms active at the microstructure level at different stages during fatigue crack growth and fracture. Heat treatment changes the matrix strength without changing the solidification process, and therefore it was used to investigate the effect of matrix properties on the fatigue crack growth mechanisms.

II. EXPERIMENTAL PROCEDURE

II.A. Alloys, casting procedure, and heat treating conditions

Al-Si-Mg alloys of fixed Mg content (0.45%) and three Si levels 1, 7, and 13% were investigated¹. Si levels were selected such that each microstructural constituent specific to this class of alloys was individually represented, i.e. primary α -Al dendritic structure in 1%Si alloy and Al/Si eutectic phase in 13%Si alloys as well as hypoeutectic alloys represented in this study by the 7%Si composition (hybrid alloys resembling the microstructure of commercial A356/357 alloys where the two phases coexist). High purity alloys were used, and all the other elements besides Si, Mg, and Fe were kept at low levels (<0.002%). Fe concentration was <0.02%. The eutectic Si in 7 and 13%Si alloys was studied in both unmodified (UM) and Sr-modified (M) conditions. The eutectic Si was modified using a commercial Al-10%Sr master alloy, and appropriate additions were made for each Si content (0.018-0.021%Sr for the

¹ All compositions are given in weight%.

7%Si alloys, and 0.024-0.027%Sr for the 13%Si alloys). The average size of the Si particles and the shape factors for each condition after heat treatment are given in Table 1. The distance between consecutive eutectic Si particles is $\sim 2-4 \mu\text{m}$ (depending on the degree of modification), between interdendritic eutectic regions $\sim 25 \mu\text{m}$ (similar to the SDAS or cell size of the material), and the mean free path between three-grain junction eutectic zones is in the 75-200 μm range. In addition to the above five alloy systems, a sixth alloy was produced using the "slurry on demand" semi-solid processing (SSM) method. The alloy was brought to the semi-solid temperature range and cast into a die under high pressure. The composition of the SSM samples was similar to the conventionally cast modified A356 alloy, and the Si morphology after T61 heat treat is reported in Table 1.

Table 1. Average Si particle size and shape factor for the modified and unmodified alloys

	Alloy systems examined					
	7%Si-UM (A356-UM)	7%Si-M (A356-M)	7%Si-M (SSM-M)		13%Si-UM (Eutectic-UM)	13%Si-M (Eutectic-M)
			T61	T5		
Si avg. particle size (μm)	2.77	2.19	2.01	1.31	2.94	2.05
Si particle shape factor ^a	1.41	1.21	1.17	2.01	1.86	1.19

^a Shape factor was calculated as: shape factor = perimeter²/(4 \cdot π \cdot area).

All conventionally cast alloys were grain refined using additions of a commercial Al-5%Ti-1%B master alloy. To achieve the same grain size irrespective of alloy, the amount of grain refiner was adjusted depending on the Si level of the alloy, as well as the extent of modification of the eutectic Si. Three grain size levels were studied, and the grain refiner level for each alloy and condition is given in Table 2. The majority of the studies however, were conducted on samples with grain size in the 280-320 μm range.

Table 2. Titanium levels (in wt%) corresponding to three grain sizes for all alloys in unmodified and modified conditions

Grain size (μm)	Alloy systems examined				
	1%Si	7%Si-UM ^b (A356-UM)	13%Si-UM (Eutectic-UM)	7%Si-M ^c (A356-M)	13%Si-M (Eutectic-M)
180-220	0.0080-0.0090	0.080-0.090	---	0.070-0.080	0.27-0.33
280-320	0.0065-0.0075	0.035-0.045	0.25-0.30	0.025-0.035	0.20-0.25
~ 520	---	0.0007-0.0009	---	0.0004-0.0006	---

^b UM = unmodified eutectic Si, ^c M = Sr-modified eutectic Si, ^d --- = case not included in the study.

For the fatigue growth studies, compact tension (CT) specimens were prepared using a specifically designed sand mold containing central top and bottom gray cast iron chills to insure that the desired SDAS was attained throughout the region of interest. By controlling the freezing rate, the SDAS of all samples were kept in the range of 20-30 μm . The castings from which the CT samples were machined had the following dimensions: 4.4in x 4.4in x 0.8in (112mm x 112mm x 20.5mm).

Subsequently, the cast parts were heat treated. The solution treatment stage is followed by a quenching procedure from a solutionizing temperature of around 1000°F (538°C). During quenching, residual stresses can be introduced in the samples especially when agitated room temperature water is used as a quenching medium. The surfaces of the samples cool faster than their interior and temperature gradients are created, causing different regions of the sample to contract at different rates. During the final stages of cooling these gradients disappear, but their presence causes an uneven distribution of residual stresses in the part. These residual stresses are compressive on the surface of the sample and tensile in the center. After quenching, the tensile and compressive stresses are balanced and the total net stress for the whole sample equals zero. Several heat treat procedures were applied: two T61 treatments (uphill quench and room temperature), T4, and T5. These are detailed below.

The two T61 heat treat procedures resulted in samples with similar mechanical properties, a consistent micro-hardness of the α -Al matrix in all the alloys (either primary or eutectic α), and distinctly different eutectic Si morphologies between unmodified and modified alloys. However, the residual stress level induced in the samples by these two heat treatments was significantly different.

The first T61 heat treatment applied, also called "uphill quench", consists of the following steps:

- Solution treatment for 1.5 hrs at 1000°F (538°C);
- Boiling water quench for 15 min;
- Liquid N₂ immersion for 30 min;
- Boiling water reverse quench for 15 min;
- Natural age for 12 hrs;
- Artificial age for 12 hrs at 311°F (155°C).

The role of liquid nitrogen-boiling water reverse quench is to eliminate residual stresses from the samples [27], in order to delineate the superimposed effects of residual stress on crack growth. The concept of an up-hill heat treatment is based on the rationale that by developing thermal gradients (residual stresses) of an opposite nature one can counteract and cancel the quenching stresses. The residual stress level on the CT samples after the uphill quench was found to be near zero.

The second procedure applied is the room temperature T61 heat treatment (referred to as T61-RT henceforth); it consisted of the following steps:

- Solution treatment for 1.5 hrs at 1000°F (538°C);
- Room temperature water quench;
- Natural age for 12 hrs;
- Artificial age for 12 hrs at 311°F (155°C).

The effect of matrix strength on fatigue crack growth was investigated by using a T4 heat treatment consisting of solutionizing followed by a natural age of minimum three weeks. The absence of artificial (high temperature) aging prevented the development of Mg-Si strengthening precipitates and samples with lower yield strengths and higher ductility were obtained (Table 3).

The T4 heat treatment procedure consisted of the following steps:

- Solution treatment for 1.5 hrs at 1000°F (538°C);
- Boiling water quench for 15 min;
- Liquid N₂ immersion for 30 min;
- Boiling water reverse quench for 15 min;
- Natural age at room temperature.

Sample transfer time from one medium to another was less than two seconds for both the regular quench and the reverse (uphill) quench.

Table 3. Ultimate tensile strength (UTS), yield strength (YS), and elongation (e%) for unmodified and Sr-modified 7%Si alloys in T61 and T4 heat treating conditions tested at room temperature per ASTM B557

Alloy	UTS		YS		Total elongation (%)
	US (ksi)	SI (MPa)	US (ksi)	SI (MPa)	
1%Si-T61	40.6	280.2	29.6	204.2	13.93
7%Si-UM ^a -T61	45.1	311.3	33.9	233.7	7.34
7%Si-M ^b -T61	45.2	312.0	35.0	241.0	6.08
7%Si-UM-T4	38.5	265.8	20.1	138.7	11.95
7%Si-M-T4	38.3	264.5	20.2	139.4	14.69
13%Si-UM-T61	51.5	355.0	38.3	264.1	7.47
13%Si-M-T61	49.7	342.7	39.0	269.1	7.33

Besides the T61 uphill quench, the SSM samples were additionally subjected to a T5 heat treatment consisting of:

- Artificial age for 8 hrs at 437°F (225°C).

The resultant microstructures of the alloys subsequent to heat treatment are shown in Figure 1. Porosity level in all alloys was kept very low (<0.005%) such that no porosity significantly interferes with the crack advance.

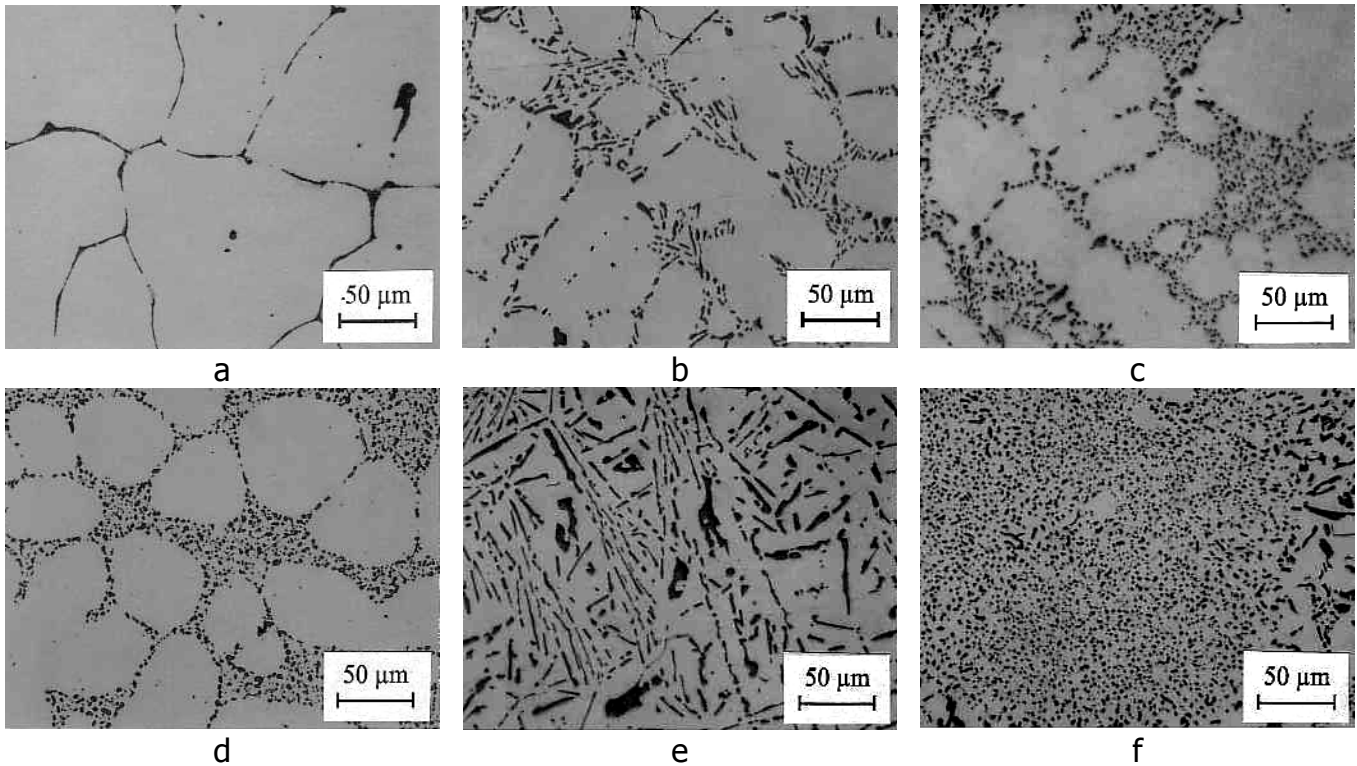


Figure 1. Alloy microstructures after heat treatment (etched with 1%HF for 10-15 seconds): 1%Si (a); 7%Si-UM (b); 7%Si-M (c); 7%Si-SSM-M (d); 13%Si-UM (e); 13%Si-M (f).

II.B. CT samples preparation and testing

II.B.1. CT specimens

The heat treated castings were machined to the test dimensions, 3.75 in x 3.6 in x 0.4 in (95 mm x 91 mm x 10 mm). An end mill was used for the edges and a fly cutter was used for the reduction in thickness. A 0.006 in (0.15 mm) diameter wire was used for the wire EDM (electric discharge machining) notch. The notch length was 1.5 in (38 mm) measured from the front face of the sample, and 0.75 in (19 mm) measured from the pinholes. The specimens complied with ASTM E647 [28].

II.B.2. Fatigue crack growth (FCG) testing

The compact tension specimens were tested according to ASTM E647 [28] using a non-visual automated computer controlled method. The tests were conducted at room temperature (75°F) in air with a relative humidity 40-50%. The specimens were tested under K-control, first under a decreasing crack driving force range (Region I) to evaluate the thresholds, and then under increasing crack driving force range (Regions II and III to fracture). Above 10^{-4}

inches/cycle, the test was continued using a more shallow K-gradient to obtain the steeper Region III data. The upper limit of the crack driving force was referred to as the "pseudo" fracture toughness of the materials because the crack growth specimens did not meet the dimensional requirements for plane strain fracture toughness. A compliance measurement technique was used to monitor the crack advance and the frequency was set to 25 Hz (except in Region III where it was decreased to as low as 0.1 Hz to capture sufficient data points). All the samples were tested under a constant stress ratio, $R=0.1$.

III. RESULTS AND DISCUSSION

As opposed to safe-life design, damage-tolerant design was developed for components that contain initial flaws and their propagation life allows timely replacement of the damaged component, and when inspection is possible, provides a good indication of how many cycles are still left in the lifetime of the component. This approach can also be used for components that are neither regularly inspected nor replaced during service when the design predicted life far exceeds the desired operating life of the component. In this light, the mechanisms active at different stages during the early crack advance (stage I corresponding to near-threshold regime), the subsequent propagation (stage II) and fast fracture mode (stage III) are discussed with emphasis on their relationship with the microstructure characteristics of the alloys. First, the near threshold regime behavior is explained in terms of closure phenomena. Next, the changes in mechanisms observed in Paris region are explained in terms of plastic zone evolution with increasing crack driving force, ΔK , and how the extent of the plastic zone affects the crack path through the damaged microstructure. A thorough understanding of the microstructure impact on the rate of crack propagation, and the ability to delineate the stages at which crack enters the fast fracture mode, allows timely replacement of components that reached a critical level and also provide useful design tools to prevent premature failures for given applications.

III.A. Crack evolution mechanisms in the near threshold regime

There are two life regimes of interest in engineering applications, and each of them requires understanding of different mechanisms and different stages in the crack evolution. In low cycle fatigue applications, 10^4 cycles or less, life can be achieved primarily from the propagation life of a crack; crack initiation and the slow growth regime are of secondary importance. In such cases material toughness plays an important role, and it is the decisive selection criterion. However, for high cycle fatigue applications, when the components must endure more than 10^7 cycles, the near threshold regime becomes of great importance considering that most of the life is spent in the near threshold region of the crack growth. Therefore, a good understanding of the near threshold behavior is

imperative for appropriate design and material selection, especially for high cycle fatigue applications.

Over the years numerous micro-mechanisms have been proposed to describe near-threshold behavior, but no general knowledge exists yet to allow accurate prediction of the dominating mechanism under given circumstances. It is generally accepted that the experimentally measured value of ΔK_{th} from a long crack sample (such as compact tension) is generally higher than a short crack test value for the same stress ratio, R . This is mostly a result of crack closure phenomena that dictate the crack to be closed during the lower part of the fatigue cycle. While closed, the crack transmits compressive stresses across its faces, and thus that part of the loading cycle is assumed to shelter the crack tip from cyclic strain. Various sources of closure have been identified, and were reviewed by Taylor [29]. However, recently several authors tried to explain the values and differences in threshold through other mechanisms than crack closure due to experimentally observed fatigue crack growth even during the part of the loading cycle when the crack was closed. The need for reinterpretation of the physical significance of crack closure was raised, and theories based on no closure or partial closure (rather than total closure) effects were proposed. A single stress intensity factor range (ΔK_{th} , whose interpretation is usually related to crack closure) was found insufficient to explain the effects of stress ratio and the concept of dual-parameter threshold (K_{max} and ΔK_{th}) was introduced. Fatigue mechanisms based on microstructural stress singularities and dislocation generation have been some of the most vigorously debated alternatives to closure, but several other mechanisms were also proposed, most of them being detailed in a recent review by Lawson et al. [30]. Most of the alternatives to closure mechanisms are still inconsistent and somewhat contradictory. Therefore, crack closure remains the most pertinent near-threshold related concept, and an interpretation of the threshold variation in terms of the microstructural features of the material (intrinsic crack closure) is considered of great importance to the physical understanding of this important parameter.

Crack closure represents an interference of the crack's mating faces behind the crack tip that reduces the magnitude of the applied stress intensity factor range. In these conditions, some of the applied force is spent in reopening the interfering faces, thus protecting the crack tip from the potential damage caused by the application of the entire force. Closure can be the result of various causes, such as plasticity, oxide or debris, roughness/microstructure, residual stress, viscous fluid penetration, phase transformation, etc. The first closure mechanism, proposed by Elber [31], was related to the plastic deformation in the crack wake, on the sides of the crack faces, regions that have been prior part of the plastic zone at the crack tip and that are able to induce residual compressive stresses. However, in the absence of overloads this mechanism is very limited in the near-threshold regime, and it is often dominated by other mechanisms.

The most common form of debris is the oxide layer resulting from crack faces fretting, but other corrosion products and foreign particles from the surrounding medium can also contribute. When similar materials, tested under similar environmental conditions are compared, this type of closure is not relevant and it was not analyzed in this study. Depending on the microstructural features of the material, roughness induced closure can play a very significant role, and this aspect of closure will be elaborated on subsequently in this work for alloys with considerably different microstructures. A tortuous crack path gives rise to rough surfaces, and the imperfect mating of these surfaces leads to premature contact during the unloading part of the cycle. Another important source of closure is residual stress. This mechanism was studied extensively and reviewed by Suresh [32, pp. 222-313]. Most residual stress considerations, however, were related to the formation of residual tensile stresses as a result of unloading, particularly in the first cycle. On the other hand, overloading can create regions of compression ahead of the crack tip, leading to effects similar to crack closure and blunting. There is another category of residual stresses, externally induced (such as quenching during heat treatment), that can leave significantly high residual stresses in the material, and its presence can override by far all the other closure mechanisms. This type of residual stress induced closure was investigated in the present study and the results are presented next.

III.A.1 Residual stress induced closure

The room temperature and uphill quench T61 procedures produced samples with high residual stress and virtually zero residual stress respectively. The high and low residual stress distribution in the samples is schematically shown in Figure 2.

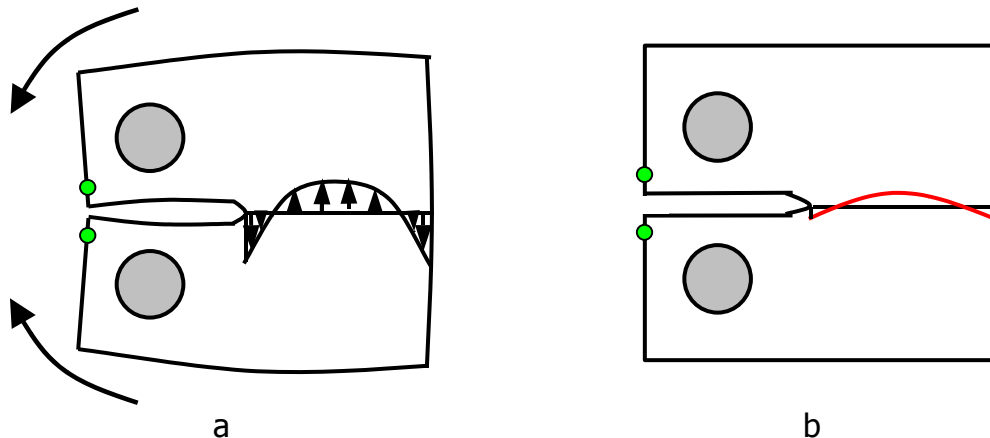


Figure 2. (a) Sample with high residual stress after machining and notch cutting; (b) Sample with low residual stress.

The fatigue crack growth curves for both sets of samples with and without residual stress are presented in Figures 3a and b. Closure mechanisms were

found to play a significant role at low crack growth rates. Closure corrected data were generated based on a method proposed by Bray and Donald [33].

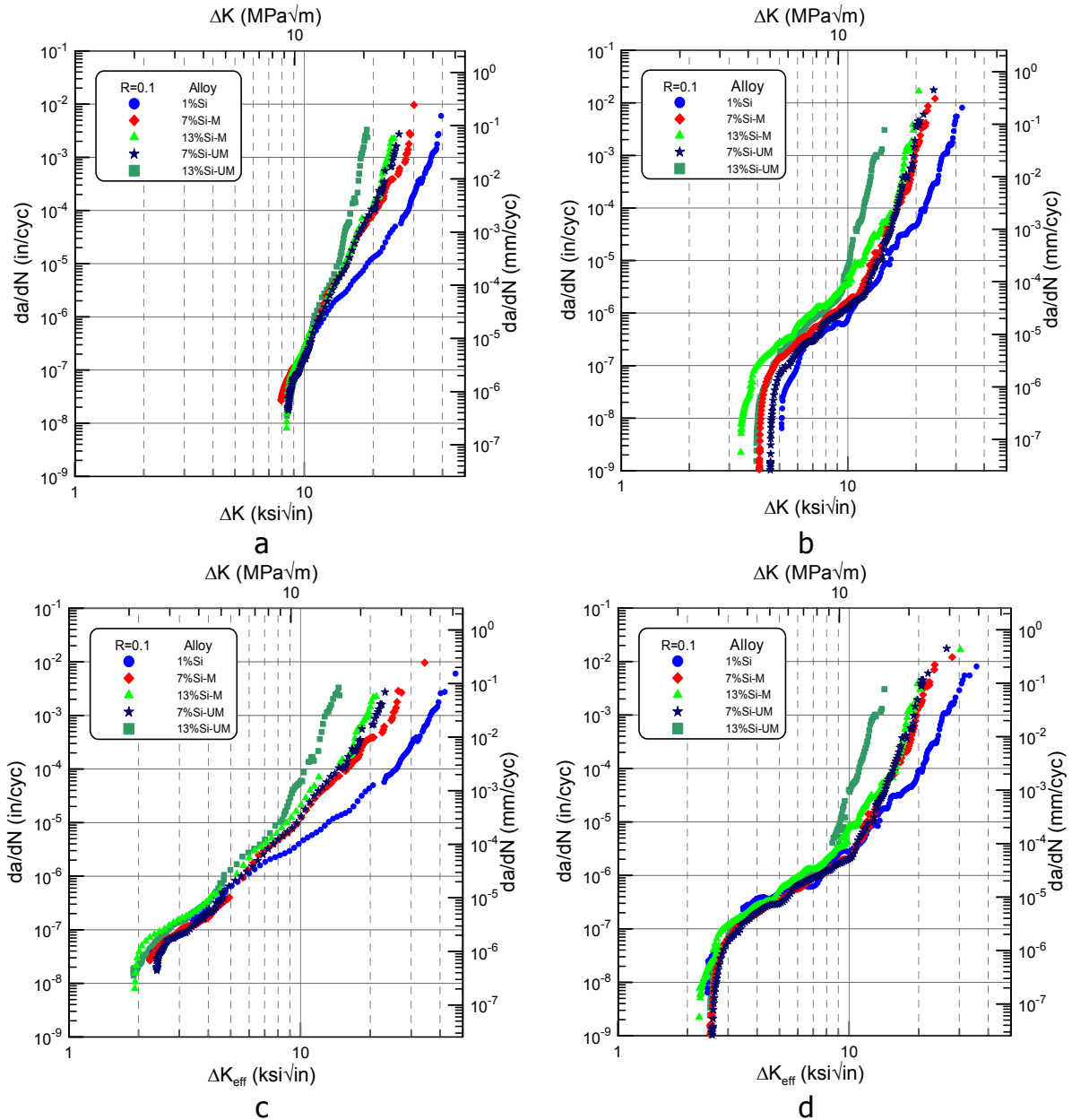


Figure 3. Fatigue crack growth behavior of the studied alloys under (a) high residual stress conditions, (b) no residual stress, (c) high residual stress after closure correction, (d) low residual stress after closure correction.

The coincidence of the data as a result of closure correction, Figures 3c and d, confirmed the idea that the observed differences in threshold between alloys with low and high residual stress as well as between alloys with different microstructures and low residual stress are primarily originated in closure

phenomena. Closure correction provides data similar to those generated for small cracks.

It is important to remember that closure phenomena were observed for cracks as small as 50-300 μm for wrought aluminum alloys [34-38] and Al-Si cast alloys [39]. Therefore, close attention needs to be paid to closure mechanisms, and a good understanding of their impact and relationship with microstructure become necessary.

The tests conducted on room temperature quenched samples with high residual stress were terminated prematurely due to high closure levels and the true thresholds were estimated by extrapolating the experimental data down to 10^{-7} mm/cycle. The uphill quenched set of samples did not have residual stress induced closure, the primary source of closure being due to the characteristic features of the alloys (roughness-microstructure induced closure). A clear indication of the presence of high residual stress is the elevation in threshold values because of the high closure levels created by the compressive residual stresses active at the specimen notch. High closure restricts the applied force that effectively acts on the crack tip (i.e. shelters the crack tip), and therefore higher residual stress samples require greater cyclic forces to exceed threshold and propagate the crack. On the other hand, if the notch is found in a tensile stress field (for example, when a center crack tension specimen is used instead of compact tension specimen) the opposite effect is found. In this case, the threshold is lower compared to the residual stress free threshold, the crack being open at all times, and the crack tip being continuously exposed to the whole applied cyclic load range. More details can be found in Lados and Apelian [26]. Significant compressive residual stresses can cause the measured threshold to double from 3-5 $\text{ksi}\sqrt{\text{in}}$ (3.5-5.5 $\text{MPa}\sqrt{\text{m}}$), values characteristic to this class of cast Al alloys, to 8-9 $\text{ksi}\sqrt{\text{in}}$ (9-10 $\text{MPa}\sqrt{\text{m}}$), as shown in Figure 3. At the same time, the threshold ranking observed in Figure 3b for the residual stress free samples is lost when high residual stresses are present. In this case, even though they are present, the microstructure characteristics of the alloys are not perceptible, and the thresholds are controlled by the dominant residual stresses induced closure mechanisms.

Analysis of the load-displacement records provides information about the closure levels in samples with low and high residual stress, Figure 4. Closure in the low residual stress samples is predominantly caused by roughness while samples with high residual stress have both residual stress- and roughness/microstructure-induced closure. Load-displacement data, however, cannot be used to partition the individual contributions of residual stress and roughness to total closure. Low values of residual stress are not sufficient to overcome the effects of roughness-induced closure active in the vicinity of the crack tip. However, if the residual stress is significant, crack tip can remain open while the

surfaces near the notch are closed with no external force applied (bulge effect). Therefore, the impact of roughness-induced closure is minimized due to the fact that interference is no longer near to the crack tip and the height of the interfering features near the notch have less contribution to the crack closure level. The mechanisms will be explained in section II.A.2.

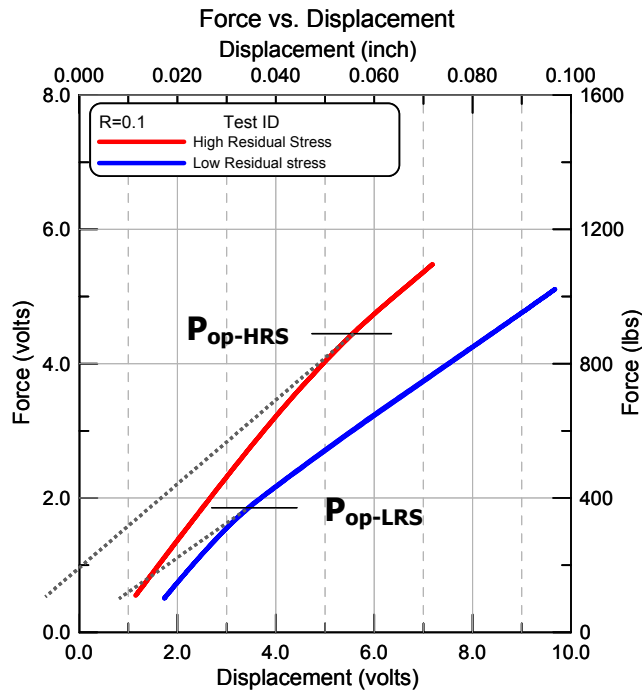


Figure 4. Load displacement records showing the predominant effect of residual stress on crack closure level (left curve) and roughness-microstructure effect on crack closure (right curve). P_{op} is the force needed to fully open the crack.

III.A.2 Microstructure-roughness induced closure

When residual stress is removed from the samples, the contribution of roughness-microstructure induced closure becomes evident, and a threshold ranking as function of Si content is observed, Figure 3b. The higher the Si level, the lower the threshold as seen in Figure 5a for a set of three samples with 1, 7 and 13%Si in unmodified conditions. This behavior can be explained by considering the contribution of Si amount/morphology to the roughness-induced closure level. Near threshold, the fracture path has a crystallographic, faceted appearance characterized by the deflection of the crack when hard eutectic Si particles or grain boundaries are encountered. Crack deflection determines the fracture surface roughness, and thus it affects the fatigue crack growth behavior. Eutectic Si particles deviate the crack (change the planar slip direction and reduce the slip length). Therefore, more frequent crack-Si particles encounters at higher Si levels lead to less variation in the crack path, thus lower overall

roughness, and consequently lower ΔK_{th} , Figure 6. In Figure 6, crack path deflection for alloys of different Si levels is presented for a fixed ΔK level in the near-threshold regime. Roughness induced closure was invoked by other researchers to explain threshold behavior of cast Al alloys [22] and Al alloy composites [21,23,24].

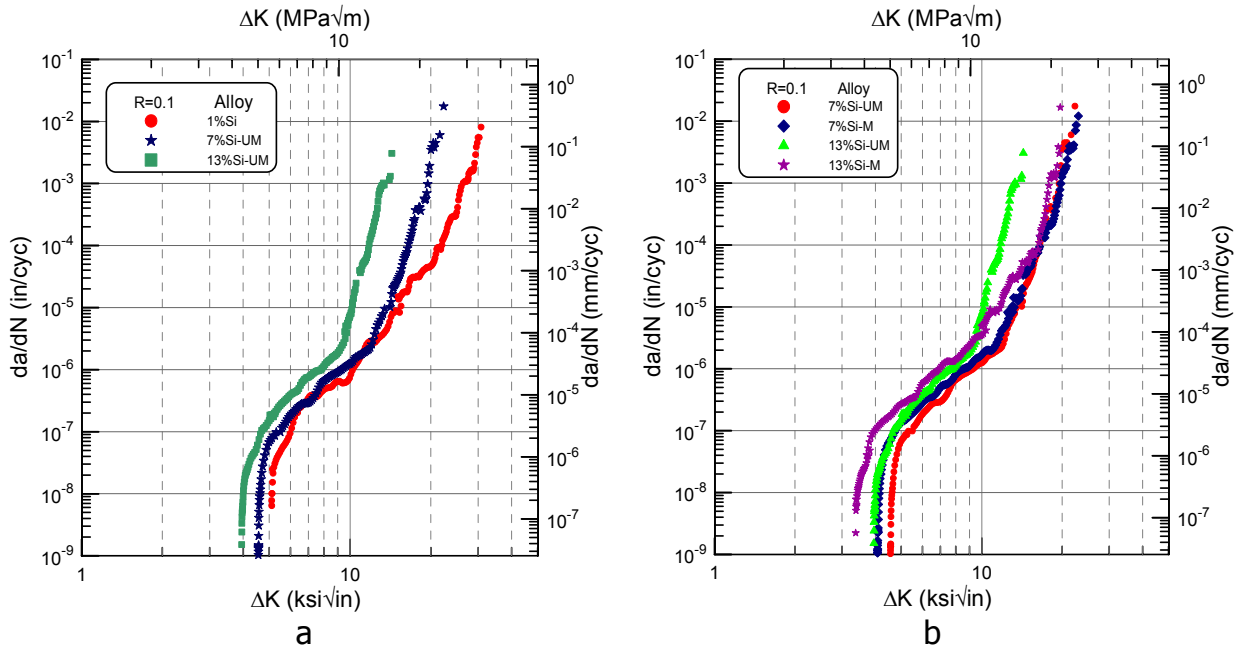


Figure 5. Fatigue crack growth behavior of: alloys with different Si levels, 1, 7, 13% (a), and alloys with unmodified and modified eutectic Si (b).

Unmodified alloys have higher thresholds than modified alloys for both 7 and 13%Si, Figure 5b. The higher thresholds, ΔK_{th} , enhance high cycle fatigue properties. This behavior can be explained by considering the impact of Si morphology on the crack advance mode. For the same vol.% Si, the Si particles are coarser (Table 1) and more distantly spaced in the unmodified alloys (especially in the 13%Si alloys), and as a result, in these alloys, the crack may not always be deflected by Si particles at the edge of the dendrites. Also, if the crack either debonds or passes through the Si particles, larger deflection is created in the unmodified alloys compared to the modified alloys. Larger deflections in the unmodified alloys generate rougher surfaces, more roughness induced crack closure, and thus higher thresholds, ΔK_{th} . Similar differences between unmodified and modified alloys in the near-threshold regime were reported by others [15] with the explanation that plate-like Si morphology increases the interference with dislocation motion, decreases the mean free path of dislocations, which results in higher threshold.

In low Si alloys (1%Si with no eutectic Si), the crack advances by material separation on certain slip systems until an obstacle such as an imperfection in

the crystal structure, a grain boundary, etc. causes an orientation change, Figure 6a. They exhibit extended planar slip behavior that increases crack surface interference resulting in higher thresholds.

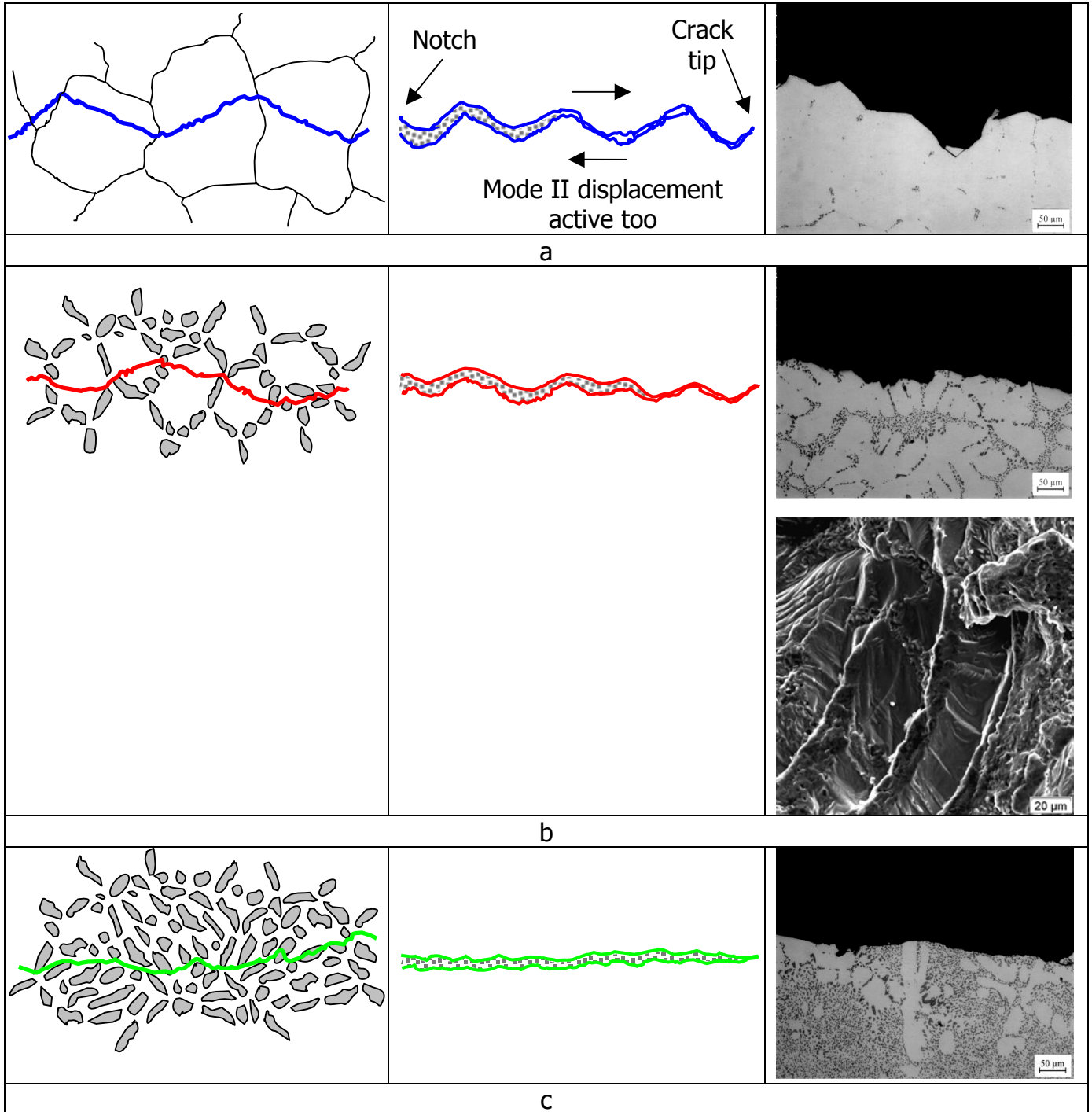


Figure 6. Crack path deflection and roughness induced closure in Al-Si-Mg alloys with: 1%Si (a), 7%Si (fracture path side view and fracture surface view) (b), and 13%Si (c); mode II displacement is also present.

The proposed mechanisms were extrapolated to explain the threshold behavior of A356 alloys with larger SDAS, characterized by larger α -Al dendritic regions, i.e. larger distances between consecutive Si regions, larger Si particles and larger eutectic regions, Figure 7a. The results are qualitative since samples with larger SDAS have not been experimentally tested.

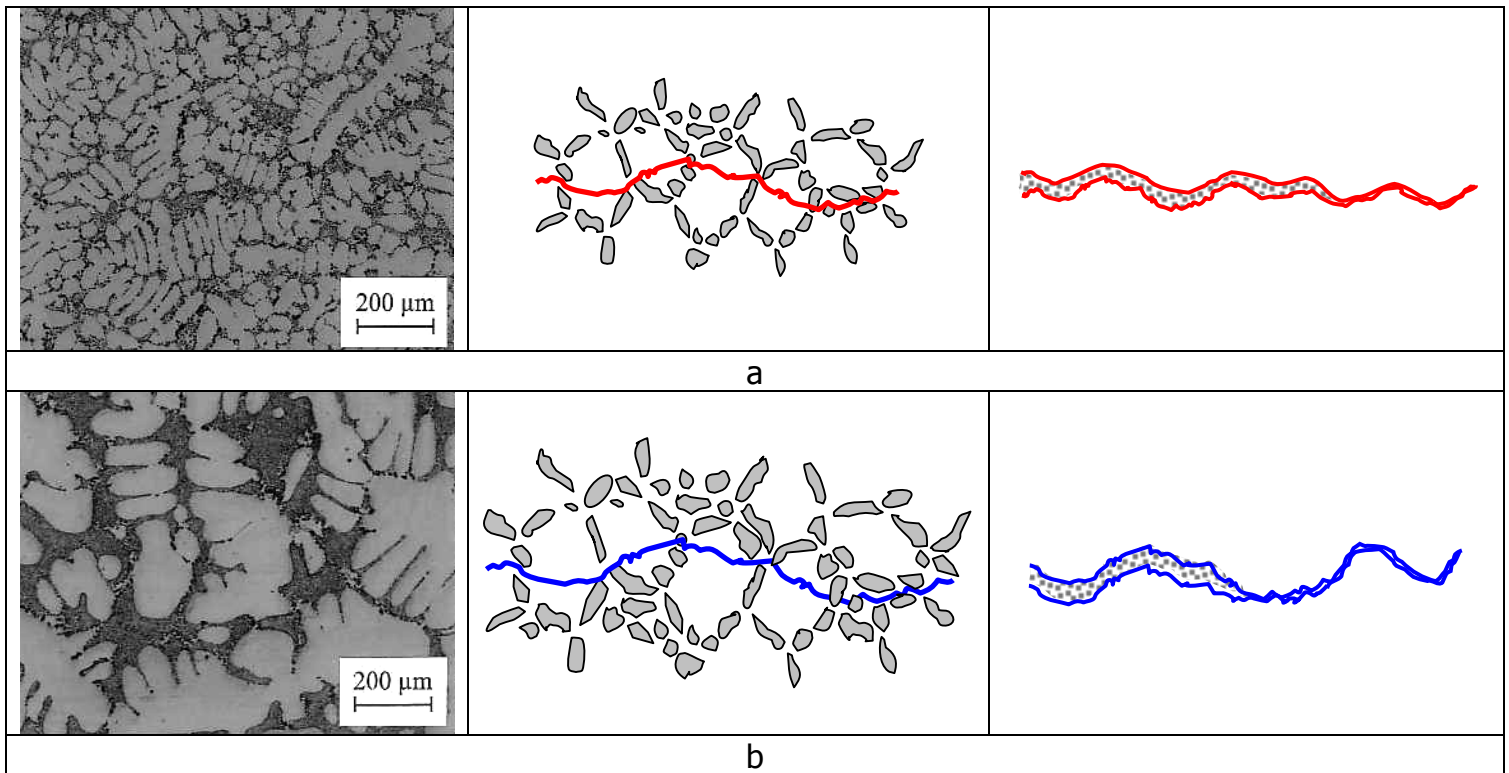


Figure 7. Closure mechanisms postulated for alloys of different SDAS: (a) small SDAS, and (b) large SDAS.

For large SDAS materials, the encounters with Si particles on the dendrite cell boundaries or in the eutectic regions are coarsely spaced, resulting in higher roughness, higher closure, and higher thresholds respectively, Figure 8a. Higher thresholds for larger SDAS alloys were experimentally observed for A356 squeeze and sand mold castings [14], A356 permanent mold and sand mold castings [15], and W319-type castings provided by a wedge mold with a copper chill at the nose of the wedge [16].

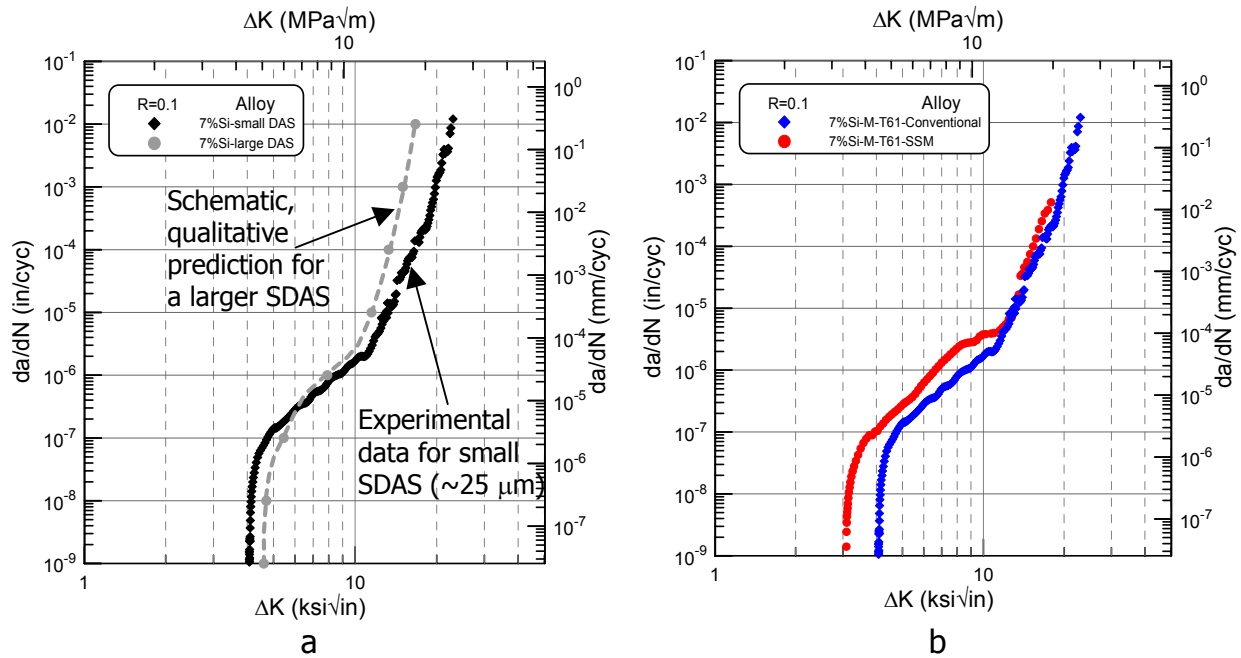


Figure 8. Fatigue crack growth behavior for modified A356 alloys with: different SDAS (a), and different solidification structure, conventional vs. SSM (b).

Similar analogies can be made for an A356 alloy produced by different casting technologies, Figure 9. The fatigue crack growth behavior of a modified A356 alloy of similar composition, but with significantly different solidification structure is presented in Figure 8b. The SSM sample has a lower crack growth resistance in the near threshold regime compared to the conventional castings due to crack interactions (as it advances through the primary α globular structure) with larger Si regions. The effect of the large α -Al globules (compared to the SDAS of the conventional A356 alloy) is overridden by the presence of large, concentrated Si regions, leading to an overall lower roughness. This results in less closure and lower threshold.

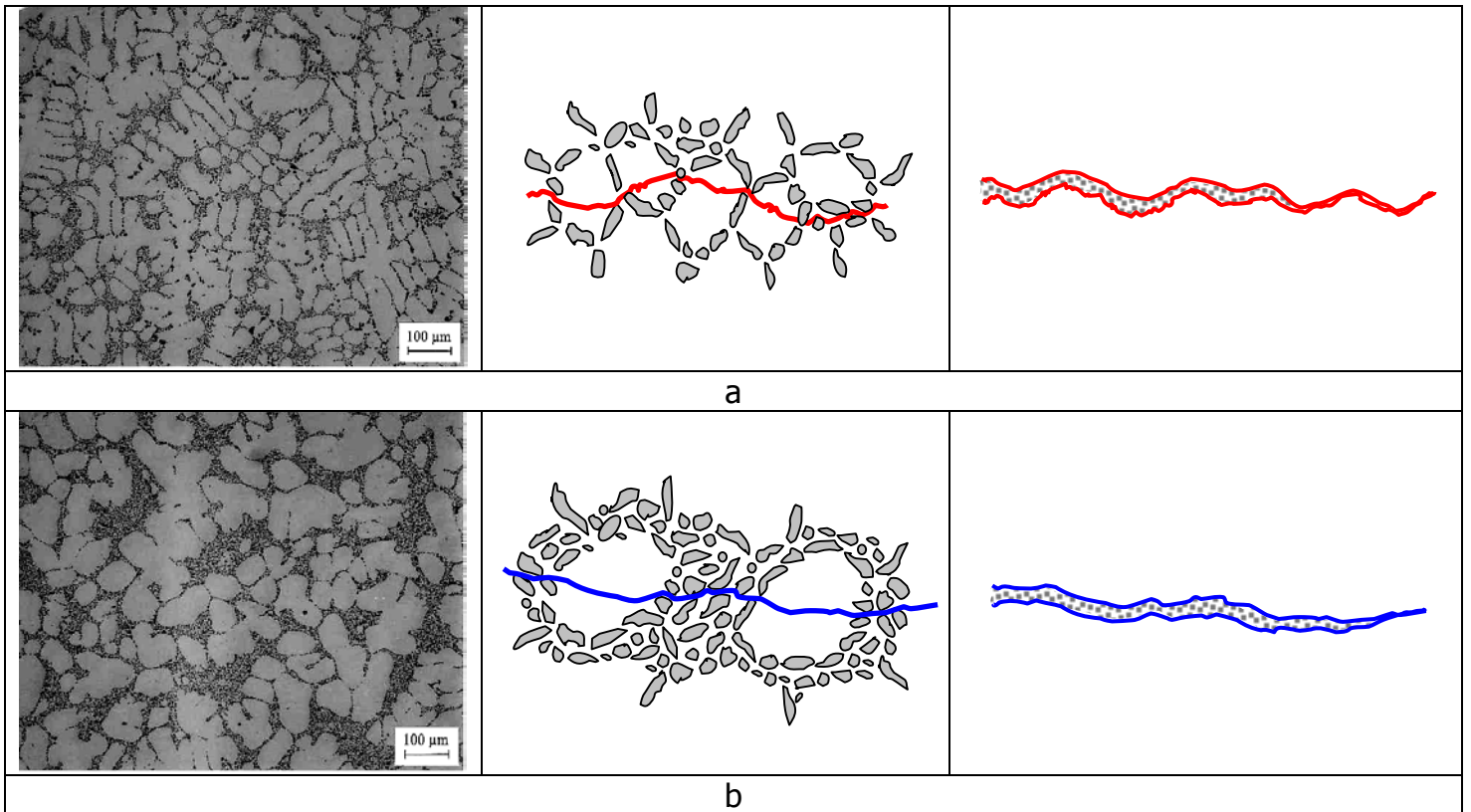


Figure 9. Closure mechanisms in A356 alloys with different solidification structures: (a) conventional-dendritic primary α phase, and (b) SSM-globular primary α phase.

The theory that roughness induced closure mechanisms dominate in the near-threshold regime is strengthened by the threshold similarities of samples subjected to various heat treatments. Similar thresholds were observed for conventionally cast A356 alloys in T4 and T61 conditions. After T4 and T61 heat treatments, the Si particle morphology and distribution are identical even though the strength of the matrix is considerably different (Table 3). This indicates that, in the near-threshold regime, the contribution of matrix strength is overshadowed by the roughness induced closure that is strongly dependent on the secondary phases present in the alloys. Even if the softer matrix is more susceptible to planar slip, the presence of eutectic Si particles diminished the influence of the slip tendency on the surface roughness. At higher ΔK however, the properties of the Al matrix play a critical role in the crack growth mechanisms as shown in section III.B.

Even though roughness induced closure has an important effect on the threshold behavior of residual stress free samples (a threshold ranking was observed for alloys with different Si content), the contribution of microstructurally related roughness is significantly overwhelmed by the presence of high residual stress, Figure 3a. In the case of low residual stress, roughness induced closure is active in the vicinity of the crack tip and therefore the height of the interfering asperities (angle of crack path deflection) dictate the closure level, Figure 10a. However, if the residual stress is high, crack tip remains open and closure mechanisms become operative near the notch instead, Figure 10b. As a result, the contribution of roughness to total closure is diminished, as the height of the interfering features near the notch has less contribution to the total crack closure level. This can be explained by considering that for contact near the notch (as opposed to at the crack tip), the difference in vertical height of the interference for various Si levels is small compared to the total crack opening displacement (COD), as shown in Figure 11. The differences between various alloys are relatively small, when compared to the total COD, and therefore the alloys ranking is lost.

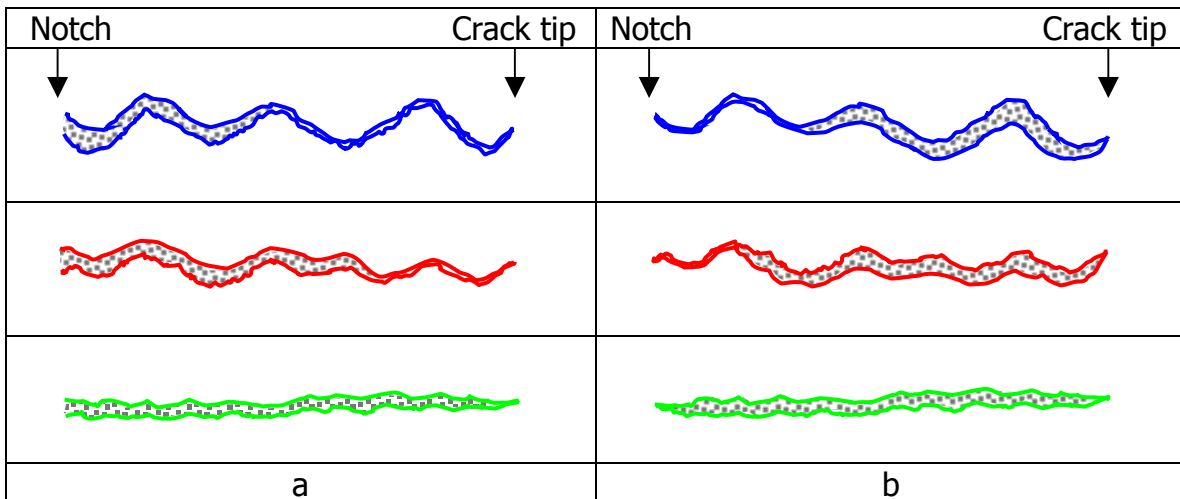


Figure 10. Closure mechanisms in Al-Si-Mg alloys with different Si levels, in low residual stress conditions (a), and high residual stress conditions (b).

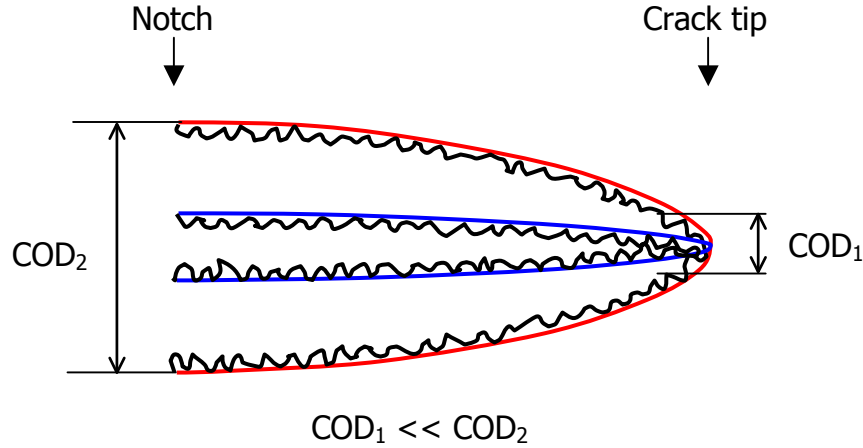


Figure 11. Schematic representation of the magnitude of surface asperities interference when contact takes place near the crack tip (right), and away from the crack tip (near the notch) (left).

Using these mechanisms a good understanding of the near threshold behavior of various alloys can be achieved, and by analyzing the alloy microstructure (amount, morphology, and distribution of second phases) threshold predictions can be made. In the near threshold regime, the morphology and distribution of the microstructural features, that influence the roughness induced closure, are more important than their strength. As a general trend, higher thresholds and lower near threshold growth rates are achieved for coarser microstructures, which result in rougher fracture surfaces, and higher closure. In this context, larger SDAS, coarser Si particles, and non-homogeneous Si distribution (such as 7%Si alloys when compared to 13%Si that have a more homogeneous distribution of Si particles), are expected to induce a better low ΔK performance, benefits that are diminished with increasing ΔK , as discussed in the next section. It was also observed (Figure 5a) that the thresholds of the 7%Si alloys can be determined from the thresholds of the constituent phases alloys (1 and 13%Si). Therefore, a relationship applicable to each family of alloys (unmodified or modified) was derived to determine the thresholds of intermediate Si levels:

$$\Delta K_{th(x\%Si, UM \text{ or } M)} = \Delta K_{th(13\%Si, UM \text{ or } M)} + \frac{\frac{13-1}{13-1} - 1}{x-1} (\Delta K_{th(1\%Si)} - \Delta K_{th(13\%Si, UM \text{ or } M)}) [1]$$

where $1\%Si < x < 13\%Si$.

Eq. [1] holds true because, in the threshold regime, roughness induced closure is the dominant mechanism, and this is controlled by the amount and distribution of Si particles.

III.B. Crack propagation mechanisms in the Paris region and Region III

Near threshold, the small crack tip opening displacements allow considerable interference of the crack surface asperities (closure) to occur, and therefore, at this stage, these mechanisms govern the crack behavior. With increasing crack driving force, ΔK , and crack tip opening displacements, the sheltering of the crack tip due to closure mechanisms diminishes as the surface interference becomes a progressively smaller amount of the total crack tip opening displacement. Therefore, even though the closure level remains almost constant, Figure 12, its influence on crack growth rate considerably diminishes as the cyclic stress intensity increases from the upper near-threshold regime to the Paris region. It is also noticeable that the matrix alloy (1%Si, no eutectic phase) shows the highest level of crack closure, followed by the 7%Si alloys, and the eutectic alloys (13%Si, predominantly eutectic structures with very low amount of primary α -Al formation). This observation is important especially for the near threshold behavior and it reinforces the fact that roughness induced crack closure decreases with increasing level of Si based on the mechanisms presented earlier.

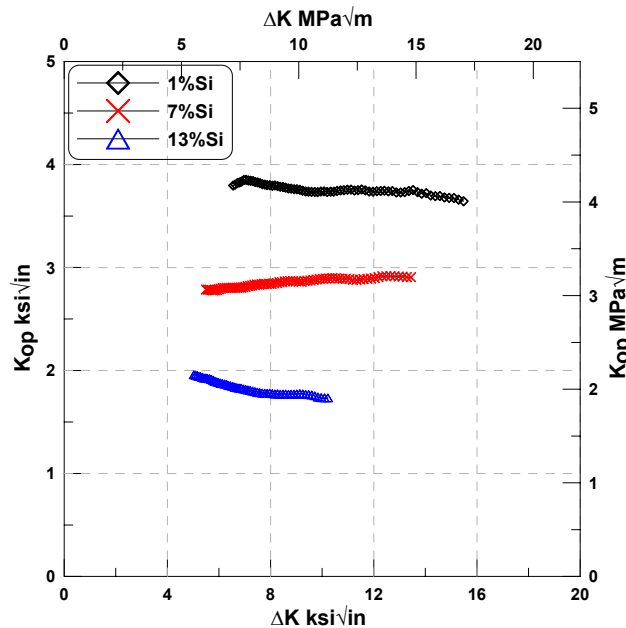
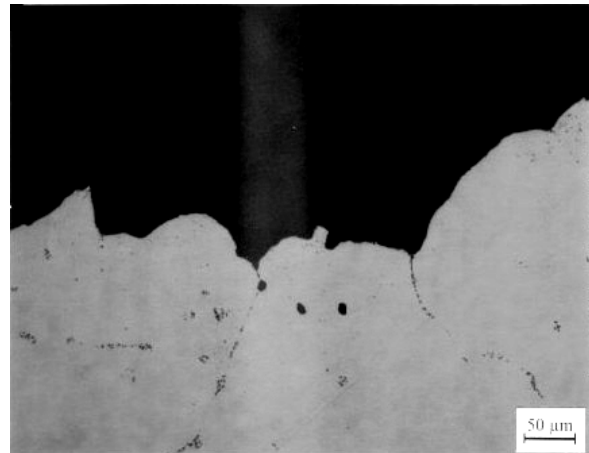
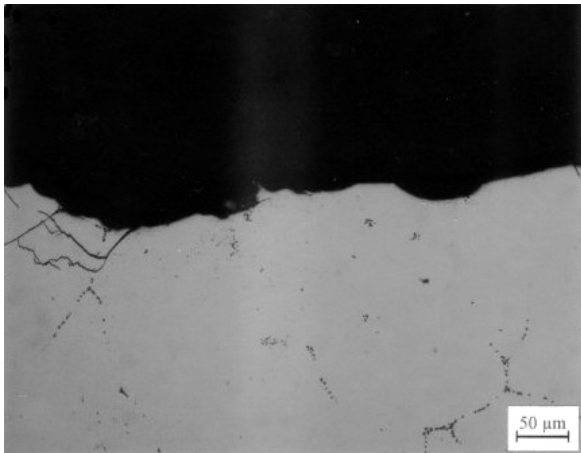


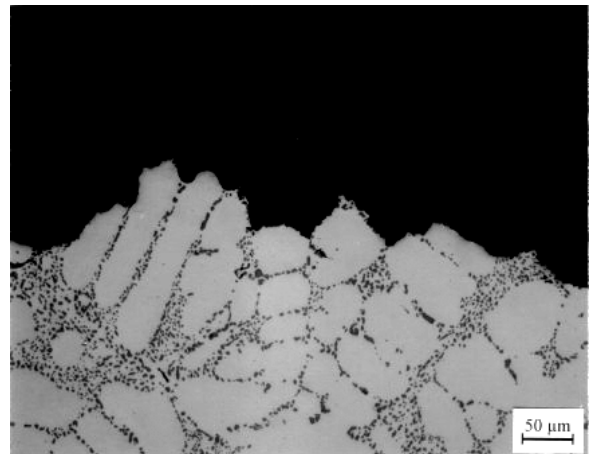
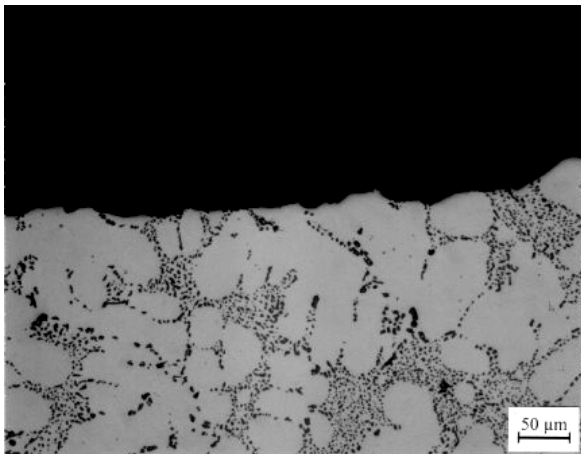
Figure 12. Evolution of closure level with increasing ΔK .

Once the closure mechanisms become less important, the fatigue crack growth mechanisms become strongly dependent on the matrix strength and the interface strength between primary α -Al structure and eutectic Si particles. As a general rule a crack always seeks the path of least resistance offered by the most damaged microstructural features ahead of it. This idea leads to the understanding of the operating mechanisms behind the microstructural changes observed at different stages of the crack growth.

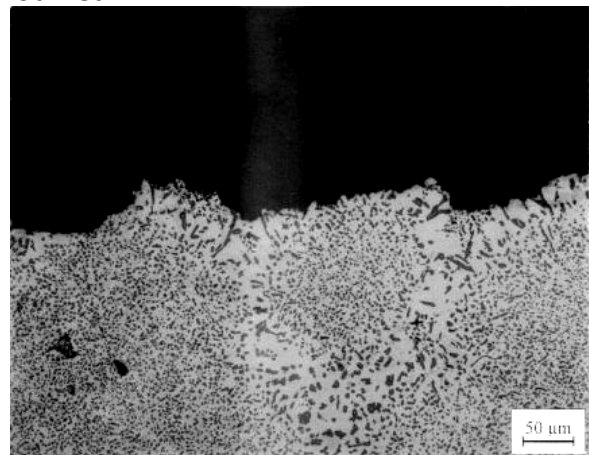
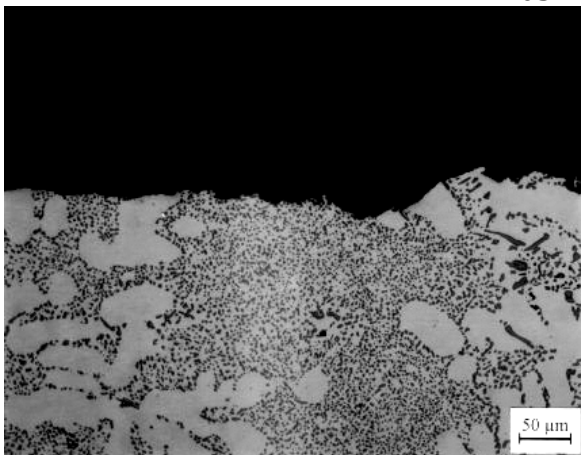
Observations of the fracture surface of all tested samples revealed a significant increase in roughness, from a rather flat crack path mainly perpendicular to the tensile axis to a torturous one, as the crack propagated from Region II to Region III. The changes in surface roughness were captured for each alloy in lower Region II and lower Region III, and they are presented in Figure 13.



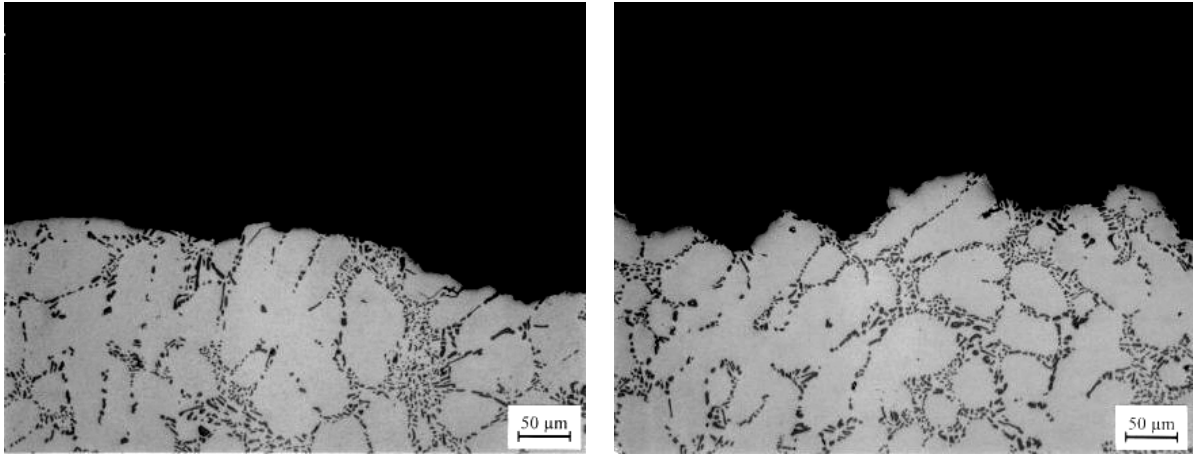
1%Si



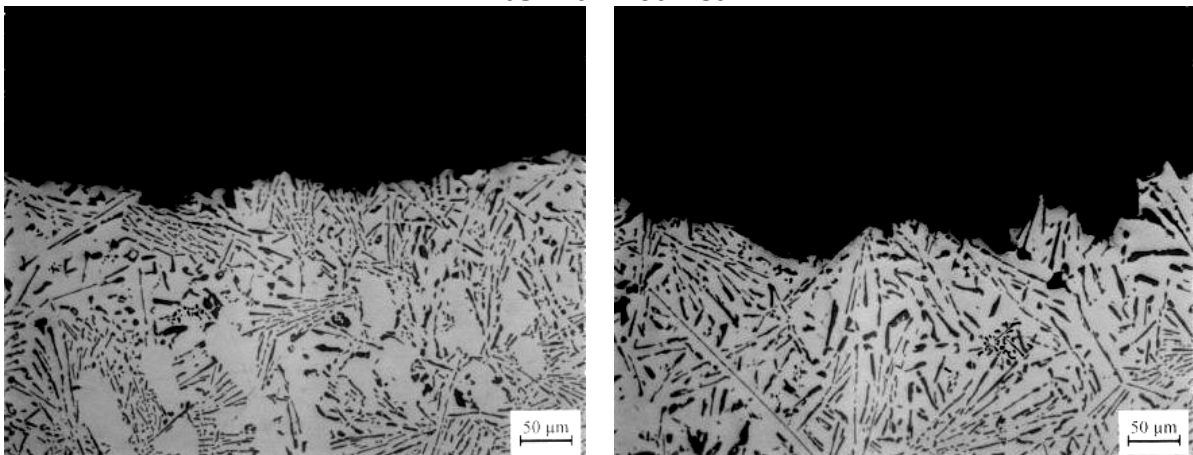
7%Si - modified



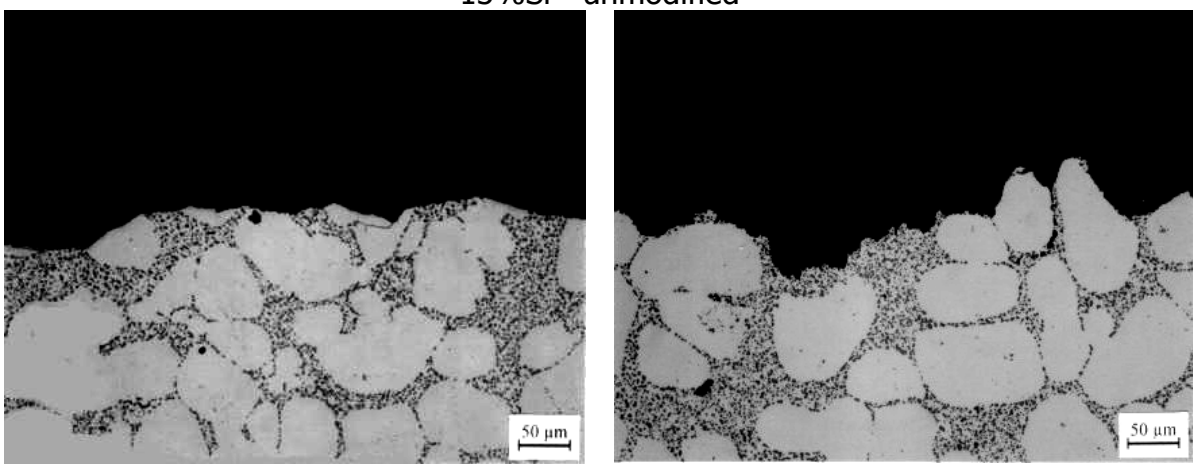
13%Si - modified



7%Si - unmodified



13%Si - unmodified



7%Si - modified - SSM

a

b

Figure 13. Changes in fracture surface roughness of the studied alloys with increasing ΔK : (a) lower Region II and (b) lower Region III.

The surface roughness index, S.R.I. (true fracture surface length divided by the length of a straight line drawn between the same end points) can be used to quantify fracture surface roughness. An example of the increase in roughness between different stages of crack growth is shown in Figure 14 for the modified A356 alloy. The S.R.I. increased from 1.2 in lower Region II to 1.8 in lower Region III. This increase in roughness was accompanied by an increase in crack growth rate from 0.01in/38,000cycles to 0.01in/2,700cycles.

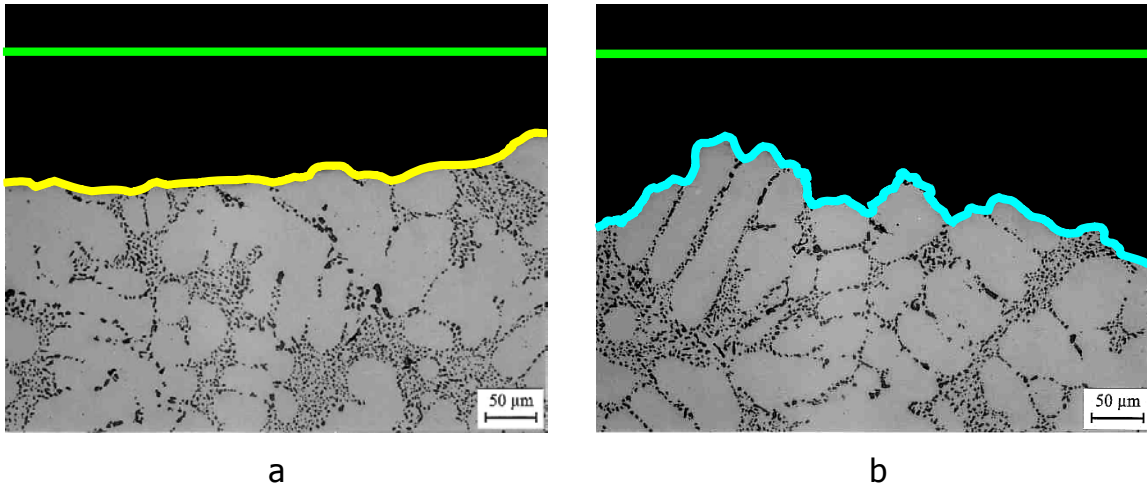


Figure 14. Changes in fracture surface roughness of a modified A356 alloy with increasing crack driving force: (a) lower region II ($\Delta K \sim 5 \text{ ksi}\sqrt{\text{in}}$ or $\sim 5.5 \text{ MPa}\sqrt{\text{m}}$), and (b) lower region III ($\Delta K \sim 11 \text{ ksi}\sqrt{\text{in}}$ or $\sim 12 \text{ MPa}\sqrt{\text{m}}$).

The observed changes in roughness are associated with a gradual change in propagation mechanisms at the microstructure level. At low ΔK levels, the flat crack appearance corresponds to an advance of the crack through primary α -Al matrix, more appropriately said, through the microstructural constituent found directly ahead of it, with increasing benefits from the presence of Si particles at increasing ΔK . This could be understood considering that surface area% (not to be confused with volume%) covered by the α -Al matrix phase is predominant ($\sim 85\%$), the rest being populated with eutectic silicon. At high ΔK , however, the crack preferentially progresses through the Al-Si eutectic islands and its appearance becomes highly torturous. A crack has a general tendency to grow perpendicular to the direction of principal stress unless the damaged material away from the crack front makes it energetically more favorable to meander. The number of Si particles along the crack path increases with the increase in stress intensity factor range and crack length as reported by others [19,23,24]. This clearly indicates the increasing crack preference for interaction with Si particles at higher driving forces. These changes in mechanisms were explained based on the amount of damaged material ahead of the crack tip at various stress intensity levels. The monotonic plastic zone size was found to be the

appropriate parameter to characterize the extent of the damaged material and to correlate ΔK levels with fatigue crack growth mechanisms that occur at the microstructure level. The use of the monotonic plastic zone instead of the cyclic plastic zone was based on two considerations. First, it reflects more accurately the stress intensity levels at which changes in mechanisms occur (as revealed by the fractographic observations). Second, the damage of the Al-Si interfaces or Si particles is the rate controlling parameter in the crack propagation, and this tensile damage is mainly introduced on maximum loading (K_{\max} process) of each cycle. The remaining part of the cycle causes compressive damage mostly to the α -Al matrix inside the cyclic plastic zone. An expression for the monotonic plastic zone, eq. [2], that takes into account both effects from plane strain and plane stress was developed [40], and this equation has been used to compute the extent of the damaged material ahead of the crack tip at different stress intensity levels.

$$r_p \approx \left(\frac{1}{2\pi}\right)^n \left(\frac{1}{6\pi}\right)^{1-n} \frac{K_{\max}^2}{\sigma_{YS}^2} \cos^2 \theta \frac{\theta}{2} \left(1 + 3 \sin^2 \frac{\theta}{2}\right) \quad [2]$$

where $n = \text{degree of plane stress} = \frac{1.33 \cdot r_{p(\text{plane-stress})}}{B}$ $0 < n \leq 1$;

It is well known that plastic strain is the most damaging parameter in fatigue and therefore the size of the plastic zone at the crack tip is decisive for the future advance of the crack. The micro-constituents enclosed in these weakened regions are preferred by the crack (the path of least resistance is always preferred). Therefore, a relationship between the size of the plastic zone and the micro-constituent dimensions is critical for understanding fatigue crack growth behavior at different stages.

The plastic zone radius computed using eq. [2] needs to be compared with a critical microstructural feature that controls the crack advance, which in the case of alloys with secondary phases, such as 7%Si alloys containing eutectic Si particles, is the SDAS. The SDAS value is a microstructural indication of the plastic zone extent that is required such that Si particles are enclosed in it and provide a weak link for the incoming crack. For the studied alloys the average SDAS was around 25 μm , which means a plastic zone at least that large contains Si particles that are either damaged or whose interface with the α -Al matrix has been weakened. A plastic zone, $r_p \sim \text{SDAS}$, corresponds to a crack driving force, ΔK , around 5 $\text{ksi}\sqrt{\text{in}}$ (5.5 $\text{MPa}\sqrt{\text{m}}$), which on the fatigue crack growth curves roughly corresponds to the transition from the near threshold regime to the stable growth in the Paris region. The defective role attributed to the Si particles in the near threshold regime becomes a crack beneficial decohesion mechanism which represents the most probable failure mode at low crack driving

forces [19,24]. The strain energy required to completely fracture a Si particle cannot be provided by small plastic zones, unless the particles have an irregular shape, and their principal axis is perpendicular to the crack plane. Such particles have a fairly high resistance to debonding due to the large interface area located parallel to the loading direction [41]. It was observed that particles with an inclination angle to the crack plane between 45° - 135° have a tendency to break even at low crack driving forces, while angles lower than 45° or higher than 135° , are more favorable to debonding, Figures 15a and b. However, when a Si twin plane is parallel to the crack front, Si particles can fracture at angles lower than 45° or higher than 135° , Figure 15c.

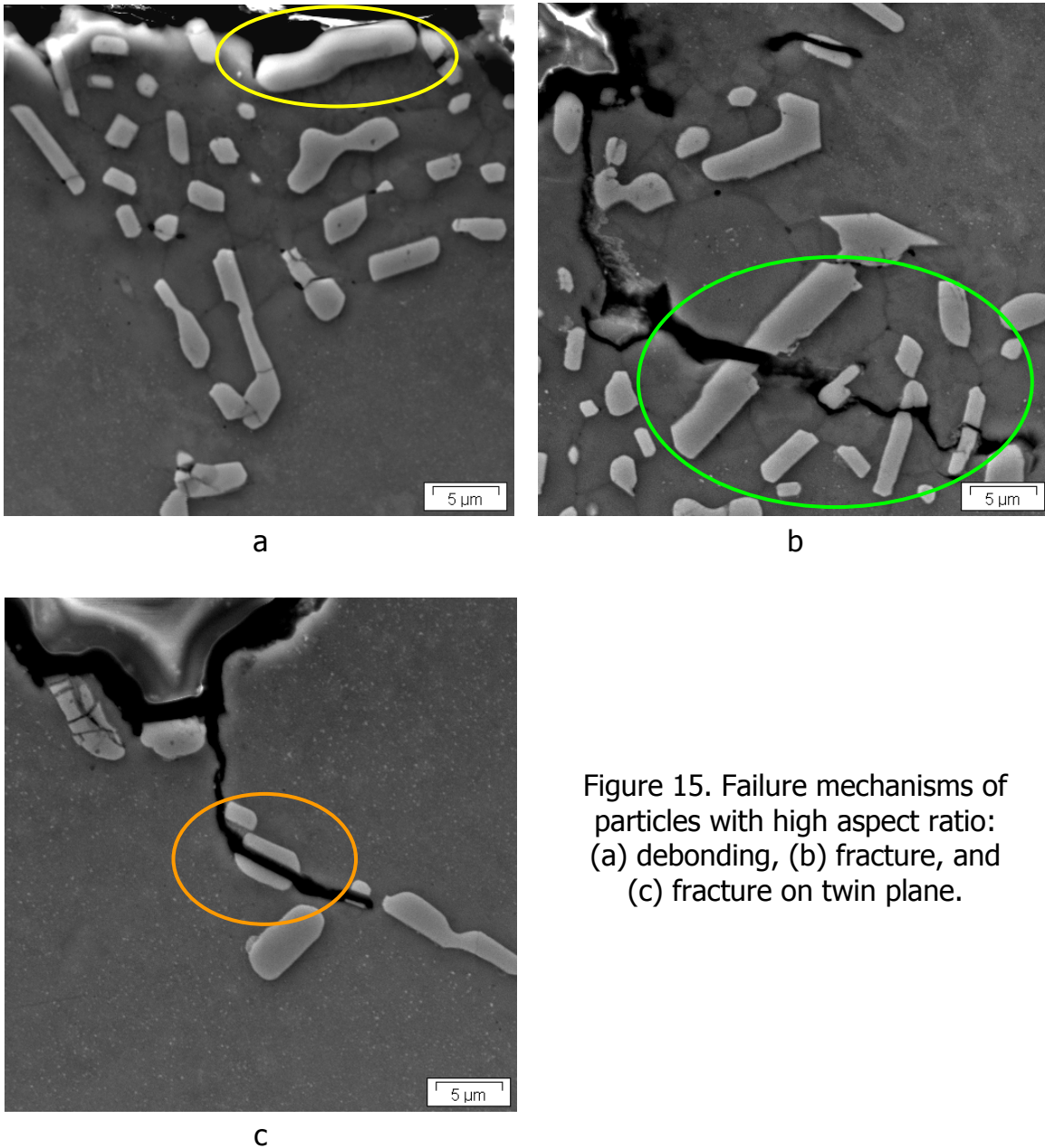
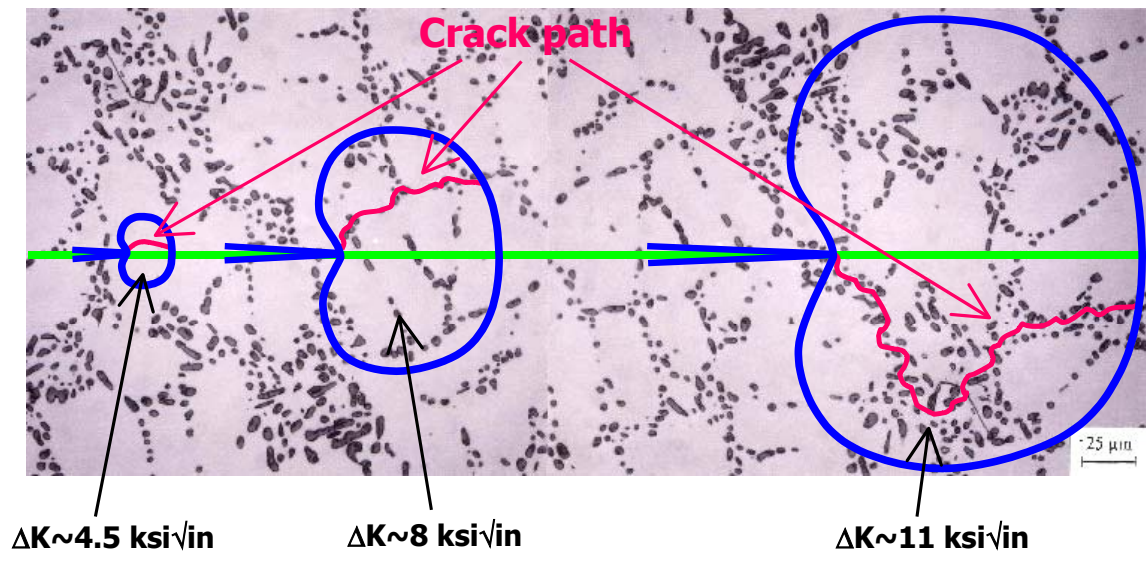


Figure 15. Failure mechanisms of particles with high aspect ratio: (a) debonding, (b) fracture, and (c) fracture on twin plane.

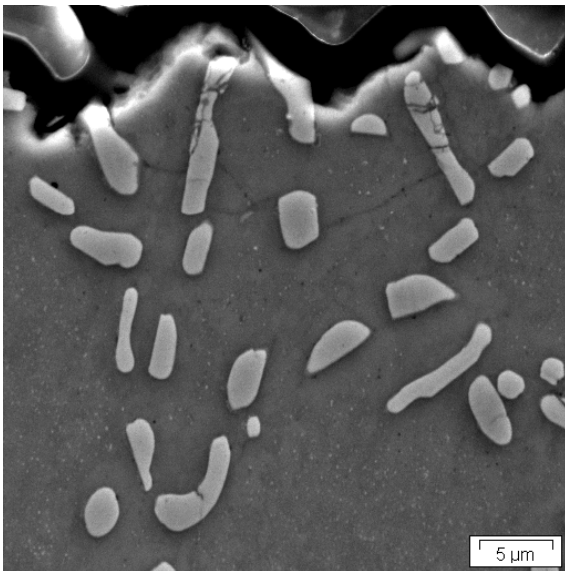
The decohesion/fracture mechanism is a result of the plastic deformation ahead of the crack tip, which involves dislocation pile-ups along the slip planes when an obstacle, such as a Si particle is encountered. The high shear stress buildup at the head of dislocation pile-ups can nucleate a microcrack and depending on the stored elastic strain energy, the microcrack can either stagnate, crack the Al-Si interface bonds (decohesion), or fracture Si particles. The mixed effects of stress intensity level (degree of plastic deformation ahead of the crack tip) and Si particle morphology, orientation, and distribution dictate the dominant damage mechanism.

At low crack driving forces, even though the plastic zone starts sampling Si particles, the amount of Si particles on the fracture surface is low, and the appearance of the crack is flat and still dominated by the presence of primary Al matrix. The crack's opportunity to select weak regions is restricted to sporadic particles available in its process zone (in the immediate vicinity of the crack and almost in line with the crack tip), which makes Al matrix the dominant propagation mode and the appearance of the crack rather flat. The crack crosses the damaged dendritic structure, and when Si particles with weakened interface are encountered, the crack follows the weak path; however, the availability of such particles is still limited for ΔK between 4.5 and 8 ksi $\sqrt{\text{in}}$ (5 and 8.8 MPa $\sqrt{\text{m}}$), Figure 16a.

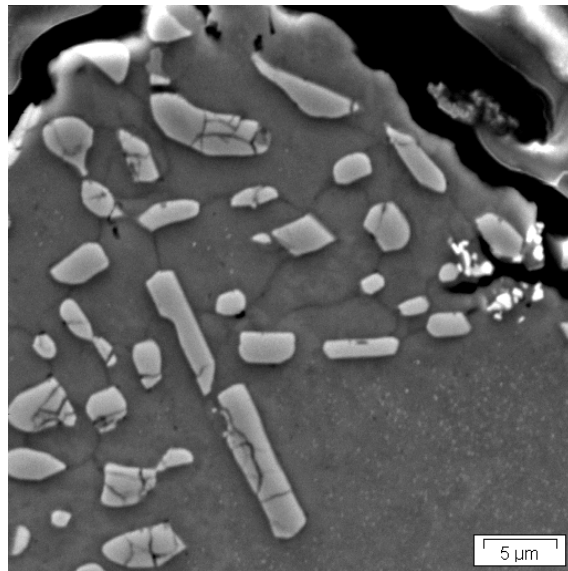
As the ΔK increases, the number of Si particles on the surface increases significantly and crack's bias towards advancing around and/or through Si particles becomes more and more evident. For the crack to exclusively follow Si particles, it is necessary to constantly locate ahead of it prior debonded or cracked Si particles. This requirement implies a plastic zone size that samples a significant number of Si particles to create a continuous path of least resistance. In this case, it becomes energetically more favorable for the crack to deviate from the planar advance and meander through the regions of least resistance. Therefore, the crack samples a progressively larger number of Si particles. For the case of A356 alloys, in lower Region II, the crack interacts with individual particles, then it follows a sequence of Si particles primarily located on the cell boundaries (eutectic islands are observed too) not too far from the main crack direction, at $\Delta K > 7\text{-}8\text{ksi}\sqrt{\text{in}}$ (7.7-8.8 MPa $\sqrt{\text{m}}$). As ΔK further increases, the crack follows almost exclusively the large Al-Si eutectic islands separating primary Al structures, at $\Delta K > 10\text{-}11\text{ksi}\sqrt{\text{in}}$ (11-12MPa $\sqrt{\text{m}}$). The transitions are portrayed by the changes in the fracture surface roughness. Si particles can be regarded as brittle reinforcing particles in a composite material and the boundaries between them and the matrix are highly stressed, weak regions favorable for crack propagation; at higher ΔK levels, when the energy is higher, the number of fractured Si particles increases, and the crack can propagate through them rather than debonding them, Figures 16b and c.



a



b



c

Figure 16. Plastic zone size representation at the microstructure scale for an A356-T61 alloy at different ΔK levels (a); enlargements of the damaged regions in the plastic zones near the crack at $\Delta K \sim 8$ ksi $\sqrt{\text{in}}$ (b), and $\Delta K \sim 11$ ksi $\sqrt{\text{in}}$ (c).

In Figure 16 (third case, $\Delta K \sim 11$ ksi $\sqrt{\text{in}}$), it can be observed that a plastic zone able to damage a complete Al-Si eutectic region (or a succession of Al-Si eutectic regions) needs to be reached before a continuous network of damaged Al-Si eutectic islands are available to the incoming crack. This scenario roughly corresponds on the fatigue crack growth curve to the transition from Paris

regime to Region III, fast propagation mode. It should be noticed that the transition points in fatigue crack mechanisms are direct functions of the distances between consecutive available Si particle or whole Al-Si eutectic domains, or in other words the Si particle distribution. SDAS is considered to determine the distribution as well as the size of the Al-Si eutectic regions and consequently it plays a critical role in the crack advance process, Figure 17a. Large SDAS, besides giving a higher threshold, induces a higher ΔK transition from a predominant α -Al planar propagation mode to a preferential Si particle growth. A large SDAS is also associated with larger Al-Si eutectic regions and coarser Si particles for the same heat treating conditions. Si particles and their distribution dictate the crack growth resistance at high ΔK levels once the crack starts preferentially selecting Si. Larger SDAS materials have a larger localized number of coarser Si particles that are easier to damage. This results in higher growth rates at high ΔK levels and lower pseudo-fracture toughness. Predictions for two samples with similar composition (modified A356) but larger SDAS values were qualitatively developed (SDAS \sim 70-80 μm and 150-170 μm) and schematically presented in Figure 17a. Similar behavior was experimentally observed for A356 squeeze and sand mold castings [14], A356 permanent mold and sand mold castings [15], and W319-type castings provided by a wedge mold with a copper chill at the nose of the wedge [16].

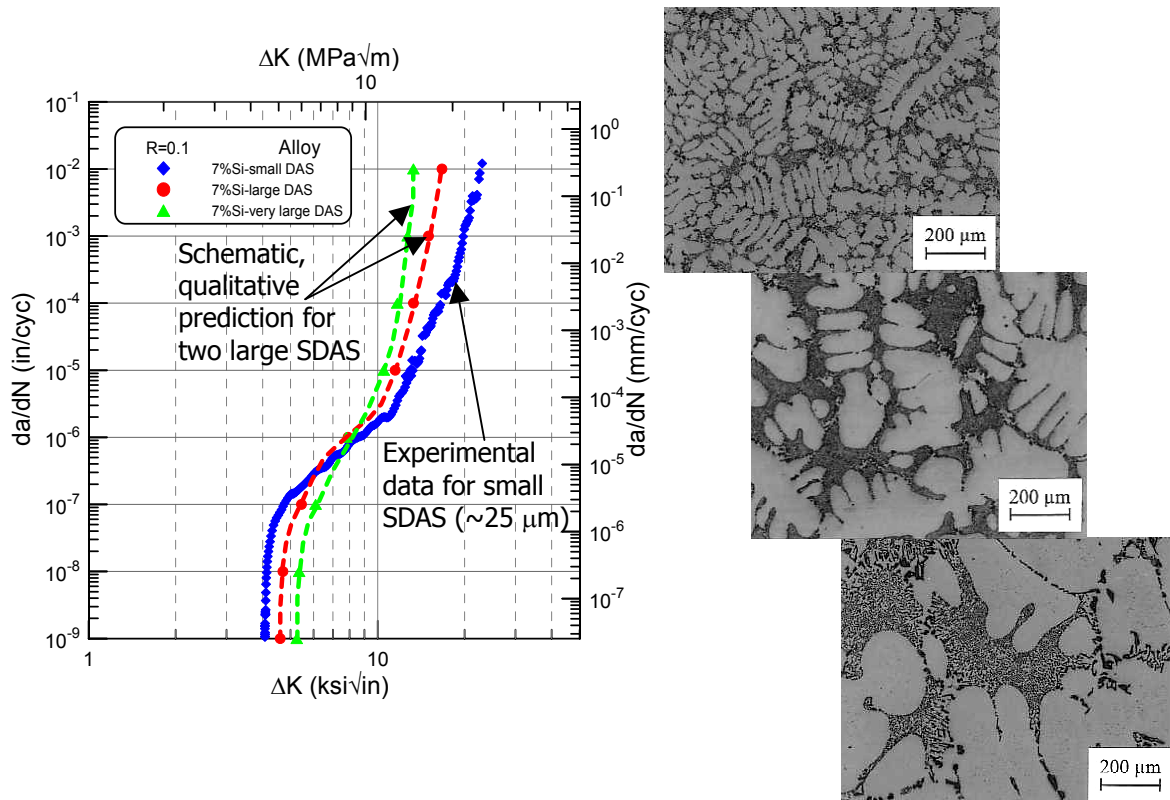


Figure 17. Postulated effect of SDAS on the fatigue crack growth behavior of a modified A356 alloy.

As already mentioned, the other critical parameter controlling the rate and mode of crack advance is related to the Si particles themselves. Alloys with higher Si content have more Si particles available at low crack driving forces, faster crack advance at high ΔK levels, and a lower pseudo-fracture toughness.

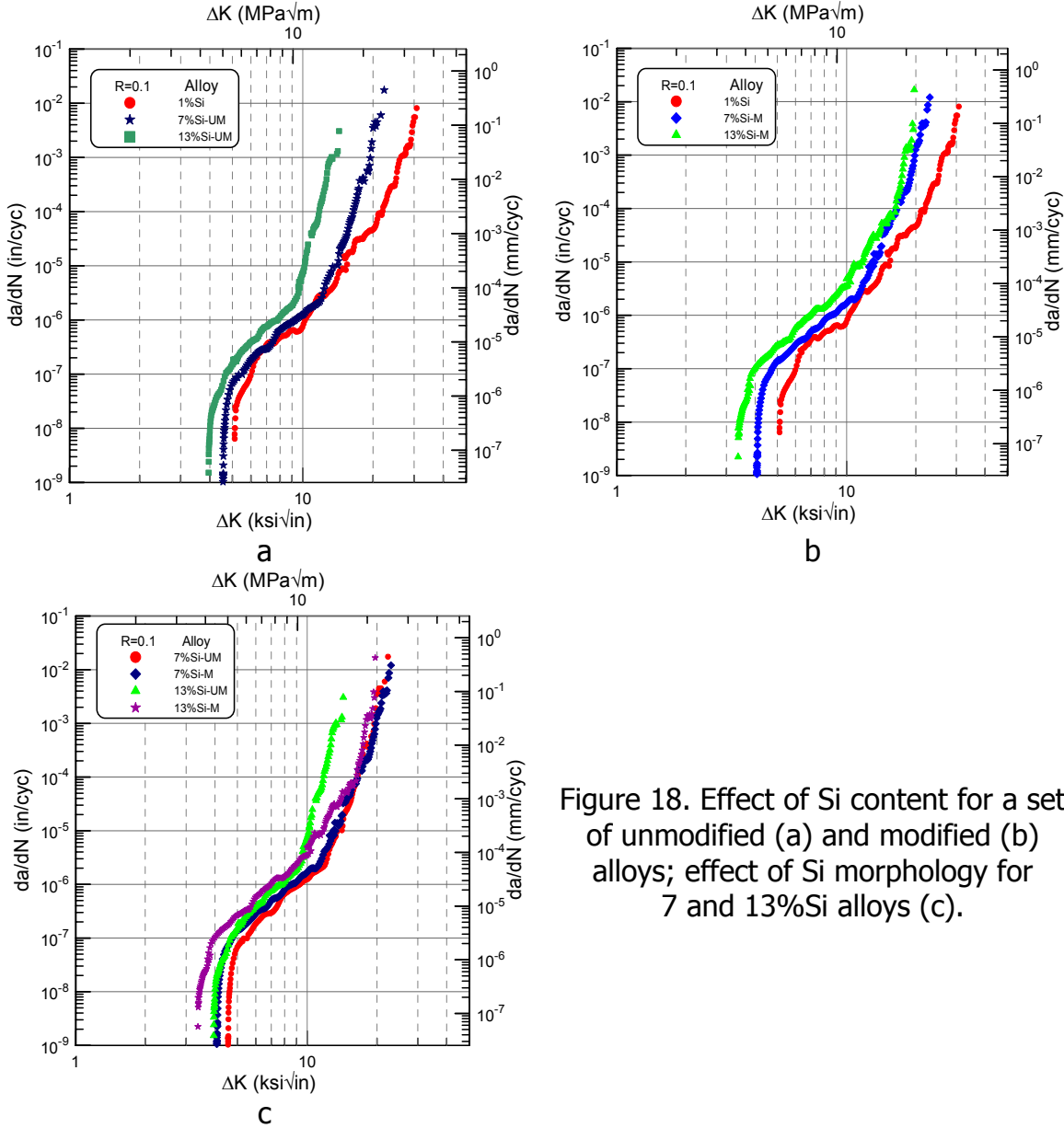


Figure 18. Effect of Si content for a set of unmodified (a) and modified (b) alloys; effect of Si morphology for 7 and 13%Si alloys (c).

Crack behavior in Region III, is characterized by a tensile overload process involving fast crack growth. The overload fracture in upper Region III occurs almost entirely through a ductile tearing in the Al-Si eutectic islands. As a result fracture toughness is, to a large extent, determined by the Si particles morphology. The ductile matrix fails through growth and coalescence of voids.

At high ΔK levels, when the crack exclusively follows the eutectic regions, the coarse Si morphology provides convenient paths for the crack to debond along or cut through. The modified Si morphology exerts more resistance by crack deviation around particles, and the particles themselves are more fracture resistant, Figure 18c. The irregular shaped unmodified Si particles are exposed to higher local stress concentrations compared to the rounder modified Si particles and therefore offer lower resistance to the crack propagation.

A crack advancing with a high crack tip driving force is also biased towards growth through irregular Si particles when available, as observed also during monotonic material failure [42]. Modified A356 alloys show slightly improved behavior in Region III compared to the unmodified A356 alloys, but the difference is less evident than in the case of 13%Si alloys. After heat treatment, the differences in Si morphology between unmodified and modified alloys are minimized due to the thermal modification of the plate-like eutectic Si structure. However, the more and larger plates in 13%Si alloys require a longer time to fragment and spheroidize during heat treatment, and the preservation of the plate-like structure specific to unmodified alloys drives larger differences between the fatigue crack growth behavior of unmodified and modified 13%Si alloys in Region III. Larger differences in pseudo-fracture toughness are caused by larger differences in Si morphology that are function of Si content and heat treat time. The size and aspect ratio of Si particles for all the alloys are given in Table 1, and the Si morphology ranking is in perfect agreement with the fracture toughness ranking of the Si containing alloys. Results of this study agree with the literature for A356 alloys [15,43] and an Al-12%Si-0.35%Mg alloy [20] for tests conducted under constant stress ratio $R=0.1$.

The Si% based deconstruction/reconstruction technique used to model the threshold behavior (see eq. [1]) of hypoeutectic alloys (from its constituent phases, primary Al 1%Si and eutectic phases 13%Si) cannot directly be applied to derive toughness. Toughness values are strongly dependent on the Si morphology (rather than mostly Si content) and therefore, model equations based on the size and the shape of the Si particles are needed instead: $\Delta K_{FT}=f(\text{Si shape, Si size, Si distribution, Si content})$. The importance of Si morphology rather than Si content can be clearly seen in Figures 18a and b for the unmodified and modified family of alloys. The modified alloys with 7 and 13%Si have similar toughness due their comparable Si morphology while the unmodified alloys show a toughness shift equivalent to the Si morphological differences.

The effect of Si morphology on the fast growth mode, and its influence on the fracture toughness of the alloys are reiterated by the similarities in Region III between conventionally cast and SSM cast modified A356 alloys. Even though the two alloys have significantly different fatigue crack growth behavior in Regions I and II, the similarities in Si morphology lead to an almost identical

behavior in Region III as well as similar fracture toughness, Figure 19. Other researchers [44] reported lower fracture toughness for higher aspect ratio Si particles in SSM Al-Si-Mg alloys of similar grain size and α -Al particle size. However, the T5 SSM sample showed much lower fracture toughness due to a coarser, coral-like, Si morphology in the absence of solution treatment, which is more favorable to fast propagation rates once the crack exclusively goes through the Al-Si eutectic regions.

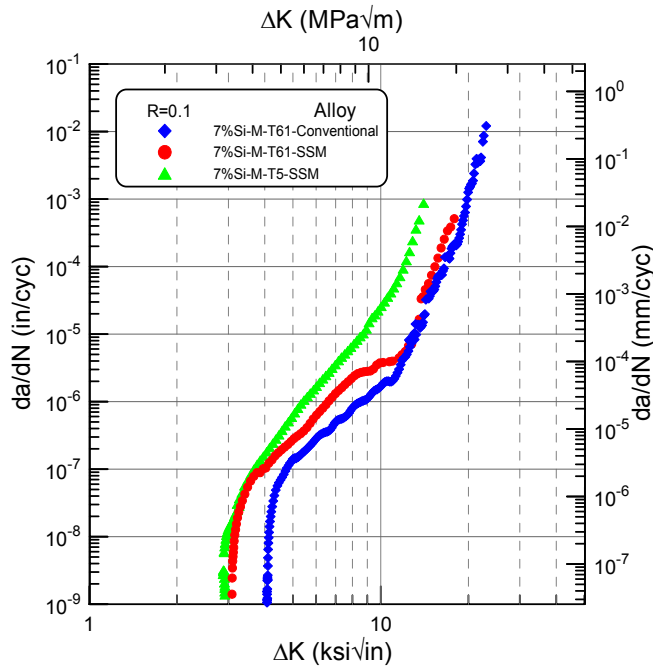


Figure 19. Conventionally cast and SSM cast modified A356 alloy show similar crack growth rates and toughness in Region III when Si morphology and matrix strength are kept constant.

SEM analysis of the fracture surfaces for three alloys from 1 to 13%Si reveal the same characteristics explained earlier. In the hypoeutectic alloys, at low ΔK , fatigue striations corresponding to the crack advance through the Al matrix were observed on the fracture surfaces (the average striation spacing is comparable to the fatigue crack propagation rate at a given ΔK level) along with debonded or cracked Si particles or holes from where the Si particles were debonded. The eutectic alloys show no evidence of striations due to the absence of primary α -Al matrix, Figure 20. At high ΔK , characteristic dimples representing the ductile fracture in the matrix are found between Si particles.

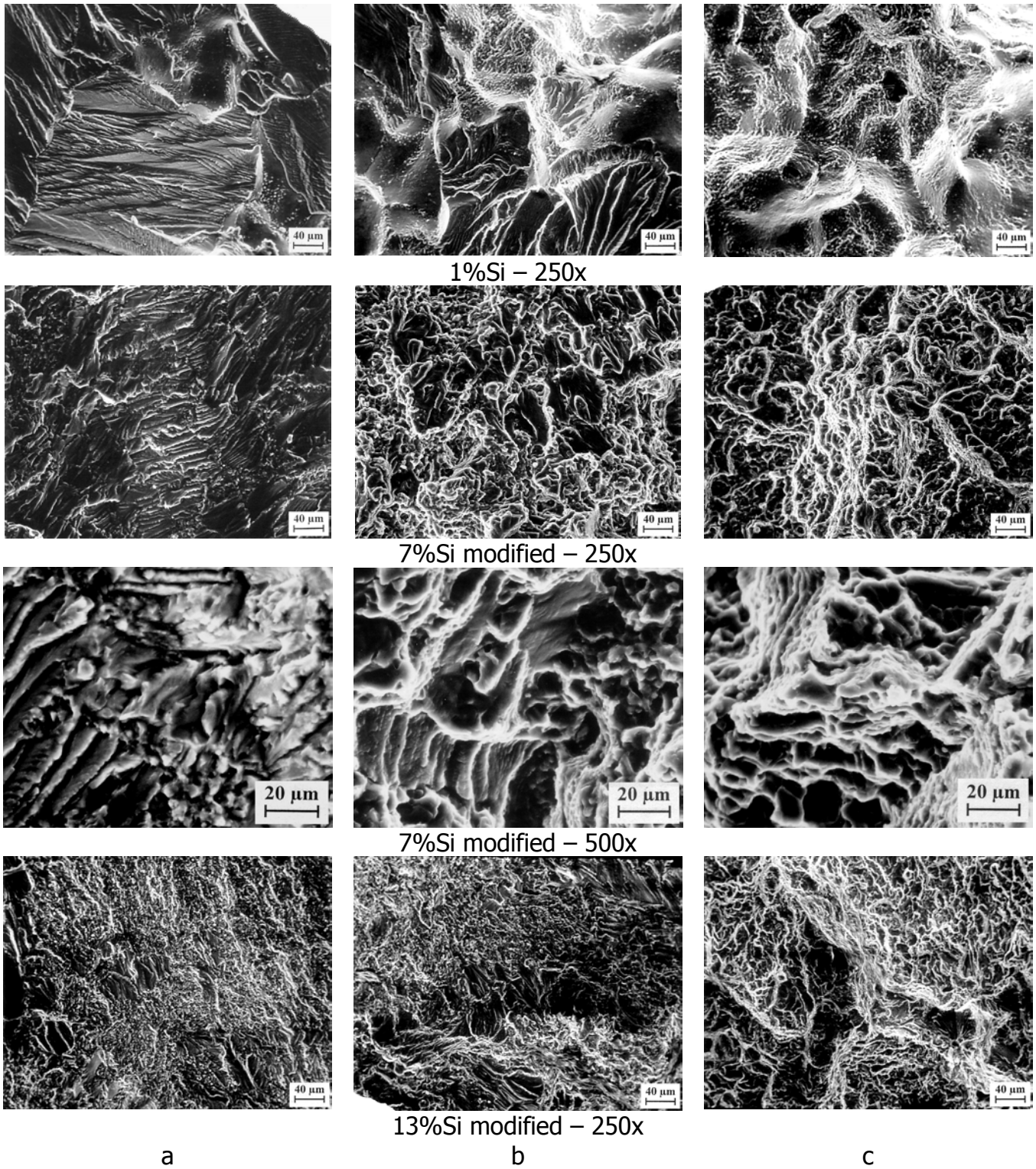


Figure 20. Fracture surface appearance at different ΔK levels: (a) lower region II, (b) upper region II, and (c) region III.

Another important set of tests was performed on samples of the same composition subjected to various heat treatments, T4 and T61, Figure 21. For the SSM samples a T5 heat treatment was also applied. Even though no significant differences were observed in the near threshold regime and lower Region II (section III.A), differences were observed both in higher Region II and Region III. In upper Region II both the unmodified and modified A356 alloys in T61 showed better fatigue crack growth resistance, while in Region III the T4 samples lead to higher fracture toughness. The SSM T5 sample is characterized by higher propagation rates in Region II compared to the SSM T61 sample, as well as lower fracture toughness, Figure 19.

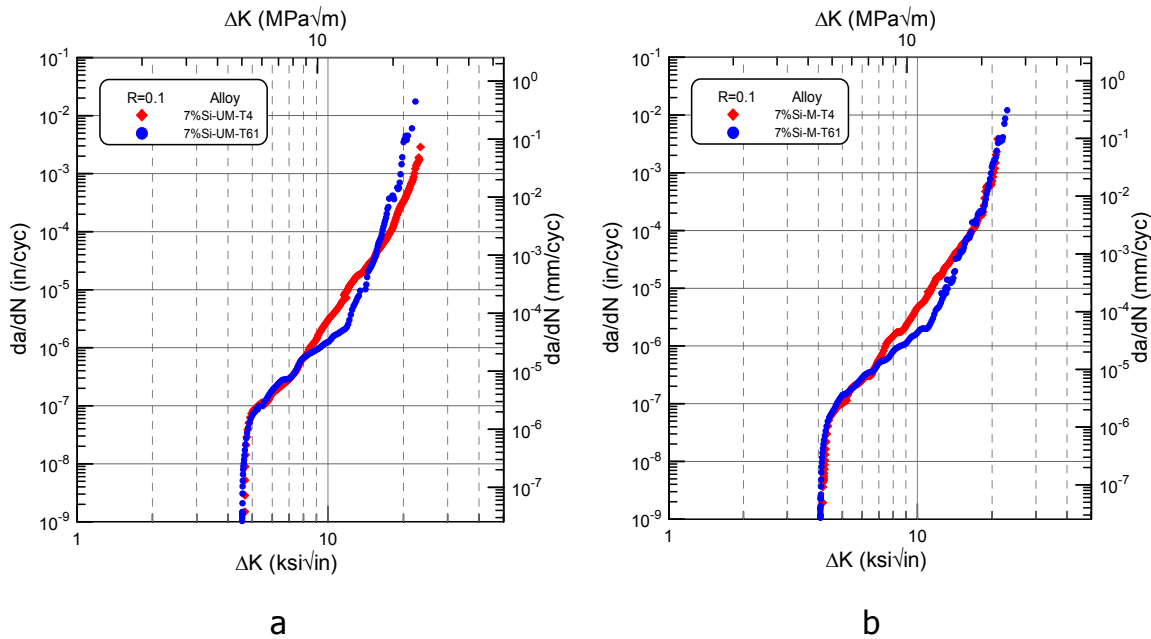


Figure 21. Fatigue crack growth behavior of (a) unmodified and (b) modified A356 alloys in T61 and T4 heat treat conditions.

The differences in crack growth behavior of the T4 and T61 samples can be explained by associating the tendency of the crack to grow straight on a direction perpendicular to the applied load direction to the path of least resistance provided by the two microstructures, Figure 22.

The matrix of the T4 samples is characterized by a low yield strength (compared to T61) due to the absence of Mg-Si strengthening precipitates, which provides a path of low resistance in front of the incoming crack (path 1 in Figure 22, which results in a flatter fracture surface than matrix fracture surface in T61) in addition to the damaged Si-particles/matrix interfaces and/or Si particles (path 2 in Figure 22). The reason for the observed higher propagation rate in T4 samples is because there are alternative least resistance local paths for the crack to follow and local meandering is preferred over large scale meandering, Figure

22 (higher ΔK for T4). In upper Region III, T4 samples show a better fatigue crack growth resistance and higher pseudo-fracture toughness due to the ductile tearing of the softer Al matrix in the T4 samples. Plastic flow at the crack tip blunts the crack and decreases the local stress. The crack growing by ductile tearing consumes a significant amount of energy by plastic flow, and the bigger the plastic zone (T4), the more energy is absorbed. Higher energy absorption leads to higher ΔK and ultimately higher fracture toughness, ΔK_{IC} . The differences in upper Region III are more evident when the linear elastic fracture mechanics definitions are corrected for plasticity contributions [40]. Similar observations in the threshold and upper Region III regions were given in the literature for under-aged and peak aged samples of A356 alloys [5,15]. In the case of the SSM T5 sample the poor response is again justified by the lower yield strength (the T5 heat treatment does not include a solution step). Moreover, the coral-like Si morphology in T5 conditions is coarse and weak, therefore favorable to faster propagation rates.

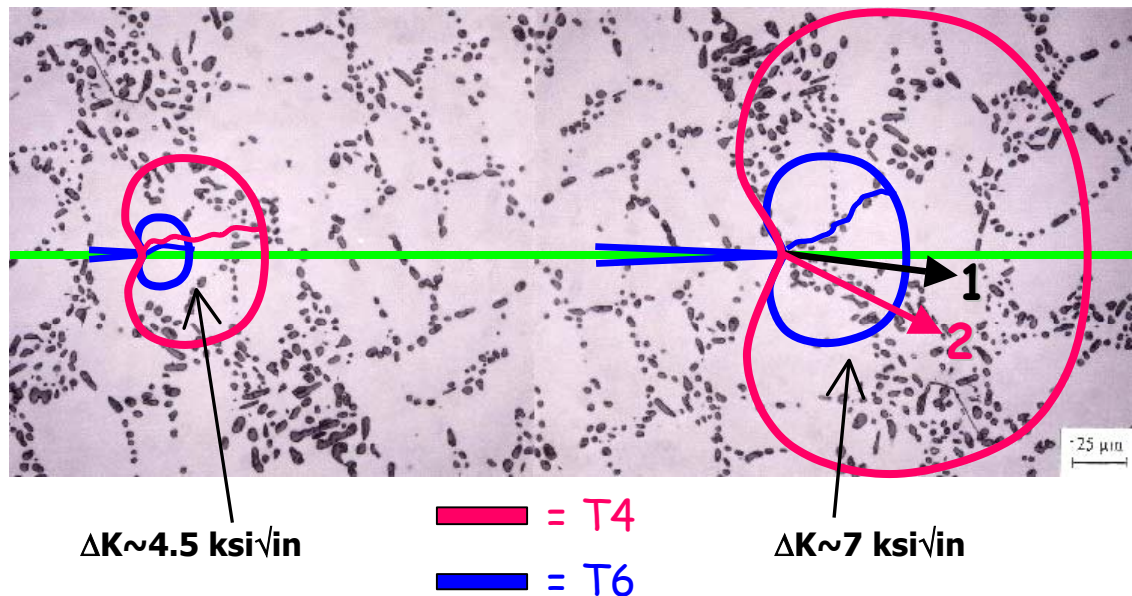


Figure 22. Comparative changes in crack growth mechanisms with increasing ΔK for A356 alloys in T4 and T61 heat treat conditions.

On the fracture surface angular cusps were observed, Figures 23a and b, corresponding to the crack initially growing outwards from the main propagation direction under an angle close to 45° (either towards a Si particle or not) and subsequently changing direction and rejoining the main path. This can be explained by considering the shear stress distribution ahead of the crack tip, especially the maximum local shear stress. This parameter drives the crack path changes and the possible mechanisms are presented in Figure 23c. When maximum shear stress acts on one of the preferred (111) slip planes, cusps can form. The absolute value of the maximum shear stress (regardless if positive or

negative) that favors propagation in the general direction of growth dictates the advance of the crack. Similar explanations can be used to explain the tendency of the crack to macroscopically maintain the main path after interaction with Si particles or islands (see Figure 16, high ΔK). However, in this case a more complex interaction of the shear strains with Si particles needs to be considered to determine the local propagation direction changes. The shear stresses were interpreted for certain K_{max} levels as functions of location ahead of a crack tip.

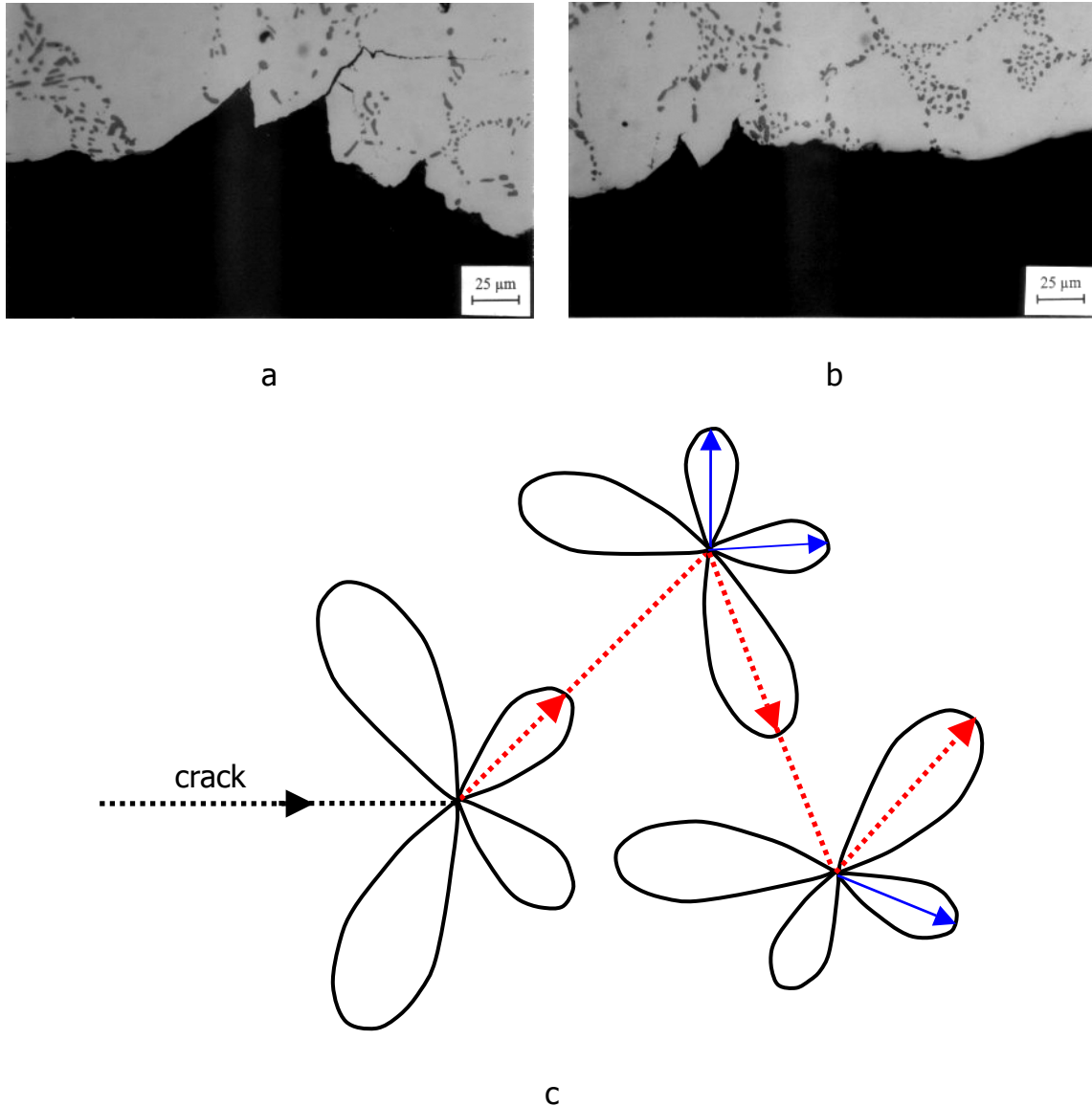


Figure 23. Influence of shear stresses in directional local crack path changes: (a,b) fractographic observations, (c) shear stress distribution and the effect of maximum shear stresses on crack advance.

The mechanisms presented in this study were reinforced by another set of experiments on unmodified and modified A356 alloys of various grain size levels in the range 180-520 μm . Contrary to wrought alloys where grain size plays an important role in fatigue crack growth and failure mechanisms [45-47], cast alloys show low sensitivity to changes in grain size, Figure 24.

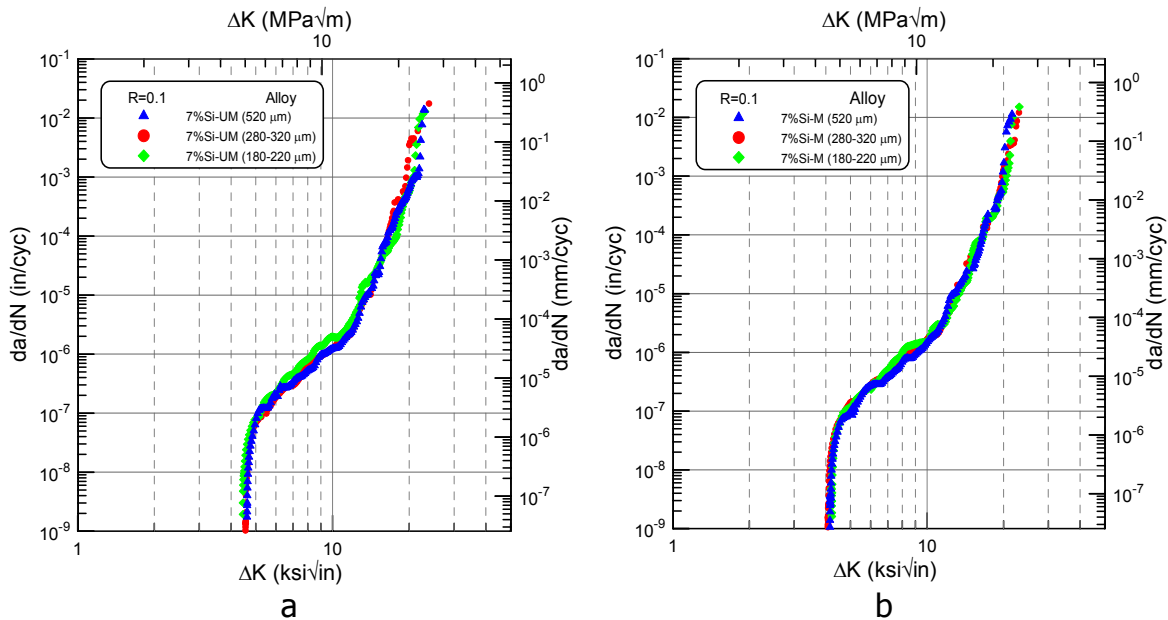


Figure 24. Fatigue crack growth behavior of (a) unmodified A356, and (b) modified A356 alloys of various grain size.

This behavior can be rationalized by taking into account the fact that cast alloys contain microstructural features smaller than grain size, such as eutectic Si particles and SDAS, that control the advance of the crack as well as the levels where changes in mechanisms occur, Figure 25.

The extent of the plastic zone ahead of the crack tip affects these microstructural constituents as well as the interface between them first; under these circumstances the presence of grain boundaries becomes of secondary importance for grain size ranges typical of cast Al-Si alloys, 100-1000 μm . The interaction of the crack with the Si particles, and the strength of the Al matrix/Si particles interface are the critical factors determining the crack advance rate at different crack driving forces.

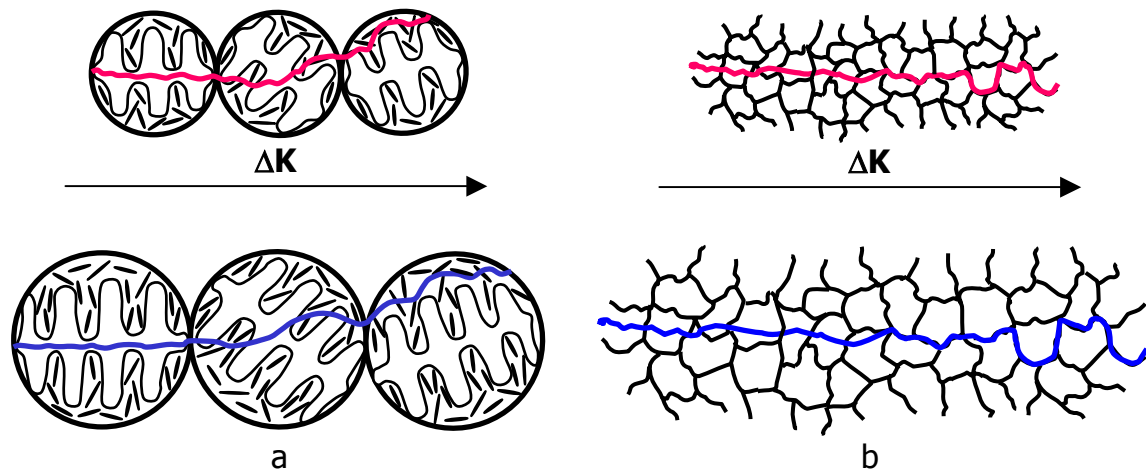
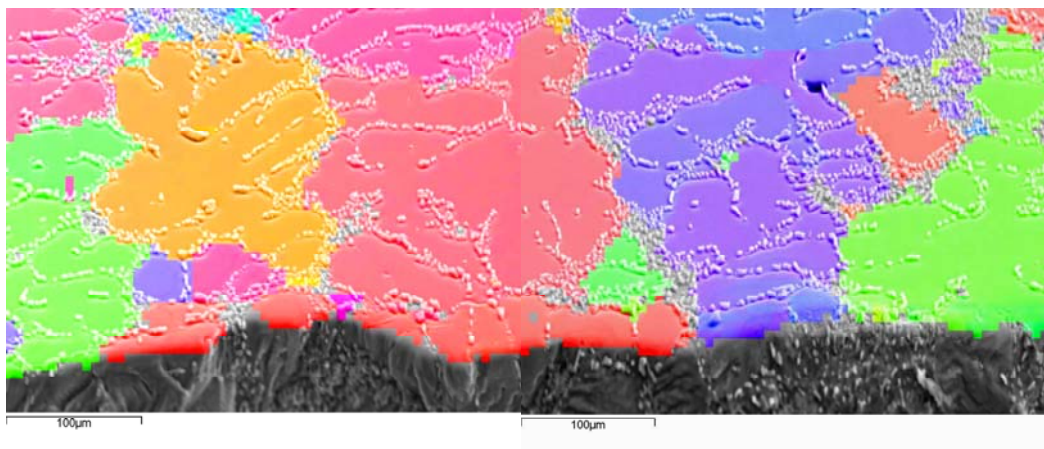
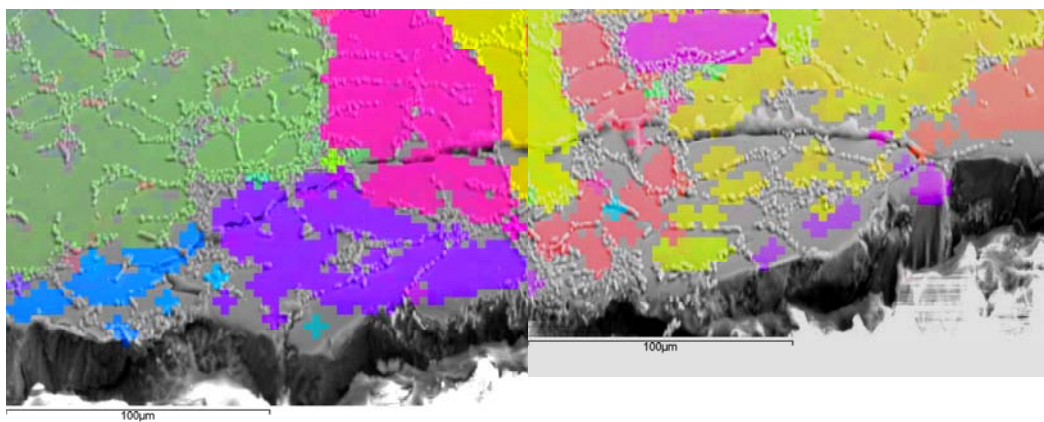


Figure 25. Microstructural feature smaller than grain size govern fatigue crack growth behavior of A356 alloys (a); grain size effect in alloys with no eutectic structure (b).



Lower
Region II



Upper
Region II

Figure 26. Grain structure of a modified A356 at two ΔK levels.

Electron backscatter diffraction (EBSD) techniques were also used to observe the grain structure at different ΔK levels, Figure 26. The main objectives were to reveal any possible preference of the cracks for certain crystallographic planes, and also to analyze if the preferential propagation through Al-Si eutectic regions at high ΔK is related to grain boundaries. No preferred orientation of the primary Al grains along the crack path was observed. No effects of the grain (or subgrain) boundaries on the crack propagation through the eutectic regions at high crack driving forces were found. The secondary crack in Figure 26 reveals sampled Si particles located inside the grains, on the dendrite cell boundaries.

However, in the 1%Si alloy, with no eutectic Si, grain size has an effect both in near threshold regime (due to differences in roughness induced closure) and Region III (due to differences in crack path length during intergranular crack propagation), Figures 27 and 28.

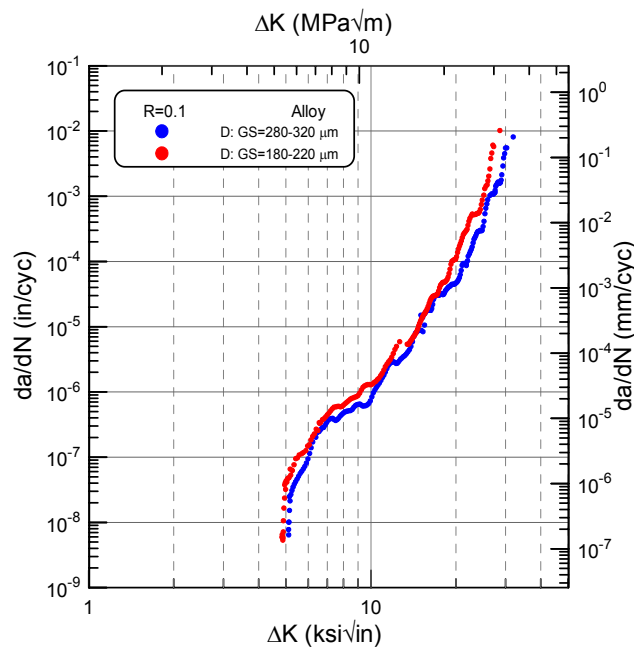


Figure 27. Fatigue crack growth behavior of 1%Si alloys of different grain size.

The absence of the first inflection point, between near threshold regime and Region II, is a reflection of a gradual increase in the sampled grain boundaries with increasing ΔK until the plastic zone becomes sufficiently large and the crack propagates exclusively along grain boundaries leading to final failure (Region III). Therefore, in this case grain size is the parameter controlling the fatigue crack growth mechanisms similar to wrought alloys, Figure 28.

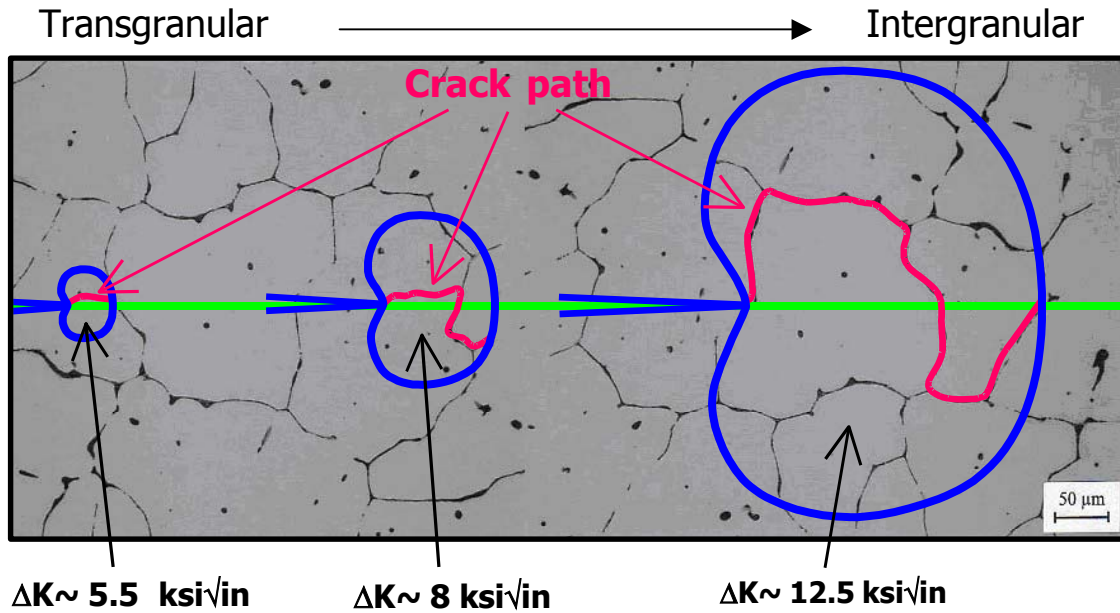


Figure 28. Crack evolution with increasing ΔK for cast alloys with no eutectic phase.

Residual stress was found to be almost constant in the region of the CT sample where the sample was tested [26]. Therefore, the effect of residual stress on crack growth rates decreases with increasing ΔK because the ratios of residual stresses to applied stresses become increasingly lower. For the residual stresses in this study, ΔK_{th} was nearly doubled by the compressive residual stress, but fracture toughness was only 20% higher than that in the residual stress free samples.

SUMMARY

The behavior of the studied Al-Si-Mg alloys in the near threshold regime is dominated by closure mechanisms. The two main sources of closure were residual stress (introduced during quenching) and microstructurally induced fracture surface roughness. In the presence of high residual stress, microstructure induced closure plays a secondary role, its effects being masked by residual stress. At low residual stress levels, the effect of microstructure becomes evident and the thresholds, ΔK_{th} , are inversely proportional to the vol% eutectic Si. The higher the Si content the lower the roughness induced closure level, and lower threshold respectively. These differences were attributed to crack deflection when encountering Si particles. Similarly, rougher fracture

surfaces were found in the unmodified alloys at both 7 and 13%Si levels. The unmodified alloys showed higher threshold and therefore better high cycle fatigue life.

With increasing ΔK , the effects of crack closure are less significant, and the fatigue crack growth mechanisms become strongly dependent on the matrix strength and the interface strength between primary α -Al structure and eutectic Si particles. With increasing ΔK from lower Region II to upper Region II and Region III, the fracture surface roughness increases. This increase is associated with a change in fatigue crack growth mechanisms. While a flat surface corresponds to a crack propagating along the Al dendritic structure, the rougher surface is a reflection of a preferential growth through the Al-Si eutectic regions. As a general rule a crack always seeks the path of least resistance that is represented by the damaged (most damaged) microstructural features ahead of it. Therefore, these changes in mechanisms were explained using correlations of the plastic zone size at various ΔK levels with the microstructural features enveloped by it. Small plastic zones restrict the availability of damaged Si particles (or interfaces with the Al matrix) and therefore restrain the possibility of crack meandering. This corresponds to a flat appearance of the crack with sporadic Si encounters. At high ΔK , however, the larger plastic zone size permits crack meandering through severely damaged Si particles away from the crack front, and this explains the preferential growth through the eutectic regions.

In Region III, the crack advances preferentially through the Al-Si eutectic regions, and high crack growth rates (in upper Region III) are governed by ductile tearing. The alloys' behavior in this region was well correlated with Si morphology, and a fracture toughness ranking based on Si morphology was observed. Modified and low Si content alloys showed higher fracture toughness, and therefore better low cycle fatigue response.

Differences in the behavior of T4 and T61 samples were observed away from the closure affected regions. While T61 shows a better fatigue crack growth resistance in upper Region II, T4 leads to higher toughness. The behavior of the T4 samples in Region II was explained by considering the alternative paths of least resistance available. In Region III, the increased plasticity levels at the crack tip result in more blunted cracks, increasing the crack growth resistance and fracture toughness.

In the grain size range investigated, grain size plays a minimal role in the fatigue crack growth response of the studied alloys, due to the fact that fatigue crack

growth advance is controlled by microstructural features smaller than the grain size (Si particles, SDAS). In the alloys with no eutectic Si (1%Si), grain size shows an effect similar to wrought alloys.

ACKNOWLEDGEMENTS

The authors address their thanks to General Motors Corp. for partly supporting the fatigue crack growth testing and Alcan for providing high purity aluminum needed in this work as well as evaluating the 3D fracture surface roughness of the tested samples. Special thanks are directed to Palmer Foundry for the significant contribution in the sand mold design and the preparation of the molds. The authors address their gratitude to Dr. Peggy Jones of General Motors and Dr. Fred Major of Alcan for their contributions, guidance, and technical assistance during the entire duration of the study. Dr. Libo Wang's assistance to the castings preparation is greatly appreciated. The fatigue crack growth testing was done at Fracture Technology Associates. Special thanks go to Mr. Keith Donald for his important contribution to the critical issues related to residual stress impact on the fatigue crack growth response. The authors also direct their thanks to Mr. Thomas Murphy of Hoeganaes for his assistance with the 2D roughness index determination.

REFERENCES

- [1]. D.A. Lados, D. Apelian, and A.M. de Figueredo, in: M. Tiryakioglu, J. Campbell (Eds.), *Advances in Aluminum Casting Technology II, Proceedings from Materials Solutions 2002*, ASM, Metals Park, OH, 2002, pp. 185-196.
- [2]. M.J. Couper, A.E. Neeson, and J.R. Griffiths, *Fatigue Fract. Engng Mater. Struct.*, 13, 3, 1990, pp. 213-227.
- [3]. Q.G. Wang, D. Apelian, and D.A. Lados, *J. Light Metals* 1, 1, 2001, pp. 73-84.
- [4]. H. Jiang, P. Bowen, and J.F. Knott, *J. Mater. Sci.*, 34, 1999, pp. 719-725.
- [5]. B. Skallerud, T. Iveland, and G. Harkegard, *Engng Fract. Mechanics*, 44, 6, 1993, pp. 857-874.
- [6]. J.A. Odegard and K. Pedersen, SAE Technical Publication 940811, 1994, pp. 25-32.
- [7]. J.C. Ting and F.V. Lawrence, Jr., *Fatigue Fract. Engng Mater. Struct.*, 16, 6, 1993, pp. 631-647.
- [8]. A. Wickberg, G. Gustafsson, and L.E. Larsson, SAE Technical Publication 840121, 1984.
- [9]. C. Nyahumwa, N.R. Green, and J. Campbell, *AFS Trans.*, 106, 1998, pp. 215-223.
- [10]. K. Shiozawa, Y. Tohda, S.-M. Sun, *Fatigue Fract. Engng Mater. Struct.*, 20, 2, 1997, pp. 237-247.

- [11]. B. Zhang, W. Chen, and D.R. Poirier, *Fatigue Fract. Engng Mater. Struct.*, 23, 2000, pp. 417-423.
- [12]. S. Gungor and L. Edwards, *Fatigue Fract. Engng Mater. Struct.*, 16, 4, 1993, pp. 391-403.
- [13]. Q.G. Wang, D. Apelian, and D.A. Lados, *J. Light Metals*, 1, 1, 2001, pp. 85-97.
- [14]. S. Kumai, J. Hu, Y. Higo, and S. Nunomura, *J. Jap. Inst. Light Metals*, 45, 4, 1995, pp. 198-203. (in Japanese)
- [15]. S. Kumai, S. Aoki, S.-W. Han, and A. Sato, *Mater. Trans., JIM*, 40, 7, 1999, pp. 685-691.
- [16]. M.J. Caton, J.W. Jones, J.M. Boileau, and J.E. Allison, *Metall. Mater. Trans. A*, 30A, 1999, pp. 3055-3068.
- [17]. D.A. Lados and D. Apelian, "Fatigue Crack Growth Characteristics in Cast Al-Si-Mg Alloys – Part I: Effect of Processing Conditions and Microstructure", submitted to *Mater. Sci. Eng. A*, 2003.
- [18]. K.S. Chan, P. Jones, and Q. Wang, *Mater. Sci. Eng.*, A341, 2003, pp.18-34.
- [19]. K. Gall, N. Yang, M. Horstemeyer, D.L. McDowell, and J. Fan, *Metall. Mater. Trans. A*, 30A, 1999, pp. 3079-3088.
- [20]. F.T. Lee, J.F. Major, and F.H. Samuel, *AFS Trans.* 104, 1996, pp. 785-795.
- [21]. S. Kumai, J. Hu, Y. Higo, and S. Nunomura, *Acta Mater.*, 44, 6, 1996, pp. 2249-2257.
- [22]. M. Kubota, Y. Ochi, A. Ishii, R. Shibata, *Mater. Sci. Research. Int.*, 4, 3, 1998, pp. 193-199.
- [23]. J.K. Shang, W. Yu, and R.O. Ritchie, *Mater. Sci. Eng. A*, 102, 1988, pp.181-192.
- [24]. Y. Sugimura and S. Suresh, *Metall. Mater. Trans. A*, 23A, 1992, pp. 2231-2242.
- [25]. S. Kumai, A. Sekikawa, J. Hu, Y. Higo, and S. Nunomura, *J. Jap. Inst. Light Metals*, 45, 4, 1995, pp. 204-208. (in Japanese)
- [26]. D.A. Lados and D. Apelian, "The Effect of Residual Stress on the Fatigue Crack Growth Behavior of Cast Al-Si-Mg Alloys – Mechanisms and Corrective Mathematical Models", to be submitted to *Metall. Mater. Trans. A*.
- [27]. D.A. Lados and D. Apelian, "Quenching Modes and Residual Stress Levels in Cast Al-Si-Mg Alloys - Mechanisms and Effects on Static and Dynamic Properties", to be submitted to *Metall. Mater. Trans. A*.
- [28]. ASTM Standard E647, Standard Test Method for Measurement of Fatigue Crack Growth Rates, Annual Book of ASTM Standards, Vol. 03.01, 2000.
- [29]. D. Taylor, *Int. J. Fatigue*, 10, 2, 1988, pp. 67-79.
- [30]. L. Lawson, E.Y. Chen, and M. Meshii, *Int. J. Fatigue*, 21, 1999, pp. S15-S34.
- [31]. W. Elber, *Engng Fract. Mechanics*, 2, 1970, pp. 37-45.
- [32]. S. Suresh, *Fatigue of materials*, Cambridge University Press, First Edition, 1991.

- [33]. G.H. Bray and J.K. Donald: in *Advances in Fatigue Crack Closure Measurement and Analysis-Second Volume*, ASTM STP 1343, American Society for Testing and Materials, 1999, pp. 57-78.
- [34]. S. Pearson, *Engng Fract. Mechanics*, 7, 1975, pp. 235-247.
- [35]. C.Y. Kung and M.E. Fine, *Metall. Mater. Trans. A*, 10A, 1979, pp. 603-610.
- [36]. A. Fathulla, B. Weiss, and R. Stickler, *Proc. Spring Meeting French Metals Society*, Paris, 1984, p. 182.
- [37]. A. Fathulla, B. Weiss, and R. Stickler, *Fatigue 84 (EMAS, Warley)*, 1984, p. 1913.
- [38]. M.N. James and R.E. Garz, *Int. J. Fatigue*, 13, 2, 1991, pp. 169-173.
- [39]. A. Plumtree and S. Schafer, in *The Behavior of Short Fatigue Cracks*, EGF Pub. 1, edited by K.J. Miller and E.R. de los Rios, Mechanical Engineering Publications, London, 1986, pp. 215-227.
- [40]. D.A. Lados and D. Apelian, "Validity Limits for Elastic Definitions in Cast Al-Si-Mg Alloys with Enhanced Plasticity-Linear Elastic Fracture Mechanics versus Elastic/Plastic Fracture Mechanics", to be submitted to *Engng Fract. Mechanics*.
- [41]. R.C. McClung and H. Sehitoglu, *Engng Fract. Mechanics*, 33, 1989, pp. 237-271.
- [42]. M.D. Dighe and A.M. Gokhale, *Scr. Met.*, 37, 1997, pp. 1435-1440.
- [43]. M. Schaefer and R.A. Fournelle, *Metall. Mater. Trans. A*, 27A, 1996, pp. 1293-1302.
- [44]. S.-W. Kim, S.-W. Han, U.-J., Lee, K.-D. Woo, *Materials Letters*, 58, 2003, pp. 257-261.
- [45]. J.A. Odegard, "Fatigue Behavior in a DC-Cast A356 (AlSi7Mg) Aluminum Casting Alloy", Ph.D. thesis, Norwegian Institute of Technology, Trondheim, Norway, 1992.
- [46]. A. Turnbull, E.R. de los Rios, *Fatigue Fract. Engng Mater. Struct.*, 18, 11, 1995, pp. 1355-1366.
- [47]. G.A. Osinkolu, G. Onofrio, M. Marchionni, *Mater. Sci. Eng.*, A356, 2003, pp. 425-433.

Chapter 6

Fatigue Crack Growth Characteristics in Cast Al-Si-Mg Alloys – Part II: *Life Predictions Using Fatigue Crack Growth Data*

D. A. Lados and D. Apelian
Worcester Polytechnic Institute, Worcester, MA, USA

ABSTRACT

Fatigue crack growth data are critical inputs for damage tolerant designs, which acknowledge initial flaws in materials subject to cyclic loading. Not only are the fatigue crack growth data used for life predictions; they also provide understanding of the microstructural effects on crack propagation at different stages during service life. The Paris law, $\frac{da}{dN} = C(\Delta K)^m$, represents an important link between linear elastic fracture mechanics (fatigue crack growth concepts) and fatigue life, and it applies when the plastic contributions at the crack tip are small enough to allow linear elastic formulations. Using this relationship, when K is known for a component under specified loading conditions, fatigue crack growth life can be determined by integrating between initial and final conditions of the crack. This analysis, however, involves complex numerical computations. Therefore, based on it, a unified tool has been developed (AFGROW) that enables one to predict fatigue life and fracture mode from the material properties, fatigue crack growth parameters, initial flaw size, stress level, etc. In this paper, fatigue crack growth data for several cast Al-Si-Mg alloys in various heat treat conditions are used to evaluate low and high cycle fatigue behavior using a life predictive software, AFGROW. Thus, this method can be used to optimize alloy's microstructure and heat treatment for a given design requirement. Several examples of life predictions are presented through case studies representing real life applications.

Keywords: Al-Si-Mg alloys; Fatigue crack growth; Life Predictions-AFGROW; Low and high cycle fatigue.

I. INTRODUCTION AND BACKGROUND

There are two design philosophies, "safe life or damage intolerant" and "damage tolerant", that dictate the material selection for a component under certain operating conditions. The two design methods also correspond to two distinct ways of collecting and presenting the data. The first, basic method of presenting fatigue data is by using S-N curves, representing a plot of stress, S, versus numbers of cycles to failure, N. The second method examines fatigue crack growth rate as a function of stress intensity factor range, ΔK , and allows the user to delineate between safe and fail regions. Each of these will briefly be addressed below.

In the first design approach, the relationship between S and N is determined for selected mean stress, stress ratio, and amplitude relevant for the type of application the component is subjected to. The tests can be conducted in rotating bending, axial, or shear loading, and commonly the conditions met in engineering applications involve mean stresses different from zero when an alternating stress and a mean, steady stress are superimposed.

S-N curves are most often determined for fatigue failures at high numbers of cycles (high cycle fatigue, $N > 10^5$ cycles) when the stress is elastic on a large scale even though the material exhibits localized plasticity. This is experienced in applications such as turbine engines, turbine blades, jet engines, and in automotive, engine blocks, cylinder heads, pistons, rotating shafts, suspension components, etc. The number of cycles to failure increases with decreasing stress. For ferrous materials and other materials that have fatigue limits (limiting stress below which the material is presumably subjected to an infinite number of cycles without failure), the number of cycles is at least 10^7 . The fatigue "limit" of other materials (mostly non-ferrous) that do not exhibit fatigue a distinct limit, such as aluminum, magnesium, and copper alloys, the "limit" is generally characterized by reporting the fatigue strength at an arbitrary number of cycles, 10^8 or 5×10^8 cycles. The S-N curve for high cycle fatigue, Figure 1a, is usually described by the Basquin equation [1] given as $\sigma_a = A(N)^B$, or alternatively written, $\sigma_a = \Delta\sigma/2 = \sigma'_f(2N)^b$.

Certain applications require investigation of the material behavior at high stresses and low number of cycles (nuclear pressure vessels, most other types of power machinery, applications with stresses of thermal origin, as well as automotive parts such as steering knuckles, control arms, etc.). Under high stresses fatigue life is progressively decreased, and the associated plastic deformation makes the use of stress as a relevant parameter quite difficult. Therefore, for low number of cycles (low cycle fatigue, $N < 10^4$, 10^5 cycles), the tests are usually conducted under controlled strain instead of load or stress. Low cycle fatigue test results are presented by plotting the plastic strain range, $\Delta\varepsilon_p$, versus the number of cycles, N. This relationship is known as Coffin-Manson equation [2-4], $\Delta\varepsilon_p = C(N)^D$ or alternatively, $\Delta\varepsilon_p/2 = \varepsilon'_f(2N)^c$

For safe life design the allowable stress for a given life (that can range from 10^4 - 10^9 cycles) is conservatively determined from ε -N or S-N data modeled by the Basquin equation or the Coffin-Manson equation respectively. This approach does not consider the presence of flaws in the material.

Numerous studies have been conducted and several S-N curves were generated for various alloys with different microstructural features (including defects). Life

studies found in the literature targeted different materials and manufacturing processes such as: squeeze cast A356 and A390, Al based metal matrix composites [5]; Al-Zn-Mg-Cu (7010) squeeze cast, chill cast, and rolled plates [6]; Al-Si-Cu die cast alloys [7]; Al 206, 319, 390 [8]; cast Al-Si-Cu W319 [9]; Al-Si-Mg-Cu alloys [10]; and cast and forged fatigue life behavior of aluminum alloys have been contrasted and studied [11].

The role of microstructural features on fatigue life has been reported in the literature by many authors [9,12-14]. Several studies showed the effect of different degrees of porosity on fatigue life [12,15,16], as well as the effect of pore size and distribution [17,18]. The influence of new and old oxides in filtered and unfiltered castings has been investigated [16,18]. The effects of casting defects, especially surface and subsurface defects in Al-Si-Mg alloys [19] and the importance of surface texture [20] were also discussed. An influence of Fe level on fatigue life was observed [12,14] and a decrease in fatigue life with Mg content was reported [14]. Different heat treatment responses of this class of alloys with respect to fatigue were observed [21,22]. As can be seen, many empirical relationships have been reported in the literature when it comes to Al-Si-Mg cast alloys.

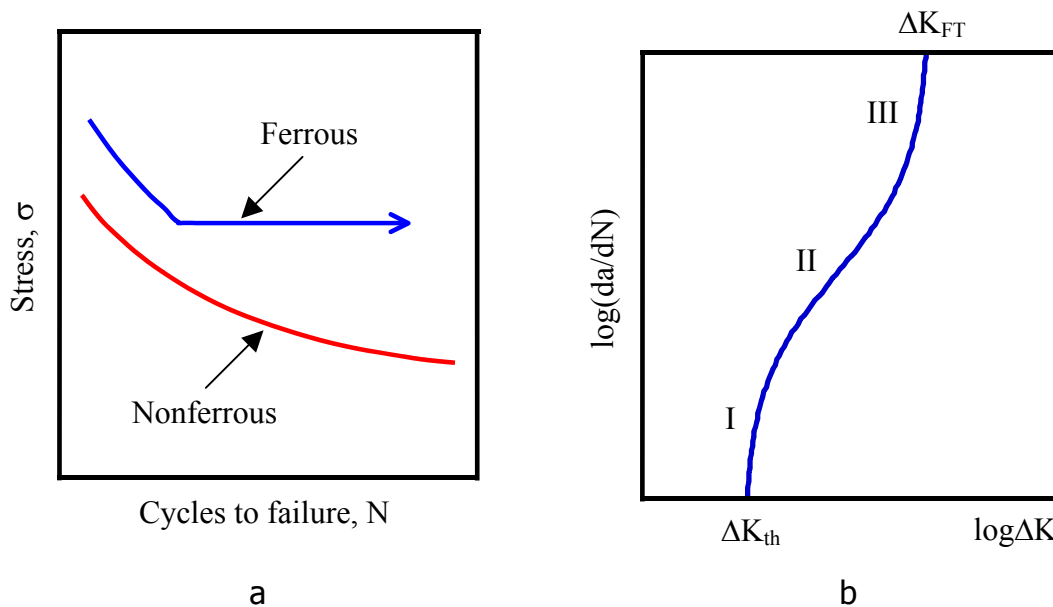


Figure 1. Typical fatigue curves for ferrous and nonferrous materials (a) and fatigue crack growth curve (b).

There is, however, a second design philosophy in which crack propagation relationships allow a fail-safe design when the unavoidability of flaws is recognized, and the safe load and flaw size that prevent failure within a given service life are determined. There is a relationship between fatigue crack growth rate and stress intensity factor range, ΔK that has a sigmoidal shape as shown in

Figure 1b. ΔK is a function of the crack length (a), applied stress (σ), and specimen, and crack geometry (Y), and has the general form: $\Delta K = Y \cdot \Delta\sigma \cdot \sqrt{\pi a}$ [23]. Region I is limited by a threshold value ΔK_{th} , below which there is no detectable fatigue crack growth, while Region III is a region of fast crack advance and the curve asymptotically approaches the “pseudo-fracture” toughness of the material (the term “pseudo” was used because the crack growth specimens did not meet the dimensional requirements for plane strain fracture toughness although they were valid for crack growth testing per ASTM E647). Region II is represented by a linear relationship between crack growth rate da/dN and stress intensity factor range, ΔK , called the Paris law $\frac{da}{dN} = C(\Delta K)^m$ [23]. The effect of increasing stress ratio, R , is generally more pronounced in Regions I, and III compared to Region II. To appropriately characterize Regions I and III, a similar relation (Forman equation, [24]): $\frac{da}{dN} = \frac{C(\Delta K)^m}{(1-R)K_{FT} - \Delta K}$ has been developed, which takes into account the increase in crack growth rate due to increases in stress ratio, R . These relationships connect fracture mechanics to fatigue, and through integration, the number of cycles to failure can be determined for each loading condition and existing flaw. Or, in other words, for damage tolerant design the allowable stress is determined by integrating the fatigue crack growth curves for a conservatively estimated service life. In this manner both life predictions and crack growth mechanisms at the microstructural level can be assessed. The latter leads to a mechanistic understanding of the alloys’ fatigue behavior.

Several authors have concentrated on fatigue crack growth studies of different aluminum alloys. Various microstructural features such as Si morphology, SDAS, etc., heat treatment, porosity level, loading/testing conditions (mean stress, stress ratio, frequency), operating atmospheres (corrosion fatigue), operating temperature, etc. were commonly investigated. Si morphology influence on fatigue crack growth of A356 [25,26]; die cast alloys [27]; Al-12%Si-0.35%Mg [28]; rheocast and thixocast A356 alloys [29], have been reported. SDAS was observed to play an important role in the fatigue behavior of hypoeutectic A356 [25,26] and 319 alloys [30]. Different heat treating conditions were compared for A356 alloys [22,25,26,31] and B319 [31]. Porosity-fatigue crack growth interactions are reported for Al-Si-Mg [32], Al-Cu [32,33], and Al-Mg [32] alloys. Mean stresses [34], stress ratios [28,34], and test frequency [35] have been observed to influence fatigue crack growth. Corrosive atmospheres [35], as well as high temperatures [36] were reported to affect fatigue crack growth behavior of Al-Si-Mg-Cu alloys.

There is need for a convenient methodology to convert these data to life predictions; such an enabling procedure can be an extremely useful and powerful design tool. In this paper a simple method to use fatigue crack growth data for

fatigue life predictions is presented. A public domain software package was used to rank Al-Si-Mg alloys with various Si level/morphology, different SDAS and heat treatment conditions for both low cycle and high cycle fatigue applications. Specific initial flaw sizes and locations, as well as maximum applied stress were introduced in the simulations. Two stress ratios, $R=0.1$ and $R=0.8$, were selected and compared.

II. EXPERIMENTAL PROCEDURE

II.A. *Alloys, fatigue crack growth specimens, and testing conditions*

Five Al-Si-Mg alloys, Al-1%Si-0.45%Mg, Al-7%Si-0.45%Mg (A356, unmodified=UM), Al-7%Si-0.45%Mg (A356, Sr-modified=M), Al-13%Si-0.45%Mg (eutectic, unmodified=UM), and Al-13%Si-0.45%Mg (eutectic, Sr-modified=M) were investigated. A similar grain size level (280-320 μm) was achieved in all alloys by appropriate additions of Al-5%Ti-1%B master alloy. All five alloys were T61 heat treated and the A356-like alloys with 7%Si were T4 heat treated as well. A comparison T61 to T4 reveals the influence of heat treatment on the fatigue crack growth behavior of the alloys, and it quantifies heat treating effects in fatigue life predictions.

The compact tension (CT) specimens used for the fatigue crack growth work were produced using a sand mold with central top and bottom gray cast iron chills to insure a uniform, well controlled SDAS throughout the testing regions. The test dimensions of the CT samples are 3.75 in x 3.6 in x 0.4 in (95 mm x 91 mm x 10 mm). The notch length is 1.5 in (38 mm) measured from the front face of the sample, and 0.75 in (19 mm) measured from the pinholes. Further details regarding the alloys evaluated and specimen preparation can be found elsewhere [26].

Fatigue crack growth testing was performed as per ASTM E647 specifications [37]. First, the specimens were tested under decreasing crack driving force, K , to evaluate the thresholds (Region I), and subsequently under increasing crack driving force range (Regions II and III). The upper limit of the crack driving force was assumed to be the "pseudo" fracture toughness of the material. However, due to increased plasticity and tearing at high ΔK , the actual fracture toughness of the materials (J_{max}) was determined from static fracture toughness tests according to ASTM E1820 standard [38]. J_{IC} and J_{max} , represent the lower and upper bound toughness values, respectively. The use of J_{IC} is a conservative approach, which gives rise to fracture toughness values lower than the one provided by the elastic K analysis from the fatigue crack growth experiments. Therefore, the actual static fracture toughness of the material was calculated based on J_{max} values and subsequently used in the AFGROW simulations. Even though, unlike J_{IC} , J_{max} is specimen size sensitive, this choice is valid considering

that fatigue crack growth and fracture toughness testing was performed on identical samples.

II.B. AFGROW simulations – background and input/output parameters

To assess and rank the performance of the studied materials, the AFGROW structural life prediction program [39] developed by the Wright-Patterson Air Force Research Laboratory was used. The origins of the program go back 20 years when ASDGRO (AFGROW'S predecessor) was first released. Over the years, several changes and updates were implemented to accommodate the new advances in fracture mechanics definitions and interpretation. Based on the experimentally generated fatigue crack growth data, various case studies were run using AFGROW software to predict numbers of cycles to failure.

The input data necessary to run AFGROW require:

- Crack growth data (ΔK_{th} , Paris law coefficients, C, m, and other exponents and limits needed in the da/dN vs. ΔK relation),
- Material properties (i.e. yield strength, ultimate stress, flow stress, Young's modulus, plane strain and plane stress fracture toughness, etc.),
- Geometry and dimensions of the component, initial flaw geometry, size, and location,
- Maximum applied load, stress ratio, choice of constant/variable amplitude, retardation/closure corrections, residual stress adjustments for known residual stresses, environmental conditions, etc.

Although the Forman crack growth rate equation introduced earlier, accounts for the stress ratio, R, effect at low and high growth rates, it does not permit any data shifting modeling as a function of stress ratio. There is no parameter in the equation to allow a direct R shift adjustment. The amount of shifting is controlled by the plane stress fracture toughness of a given material.

Accordingly, AFGROW introduces an alternative formulation of the da/dN vs. ΔK relation, similar to NASGRO equation, used in NASA's crack growth life prediction program:

$$\frac{da}{dN} = C \left[\left(\frac{1-f}{1-R} \right) \Delta K \right]^m \frac{\left(1 - \frac{\Delta K_{th}}{\Delta K} \right)^p}{\left(1 - \frac{K_{max}}{K_{FT,crit}} \right)^q}$$

Regarding the crack configuration, there are several predefined crack models for which closed form or tabular stress intensity factor solutions are available, as well as crack models with weight function stress intensity solutions. In this study crack solutions from the first category were selected.

The output data consist of life predictions (cycles to failure) and failure modes for various applications, and some examples are presented in the next section.

III. RESULTS AND DISCUSSION

Fatigue crack growth behavior of the studied alloys is presented in Figure 2. A threshold ranking as well as a toughness ranking as a function of the Si level of the alloy can be observed. Lower Si contents increase both crack growth threshold and fracture toughness. A decrease in Si also decreases the crack growth rate in the Paris region. Alloys with higher thresholds and toughness, and lower crack growth rates provide more resistance to the advancing crack, and therefore have longer lives. However, when some of these characteristics are favorable to fatigue resistance and others are less favorable (for example high threshold but low toughness), the alloy selection becomes application oriented and only a thorough understanding of the operating conditions can guide which one of these characteristics controls the fatigue behavior. Certainly, fatigue crack growth resistance needs to be balanced against other material properties when the alloy selection is made. Needless to say, judgment is required, and the AFGROW simulation tool allows the engineer to have the needed information, such that an informed alloy and process selection can be made.

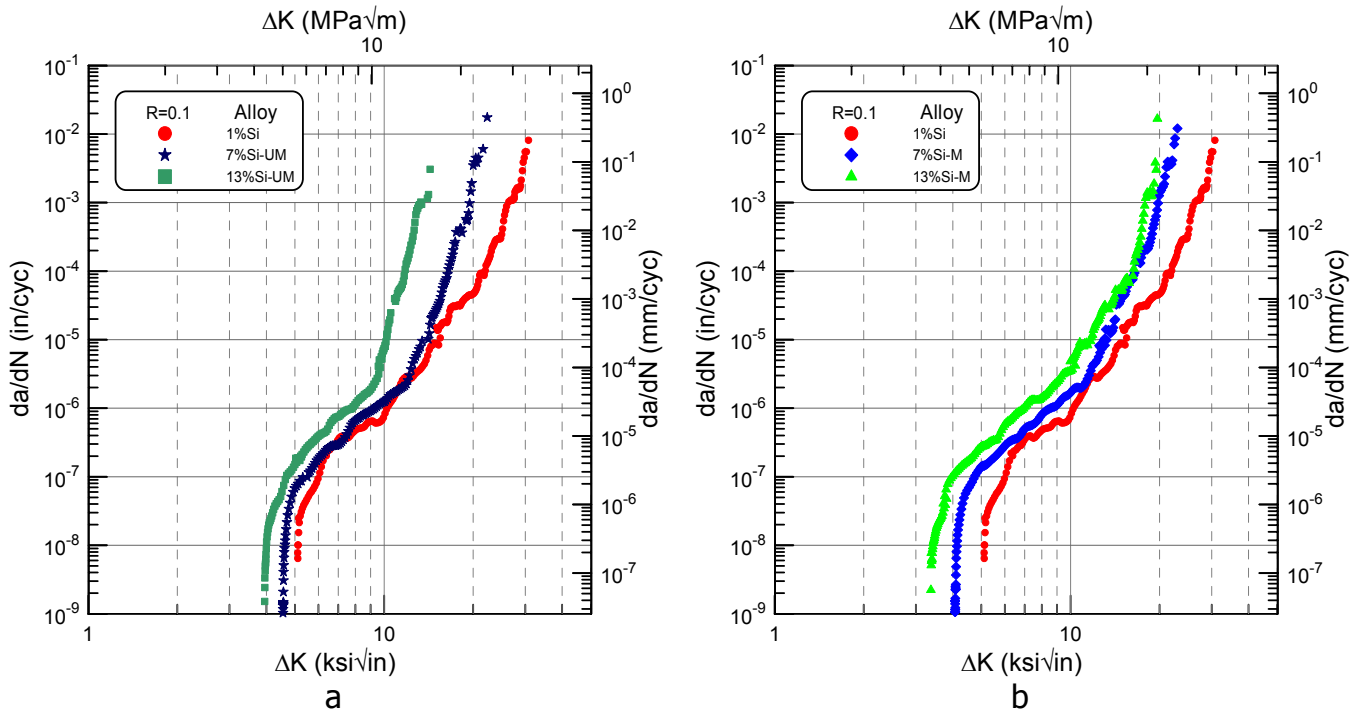


Figure 2. Fatigue crack growth behavior of unmodified alloys (a) and Sr-modified alloys (b) with different Si contents.

Fatigue crack growth and fatigue lives are influenced not only by changes in microstructural features such as SDAS and Si morphology (size, shape, distribution), but also by differences in the matrix strength that are determined by the heat treatment conditions. The effect of these material parameters and

testing conditions (stress ratio, R) on fatigue crack growth characteristics, are presented in Figure 3.

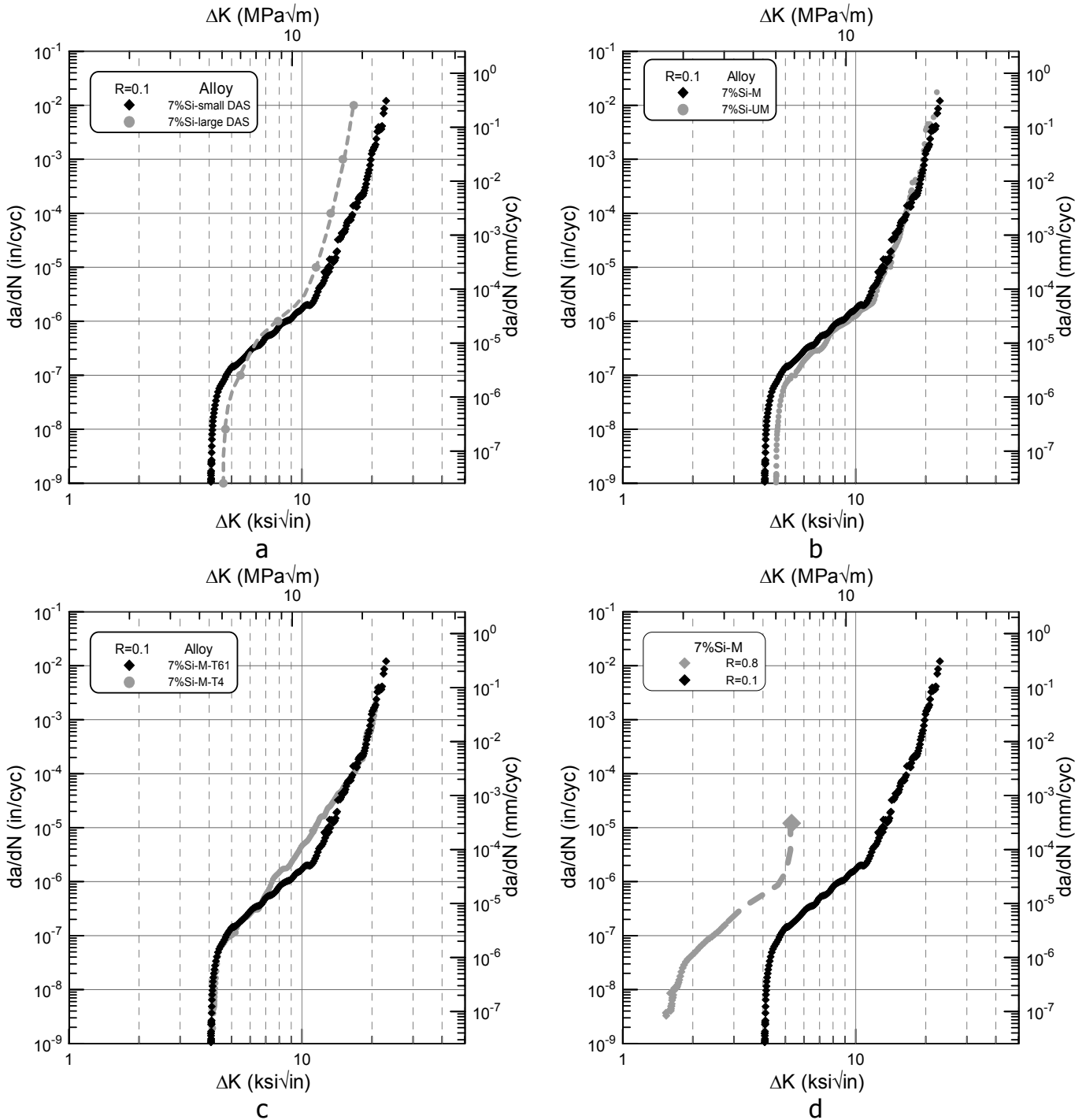


Figure 3. Fatigue crack growth characteristics of A356 with different SDAS (a), Si morphology (b), heat treatment (c), and stress ratio (d); UM is unmodified and M is Sr-modified.

III.A. Life predictions using fatigue crack growth data

From AFGROW database the geometry of the component was selected. A plate 4 in (101.6 mm) thick and 0.5 in (12.7 mm) wide was used for simulations (resembling a part of a cylinder head for instance – Figure 4). Three flaw types were assumed: a center semi-circular edge surface flaw, a center full-circular embedded flaw, and a single edge corner flaw as shown in Figures 4a-c. All simulations assumed residual stress free samples and constant amplitude loading.

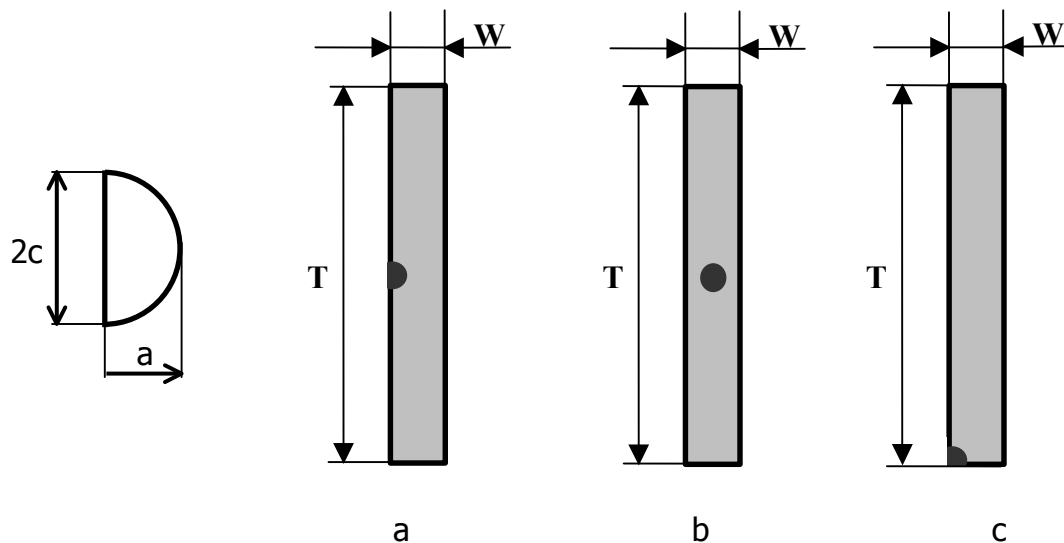


Figure 4. Rectangular plate with an: initial center semi-circular edge surface flaw (a), center full-circular embedded flaw (b), single edge corner flaw (c).

One remark needs to be made before presenting the results of the simulations. Life predictions are based on applications that require high cycle life and not excessively high maximum applied stresses; or low cycle fatigue applications that involve higher maximum applied stresses. The first class (high cycle) is threshold dominated, and life ranking is anticipated to be similar to the alloy's threshold ranking, while the latter (low cycle) is fracture toughness dominated and the life ranking of the alloy follows the fracture toughness.

Five stress levels and two initial flaw sizes were studied to establish an overall view of the material's response and magnitude of changes under a wide range of conditions. The flaws were assumed to be centered, semi-circular, edge surface flaws. Life predictions were determined for all the alloys in T61 conditions, as well as for the unmodified and modified A356 in T4 conditions. The results of the simulations are presented in Figures 5 and 6, respectively.

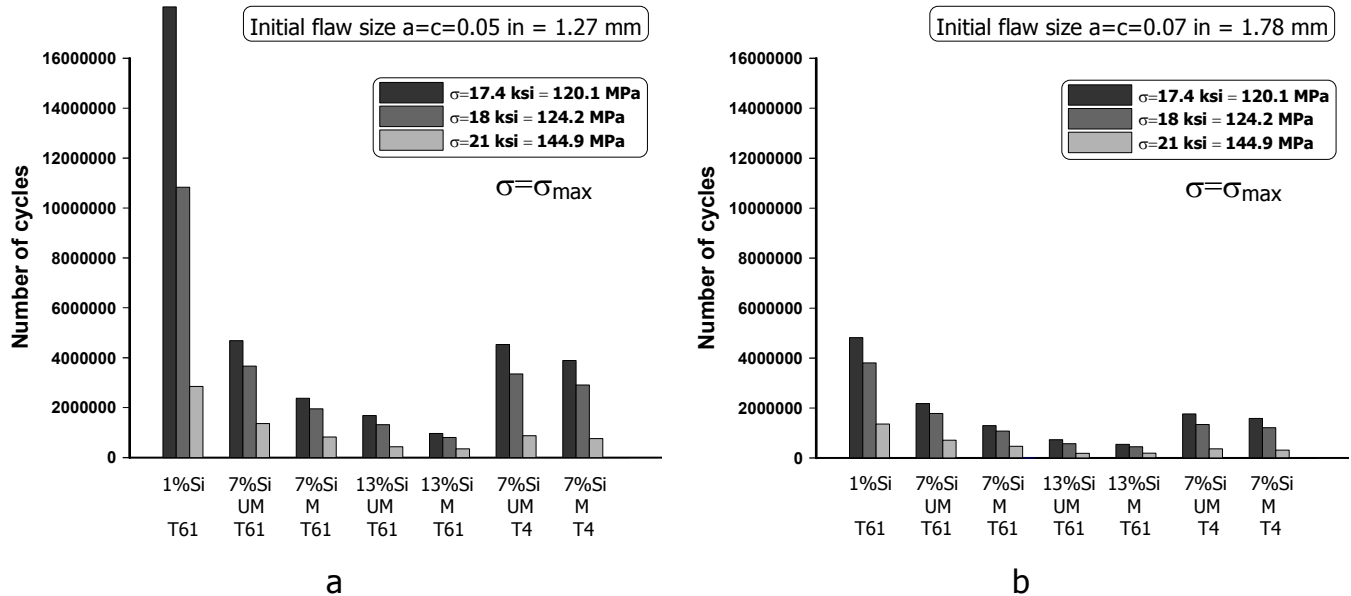


Figure 5. AFGROW life predictions demonstrating the effects of stress level and flaw size on fatigue life of various materials in the high cycle fatigue range; three low stress levels for: (a) 0.05 in (1.27 mm) initial flaw size, and (b) 0.07 in (1.78 mm) initial flaw size.

High cycle fatigue is threshold dominated and the alloy with the higher threshold, which is the unmodified, Figure 3b, has a longer fatigue life, Figure 5. When higher stresses are applied, a low cycle fatigue regime is reached, and the higher toughness alloy (modified) has an improved fatigue life, Figure 6. In Figure 6 we can note that 1 and 7%Si are in the high cycle fatigue regime, while the 13%Si alloy reached the low cycle fatigue regime. This conclusion is based on the change in fatigue response of the unmodified versus modified 13%Si alloys. For a given flaw size, the transition from high cycle to low cycle, for the 13%Si alloy occurs at a stress level of $\sigma \sim 21$ ksi (145 MPa), Figure 5a. A similar behavior is exhibited by the A356, 7%Si alloys, but at higher stress values, $\sigma \sim 30$ ksi (207 MPa).

The A356 alloys T4 heat treated present somewhat lower fatigue resistance compared to A356 T61 heat treated alloys. Even though T4 samples have similar thresholds and higher fracture toughness (the true fracture toughness was determined from static fracture toughness testing that accounts for plasticity effects in Region III), the crack growth rates in Paris region are higher and affect the overall fatigue life of the samples.

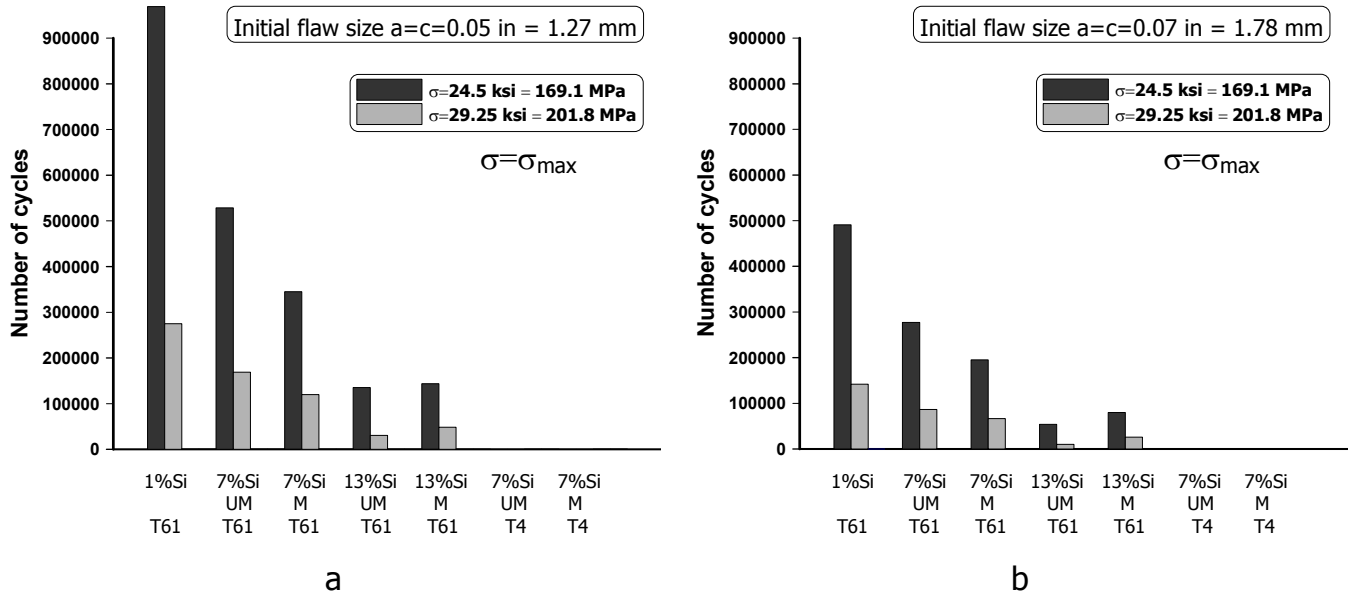


Figure 6. AFGROW life predictions demonstrating the effects of stress level and flaw size on fatigue life of various materials in the low cycle fatigue range; two high stress levels for: (a) 0.05 in (1.27 mm) initial flaw size, and (b) 0.07 in (1.78 mm) initial flaw size.

III.B. Case studies

Several design problems were constructed to understand how different parameters influence fatigue behavior of Al-Si-Mg cast alloys. Unless otherwise noted the stress ratio, R , was 0.1. Specifically eleven cases were addressed as follows:

1. Knowing that the maximum applied stress during service is $\sigma_{\max}=20$ ksi (138 MPa), and the component is expected to last $N=1,000,000$ cycles, the critical initial flaw size, tolerated by each alloy and heat treatment, was determined, Figure 7a.
2. Knowing that the casting process produces flaws smaller or equal to 0.05 in (1.27 mm), and the component is expected to last $N=1,000,000$ cycles, the critical maximum applied stress was determined for each model alloy and heat treatment, Figure 7b.

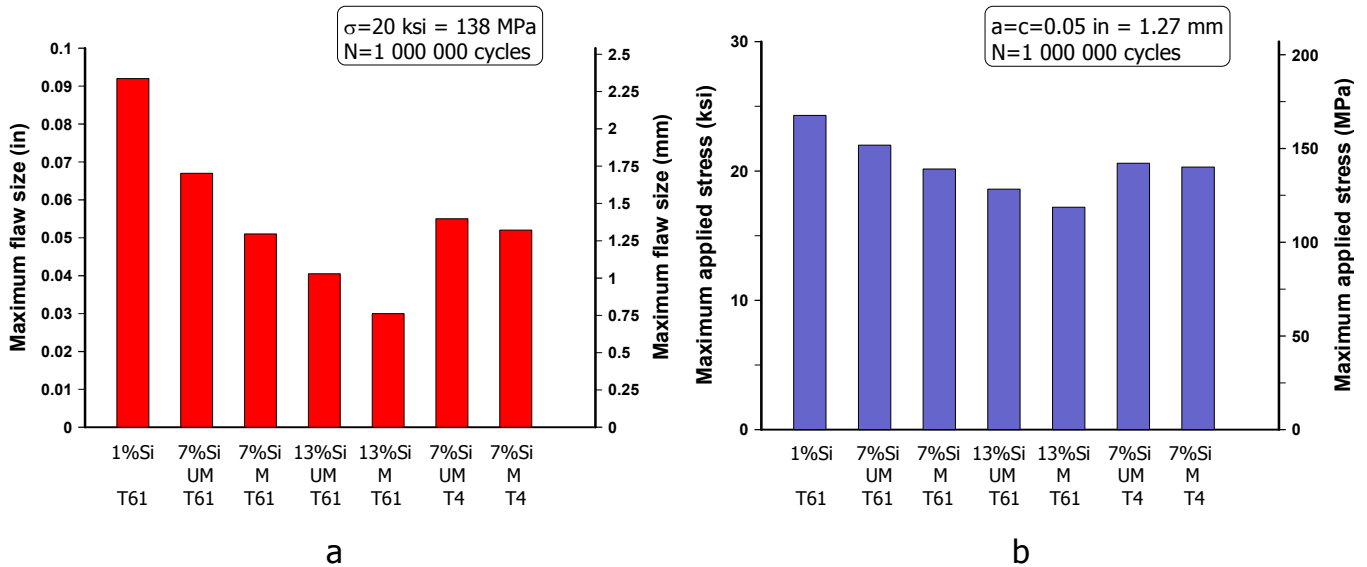


Figure 7. Initial flaw size requirements for selected maximum stress (a), and maximum applied stress requirements for selected flaw size (b) at 1,000,000 cycles.

3. Knowing that the maximum applied stress during service is $\sigma_{\max}=20 \text{ ksi}$ (138 MPa), and the component is expected to last $N=10,000$ cycles, the critical initial flaw size was determined for each model alloy and heat treatment, Figure 8a.

4. Knowing that the casting process creates flaws smaller or equal to 0.15 in (3.81 mm), and the component is expected to last $N=10,000$ cycles, the critical maximum applied stress was determined for each model alloy and heat treatment, Figure 8b.

For cases 3 and 4, the modified alloys show better life due to higher fracture toughness while in cases 1 and 2 the unmodified alloys are superior to the modified ones due to higher thresholds. As mentioned earlier in such cases, knowing the application (and thus the conditions the component will need to withstand) determines the alloy selection. It should be also noted that an increase in the desired number of cycles from 10,000 to 1,000,000 decreased the tolerable flaw size by a factor of 3 to 5 depending on the alloy composition. The large flaw sizes tolerated by the alloys in both low and high cycle fatigue applications (Figures 7 and 8) are dependent on the maximum applied stress; the higher the stress the smaller the acceptable defects.

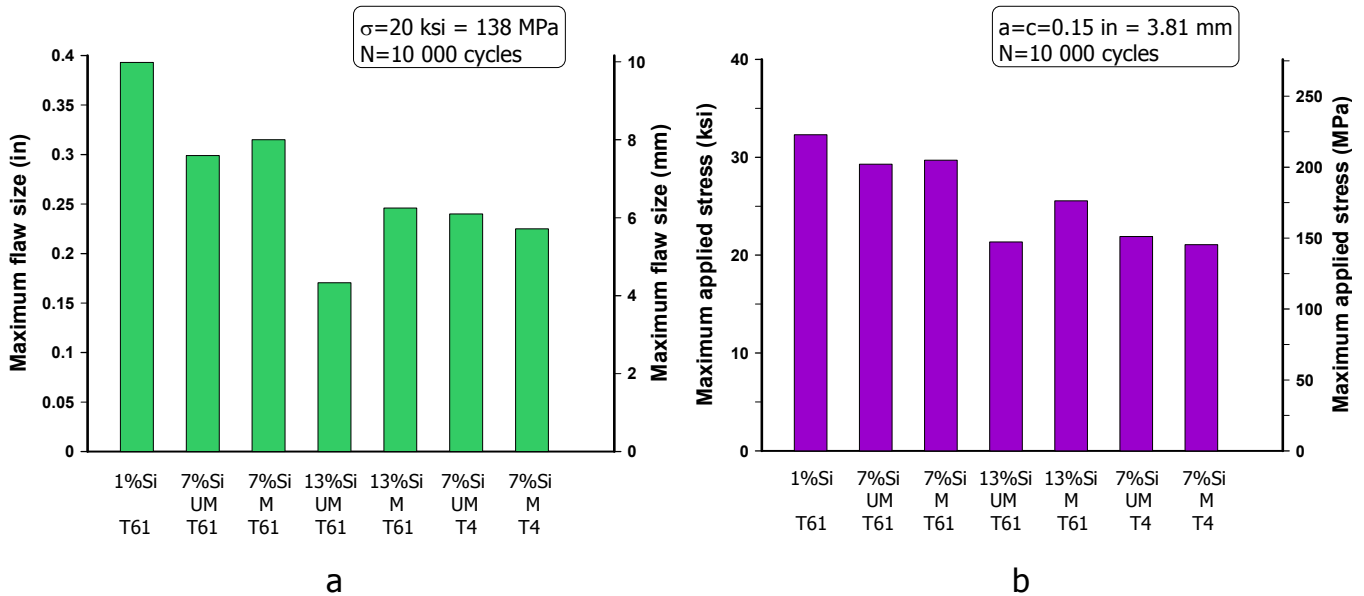


Figure 8. Initial flaw size requirements for selected maximum stress (a), and maximum applied stress requirements for selected flaw size (b) at 10,000 cycles.

To make the proper material selection the designer needs to understand the operating conditions of the component, and the potential damage the component is subjected to before making a final decision. Certainly a safe choice for fatigue crack growth resistance will always be a material with both high threshold and fracture toughness (i.e., Al-1% Si alloy). However, when considerations others than fatigue crack growth resistance are important, a balance should be reached, and the "best compromise" should be adopted.

All four cases above were solved for a constant SDAS of 20-30 μm . The next set of examples show how an increase in DAS influences the fatigue response of an A356 modified alloy. Figure 3a shows a higher threshold and a lower toughness for the sample with large SDAS values. Therefore, smaller differences are anticipated between the responses of the samples with different SDAS in high cycle fatigue regime compared to low cycle fatigue. This can be explained by considering the effects of threshold and toughness on different life regimes, as well as the additional contribution of the crack growth rates. Case studies 5 and 6 were developed to emphasize the influence of SDAS on fatigue life:

5. Knowing that the maximum applied stress during service is $\sigma_{\max}=20$ ksi (138 MPa), and the component is expected to last $N=10,000$ cycles and $N=1,000,000$ cycles respectively, the critical initial flaw sizes were calculated for a modified A356 alloy of different DAS, Figure 9a.

6. Knowing that the maximum applied stress during service is $\sigma_{\max}=25$ ksi (172.5 MPa), and the casting process creates flaws smaller or equal to 0.05 in (1.27 mm) and 0.15 in (3.81 mm) respectively, the number of cycles to failure are determined for the same A356 alloy of different SDAS values. The superiority of small SDAS samples becomes more evident when the stress and the flaw size are increased, Figure 9b.

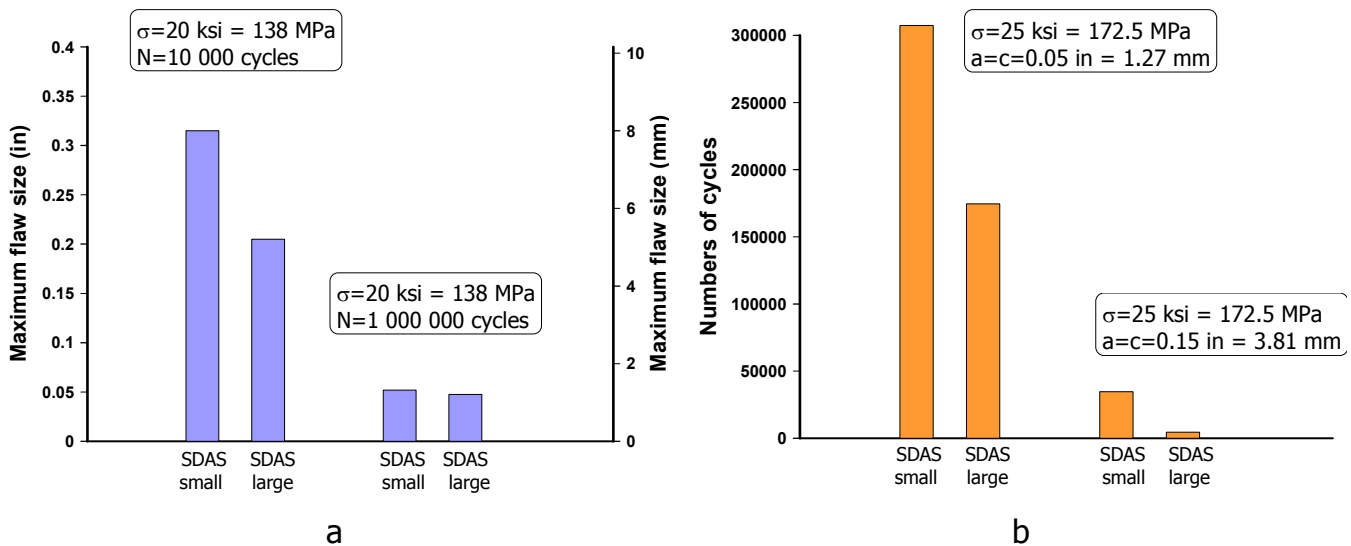


Figure 9. Initial flaw size requirements for selected maximum stress at two fatigue lives (a) and fatigue lives for selected maximum stress and flaw sizes (b) for modified A356 with two SDAS values.

The next two cases, 7 and 8, are directed towards the effects of Si morphology, Figure 10a, and stress ratio, Figure 10b on the fatigue behavior.

7. Knowing that the maximum applied stress during service is $\sigma_{\max}=20$ ksi (138 MPa), and the component is expected to last $N=10,000$ cycles and $N=1,000,000$ cycles respectively, the critical initial flaw sizes were calculated for an A356 alloy in unmodified and modified conditions, Figure 10a.

8. Knowing that the maximum applied stress during service is $\sigma_{\max}=20$ ksi (138 MPa), and the component is expected to last $N=10,000$ cycles and $N=1,000,000$ cycles respectively, the critical initial flaw sizes were calculated for a modified A356 alloy operating under low and high stress ratios, Figure 10b.

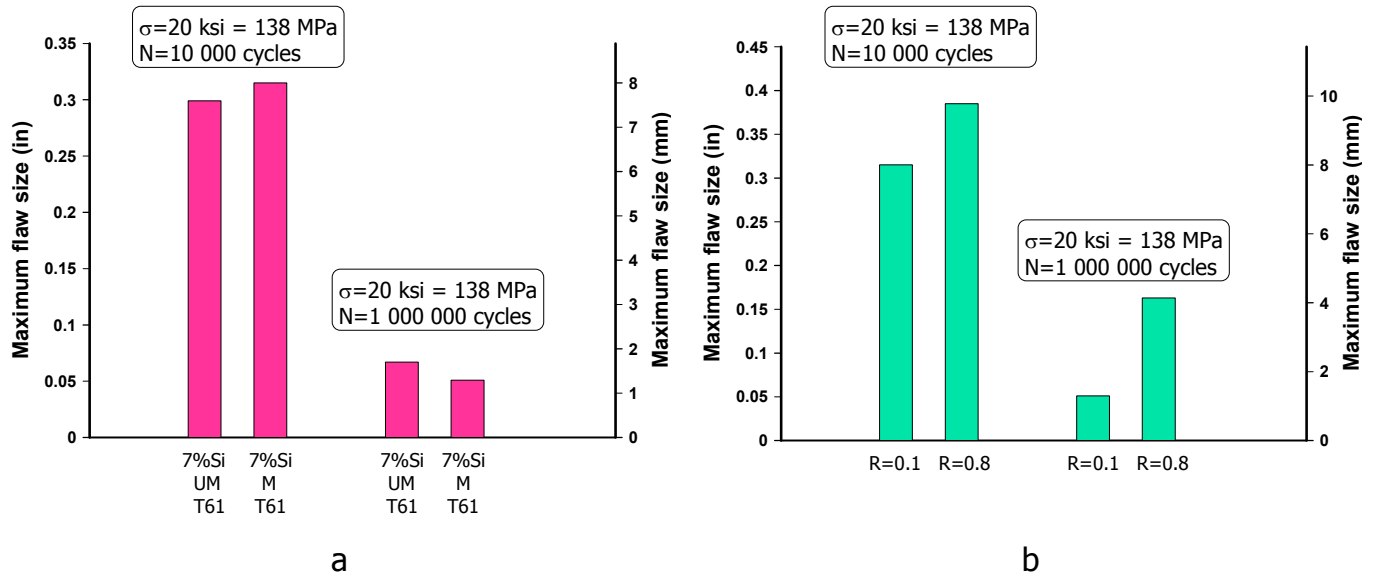


Figure 10. Initial flaw size requirements for selected maximum stress at two fatigue lives: for A356 unmodified and modified alloys (a), and for A356 modified alloys exposed to the same σ_{max} at different stress ratios (b).

As explained earlier, for high cycle fatigue, when most of the component life is spent in the near threshold regime, the unmodified A356 alloy is more resistant, or allows a larger flaw, while in low cycle fatigue the modified alloy shows a better response, case 7 – Figure 10a.

Due to lower crack growth threshold, fracture toughness, and higher crack propagation rates the sample tested under high stress ratio conditions (R=0.8) should exhibit a lower flaw tolerance, or for similar flaw and stress, a significantly lower fatigue life. However, in Figure 10b the opposite behavior is observed. This is due to the fact that in AFGROW software the maximum applied stress is used for the computations instead of a cyclic stress. Therefore for the same maximum applied stress, the cyclic stress is more than four times larger for the tests conducted at R=0.1, which leads to shorter life or lower flaw tolerance. This is an important observation and attention needs to be paid when comparisons of this nature are made. Under similar cyclic stresses, certainly the samples subjected to R=0.8 are significantly less crack growth resistant compared to the R=0.1 tested samples.

The effect of heat treatment (i.e., T61 versus T4) was also addressed using AFGROW. Case 9 addresses the heat treatment effects.

9. Knowing that the maximum applied stress during service is $\sigma_{\max}=20$ ksi (138 MPa), and the component is expected to last $N=10,000$ cycles and $N=1,000,000$ cycles respectively, the critical initial flaw sizes were calculated for a modified A356 alloy in T61 and T4 heat treating conditions, Figure 11.

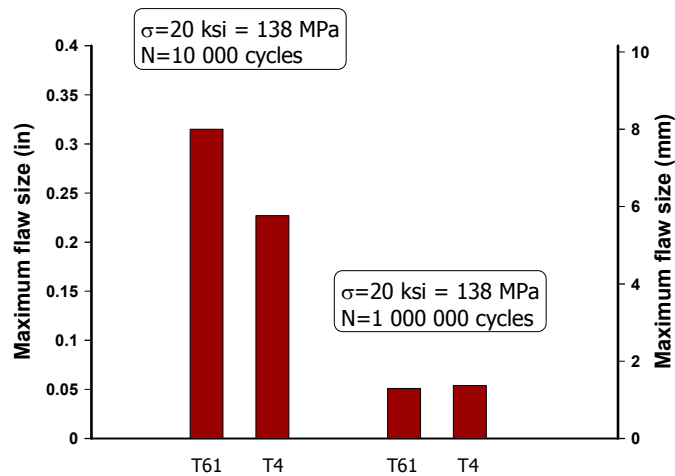


Figure 11. Effect of heat treatment on the flaw size tolerance for a modified A356 alloy.

For low stress levels around $\sigma_{\max}=10$ ksi (69 MPa), the flaw tolerance of the two materials was high and similar for both high cycle and low cycle fatigue. At higher maximum applied stress, the two materials behave similarly in high cycle fatigue, but at low cycle fatigue the artificially aged sample shows higher flaw tolerance or longer life for the same flaw size.

The effects of flaw geometry and characteristics are addressed via cases 10, and 11, as detailed below:

10. Knowing that the maximum applied stress during service is $\sigma_{\max}=20$ ksi (138 MPa), the number of cycles to failure are compared for five flaws geometries/orientations, Figure 12. The flaws are: round of increasing radius 0.0357 in (Figure 12-1), 0.05 in (Figure 12-2), 0.07 in (Figure 12-7), elliptical of the same cross sectional area as the circular of 0.05 in radius, aligned parallel to the normal stress direction (Figure 12-3) and perpendicular to the normal stress direction (Figure 12-4), and elliptical with a larger cross sectional area than 0.05 in circular but smaller than 0.07 in circular (Figures 12-5 and 6).

As can be seen from the results in Figure 12, no significant differences are observed for the round and elliptical flaws of identical cross sectional area regardless of their orientation. However, larger elliptical flaws lead to shorter fatigue lives while smaller flaws provide longer fatigue lives.

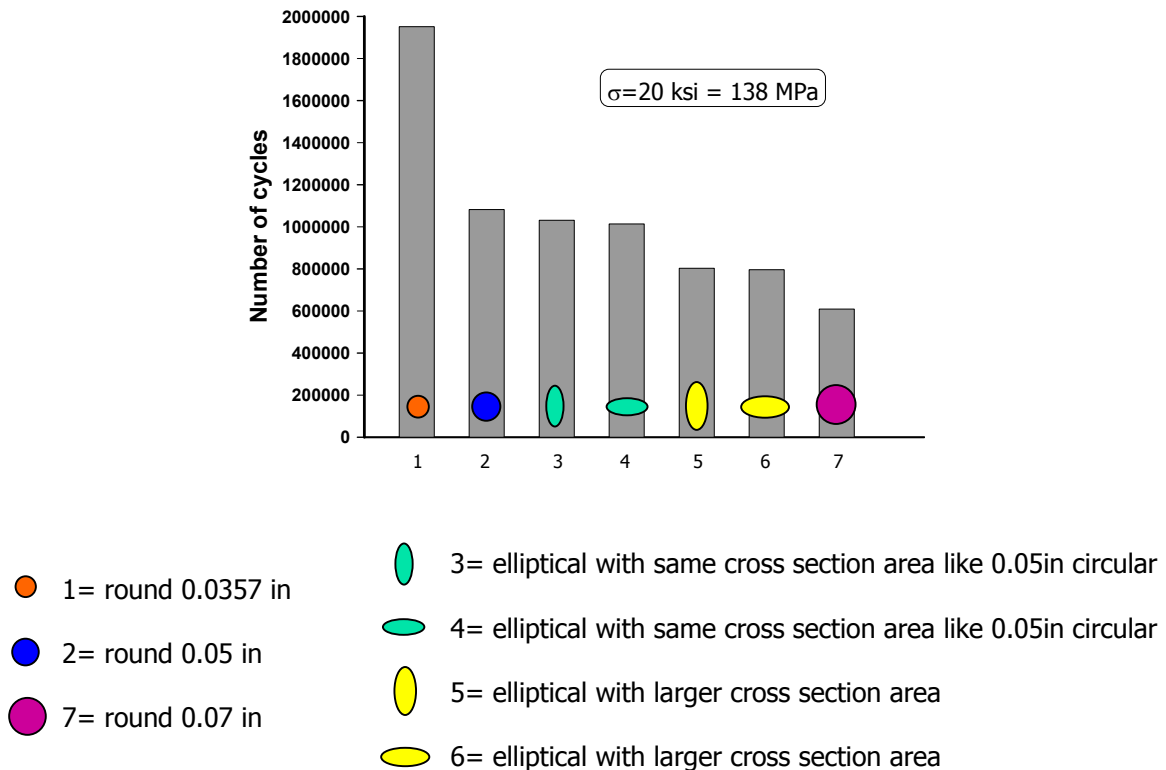


Figure 12. Effect of flaw geometry on the fatigue life of a modified A356 alloy.

11. Another study was conducted on the same specimen geometry, on modified A356 alloys that had different initial flaw types (Figure 4): a center semi-circular edge surface flaw, a center full-circular embedded flaw, and a single edge corner flaw. The critical initial flaw sizes are determined for a given stress $\sigma = 20 \text{ ksi}$ (138 MPa) and several fatigue lives from low cycle to high cycle (Figure 13).

The data for case 11, as seen in Figure 13, points out that center semi-circular edge surface flaw and the single edge corner flaw have similar impact on fatigue life of the alloy at all life regimes (the corner flaw being slightly less tolerant). However, the center full-circular embedded flaw even if is less flaw tolerant in low cycle fatigue becomes more flaw tolerant at high cycle fatigue. This behavior can be explained considering that for the same flaw size stress intensity

factor and stress are higher/lower depending on the flaw type/location (small cracks-edge surface-higher K, σ ; large cracks-embedded-higher K, σ). The number of cycles at which the transition occurs is certainly a function of the applied load. For higher loads the transition occurs at lower number of cycles (Figures 13 and 14).

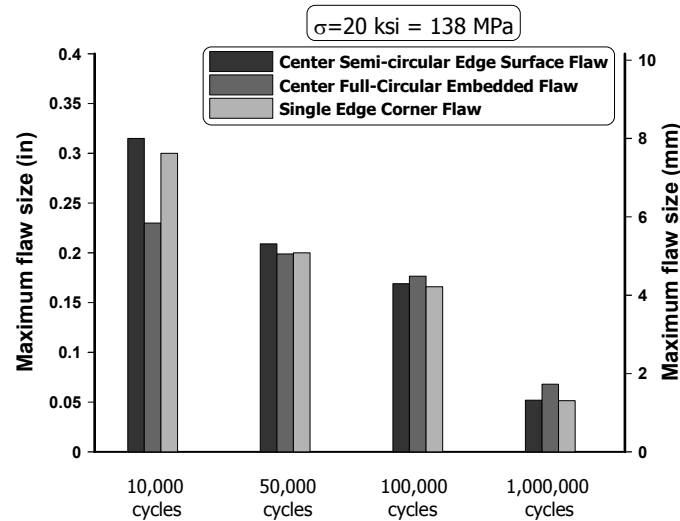


Figure 13. Effect of flaw type on the flaw size tolerance in a modified A356 alloy.

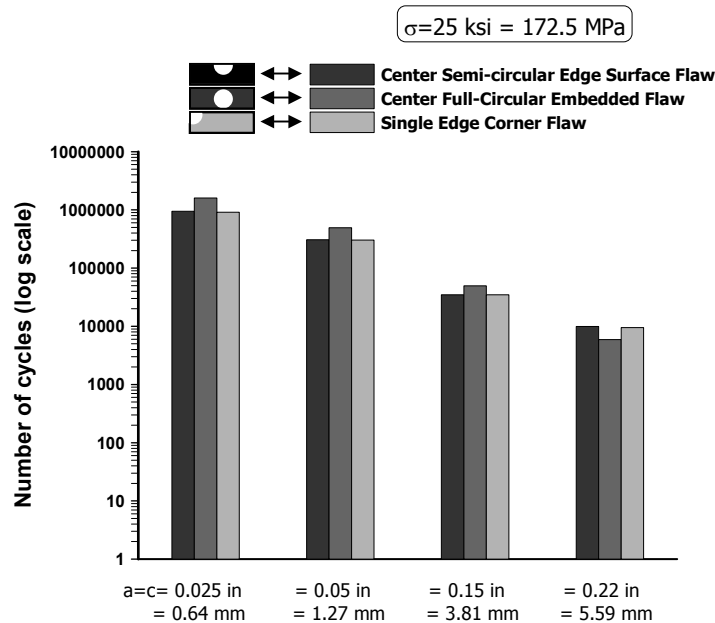


Figure 14. Effect of flaw type on fatigue life of a modified A356 alloy at constant maximum stress of 25 ksi (172.5 MPa) and variable initial flaw size.

Another perspective of the influence of flaw type on the fatigue behavior is presented by comparing the cycles to failure for different flaw sizes (Figure 14) at a specified applied load $\sigma=25$ ksi (172.5 MPa). As pointed out previously, it is seen that center full-circular embedded flaw is more beneficial at high number of cycles. Similar investigations were done for constant flaw size and various stress level and similar conclusions are drawn.

Comparisons between samples with low and high levels of residual stress were run, and better fatigue responses were observed in the latter (due to the presence of large compressive stresses in the tested compact tension specimens). However, the level of residual stress introduced during the water quench is not uniform in all the samples, and large variations from sample to sample are likely to occur. Therefore, design criteria based on high residual stress data can generate significant errors and inconsistencies in the performance of real components. From this perspective, a design based on residual stress free data is recommended along with a thorough understanding of the type of residual stress and a proper selection of the applied stress accordingly. Tensile residual stresses are detrimental to the fatigue behavior and in this case additional precautions need to be taken.

Several additional practical cases were examined using fatigue crack growth data to predict fatigue life – i.e., different flaw geometries (for example elliptical flaws with different alignment with respect to the symmetry axes of the component), different geometries of the component (for example circular, hollow, etc.), as well as other thickness-to-width ratios for rectangular plates, other stress ratios, variable amplitude loading, cases with various levels of residual stress, analyses based on weight function solutions, etc. These are not reviewed here, and follow the same analysis methodology presented above.

AFGROW can also be considered from the alloy/heat treatment optimization and new alloy development perspective by using fatigue crack growth resistance as an alloy design goal.

It must be pointed out that other software packages (similar to AFGROW) are available, such as FASTRAN II and NASGRO, which can be used for comparative analyses.

SUMMARY

Based on the simulated cases, several practical conclusions regarding the applications of different alloys, different microstructures, and heat treatments can be made.

Alloys with high toughness and low threshold (such as modified, A356, modified eutectic, large SDAS alloys, etc.) are appropriate for low cycle fatigue applications, or highly stressed operating conditions, or in cases when large initial flaw sizes are unavoidable, as well as in components that show warning before failure, or parts that after being damaged should still continue to operate (for example a wheel that hit a curb), as well as variable amplitude applications, etc.

Alloys with low toughness and high threshold (such as unmodified, A356, small SDAS alloys, etc.) are suitable for high cycle fatigue when large numbers of cycles are expected of the component and also a catastrophic failure can be tolerated, or low stress applications, components having small initial flaw sizes, etc. Under these conditions materials with higher threshold are preferred even if there is a trade off in fracture toughness acknowledging that the propagation mode contributes with a small percentage to the total life of the component.

The unmodified eutectic alloy with 13%Si is not recommended for fatigue or fracture toughness critical applications due to its low toughness. However, for less critical applications it can be an inexpensive alternative because it is often used without heat treatment.

Heat treatment effect on fatigue crack growth behavior is minimal in high cycle fatigue at any maximum stress level. In low cycle regime, T61 heat treated samples present improved fatigue resistance (higher flaw tolerance or longer fatigue life for a certain flaw).

High stress ratio applications are always more demanding on the material and therefore lower fatigue performance is expected for all materials (compared to low stress ratio applications) when the same cyclic stress $\Delta\sigma$ is applied. However, for the same maximum applied stress, σ_{max} , fatigue life of the samples tested under $R=0.8$ is longer.

High compressive residual stresses increase the life of the component, but residual stress free design is recommended, together with a good understanding of the type of residual stress (compressive residual stresses are beneficial while tensile residual stresses are detrimental to fatigue life).

As a general conclusion it needs to be emphasized that the selection of the material should be made after a complete understanding of the operating conditions the component will be subjected to, and the fatigue life expectations. In tandem, fatigue and fatigue crack growth resistance characteristics need to be coordinated with all the other property requirements, and the material that fulfills all the criteria within tolerable limits (even if this implies a material with lower fatigue crack growth resistance) ought to be selected.

ACKNOWLEDGMENTS

The authors thank Dr. Peggy Jones of General Motors for her valuable recommendations and insight on the AFGROW simulations.

REFERENCES

- [1]. O.H. Basquin, Proc. ASTM 10, Part II (1910) 625.
- [2]. R.W. Smith, M.H. Hirschberg, and S.S. Manson, NASA, TN D-1574, April 1963.
- [3]. L.F. Coffin, Jr., Trans. ASME 76, 1954, p. 931.
- [4]. S.S. Manson, Thermal Stress and Low-Cycle Fatigue, McGraw-Hill, New York, 1960.
- [5]. S.B. Kim, D.A. Koss, D.A. Gerard, in: W.O. Soboyejo, T.S. Srivatsan (Eds.), High Cycle Fatigue of Structural Materials (In Honor of Professor Paul C. Paris), TMS, 1997, pp. 355-369.
- [6]. T.M. Yue, J. of Materials Science 25 (1990) 175-182.
- [7]. L. Wang, D. Apelian, M. Makhlof, AFS Trans. 106 (1998) 155-162.
- [8]. A.A. Dabayeh, R.X. Xu, B.P. Du, T.H. Topper, Int. J. Fatigue 18 (2) (1996) 95-104.
- [9]. M.J. Caton, J.W. Jones, H. Mayer, S. Stanzl-Tschegg, J.E. Allison, Metall. Mater. Trans. A 34A (2003) 33-41.
- [10]. K. Shiozawa, Y. Tohda, S.-M. Sun, Fatigue Fract. Engng Mater. Struct. 20 (2) (1997) 237-247.
- [11]. T. Nishida, J. Mizutani, Y. Mutoh, K. Yoshii, O. Ebihara, S. Miyashita, J. Jap. Inst. of Light Metals 49 (10) (1999) 493-498. (in Japanese)
- [12]. A. Wickberg, G. Gustafsson, L.E. Larsson, SAE Technical Publication 840121 (1984).
- [13]. W. Chen, B. Zhang, T. Wu, D. Poirier, P. Sung, Q.T. Fang, The 1st International Aluminum Casting Tech. Symposium, Rosemont, IL, 13-14 October 1998.
- [14]. Q.G. Wang, D. Apelian, D.A. Lados, J. Light Metals 1 (1) (2001) 85-97.
- [15]. C.M. Sonsino, J. Ziese, Int. J. Fatigue 15 (2) (1993) 75-84.
- [16]. C. Nyahumwa, N.R. Green, J. Campbell, Metall. Mater. Trans. A 32A (2001) 349-358.
- [17]. J.F. Major, AFS Trans. 105 (1997) 901-906.
- [18]. Q.G. Wang, D. Apelian, D.A. Lados, J. Light Metals 1 (1) (2001) 73-84.
- [19]. H. Jiang, P. Bowen, J.F. Knott, J. Mater. Sci. 34 (1999) 719-725.
- [20]. S. Gungor, L. Edwards, Fatigue Fract. Engng Mater. Struct. 16 (4) (1993) 391-403.
- [21]. M.J. Couper, A.E. Neeson, J.R. Griffiths, Fatigue Fract. Engng Mater. Struct. 13 (3) (1990) 213-227.

- [22]. B. Skallerud, T. Iveland, G. Harkegard, *Engng Fract. Mechanics* 44 (6) (1993) 857-874.
- [23]. P.C. Paris, F. Erdogan, *Trans. ASME J. Basic Eng.* 85 (4) (1963) 528-534.
- [24]. R.G. Forman, V.E. Kearney, R.M. Engle, *Trans. ASME J. Basic Eng.* 89 (1967) 459.
- [25]. S. Kumai, J. Hu, Y. Higo, S. Nunomura, *J. Jap. Inst. Light Metals* 45 (4) (1995) 198-203. (in Japanese)
- [26]. D.A. Lados, D. Apelian, "Fatigue Crack Growth Characteristics in Cast Al-Si-Mg Alloys – Part I: Effect of Processing Conditions and Microstructure", submitted to *Mater. Sci. Eng. A* (2003).
- [27]. M. Schaefer, R.A. Fournelle, *Metall. Mater. Trans. A* 27A (1996) 1293-1302.
- [28]. F.T. Lee, J.F. Major, F.H. Samuel, *AFS Trans.* 104 (1996) 785-795.
- [29]. S.-W. Kim, S.-W. Han, U.-J., Lee, K.-D. Woo, *Materials Letters* 58 (2003) 257-261.
- [30]. M.J. Caton, J.W. Jones, J.M. Boileau, J.E. Allison, *Metall. Mater. Trans. A* 30A (1999) 3055-3068.
- [31]. K.S. Chan, P. Jones, Q. Wang, *Mater. Sci. Eng. A341* (2003) 18-34.
- [32]. M. Kubota, Y. Ochi, A. Ishii, R. Shibata, *Mater. Sci. Research. Int.* 4 (3) (1998) 193-199.
- [33]. G.O. Rading, J. Li, J.T. Berry, *AFS Trans.* 102 (1994) 57-61.
- [34]. M.J. Couper, J.R. Griffiths, *Fatigue Fract. Engng Mater. Struct.* 13 (6) (1990) 615-624.
- [35]. K. Shiozawa, S. Sun, R.L. Eadie, *Metall. Mater. Trans. A* 31A (2000) 1137-1145.
- [36]. P.N. Crepeau, S.D. Antolovich, J.A. Worden, in: H.A. Ernst, A. Saxena, D.L. McDowell (Eds.), *Fracture Mechanics: Twenty-Second Symposium (Volume I)*, ASTM STP 1131, ASTM, Philadelphia, PA, 1992, pp. 707-726.
- [37]. ASTM Standard E647, *Standard Test Method for Measurement of Fatigue Crack Growth Rates*, Annual Book of ASTM Standards, Vol. 03.01, 2000.
- [38]. ASTM Standard E1820, *Standard Test Method for Measurement of Fracture Toughness*, Annual Book of ASTM Standards, Vol. 03.01, 2000.
- [39]. <http://afgrow.wpafb.af.mil/downloads/afgrow/pdownload.php>.

CONCLUSIONS

The behavior of the studied Al-Si-Mg alloys in the near threshold regime is dominated by closure mechanisms. The two main sources of closure were found to be residual stress and microstructure induced roughness (Chapter 5). The differences in roughness induced closure were attributed to the crack deflection when encountering Si particles. Unmodified alloys at both 7 and 13%Si levels showed higher threshold and therefore better high cycle fatigue life because the large Si plates caused greater crack deflection and higher roughness induced closure than that observed in modified alloys of the same Si content. Alloys with different SDAS were qualitatively analyzed, and for the larger SDAS alloys higher thresholds were predicted. The same behavior was observed for 319 alloys of different SDAS (Chapter 2). It should be noted that, in addition to Si particle morphology, SDAS is the other critical parameter when designing a microstructure for fatigue crack growth resistance.

With increasing ΔK , the effects of crack closure are less significant, and the fatigue crack growth mechanisms become strongly dependent on the matrix strength and the interface strength between primary α -Al structure and eutectic Si particles. It was observed that with increasing ΔK from lower Region II to upper Region II and Region III, fracture surface roughness increases, increase associated with a change in fatigue crack growth mechanisms. While a flat surface corresponds to a crack propagating along the Al dendritic structure, the rougher surface is a reflection of a preferential growth through the Al-Si eutectic regions. As a general rule a crack always seeks the path of least resistance that is represented by the most damaged microstructural features ahead of it. Therefore, these changes in mechanisms were explained using correlations of the plastic zone size at various ΔK levels with the microstructural features enveloped by it. Small plastic zones restrict the availability of damaged Si particles (or interfaces of the Si particles with the Al matrix) and therefore restrain the possibility of crack meandering. This corresponds to a flat appearance of the crack with sporadic Si encounters. At high ΔK , however, the large plastic zone permits crack meandering through severely damaged Si particles away from the crack front, and this explains the preferential growth through the eutectic regions. Details are given in Chapter 5

In Region III, crack advances entirely through the large Al-Si eutectic regions and ductile tearing becomes the dominant mechanisms at high ΔK . The alloys'

behavior in this region was well correlated with the Si particles' morphology, and a fracture toughness ranking based on Si morphology was observed. Modified alloys generally showed higher fracture toughness, and therefore better low cycle fatigue response. The differences in toughness between the unmodified and the modified alloys were more obvious for the 13%Si alloys compared to the 7%Si alloys because the 13%Si alloys preserve larger differences in Si morphology for a similar solution treatment time (Chapter 5).

At high ΔK levels, fatigue crack growth behavior of cast Al-Si-Mg alloys is less accurately represented by elastic definitions and plasticity and tearing corrections need to be considered. Elastic-Plastic Fracture Mechanics interpretations based on the J-integral concepts were developed such that the "actual" fracture toughness of the materials can be determined directly from fatigue crack growth experiments without the additional need for fracture toughness testing. Excellent agreement between the fracture toughness determined from fatigue crack growth experiments and the values obtained from the static fracture toughness testing was obtained for all samples regardless the obvious differences in ductility level (Chapter 4). In this study, the samples did not meet the dimensional requirements for plane strain fracture toughness testing and therefore with the exception of J_{IC} data, the reported values are all specific to the sample geometry selected.

Differences in the behavior of T4 and T61 samples were observed away from the closure affected regions. While T61 shows a better fatigue crack growth resistance in upper Region II, T4 leads to higher toughness. The behavior of the T4 samples in Region II was explained by considering the alternative paths of least resistance available, as well as the difference in the intensity of localized stress at the crack front and its impact on the matrix/Si particles interface resistance. In Region III, the increased plasticity levels at the crack tip result in more blunted cracks that decrease the local stress, increasing the crack growth resistance and fracture toughness. It can be observed that fatigue crack growth response can be adjusted by changing the thermal treatment without altering the microstructural phases, type, and amount.

In the grain size range investigated (180-520 μm), grain size plays a minimal role in the fatigue crack growth response of the studied alloys, due to the fact that fatigue crack growth advance is controlled by microstructural features smaller than the grain size (Si particles morphology and distribution, SDAS). In the alloys with no eutectic Si (1%Si), grain size shows an effect similar to the one observed in wrought alloys.

Residual stress shows a significantly lower contribution at high ΔK levels considering the decrease in residual stress-to-applied stress ratios. The compressive residual stress introduced during quenching nearly doubled the crack growth thresholds, and increased fracture toughness by approximately 20%.

FUTURE WORK

Heat treatment is a potential method of controlling fatigue and fatigue crack growth response of age-hardenable alloys without any changes in the casting procedure, therefore preserving the microstructure (amount/ size/ shape/ distribution of constituent phases). Solution treatment step in the heat treatment (especially solutionizing time) was proven to affect fatigue crack growth behavior (both threshold and toughness) of the alloys through the morphological changes of the Si particles. However, aging was found to have a significant effect as well through the strength of the Al matrix as a result of the Mg₂Si precipitates (or different stages of GP zones) size and distribution. These effects were observed when the fatigue crack growth response of A356/357 alloys in T61 conditions was compared to the one in T4 and T5 conditions. To clarify the interactions of the matrix hardness (precipitates) with the advancing crack, further TEM investigations are recommended on samples subjected to T4, T5, and T61 heat treatment. Moreover, the additional investigation of T7 heat treated samples (overaged conditions) is considered a good source of information on the effect of precipitates when large incoherent Mg₂Si precipitates are formed. For 319 alloys, other researchers observed that T7 heat treatment changes the crack growth mechanisms as well (reference 18 in Chapter 5). While 319 alloys in T5 and T61 conditions involve an increasing interaction with Si particles with increasing ΔK , T7 samples seem to propagate mostly through the Al matrix with only few interactions with the Si particles. Therefore, TEM studies are needed, first to understand the size and distribution of the precipitates, and second to relate these observations to the growth of the cracks. A parallel study of several alloys of commercial importance is critical for broadening the view of precipitates formation as well as the crack growth differences due to possible coring and precipitate free zones in some of the alloys. This will appropriate allow alloys optimization through heat treatment.

Strength of the Al-matrix/Si particle interface as well as Si particle fracture strength (for different Si morphology, orientation, and Si-Si spacing) are critical parameters needed for a complete understanding of Si particles behavior in the plastic zone. This knowledge facilitates a correct interpretation of the alloys' tendency for Si debonding vs. fracture at different crack driving forces. Quantitative determination of the differences in plastic stress and strain at such Al-Si particles interfaces in alloys with different degrees of ductility (different plastic zone size) require also future investigation.

Fatigue crack growth studies on alloys with large SDAS, hypereutectic alloys, and SSM alloys with different globular α size and distribution, are necessary to confirm the mechanistic predictions provided in this study and also optimize the solidification structure.

Considering that long crack behavior of all alloys (especially in the near threshold regime) is dominated by the effect of closure, special attention needs to be directed towards small fatigue crack growth behavior in order to understand the influence of microstructural features (especially the role of Al matrix-Si particles interfaces) in the absence of closure. In this case, Si particles were considered (see references 10,19 in Chapter 5) to retard fatigue crack growth through a gradual debonding of the undamaged Al matrix-Si particles interface. Plastic zones are too small to cause damage to the Al-Si interfaces and crack retardation mechanisms were invoked. Another important use of small fatigue crack growth data is in improving and validating closure corrective methods (see reference 33 in Chapter 5) so that the difficulty of running small fatigue crack growth tests can be avoided, and still correctly estimate small crack growth behavior.

The fatigue crack growth mechanisms presented in this work were developed for room temperature conditions. However, the applicability of these concepts when high temperature applications are involved needs to be confirmed for alloys with similar compositions/microstructures subjected to thermo-mechanical fatigue conditions.